

**ISTANBUL TECHNICAL UNIVERSITY ★ GRADUATE SCHOOL OF SCIENCE**  
**ENGINEERING AND TECHNOLOGY**

**INVESTIGATION OF THE LUMINESCENCE PROCESSES and WHITE  
LIGHT PRODUCTION FROM Nd<sup>3+</sup> and Cr<sup>3+</sup> DOPED METAL OXIDE NANO-  
POWDERS**

**Ph.D. THESIS**

**Gökhan BİLİR**

**Department of Physics Engineering**

**Physics Engineering Programme**

**JANUARY 2015**



**ISTANBUL TECHNICAL UNIVERSITY ★ GRADUATE SCHOOL OF SCIENCE**  
**ENGINEERING AND TECHNOLOGY**

**INVESTIGATION OF THE LUMINESCENCE PROCESSES and WHITE  
LIGHT PRODUCTION FROM Nd<sup>3+</sup> and Cr<sup>3+</sup> DOPED METAL OXIDE NANO-  
POWDERS**

**Ph.D. THESIS**

**Gökhan BİLİR**

**Department of Physics Engineering**

**Physics Engineering Programme**

**Thesis Advisor: Prof. Dr. Gönül ERYÜREK**  
**Thesis Co-Advisor: Prof. Dr. Baldassare DI BARTOLO**

**JANUARY 2015**



**İSTANBUL TEKNİK ÜNİVERSİTESİ ★ FEN BİLİMLERİ ENSTİTÜSÜ**

**Nd<sup>3+</sup> ve Cr<sup>3+</sup> KATKILI METAL OKSİT NANO-TOZLARINDA LÜMİNESANS  
SÜREÇLERİNİN ARAŞTIRILMASI ve BEYAZ IŞIK ÜRETİMİ**

**DOKTORA TEZİ**

**Gökhan BİLİR  
(509072109)**

**Fizik Mühendisliği Anabilim Dalı**

**Fizik Mühendisliği Programı**

**Tez Danışmanı: Prof. Dr. Gönül ERYÜREK  
Tez Eşdanışmanı: Prof. Dr. Baldassare DI BARTOLO**

**OCAK 2015**



**Gökhan Bilir**, a **Ph.D.** student of ITU **Institute of / Graduate School of Science, Engineering and Technology** with student ID **509072109**, successfully defended the **thesis/dissertation** entitled “**INVESTIGATION OF THE LUMINESCENCE PROCESSES and WHITE LIGHT PRODUCTION FROM Nd<sup>3+</sup> and Cr<sup>3+</sup> DOPED METAL OXIDE NANO-POWDERS**”, which he prepared after fulfilling the requirements specified in the associated legislations, before the jury whose signatures are below.

**Thesis Advisor :**      **Prof. Dr. Gönül ÖZEN** .....  
İstanbul Technical University

**Co-advisor :**          **Prof. Dr. Baldassare DI BARTOLO** .....  
Boston College

**Jury Members :**      **Prof. Dr. Cenap ÖZBEN** .....  
İstanbul Technical University

**Prof. Dr. Ayhan MERGEN** .....  
Marmara University

**Doç. Dr. Haluk ÖZBEK** .....  
İstanbul Technical University

**Doç. Dr. Şaziye UĞUR** .....  
İstanbul Technical University

**Doç. Dr. Rıza DEMİRBİLEK** .....  
Yıldız Technical University

**Date of Submission : 21/11/2014**

**Date of Defense : 19/01/2015**



*To Hilal and Girayhan*



## FOREWORD

Since this dissertation is the product of a 7 years long and a difficult period, there has been material and spiritual support by many people and organizations from the first day until today. I therefore owe to thank all those persons and institutions.

First of all I would like to thank my supervisor Prof. Dr. Gonul Ozen for her helps and supports at every stage of my thesis study. I am grateful her for her continuous guidance and efforts to provide a free working atmosphere without any strict obligations.

I am grateful also to my co-supervisor Prof. Baldassare Di Bartolo who unsparingly gave me his financial and spiritual supports, particularly for considering me and my family as a part of his family and mobilizes his entire means to provide me a comfortable work environment during the two and half years I spent in the U.S. I also would like to thank Mr. Ottavio Forte for his help and friendship. I would like to express my thanks to Prof. John Collins who was guiding me with his knowledge, experience and foresights during the entire time I spent in the U.S. I would like to thank Prof. Marco Bettinelli for giving me the opportunity to work with him.

I am also thankful to Boston College Physics Department and employees, particularly the chairman Prof. Michael Naughton and Jane Carter, for making all departmental facilities available to me.

I want also to thank the Istanbul Technical University and all of the employees, especially the Physics Engineering Department family and my colleagues.

I thank my thesis monitoring committee, Assoc. Prof. Haluk Özbek and Assoc. Prof. Rıza Demirebilek for their time to evaluate my thesis progress reports. I would also like to thank my thesis juries for their time and their valuable suggestions.

I forward my thanks to all persons and organizations, that I may have forgot to mention here, for their contributions.

I would like to express my deepest thanks and love to my dear parents and my brother, especially my father Kenan Bilir who deceased during my studies in the U.S., for sharing all my hardship and joys, unrequitedly supporting me and making many sacrifices to provide opportunities for me to have a good education.

My special and grateful thanks goes to my dear wife Hilal Bilir because she stood by me in any circumstances, with her support, patience, many sacrifices for my education, her belief in me and her love for me.

Finally, I am really grateful to my dear son Girayhan Bilir who turned our grief to joy and brought us happiness by being born close to time of the decease of my father.

December 2014

Gökhan BİLİR  
(Physicist)



## TABLE OF CONTENTS

	<u>Page</u>
<b>FOREWORD</b> .....	<b>ix</b>
<b>TABLE OF CONTENTS</b> .....	<b>xi</b>
<b>ABBREVIATIONS</b> .....	<b>xv</b>
<b>LIST OF TABLES</b> .....	<b>xvii</b>
<b>LIST OF FIGURES</b> .....	<b>xix</b>
<b>SUMMARY</b> .....	<b>xxiii</b>
<b>ÖZET</b> .....	<b>xxv</b>
<b>1. INTRODUCTION</b> .....	<b>1</b>
<b>2. THEORETICAL BACKGROUND</b> .....	<b>5</b>
2.1 Rare Earth Ions .....	5
2.1.1 Common properties of the rare earths .....	9
2.2 Properties of the Yttrium Oxide (Y <sub>2</sub> O <sub>3</sub> ) Crystal .....	10
2.3 Quantum Confinement and Surface Effects .....	12
2.3.1 Quantum confinement effect .....	12
2.3.2 Particle in a one-dimensional potential well .....	12
2.3.3 Particle in a general three-dimensional potential .....	15
2.3.4 Density of states in low dimensional structures .....	16
2.3.5 Low-dimensional structures .....	18
2.3.6 Surface effects .....	19
2.4 Spectroscopic Properties of Lanthanides in Nanocrystals .....	19
2.4.1 Size effects on the structure of electronic levels .....	22
2.4.2 Confinement on excited-state dynamics .....	22
2.4.2.1 Radiative and nonradiative relaxation .....	22
2.4.2.2 Line broadening and shifts .....	24
2.4.2.3 Modification of radiative lifetimes .....	26
2.4.2.4 Modification of phonon density of states and confinement on electron-phonon interaction .....	27
<b>3. MATERIALS AND METHODS</b> .....	<b>29</b>
3.1 Synthesis of the Nd <sup>3+</sup> Doped Y <sub>2</sub> O <sub>3</sub> Nano-Powders .....	29
3.1.1 Thermal decomposition method .....	29
3.2 Structural Characterization of Nd <sup>3+</sup> Doped Y <sub>2</sub> O <sub>3</sub> Nano-powders .....	30
3.2.1 X-ray diffraction (XRD) .....	30
3.2.2 Scanning electron microscope (SEM) .....	31
3.2.3 Transmission electron microscope (TEM) .....	32
3.3 Optical Characterization .....	33
3.3.1 Components of the optical Set-up .....	34
3.3.1.1 Optic components .....	34
3.3.1.2 Sample environment .....	35
3.3.1.3 Signal conditioning .....	35
3.3.2 Luminescence spectral measurements set-up .....	36

3.3.3	Response to pulsed excitation measurements set-up.....	37
<b>4.</b>	<b>FABRICATION AND SPECTRAL INVESTIGATION OF 1% Nd<sup>3+</sup> DOPED Y<sub>2</sub>O<sub>3</sub> NANO-PARTICLES .....</b>	<b>39</b>
4.1	Introduction .....	39
4.2	Experimental .....	40
4.2.1	Preparation of the Nd <sup>3+</sup> doped Y <sub>2</sub> O <sub>3</sub> powders.....	40
4.2.2	Structural characterization.....	40
4.2.3	Spectroscopic measurements.....	41
4.3	Experimental Results.....	42
4.3.1	Structural characterization.....	42
4.3.2	Spectroscopic characterization .....	44
4.4	Discussion of Results .....	50
4.4.1	Structural properties .....	50
4.4.2	Spectroscopic response .....	51
4.5	Conclusions .....	54
<b>5.</b>	<b>SYNTHESIS AND SPECTRAL CHARACTERIZATION OF YTTRIUM OXIDE NANO-POWDERS DOPED WITH Nd<sup>3+</sup> IONS WITH A LARGE RANGE OF CONCENTRATIONS.....</b>	<b>57</b>
5.1	Introduction .....	57
5.2	Experimental Part .....	58
5.2.1	Preparation of the samples .....	58
5.2.2	Structural characterization.....	58
5.2.3	Spectroscopic measurements.....	59
5.3	Experimental Results.....	59
5.4	Discussion of the Results.....	70
5.5	Conclusions .....	71
<b>6.</b>	<b>UNCONVENTIONAL PRODUCTION OF BRIGHT AND EFFICIENT WHITE LIGHT EMISSION BY ND - DOPED AND NOMINALLY UN-DOPED Y<sub>2</sub>O<sub>3</sub> NANO-POWDERS.....</b>	<b>73</b>
6.1	Introduction .....	73
6.2	Experimental.....	74
6.2.1	Preparation of the Y <sub>2</sub> O <sub>3</sub> :Nd <sup>3+</sup> nano-powders .....	74
6.2.2	Structural characterization of the Y <sub>2</sub> O <sub>3</sub> :Nd <sup>3+</sup> samples .....	75
6.2.3	Emission characterization .....	75
6.3	Experimental Results.....	76
6.3.1	Results of 803.5 nm excitation.....	78
6.3.2	Results of 975 nm excitation.....	91
6.4	Discussion of the Results.....	95
6.5	Conclusions .....	98
<b>7.</b>	<b>BROADBAND VISIBLE WHITE LIGHT EMISSION FROM NOMINALLY UN-DOPED AND Cr<sup>3+</sup> DOPED GARNET NANOPOWDERS .....</b>	<b>101</b>
7.1	Introduction .....	101
7.2	Experimental.....	102
7.2.1	Synthesis procedures.....	102
7.2.2	Structural characterization.....	103
7.2.3	Spectroscopic measurements.....	104
7.3	Results and Discussion.....	104
7.3.1	Structural characterization of the samples .....	104
7.3.2	Spectroscopic investigation of the samples.....	107
7.4	Conclusions .....	116

<b>8. LASER DIODE INDUCED WHITE LIGHT EMISSION OF <math>\gamma</math>-Al<sub>2</sub>O<sub>3</sub> NANO-POWDERS .....</b>	<b>117</b>
8.1 Introduction .....	117
8.2 Experimental .....	117
8.3 Experimental Results.....	119
8.4 Discussion of the Results .....	128
8.5 Conclusions .....	130
<b>9. PECULIAR EFFECTS ACCOMPANYING THE PRODUCTION OF WHITE LIGHT BY IR EXCITED NANOPARTICLES.....</b>	<b>131</b>
9.1 Introduction .....	131
9.2 Experimental .....	132
9.3 Experimental Results.....	132
9.4 Peculiar Occurrences .....	135
<b>10. CONCLUSIONS .....</b>	<b>139</b>
<b>REFERENCES .....</b>	<b>143</b>
<b>APPENDIX .....</b>	<b>153</b>
<b>CURRICULUM VITAE.....</b>	<b>171</b>



## **ABBREVIATIONS**

<b>CCT</b>	: Correlated Color Temperature
<b>CIE</b>	: Commission Internationale de L'Eclairage
<b>CRI</b>	: Color Rendering Index
<b>DOS</b>	: Density of States
<b>EDS</b>	: Energy Dispersive X-Ray Spectroscopy
<b>GGG</b>	: Gadolinium Gallium Garnet
<b>Nd</b>	: Neodymium
<b>PDOS</b>	: Phonon Density of States
<b>PMT</b>	: Photomultiplier Tube
<b>REI</b>	: Rare Earth Ion
<b>QD</b>	: Quantum Dot
<b>SEM</b>	: Scanning Electron Microscope
<b>TEM</b>	: Transmission Electron Microscope
<b>XRD</b>	: X-Ray Diffractometer
<b>WL</b>	: White Light
<b>YAG</b>	: Yttrium Aluminium Garnet



## LIST OF TABLES

	<u>Page</u>
<b>Table 2. 1 :</b> The number of 4f electrons ( $n$ ) in trivalent lanthanide ions.....	6
<b>Table 2. 2 :</b> Physical properties of $Y_2O_3$ .....	11
<b>Table 4. 1 :</b> Formulations of yttrium-neodymium alginate solution prepared, synthesis and annealing temperatures and mean particle sizes estimated from Scherrer Equation. ....	39
<b>Table 4. 2 :</b> Best fit parameters ( $\alpha$ , $\alpha$ , $T_D$ , and $\Delta E_0$ ) obtained from line-shift and line- width measurements.....	52
<b>Table 6. 1 :</b> Summary of results when using 803.5 nm excitation. ....	80
<b>Table 6. 2 :</b> Summary of results when using 975 nm excitation. ....	94
<b>Table 7. 1 :</b> Garnet samples under investigation. ....	103
<b>Table 7. 2 :</b> Structural characterization of the garnet samples under investigation. ....	105
<b>Table 9. 1 :</b> The samples studied, synthesizing procedure, average particle sizes..	132



## LIST OF FIGURES

	<u>Page</u>
<b>Figure 2.1</b> : An energy-level diagram for trivalent lanthanide rare earth ions in lanthanum chloride. ....	7
<b>Figure 2.2</b> : The absorption spectrum of Nd <sup>3+</sup> ions in TeO <sub>2</sub> +WO <sub>3</sub> glass system, taken at room temperature (right-hand side). The Dieke diagram levels corresponding to the Nd <sup>3+</sup> ion are shown on the left-hand side. ....	8
<b>Figure 2.3</b> : The low-temperature emission spectrum of Nd <sup>3+</sup> ions in Y <sub>2</sub> O <sub>3</sub> and the Dieke diagram for the Nd <sup>3+</sup> ion for interpretation. ....	9
<b>Figure 2.4</b> : Crystal structure of Y <sub>2</sub> O <sub>3</sub> .....	11
<b>Figure 2.5</b> : Energy levels and wave functions for (a) particle in a well with infinitely high walls, and (b) particle in a well with finite height. (c) The dispersion curve for a free particle. The dots on these curves are the quantized energy values for a particle in a box. In case of a finite well, above U <sub>0</sub> the dispersion curve for a free particle is obtained. ....	14
<b>Figure 2.6</b> : Density of states for 3, 2, 1, and zero dimensional systems .....	18
<b>Figure 3.1</b> : Block diagram of typical TEM with STEM capability .....	33
<b>Figure 3.2</b> : Luminescence setup for the continuous light source.....	37
<b>Figure 3.3</b> : Block scheme of the response to pulsed excitation measurements set-up. ....	38
<b>Figure 4. 1</b> : XRD patterns of the 1 % Nd <sup>3+</sup> doped Y <sub>2</sub> O <sub>3</sub> nanopowders. ....	42
<b>Figure 4. 2</b> : (a) SEM image of as-prepared(500 °C) 1 % Nd <sup>3+</sup> doped Y <sub>2</sub> O <sub>3</sub> nanopowders (inset: corresponding EDS spectrum) (b) SEM image of 1 % Nd <sup>3+</sup> doped Y <sub>2</sub> O <sub>3</sub> nanopowders annealed at 1000 °C (inset: corresponding EDS spectrum).....	43
<b>Figure 4. 3</b> : Representative TEM micrographs of 1 % Nd <sup>3+</sup> doped Y <sub>2</sub> O <sub>3</sub> sample (a) synthesized at 350°C and (b) annealed at 1000°C.....	44
<b>Figure 4. 4</b> : Continuous emission spectra of samples at (a) 35 K and (b) 300 K....	45
<b>Figure 4. 5</b> : Energy level scheme of Nd <sup>3+</sup> in Y <sub>2</sub> O <sub>3</sub> . ....	46
<b>Figure 4. 6</b> : Red-shift of a line position of different samples with respect to the crystal line. ....	47
<b>Figure 4. 7</b> : Variation of linewidth as a function of temperature in 1 % Nd <sup>3+</sup> doped Y <sub>2</sub> O <sub>3</sub> . The dots are experimental results and the solid curve is the theoretical fittings with respect to the crystal line.....	47
<b>Figure 4. 8</b> : Line-shift as a function of temperature 1% Nd <sup>3+</sup> doped Y <sub>2</sub> O <sub>3</sub> . The solid red line is the theoretical fitting to the crystals' experimental data.....	48
<b>Figure 4. 9</b> : Response to pulsed excitation results of all powders at (a) 33 K (b) 300K (c) 600 K (d) 700 K. ....	49
<b>Figure 4. 10</b> : Variation of lifetimes with the temperature.....	50

<b>Figure 5. 1 :</b> XRD patterns of the samples (a) as-synthesized, (b) annealed at 1000 °C. ....	61
<b>Figure 5. 2 :</b> SEM images of the (a) 0.2 %, (b) 0.5 %, (c) 1 %, (d) 2 %, (e) 5 %, (f) 10 % Nd <sup>3+</sup> doped Y <sub>2</sub> O <sub>3</sub> annealed at 1000 °C. ....	62
<b>Figure 5. 3 :</b> Continuous emission spectra at (a) 30 K and (b) 300 K. ....	63
<b>Figure 5. 4 :</b> Representative broadening and shifting of the sharp emission peaks of 0.2 % Nd <sup>3+</sup> doped Y <sub>2</sub> O <sub>3</sub> . ....	64
<b>Figure 5. 5 :</b> Particle size dependence of the emission spectra of 10 % Nd <sup>3+</sup> doped Y <sub>2</sub> O <sub>3</sub> . ....	65
<b>Figure 5. 6 :</b> Decay patterns of the samples with 20 nm particle size at (a) 30 K, (b) 300 K and (c) the variation of the decay times as function of concentration. ....	66
<b>Figure 5. 7 :</b> Decay patterns of the samples with 60 nm particle size at (a) 30 K, (b) 300 K and (c) the variation of the decay times as function of concentration. ....	67
<b>Figure 5. 8 :</b> Variation of the decay times of the samples with (a) 20 nm and (b) 60 nm particle sizes as a function of temperature. ....	68
<b>Figure 5. 9 :</b> Variation of the decay times as a function of particle size at (a) 30 K and (b) 300 K. ....	69
<b>Figure 6. 1 :</b> XRD patterns of the samples. ....	77
<b>Figure 6. 2 :</b> Representative SEM image of the Y <sub>2</sub> O <sub>3</sub> :Nd(2 %). ....	78
<b>Figure 6. 3 :</b> Environment temperature dependence and the general aspect of the white light spectrum under 803.5 nm excitation (a) uncorrected spectrum of 20% Nd doped sample (b) uncorrected spectrum of un-doped sample (c) corrected spectrum of 20% Nd doped sample for system response (d) corrected spectrum of un-doped sample for system response. ....	79
<b>Figure 6. 4 :</b> (a) Measured spectrum of 20% Nd doped sample by using illuminance meter (b) measured spectrum of un-doped sample by using illuminance meter (c) the CIE coordinates and the measured CCT, CRI values for 20% Nd doped sample (d) the CIE coordinates and the measured CCT, CRI values for un-doped sample. ....	80
<b>Figure 6. 5 :</b> (a) Measured spectrum, (b) CCT, CRI and illuminance values, and (c) CIE coordinates of a commercial 60W incandescent bulb obtained by using illuminance meter. ....	82
<b>Figure 6. 6 :</b> Pressure dependence of the white light intensity in nominally un-doped Y <sub>2</sub> O <sub>3</sub> . ....	83
<b>Figure 6. 7 :</b> White light intensity variation with pumping power in nominally un-doped Y <sub>2</sub> O <sub>3</sub> . ....	84
<b>Figure 6. 8 :</b> Dependence of decay patterns on environment temperature in nominally un-doped Y <sub>2</sub> O <sub>3</sub> . ....	85
<b>Figure 6. 9 :</b> Variation of decay patterns with environment pressure in nominally un-doped Y <sub>2</sub> O <sub>3</sub> . ....	85
<b>Figure 6. 10 :</b> Dependence of decay patterns on pumping power in nominally un-doped Y <sub>2</sub> O <sub>3</sub> . ....	86
<b>Figure 6. 11 :</b> Rise pattern dependence on pumping power in nominally un-doped Y <sub>2</sub> O <sub>3</sub> . ....	87
<b>Figure 6. 12 :</b> Pumping power dependence of the white light spectrum in 20 % Nd doped Y <sub>2</sub> O <sub>3</sub> with size of 26 nm. ....	88

<b>Figure 6. 13 :</b>	White light decay patterns variation with the Nd concentration. ....	88
<b>Figure 6. 14 :</b>	Rise pattern dependence on Nd concentration. ....	89
<b>Figure 6. 15 :</b>	Dependence of decay patterns on powder size in 10 % Nd Y <sub>2</sub> O <sub>3</sub> . ....	90
<b>Figure 6. 16 :</b>	Rise pattern dependence on powder size 10 % Nd Y <sub>2</sub> O <sub>3</sub> . ....	90
<b>Figure 6. 17 :</b>	General aspect of the white light spectrum under 975 nm excitation (a) uncorrected spectrum of 20% Nd doped sample (b) uncorrected spectrum of un-doped sample (c) corrected spectrum of 20% Nd doped sample for system response (d) corrected spectrum of un-doped sample for system response. ....	91
<b>Figure 6. 18 :</b>	(a) Measured spectrum of 20% Nd doped sample by using illuminance meter (b) measured spectrum of un-doped sample by using illuminance meter (c) the CIE coordinates and the measured CCT, CRI values for 20% Nd doped sample (d) the CIE coordinates and the measured CCT, CRI values for un-doped sample. ....	92
<b>Figure 6. 19 :</b>	The change of the WL spectrum under 975 nm excitation with time.	93
<b>Figure 6. 20 :</b>	The change of the WL spectrum with changing pumping power of 975 nm laser diode. ....	93
<b>Figure 6. 21 :</b>	Power dependence of the WL intensity under 975 nm excitation. ....	94
<b>Figure 7. 1 :</b>	(a) Spectral profiles of the broad band emission for (YAG) <sub>co</sub> and GGG:Cr (b) corrected spectra of YAG-Co and GGG-Cr for system response. ....	107
<b>Figure 7. 2 :</b>	(a) Measured spectrum for (YAG) <sub>co</sub> by using illuminance meter (b) measured spectrum for GGG:Cr by using illuminance meter (c) CIE coordinates for (YAG) <sub>co</sub> (d) CIE coordinates for GGG:Cr (e) CCT, CRI and illuminance values for (YAG) <sub>co</sub> (f) CCT, CRI and illuminance values for GGG:Cr. ....	108
<b>Figure 7. 3 :</b>	Temperature evolution of the broad band emission of GGG:Cr in the range 33-300 K. ....	109
<b>Figure 7. 4 :</b>	Evolution of the broad band peak intensity as a function of the diode laser power for (YAG) <sub>co</sub> and GGG:Cr. The atmospheric pressure was 0.03 mbar. ....	110
<b>Figure 7. 5 :</b>	Evolution of the broad band peak intensity as a function of the atmospheric pressure for GGG:Cr. The excitation power was 2 W. ....	113
<b>Figure 7. 6 :</b>	Decay of the broadband emission intensity at 675 nm as a function of the atmospheric pressure for GGG:Cr at room temperature. The excitation power was 2 W. ....	114
<b>Figure 7. 7 :</b>	Temporal rise of the broadband intensity at 675 nm as a function of the excitation power at ambient pressure (0.03 mbar). ....	115
<b>Figure 8. 1 :</b>	Scheme of the sample environment. ....	118
<b>Figure 8. 2 :</b>	(a) Spectral profile of the WL emission from $\gamma$ -Al <sub>2</sub> O <sub>3</sub> nano-powders before and after grinding, (b) corrected spectra for the system response, (c) measured spectrum under 975 nm excitation by using illuminance meter, (d) measured spectrum under 803 nm excitation by using illuminance meter. ....	120
<b>Figure 8. 3 :</b>	(a) CIE coordinates of WL under 975 nm excitation, (b) CIE coordinates of WL under 803 nm excitation, (c) CCT, CRI and illuminance values of WL under 975 nm excitation, (d) CCT, CRI and illuminance values of WL under 803 nm excitation. ....	121

<b>Figure 8. 4 :</b>	Pumping laser power dependence of the WL emission intensity. ....	122
<b>Figure 8. 5 :</b>	Pumping laser power dependence of the WL spectrum. ....	123
<b>Figure 8. 6 :</b>	Pressure dependence of the WL emission intensity. ....	124
<b>Figure 8. 7 :</b>	Pumping laser power dependence of the decay pattern of the WL emission. ....	125
<b>Figure 8. 8 :</b>	Pumping laser power dependence of the rise pattern of the WL emission. ....	125
<b>Figure 8. 9 :</b>	Decay times measured at different wavelength positions in the WL spectrum. ....	126
<b>Figure 8. 10 :</b>	Risetimes measured at different wavelength positions in the WL spectrum. ....	126
<b>Figure 8. 11 :</b>	Environment temperature dependence of the decay pattern of the WL. .....	127
<b>Figure 8. 12 :</b>	Environment temperature dependence of the rise pattern of the WL. .....	127
<b>Figure 9. 1 :</b>	WL spectrum of all samples. The spikes in the spectrum are due to spurious modes in the laser diode emission. ....	133
<b>Figure 9. 2 :</b>	Rise pattern dependence on pumping power in un-doped $\text{Y}_2\text{O}_3$ (803.5 nm excitation). ....	135
<b>Figure 9. 3 :</b>	Rise pattern of un-doped $\text{Y}_2\text{O}_3$ under 975 nm excitation. The inset is the expanded sharp rise of the pattern. ....	136
<b>Figure 9. 4 :</b>	The blue shift of the WL spectrum of $\text{Y}_2\text{O}_3$ with time under 975 nm excitation. ....	137
<b>Figure 9. 5 :</b>	Representative decay patterns of nominally un-doped $\text{Y}_2\text{O}_3$ .measured at different part of the WL spectrum. ....	137
<b>Figure 9. 6 :</b>	1/e time distribution of all samples as a function of measured wavelength. ....	138

# **INVESTIGATION OF THE LUMINESCENCE PROPERTIES and WHITE LIGHT PRODUCTION FROM Nd<sup>3+</sup> and Cr<sup>3+</sup> DOPED METAL OXIDE NANO-POWDERS**

## **SUMMARY**

The main focus of this thesis is to provide a better understanding of the effect of the crystalline size on the luminescence properties of the Nd<sup>3+</sup> doped Y<sub>2</sub>O<sub>3</sub> nano-powder which is one of the best host materials for rare earth ions. Hence, the present research includes the synthesis, structural and optical characterization of Y<sub>2</sub>O<sub>3</sub>:Nd<sup>3+</sup> nano-powders.

The nano-crystals of Y<sub>2</sub>O<sub>3</sub> doped with different Nd<sup>3+</sup> concentrations were synthesized using the thermal decomposition method which is based on the thermal decomposition of the yttrium-neodymium alginate gels. The powders were thermally treated to control the particles' sizes at temperatures ranging from 600 to 1400 °C. The synthesized powders were then structurally characterized to determine the size of the nano-particles, the morphology and the crystalline phases occurred using X-ray diffractometer and electron microscopes.

The continuous emission spectra and the response to pulsed excitation measurements were conducted on the samples to determine the luminescence properties of the materials studied and to see the effect of the nano-size on the luminescence properties of the materials. The results of the optical characterization showed that the samples have enough strong emission even if they are in nano-size form and the luminescence properties of the materials are strongly related to the size of the particles. It was also shown that the Nd<sup>3+</sup> concentration has a decisive role on the emission properties of the materials and concentration quenching effect takes place due to increasing dopant ion interactions at higher dopant concentrations.

Another most important finding of this thesis which was not in its original purpose and which led us to make a patent application was the production of a bright, wideband white light emission from the studied nano-powders induced by a laser diode output. We determined most of the properties of this WL emission in detail and showed that the obtained white light emission was comparable with that of a commercial incandescent lamps and was 35 % more efficient than that of an incandescent lamp.



# **Nd<sup>3+</sup> ve Cr<sup>3+</sup> KATKILI METAL OKSİT NANO-TOZLARINDA LUMİNESANS SÜREÇLERİNİN ARAŞTIRILMASI ve BEYAZ IŞIK ÜRETİMİ**

## **ÖZET**

Her geçen gün gelişen teknolojiyle birlikte teknolojinin her alanında kullanılmak üzere yeni, uygun ve optimum özelliklere sahip malzeme ihtiyacı da artmaktadır. Özellikle fotonik teknolojisindeki hızlı gelişime paralel olarak yeni, optimum özelliklere sahip konak malzeme ihtiyacı da artmaktadır. Bu bağlamda ihtiyacı karşılayabilmek adına ilgi, boyutları küçüldükçe külçe kristal formlarına göre daha farklı ve gelişmiş optik, termal, manyetik vb gibi özellikler gösteren nano – boyutlu malzemeler üzerine odaklanmıştır. Bilhassa ıslak kimyasal metotların kullanımı ile nano – boyutlu malzeme sentezindeki önemli gelişmeler ve bu yöntemlerin ucuz olması, düşük sıcaklıklarda malzeme sentezine imkan tanımları ve malzemelerin tek külçe kristallerinin büyütülmesinin zor, imkansız veya maliyetleri artıran çok yüksek sıcaklıkları gerektirdiği durumlarda kolayca malzeme sentezine imkan tanımlarından dolayı nano – boyutlu malzemeler üzerindeki ilgiyi oldukça artırmıştır. Dolayısıyla bu tez çalışmasının başlıca amacı kristal tane boyutunun, nadir toprak iyonları için en iyi konak malzemelerinden biri olan Nd<sup>3+</sup> iyonları ile katkılanırılmış Y<sub>2</sub>O<sub>3</sub> nano-tozlarının luminesans özellikleri üzerindeki etkisinin daha iyi anlaşılmasını sağlamaktır. Dolayısıyla bu çalışma, Y<sub>2</sub>O<sub>3</sub>:Nd<sup>3+</sup> nano-tozlarının sentezi, yapısal ve optik karakterizasyonunu içermektedir.

%0.2 ile %10 aralığında değişen farklı konsantrasyonlarda Nd<sup>3+</sup> katkılanırılmış Y<sub>2</sub>O<sub>3</sub> nano-kristalleri, itriyum-neodim aljinat jellerinin termal bozunması temeline dayanan termal bozunma tekniği kullanılarak sentezlendi. Sentezleme sıcaklığının malzemelerin üretimi ve kristal tane boyutları üzerindeki etkisini araştırmal amacıyla malzemeler 350°C ile 500°C arasında değişen sıcaklıklarda sentezlendi. Tavlama sıcaklığının kristal tane boyutu üzerindeki etkisini araştırmak ve kristal tane boyutlarını kontrol etmek amacıyla tozlara 600 ila 1400 °C arasında değişen sıcaklıklarda termal işlem uygulandı. Sonrasında sentezlenen nano-tozların kristal tane boyutları, morfolojileri ve oluşan kristal fazlarını belirlemek için X-ışını difraktometresi ve elektron mikroskopları kullanılarak yapısal olarak karakterize edildi. Sentezi yapılan malzemelerin 10.6051 Å örgü sabiti ile kübik itriyum oksit fazında oldukları ve bunun dışında başka herhangi bir faz içermedikleri yapılan yapısal karakterizasyon sonucu belirlendi. Sentezlenen malzemelerin kristal boyutlarının sentezleme ve tavlama sıcaklığındaki artışla doğru orantılı olarak arttığı ve malzemelerin kristal boyutlarının 14 – 250 nm arasında değiştiği Scherrer Eşitliği kullanılarak X-ışını desenleri kullanılarak belirlendi. Yapılan elektron mikroskop ölçümleri de Scherrer Eşitliği kullanılarak elde edilen kristal boyutlarını doğrulamıştır.

Çalışılan malzemelerin luminesans özelliklerini belirlemek ve nano-boyutun malzemelerin luminesans özellikleri üzerindeki etkisini görmek için malzemelerde sürekli emisyon spektrumları ve atımlı uyarıma tepki ölçümleri gerçekleştirildi.

Optik karakterizasyon sonuçları, malzemelerin nano-boyutlu olmalarına rağmen halen daha yeterince güçlü emisyonu sahip olduklarını ve malzemelerin luminesans özelliklerinin kristal tane boyutlarına sıkıca bağlı olduğunu gösterdi. Malzemelerin kristal boyutları küçüldükçe emisyon piklerinin şiddetlerinin düştüğü ve yine pik genişliklerinin (FWHM) arttığı belirlendi. Ortam sıcaklığına bağlı olarak gerçekleştirilen emisyon ölçümleri de malzemelerin emisyon piklerinin artan ortam sıcaklığıyla kaydıklarını ve pik genişliklerinin arttığını göstermiştir. Ayrıca  $Nd^{3+}$  konsantrasyonunun malzemelerin emisyon özellikleri üzerindeki etkileri araştırılmış ve iyon konsantrasyonunun emisyon özellikleri üzerinde belirleyici rol oynadığı belirlenmiştir. Artan katkı konsantrasyonu ile düşük konsantrasyonlarda ihmal edilebilir düzeyde olan katkı iyonu etkileşimlerinin baskın hale geldikleri ve bundan kaynaklanan çapraz durulma yolu ile konsantrasyon sönümlenmesi etkisinin ortaya çıktığı gösterilmiştir. Ancak nano – boyut ile konsantrasyon sönümlenmesinin külçe kristallere oranlar daha yüksek konsantrasyonlarda gerçekleştiği belirlenmiştir.

Atımlı uyarıma tepki ölçümleri sonucunda elde edilen malzemelerin bozunma eğrilerinin eksponansiyel olmadıkları görülmüş ve sadece %1 Nd katkılı  $Y_2O_3$  tek kristali için eksponansiyel bozunma eğrisi elde edilmiştir. En uzun yaşam süresi tek kristal için elde edilmiş olup malzemelerin yaşam sürelerinin azalan kristal boyutu ile azaldıkları belirlenmiştir. Malzemelerin yaşam sürelerinin en küçük boyutlu malzemeden en büyüğüne doğru 50 – 200  $\mu s$  arasında değiştiği bulunmuştur. %1  $Nd^{3+}$  katkılı  $Y_2O_3$  tek kristali için ise en uzun yaşam süresi ölçülmüş olup değerinin 250  $\mu s$  civarında değiştiği belirlenmiştir. Yine benzer şekilde azalan kristal tane boyutu ile malzemelerin bozunma eğrilerinin eksponansiyellikten daha fazla saptıkları belirlenmiştir. Artan iyon konsantrasyonu ile de benzer bir eksponansiyellikten daha fazla sapma gözlenmiştir.

Bu tez çalışmasının orijinal kapsamı içerisinde olmayan ancak bizi farklı mecralara ve patent başvurusuna sürükleyen bir diğer ve en önemli bulgularından biri, 803.5 nm ile 975 nm dalgaboyunda çalışan lazer diyot emisyonlarının indüklediği çalışılan nano-tozlardan yayılan parlak ve geniş bantlı beyaz ışık üretimidir. Elde edilen bu beyaz ışık emisyonunun karakteristikleri sürekli emisyon spektrumları, atımlı uyarıma tepki, CIE koordinatları, renk sıcaklığı, luminesans vb gibi ölçümler yapılarak belirlendi. Yapılan ölçümler elde edilen geleneksel olmayan beyaz ışık emisyonunun 400 – 1100 nm dalgaboyu aralığında geniş bir bant olduğunu gösterdi. İlk olarak Nd katkılı itriyum oksit nano – tozlarında gözlenen beyaz ışık emisyonu sonradan %99.9999 oranında saf katkısız  $Y_2O_3$  nano – tozlarında da gözlemlendi. Ultra saf nano – tozlarda da bu emisyonun gözlenmesi bu olgunun nadir toprak katkısı tarafından asist edilse de katkıdan bağımsız olduğunu ve konak malzemenin ve nano – boyutun bir özelliği olduğu belirlendi. Beyaz ışık emisyonunun kristal tane boyutu, nadir toprak iyon konsantrasyonu, sıcaklık, basınç, uyarıcı ışık kaynağının dalgaboyu ve gücü gibi etkilere bağımlılıkları detaylı bir biçimde araştırıldı. Elde edilen beyaz ışık emisyonunun şiddetinin basınç, uyarıcı ışık kaynağının gücü gibi parametrelere güçlü bir biçimde bağlı olduğu ve beyaz ışık emisyonunun gözlemlenebilmesi için uyarıcı eşik gücüne gereksinim olduğu belirlendi. Nadir toprak iyon konsantrasyonu varlığının beyaz ışık üretim sürecini kolaylaştırdığı ve artan iyon konsantrasyonu ile doğru orantılı olduğu gözlemlenmiştir. Özellikle katkısız ultra saf  $Y_2O_3$  nano – tozlarından elde edilen beyaz ışık emisyonunun özellikleri ticari akkor lambalarla mukayese edildi ve 60W ticari akkor lambadan % 35 daha verimli olduğu gösterildi.

Nano – boyutlu  $Y_2O_3$  nano – tozlarından elde edilen beyaz ışığın karakterizasyonunu müteakip farklı kristallerden de bu ışımanın elde edilip edilemeyeceği araştırıldı. Bu

bağlamda sırasıyla kimyasal çökeltme ve Pechini metotları kullanılarak elde edilmiş, 55 ve 78 nm boyutlarındaki katkısız ve  $\text{Cr}^{3+}$  katkılı YAG (itriyum alüminyum garnet) ve GGG (galyum gadolinyum garnet) nano – tozlarından beyaz ışık üretimi araştırıldı. Yapılan denemelerde bu malzemelerden de beyaz ışık çıkışı gözlemlendi. Benzer şekilde bu malzemelerden elde edilen beyaz ışığın kristal tane boyutu, iyon konsantrasyonu, sıcaklık, basınç, uyarıcı ışık kaynağının dalga boyu ve gücü gibi etkilere bağlılığı detaylı bir biçimde araştırıldı. Katkılı malzemelerde beyaz ışık üretim sürecinin daha kolay olduğu ancak katkı iyonları olmadan da beyaz ışık üretilebileceği gösterildi. YAG ve GGG nano – kristallerinden de beyaz ışık çıkışının gözlemlenebilmesi bu beyaz ışık olgusunun tamamen malzemelerin boyutuyla alakalı olduğunu doğrulamıştır.



## 1. INTRODUCTION

Synthesis, structural and optical characterization of new and suitable materials are very important in photonics technology due to the increasing materials requirement as a result of the fast developments in this field. Phosphor materials doped with different +3 valence rare earth ions (REI) such as glasses, crystals, nanopowders, quantum dots (QD) etc. are candidates to meet these requirements in photonics technology. These materials have attracted more interest due to their potential applications to optoelectronics and photonics [1-4]. In particular, they have many application areas such as displays, florescent lamps, light emitting diodes and bio-sensing. Some phosphor materials converted infrared light to visible radiation, and are known as “optical transducers” [5].

REIs generally show an emission due to electronic transitions between the energy levels of the  $4f^n$  configuration. These 4f electrons are well-protected from the crystal field by the  $5s^2$  and  $5p^6$  electrons. So, the host material has a very small effect on REI energy levels. Among these REIs there is a particular interest in Neodymium ( $Nd^{3+}$ ) due to its strong absorption at about 808 nm, which matches with the emission wavelength of the commercially available laser diodes [6].

REIs doped materials have a very wide application area in photonics technology; a lot of research articles can be found in the literature about them. Their selection varies depending on the particular application. The priority target in the production and development of a laser is to increase its quantum yields in the wavelength range of interest. The factor that directly affects the quantum yield is the energy loss due to non-radiative interactions. So, it is important to select a material with minimum non-radiative energy loss.

In particular, among these materials, rare earth ions doped cubic  $Y_2O_3$  (yttria) crystals with controllable size and morphology are worthy of investigation due to their excellent properties, such as stability, high thermal conductivity, high corrosion resistance, wide spectral range optical transparency (0.2 – 8  $\mu m$ ) and a high

refractive index ( $\sim 1.8$ ). Also, yttria is one of the best host material for REIs due to some similarities of  $Y^{3+}$  with the REIs such as chemical properties and ionic radius. Yttria is a sesquioxide with a higher melting point ( $\sim 2410^\circ\text{C}$ ) and a phonon energies of about  $\sim 430 - 550\text{ cm}^{-1}$  [7, 8].

Synthesis, structural and optical characterization of the materials with nano-sizes have been studied over the last decade. Due to the size confinement effect, nanostructured materials possess optical, magnetic and thermal properties distinct from those of their bulk counterparts. It has been proven that as the size of the materials decreases, some optical, magnetic and thermal features of the materials are enhanced. It is expected in general that confinement may affect interionic electronic and vibronic (electron-phonon) interactions. Therefore, both radiative and nonradiative relaxation processes of optical centers in nanocrystals may be significantly influenced.

REIs are particularly effective as luminescent centers in host lattices and are commonly utilized to produce high quantum efficiency bulk phosphors. Unlike the semiconductor QDs where the electronic states are spatially extended and thus quantum confined, REI 4f electronic states are highly localized and unaffected by reduced dimensions. However nanophosphor phonon levels are delocalized and the phonon density of states is reduced by particles of nano dimensions. Because phonons are responsible for the non-radiative relaxations of luminescence in nanophosphors, and because these modes are cut off due to spatial confinement, the optical properties of nanophosphors will differ from those of their bulk counterparts [9, 10].

It is difficult to grow yttria single crystals with large dimensions and high optical quality with traditional crystal growth techniques from the melt due to the high melting temperature ( $\sim 2400^\circ\text{C}$ ) of yttria. It is also very expensive to growth yttria by using these techniques. Since these techniques are very expensive and it is difficult to obtain single crystals of yttria, in recent years, many wet chemical techniques described in literature have been used for synthesizing REIs doped yttria nanopowders such as chemical co-precipitation [11], combustion [12], sol-gel [13], chemical vapor deposition [14] etc. Thermal decomposition technique used in this study is also a cheap and efficient wet chemical technique to obtain yttria nanopowders.

Most of the research on  $\text{Y}_2\text{O}_3$  systems has concentrated on the synthesis with different REI dopants such as Europium ( $\text{Eu}^{3+}$ ) [2, 15], Thulium ( $\text{Tm}^{3+}$ ) [16], Erbium ( $\text{Er}^{3+}$ ) [17] ions, reduction and controlling of the particle sizes, structural and optical characterization and some applications such as biosensing, displays, lighting etc. There is not much detailed information available for the luminescence properties of the  $\text{Nd}^{3+}$  doped  $\text{Y}_2\text{O}_3$  powders and the effect of confinement on the luminescence properties of these powders.

In this study synthesis, structural and optical characterization of Neodymium ( $\text{Nd}^{3+}$ ) ions doped  $\text{Y}_2\text{O}_3$  nano-powders were performed in a systematic way. The powders were synthesized at different temperatures by using thermal decomposition technique and annealed at temperatures between 600 – 1400 °C to control the particle sizes. The structure, morphology and particle sizes were investigated by using X-ray diffraction, Scanning Electron Microscope (SEM) and Transmission Electron Microscope (TEM) methods. Emission spectra, response to pulsed excitation, line-width and the line-shift measurements were performed in order to investigate the effect of the particle sizes on the luminescence properties of the samples.

The outline of this thesis is as follows: The theoretical background such as physical properties of  $\text{Y}_2\text{O}_3$  crystal, properties of REIs, surface effects and effect of size confinement are presented in Chapter 2. Chapter 3 deals with the experimental procedures used for the synthesis of nano-powders, structural characterization and optical characterization. The results of the structural and optical characterization and the production of white light are presented in Chapter 4 to 9. The conclusions and the prospects for future studies of this study are given in Chapter 10.



## 2. THEORETICAL BACKGROUND

### 2.1 Rare Earth Ions

The rare earth ions (REI) are also called lanthanide ions are commonly used as luminescence activation centers in photonic materials and have wide range of applications in phosphors, lasers, amplifiers, biological sensors etc. They are formed by ionization of a number of atoms with an atomic numbers range from 58 to 70 which are ranging from the Cerium (Ce) which has an electronic configuration of  $5s^2 5p^6 5d^1 4f^1 6s^2$  to the Ytterbium (Yb) which has an electronic configuration of  $5s^2 5p^6 4f^{14} 6s^2$ , respectively. These atoms are generally incorporated in materials as an optically active centers in their divalent or trivalent forms. All of the optical properties of REIs are characterized by transitions between energy sublevels of the unfilled  $4f^n$  electronic configuration due to elimination of 5d, 6s and some  $4f^n$  electrons in the trivalent form of the REIs. On the other hand divalent ions contain one more electron and this may cause f-d interconfigurational transitions. This difference of one electron leads to differences in the spectroscopic properties of divalent and trivalent ions.

Trivalent REIs have  $4f^n$  electronic configuration with  $n$  values range from 1 to 13 which corresponds to  $Ce^{3+}$  and  $Yb^{3+}$  ions, respectively. The number of the 4f electrons for each trivalent ions are tabulated in Table 2.1.

The most important property of REIs is the shielding effect of the outer 5s and 5p electrons on the 4f electrons. As the 5s and 5p orbitals fill before the 4f orbital, these two orbitals have a shielding effect on the 4f orbital. So, these 4f electrons are weakly affected by the surrounding medium, namely crystalline field in host crystalline material. As a result of this, REIs show sharp absorption and emission lines.

When trivalent REIs are introduced into crystals, the spin-orbit interaction term of the ion Hamiltonian over the that of the crystalline field causes the splitting of the  $^{2S+1}L_J$  states of the REIs. The crystalline field may cause small shifts and additional

splittings on these states but these effects are much smaller than the spin-orbit splitting, therefore the optical spectra of REIs in crystalline field are similar to those of the free ions. Furthermore, main features of a spectrum of REI doesn't depend much on host material and does not change from one crystal to another [18, 19].

**Table 2. 1:** The number of 4f electrons ( $n$ ) in trivalent lanthanide ions.

Ion	$n$
Ce <sup>3+</sup>	1
Pr <sup>3+</sup>	2
Nd <sup>3+</sup>	3
Pm <sup>3+</sup>	4
Sm <sup>3+</sup>	5
Eu <sup>3+</sup>	6
Gd <sup>3+</sup>	7
Tb <sup>3+</sup>	8
Dy <sup>3+</sup>	9
Ho <sup>3+</sup>	10
Er <sup>3+</sup>	11
Tm <sup>3+</sup>	12
Yb <sup>3+</sup>	13

The interpretation of the REIs absorption and emission spectra can be made by employing the Dieke's energy level diagram which obtained by Dieke [20] by systematically measuring the spectroscopic properties of all REIs in LaCl<sub>3</sub> crystalline host material and is given in Figure 2.1. The diagram shows the energy values of all REIs. Since the main features of a spectrum of a REI remains similar from one crystal to another, as mentioned above, Dieke diagram can be used to interpret any spectrum obtained from REIs in any crystalline host material. A slight difference can be observed for different host material due to the energy splitting and center of gravity of the  $^{2S+1}L_J$  energy levels for a (REI)<sup>3+</sup> ion can change slightly but most of the main features remains similar. Despite the fact that the maximum number of split components for each  $^{2S+1}L_J$  multiplet is  $(2J + 1)$  for integer  $J$ , or  $(J + 1/2)$  for half-integer  $J$ , the actual number of components determined by the local symmetry around REI [18, 19].

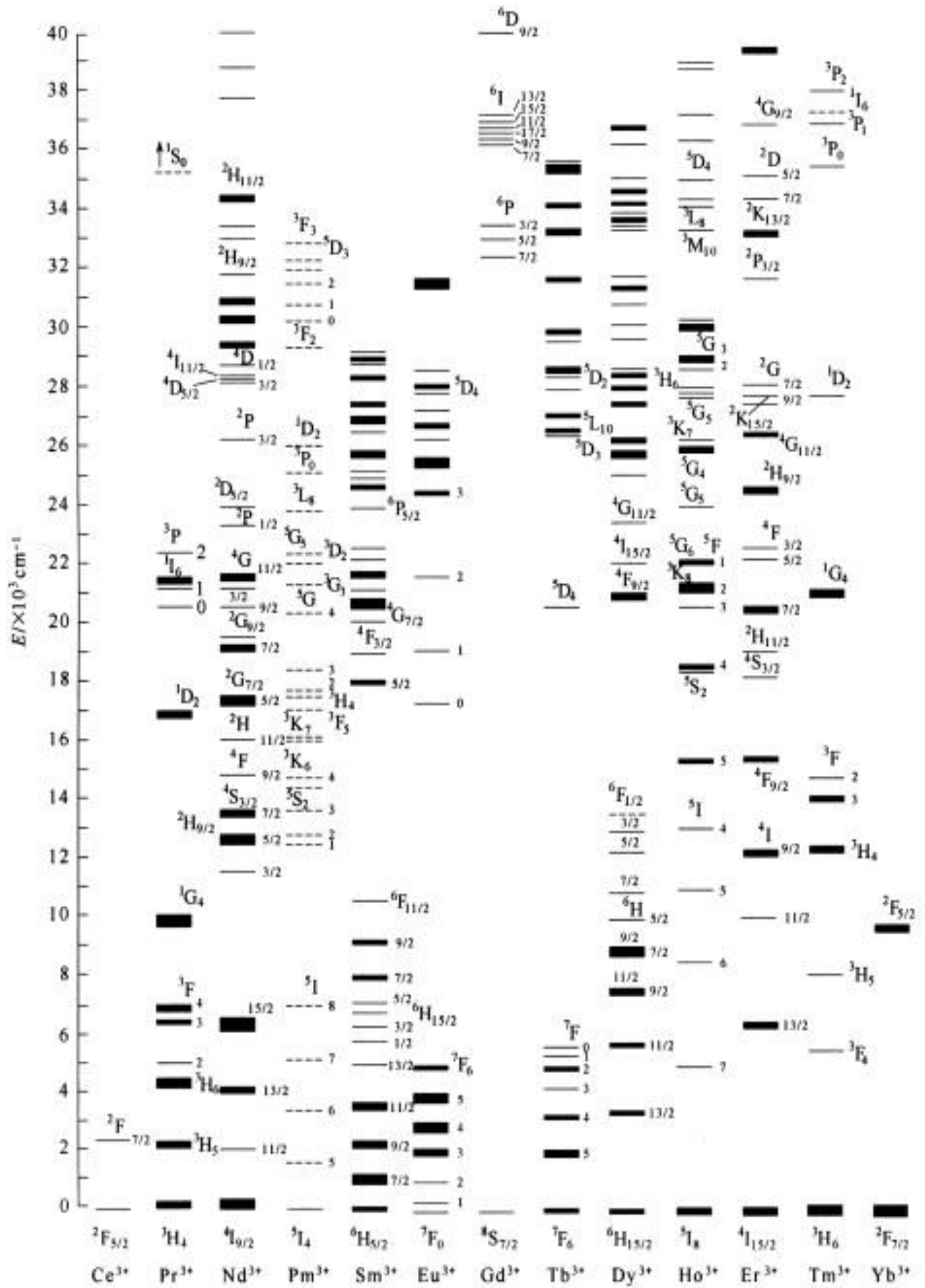


**Figure 2.1** : An energy-level diagram for trivalent lanthanide rare earth ions in lanthanum chloride[20].

As we mentioned above Dieke diagram uses to interpret both of absorption and emission spectra of REIs. Lets give an example of usage of Dieke diagram to interpret absorption spectrum of a REI. The room temperature absorption spectrum of  $\text{Nd}^{3+}$  ion in tellurite glass host [21] is given in Figure 2.2 with corresponding Dieke diagram. The sharp absorption lines given in the figure corresponds to transitions from sublevels of the ground state of  $\text{Nd}^{3+}$  to the upper excited sublevels of the different  $2S+1L_J$  states. These sublevels are the result of splitting effect of the crystalline field on the  $\text{Nd}^{3+}$ . By using Dieke diagram located on the left hand side of the figure, we can easily define which absorption line arise from which interlevels transition.

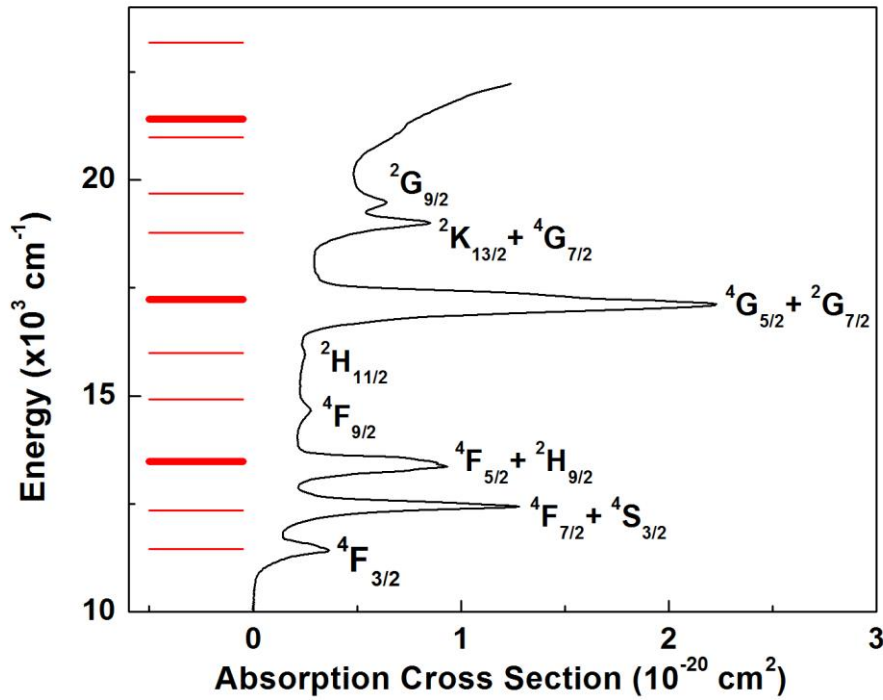


**Figure 2.2 :** The absorption spectrum of  $\text{Nd}^{3+}$  ions in  $\text{TeO}_2+\text{WO}_3$  glass system, taken at room temperature (right-hand side) [21]. The Dieke diagram levels corresponding to the  $\text{Nd}^{3+}$  ion are shown on the left-hand side.

We can also easily assign the emission spectra of REIs by using a same way given above for the absorption spectra of REIs. If we re-check the Dieke diagram, we can see that some energy levels of REIs are marked with a semicircle below them which are correspond to light emitting levels of the REIs. The levels without any semicircle below them are not give rise to direct light emission, they are non-radiatively relaxed

to the lower energy levels. As given in Figure 2.3. that every emission lines are assigned to different transition between sublevels in Dieke diagram. We can see several peaks for each emission bands in emission spectrum which are correspond to splitting of the energy levels. So, we can make a lot of similar interpretation of the emission spectrum by using Dieke diagram.

As a result, the Dieke diagram is a useful tool for spectroscopists to roughly estimate average wavelength for each interlevel transitions of REIs in any crystal host.

Also we should remind that all of these f-f transitions are parity forbidden but most of them become partially allowed at the electric dipole order, depending on crystal host, as a result of mixing with orbitals that have different parity because of a non-inversion symmetry of crystal field [18, 19].

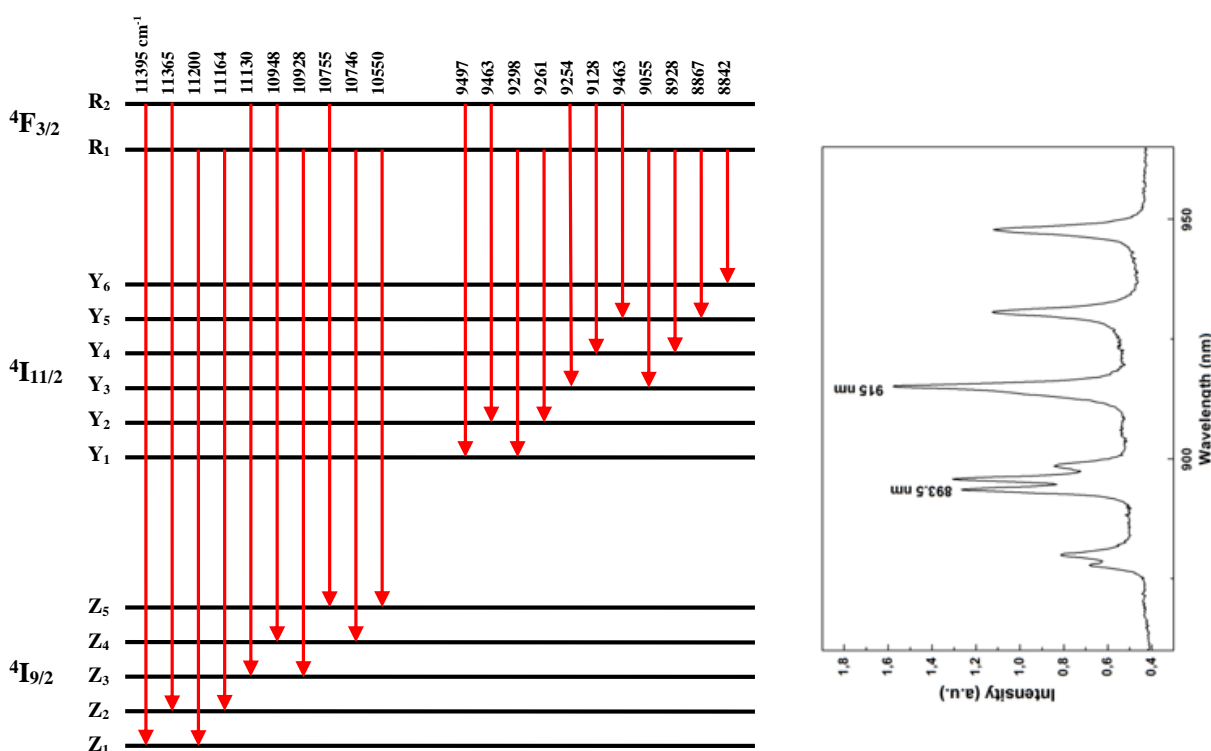


**Figure 2.3 :** The low-temperature emission spectrum of Nd<sup>3+</sup>ions in Y<sub>2</sub>O<sub>3</sub> and the Dieke diagram for the Nd<sup>3+</sup>ion for interpretation [22, 23].

### 2.1.1 Common properties of the rare earths

These common properties apply to both the lanthanides and actinides.

- The rare earths are silver, silvery-white, or gray metals.
- The metals have a high luster, but tarnish readily in air.

- The metals have high electrical conductivity.
- The rare earths share many common properties. This makes them difficult to separate or even distinguish from each other.
- There are very small differences in solubility and complex formation between the rare earths.
- The rare earth metals naturally occur together in minerals (e.g., monazite is a mixed rare earth phosphate).
- Rare earths are found with non-metals, usually in the 3+ oxidation state. There is little tendency to vary the valence. (Eu also has a valence of 2+ and Ce also a valence of 4+) [24].

## 2.2 Properties of the Yttrium Oxide ( $\text{Y}_2\text{O}_3$ ) Crystal

Yttrium oxide ( $\text{Y}_2\text{O}_3$ ) called yttria, is a sesquioxide crystal with a cubic bixbyite structure with the  $T_h^7$  - Ia3 space group and a 10.6 Å lattice constant. The elementary cell of  $\text{Y}_2\text{O}_3$  contains 16 formula units with 32 cation sites, 8 centro-symmetric sites with  $C_{3i}$  symmetry (or S6) and 24 non centro-symmetric sites with symmetry  $C_2$ , for which the trivalent REI dopants can substitute. The crystal structure of the  $\text{Y}_2\text{O}_3$  is given in Figure 2.4. The trivalent ions can occupy the two types of sites with approximately equal probability and the optical transitions mostly occur within the ions at the  $C_2$  sites.  $\text{Y}_2\text{O}_3$  is a refractory oxide with a melting point of about 2410 °C. Due to the high melting temperature of  $\text{Y}_2\text{O}_3$ , it is difficult to grow  $\text{Y}_2\text{O}_3$  crystals from the melt by using traditional crystal growth techniques. Also, yttria is the one of the best host material for the REIs due to the some similarities with the REIs' such as chemical properties and ionic radius with other REIs. Some of the physical properties of  $\text{Y}_2\text{O}_3$  crystal have been collected from the literature and tabulated in Table 2.2. [7, 8, 25].

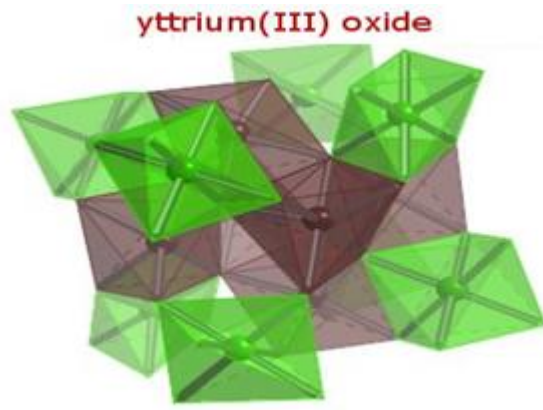


**Figure 2.4 :** Crystal structure of  $Y_2O_3$  [26].

**Table 2. 2:** Physical properties of  $Y_2O_3$  [7].

Property	Values
Crystal system	Cubic
Structure type	Bixbyite
Space group	$T_h^7$ - Ia3
$Y^{3+}$ site symmetry	$C_2$ and $C_{3i}$
$Y^{3+}$ site density	$2.681 \times 10^{22} cm^{-3}$
Lattice constant	10.607 Å
Melting point	2410 °C
Debye temperature	460 K
Phonon Energy	$\sim 430 - 550 cm^{-1}$
Specific heat	0.170 J/g · K at 100K 0.360 J/g · K at 200K 0.455 J/g · K at 300K
Thermal Conductivity	40 W/m · K at 100K 20 W/m · K at 200K 13 W/m · K at 300K
Thermal expansion	$4.2 \times 10^{-6} K^{-1}$ at 100K $6.0 \times 10^{-6} K^{-1}$ at 200K $7.5 \times 10^{-6} K^{-1}$ at 300K
Density	5.04 g/cm <sup>3</sup>
Mohs Hardness	6.8
Index of refraction	1.8892 at 1 μm

## 2.3 Quantum Confinement and Surface Effects

### 2.3.1 Quantum confinement effect

Quantum confinement effect describes how the electronic and optical properties of materials change when the materials sampled sufficiently small, typically 10 nm or less. The phenomenon originates from the electrons and holes being squeezed into small dimensions that approach to Bohr radius which is the critical quantum mechanical measurement, namely when electrons and holes confined by the crystal dimensions that is smaller than Bohr radius, the wavefunction of the electron is collapsed. Due to the size confinement effect, nano-structured materials possess optical properties different than those of their bulk counterparts. The most remarkable modifications arises from the effect of the size on the energy levels and densities of states. This phenomenon can easily describe by using the particle in potential well [27, 28].

### 2.3.2 Particle in a one-dimensional potential well

The time independent Schrodinger equation for a particle in a one-dimensional potential well is given by

$$-\frac{\hbar^2}{2m} \frac{d^2\Psi(x)}{dx^2} + U(x)\Psi(x) = E\Psi(x) \quad (2.1)$$

where  $m$  is the mass of the particle,  $U(x)$  is the potential and  $E$  is the energy of the particle with  $\Psi(x)$  wave function. The potential  $U(x)$  can be describe like below

$$U(x) = \begin{cases} +\infty, & x < -a/2 \\ 0, & -a/2 \leq x \leq a/2 \\ -\infty, & x > a/2 \end{cases} \quad (2.2)$$

As the potential  $U(x)$  infinite, the probability of finding particle is zero at outside and at the boundary of the box. So, the problem convert into a free particle problem inside the box and we will only interested in solutions for the particle inside box because of the wave functions can only generate values which differ from zero inside the box. Also we assume that the probability of finding the particle is symmetric around the center of the box ( $x=0$ ), ie  $U(x)=U(-x)$ . So, the time independent Schrodinger equation becomes,

$$\frac{d^2\Psi}{dx^2} + k^2\Psi = 0 \quad \text{with} \quad k^2 = \frac{2mE}{\hbar^2} \quad (2.3)$$

The general solution is

$$\Psi(x) = A\sin kx + B\cos kx \quad (2.4)$$

If we apply the boundary conditions and as seen from Figure 2.5 we deduce that we can find two types of solutions which are given by cosine and sine functions corresponds to odd  $n$  and even  $n$  values, respectively.

$$\begin{aligned} B = 0, \quad \Psi\left(\frac{a}{2}\right) &= A\cos\left(\frac{ka}{2}\right) \\ 1) \quad &\Rightarrow \cos\left(\frac{ka}{2}\right) = 0 \\ &\Rightarrow k = \frac{n\pi}{a}, \quad n = 1, 3, 5 \dots \\ A = 0, \quad \Psi\left(\frac{a}{2}\right) &= B\sin\left(\frac{ka}{2}\right) \\ 2) \quad &\Rightarrow \sin\left(\frac{ka}{2}\right) = 0 \\ &\Rightarrow k = \frac{n\pi}{a}, \quad n = 2, 4, 6 \dots \end{aligned}$$

So

$$\Psi_{odd} = \frac{1}{N} \cos(kx) \quad (2.5)$$

$$\Psi_{even} = \frac{1}{N} \sin(kx) \quad (2.6)$$

where  $N$  is the normalization constant and  $|x| \leq a/2$  (inside the box otherwise wavefunctions are zero). If we insert  $k$  to the above wavefunctions

$$\Psi_{odd} = \frac{1}{N} \cos\left(\frac{1}{\hbar} \sqrt{2mE} x\right) \quad (2.7)$$

$$\Psi_{even} = \frac{1}{N} \sin\left(\frac{1}{\hbar} \sqrt{2mE} x\right) \quad (2.8)$$

Finally, normalization of wavefunctions read

$$\Psi_{odd} = \sqrt{\frac{2}{a}} \cos\left(\frac{1}{\hbar} \sqrt{2mE} x\right) \quad \text{for odd } n \quad (2.9)$$

$$\Psi_{even} = \sqrt{\frac{2}{a}} \sin\left(\frac{1}{\hbar} \sqrt{2mE} x\right) \quad \text{for even } n \quad (2.10)$$

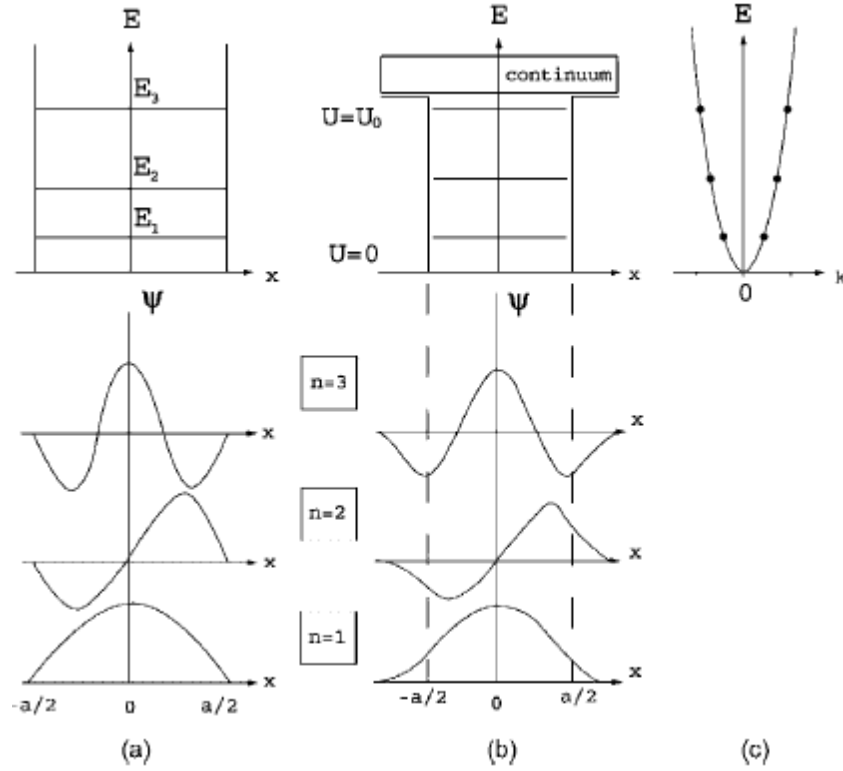


**Figure 2.5 :** Energy levels and wave functions for (a) particle in a well with infinitely high walls, and (b) particle in a well with finite height. (c) The dispersion curve for a free particle. The dots on these curves are the quantized energy values for a particle in a box. In case of a finite well, above  $U_0$  the dispersion curve for a free particle is obtained [27].

As seen from Figure 2.5, the wavefunctions vanish at  $|x| > a/2$ . When particle is in the well, the probability ( $|\Psi_n(x)|^2$ ) must be nonzero. So the minimum energy of a particle is nonzero

$$E_n = \frac{\pi^2 \hbar^2}{2ma^2} \quad (2.11)$$

The wave functions vanish at  $x > a$ . When a particle exists in the well, the product  $c$  must be nonzero somewhere. The minimum energy of a particle ( $n=1$ ) is therefore nonzero and given by (see (4)):

$$E_n = \frac{\pi^2 \hbar^2}{2ma^2} \quad (2.12)$$

All above equations can be derived by using Heisenberg uncertainty equation.

$$\Delta x \Delta p \geq \frac{\hbar}{2} \quad (2.13)$$

with  $\Delta x = a$ ,

$$\Delta E = \frac{\Delta p^2}{2m} = \frac{\hbar^2}{8ma^2} \quad (2.14)$$

The nature of the solutions obtained for the finite potential wells are almost same. There are few differences such as the probability of finding a particle outside the box is not zero and increases with increasing  $n$  value and after a certain kinetic energy value, the states form a continuum. The number of states inside the well is given by;

$$a\sqrt{2mU_0} > \pi\hbar(n-1) \quad (2.15)$$

For  $n = 1$ , there is at least one state inside the well. For a particle in an infinite potential well, the relation between  $k$  and  $E$ , called dispersion relation, consist of points on a parabola as seen from Figure 2.5. The dispersion relation is given by

$$E = \frac{\hbar^2 k^2}{2m} \quad (2.16)$$

For a particle with a finite  $U_0$  wall's height, below  $U_0$ , the solutions are quantized. Above  $U_0$  any values of  $k$  is possible. All of these results are summarized in Figure 2.5 [27-29].

### 2.3.3 Particle in a general three-dimensional potential

In three dimensions, the wave functions are consist of a radial and an angular dependent part of Schrodinger equation. In order to characterize the wavefunctions in three dimensions, we need three following quantum numbers (without spin);

- $n \rightarrow$  The principal quantum number which describes the electron shell or energy level of an atom. The  $n$  value ranges from 1 to the shell which contains outermost electron ( $n = 1, 2, 3, \dots$ )
- $l \rightarrow$  The orbital (or azimuthal) quantum number which describes the subshells, ie for any value of  $n$ ,  $n$  states (subshells) exist. The orbital quantum number determines the magnitude of orbital angular momentum through the relation

$$L^2 = \hbar^2 l(l+1) \quad (2.17)$$

The states with different  $l$  values are called  $s, p, d, f \dots$  orbitals. The orbital quantum numbers ranges from 0 to  $(n-1)$ .

•  $m \rightarrow$  The magnetic quantum number which used to describe the components of  $L$  parallel to the quantization axis and yields the projection of the orbital angular momentum along a specified axis;

$$L_z = m\hbar^2 \quad (2.18)$$

Every  $l$  states  $(2l+1)$  fold degeneracy due to  $m$  ranges from  $-l$  to  $+l$ . The priority of the wavefunction is determined by  $l$ .

If we consider again a infinite potential well, we can obtain energy values for this system [27-29].

$$E_{n,l} = \left( \frac{\hbar^2}{2ma^2} \right) \chi_{nl}^2 \quad (2.19)$$

where  $\chi_{n,l}$  are the roots of the spherical Bessel functions.

The smallest energy value for  $n = 1$  and  $l = 0$  is given by,

$$E_{1,0} = \frac{\pi^2 \hbar^2}{8ma^2} \quad (2.20)$$

### 2.3.4 Density of states in low dimensional structures

In solid state and condensed matter physics, density of states (DOS) is used to describe the number of available states per energy interval at each energy level that are waiting to be occupied by electrons. The density of states phenomenon become more important in the determination of the spectroscopic properties of the nano-sized materials.

We will consider a sphere in  $k$ -space for the evaluation of the DOS. Also we will consider the periodic boundary conditions of a crystal that is  $k = 2n\pi/L$ . The volume of the sphere with the radius  $k$  is;

$$V_{sphere} = \frac{4}{3} \pi k^3 \quad (2.21)$$

where  $k^2 = k_x^2 + k_y^2 + k_z^2$

$$\begin{aligned}
k_x &= \frac{2\pi n_x}{L_x} \\
k_y &= \frac{2\pi n_y}{L_y} \\
k_z &= \frac{2\pi n_z}{L_z}
\end{aligned} \tag{2.22}$$

Also we know from the Schrödinger equation that energy of a particle is quantized and given by;

$$E = \frac{\hbar^2 k^2}{2m} = \frac{p^2}{2m} \tag{2.23}$$

The smallest nonzero volume in this  $k$ -space,

$$V_{state} = k_x k_y k_z = \frac{8\pi^3}{L_x L_y L_z} \tag{2.24}$$

So the total number of states is given by the ratio between the volume of the sphere and the state;

$$N = 2 \frac{V_{sphere}}{V_{state}} = 2 \cdot \frac{\frac{4}{3}\pi k^3}{k_x k_y k_z} = \frac{k^3}{3\pi^2} L_x L_y L_z \tag{2.25}$$

The 2 coefficient in the Eq. (2.25) arises from the spin degeneracy of electrons. Now we can define the DOS per unit volume which is

$$\rho = \frac{N}{L_x L_y L_z} = \frac{k^3}{3\pi^2} \tag{2.26}$$

Finally if we consider an energy density,

$$\rho(E)dE = \frac{1}{2\pi^2} \left( \frac{2m}{\hbar^2} \right)^{3/2} E^{1/2} dE \tag{2.27}$$

At this point we can easily calculate the DOS for two and one dimension. DOS for the two dimensions is given by

$$\rho_2(E)dE = \frac{1}{\pi} \frac{m}{\hbar^2} \tag{2.28}$$

It is interesting to notice that the DOS of the 2D does not depend on the energy. For the 1D

$$\rho_1(E)dE = \frac{1}{\pi} \sqrt{\frac{2m}{\hbar^2}} (E)^{-1/2} dE \quad (2.29)$$

Finally, in a zero dimensional systems (QDs), the DOS of such system is described just as a series of delta functions [27-30]

$$\rho(E)dE = 2 \sum_{n_x, n_y, n_z} \delta(E - E_{n_x, n_y, n_z}) \quad (2.30)$$

All results are summarized in Figure 2.6.

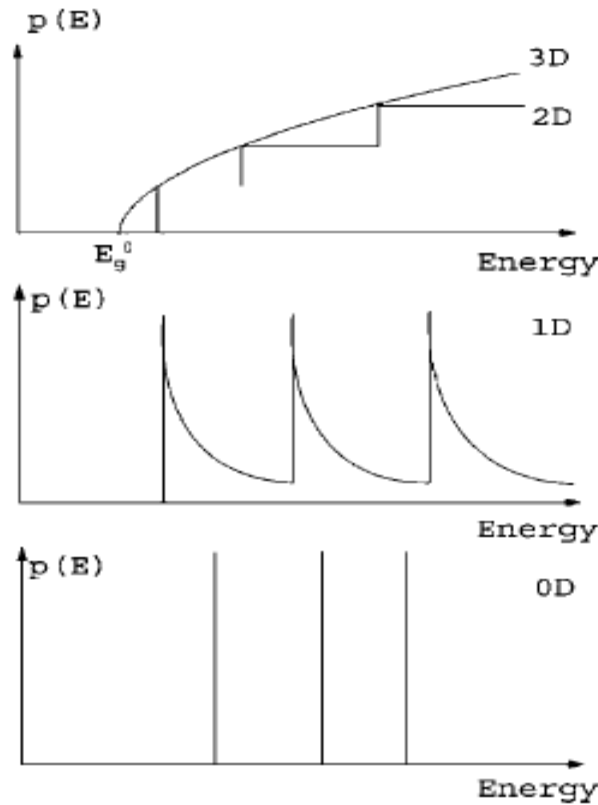


**Figure 2.6 :** Density of states for 3, 2, 1, and zero dimensional systems [27].

### 2.3.5 Low-dimensional structures

Since the dimension decrease by moving from crystal to the nano-particle, at least one of the dimensions of the nano-material may become the same order of the magnitude or even smaller than the wavelength of the electron and holes, or the Bohr radius of an exciton. This resulted in a quantized motion in the confined axis. One direction confinement results in a quantum well, two directions results in a quantum wire and finally three directions results in a QD.

We can define three limiting cases to classify confinement effect according to nano-particle radius to Bohr radius ratio. First one is the “Weak Confinement Regime” that occurs when the radius of the nano-particle is few times larger than the Bohr radius, the second one is the “Intermediate Confinement Regime” which occurs when the radius of the nano-particle is close to Bohr radius and the last one is the “Strong Confinement Regime” which occurs when the radius of the nano-particle is much smaller than the Bohr radius [27].

### **2.3.6 Surface effects**

Another most important deal of the size reduction is the surface effects. As the particle sizes decrease, the surface area to volume ratio become larger and starts to play an important decisive role on the optical, catalytic, magnetic etc. properties of the nano-materials. Since the surface area to volume ratio of a sphere is proportional to the  $1/r$ , the fraction becomes larger with the decreasing  $r$ . As a result of this, the larger fraction of the atoms are found at the surface of the nano-crystal. For example, while the fraction of the atoms at the surface for  $1\mu\text{m}$  crystal is less than 1 %, it is 15 % for 5 nm CdS nano-crystal [31].

One of the failings of the particle in a box model that mentioned above is that it does not take the surface of a QDs into account. Actually the surface of a QD is not an infinite potential barrier. Also the chemical potential of the surface is significantly differs from the interior of the materials due to the dangling bonds, reconstructions of the crystal and the possible adsorbates. Therefore, increasing ratio of surface area to volume can make particles very reactive or catalytic. As a result of this, smaller particles make more of themselves available at the surface to react chemically with other molecules [32].

Also at high temperature sintering, the high surface area to volume ratio provides a driving force for diffusion and nano-materials become more sinterable according to their bulk counterparts. So this makes low temperature sintering possible over a short time scales than for larger particles [33].

## **2.4 Spectroscopic Properties of Lanthanides in Nanocrystals**

Lanthanides doped luminescent materials are widely investigated due to their potential applications in solid-state lasers, luminescent lamps, flat panel displays,

optical fiber communication systems, biological sensors and other photonic devices. The great interest on lanthanides is due to their notable luminescent properties which originate from intraband transitions between their unique well-protected 4f orbitals. Since the 4f electrons are well protected from the crystal field by 5s and 5p electrons, lanthanides show sharp emission transitions within 4f<sup>n</sup> configuration [6, 18, 19]. The better understanding of the spectroscopic properties of the lanthanides has been provided with many researches in the literature under the illumination of the pioneer work by Dieke, Judd, Wybourne, Carnall and others [20, 34-36].

Although the spectroscopic properties of lanthanide ions are well-understood, the requirement of the understanding of the lanthanides in nano-materials has been came out with rapid evolution of the nanotechnologies. Especially, with the development of the new, cheap and low temperature methods, materials synthesis based on wet chemical techniques and the change in the physical properties of the nano-materials according to their bulk counterparts, the growing interest has been re-focused on the understanding of the spectroscopic properties of the lanthanides in nano-materials.

The understanding of these materials is important because of optimizing and adapting their emissive properties for their potential applications. Most of the researches in the literature shown that the some physical properties of nano-materials, particularly, some optical, thermal and catalytic properties enhanced with decreasing dimensions of the materials according to their bulk counterparts, but there is no definite evidence of a trend of these properties with decreasing particle size. Therefore the change in the particle size and as a result in the physical properties affect the luminescent dynamics of the optically active lanthanide ion in nano-sized materials. These effects can manifest itself as a change in the radiative lifetimes, luminescence quantum efficiency and concentration quenching phenomena. All of these observed changes are arisen from the change in the local environments of the doped lanthanide ions due to the possible structural defects induced by size reduction. As a result, the site symmetry, crystal field strength, and the index of refraction may be significantly different from that in the bulk materials. Although electronic energy levels shift and excited state lifetime varies as a function of particle size, literally, many of these effects are not considered as a result of nano-confinement on electronic states [37].

It is well known that in solid phases electrons in the  $4f^n$  orbitals of lanthanides are localized, therefore do not exhibit quantum confinement even in nanocrystals [9, 10]. According to crystal field theory, the electronic energy levels for lanthanide ions in nanoparticles may vary because of changes in the strength of local electrostatic field and site symmetry. In nanocrystals, structure disordering and surface defects are inevitable, thus induce more significant inhomogeneous line broadening than that in bulk crystals. However, in the literature, some observed variations in energy levels have been attributed to quantum-confinement effects when the particle diameter is less than 5 nm. It is reported that, for nanoparticles doped with transition metal ions such as  $\text{Mn}^{2+}:\text{ZnS}$ , the luminescence lifetime becomes shorter by several orders of magnitude. Similar effect has been reported for lanthanide ions in nanosemiconductors. Such size dependent effects are postulated to result from mixing of the s-p electrons of the host with the d-f valence electrons of the activator due to quantum confinement, causing the normally forbidden d-d or f-f transitions to become allowed. Although research in nanostructured semiconductors has long been conducted to produce a clear theoretical picture of these materials, very little theoretical work addressed the size-dependence of localized emissive ions in nanostructured hosts [9, 10, 37].

Nanophenomena due to size confinement in lanthanide nanoparticles may indeed occur because of ion-phonon coupling that directly affect excited state lifetime and energy transfer. Namely, the size confinement is not on electronic states, but lattice vibration modes. In a nanocrystal, the density of phonon states becomes discrete and application of Debye approximation of a continuous density function is inappropriate. Moreover, low-frequency acoustic phonon modes are cut off. Nanoparticles not only become thermal insulators, but electron-phonon coupling may be restricted. It is expected in general that the confinement effects on spectroscopy and luminescence dynamics can be induced by inter-ionic electronic and vibronic interactions. Significant size dependence of the excited state dynamics and luminescence properties is the most commonly observed nano-phenomenon for lanthanide ions in nanomaterials. Given the localized nature of the 4f orbitals of lanthanides in complexes, it is obvious that changes in local environment would influence, mostly through ion-phonon coupling, the dynamics of the 4f-4f transitions, whereas the static energy levels of the 4f states experience less impact.

Size effects on electron–phonon interaction are primarily due to the modification of the phonon density of states (PDOS) in a nanocrystal. Discrete phonon spectrum and the low-energy acoustic phonon modes cutoff are the consequence of the size reduction. As a result, luminescence dynamics for lanthanide ions in nanocrystals, particularly nonradiative relaxation and energy transfer efficiency are expected to differ from that in bulk materials [9, 10, 37].

#### **2.4.1 Size Effects on the structure of electronic levels**

In a  $4f^n$  configuration electrons in the partially occupied 4f orbitals are shielded by the  $5s^2$  and  $5p^6$  sub-shells and prevented from interacting with the ligands; therefore they have little participation in chemical bonding. On placing a lanthanide ion in a dielectric crystal, the energy levels split under the influence of the electric field produced by the crystalline environment. The f-electrons have very localized states that are conventionally described within the framework of crystal field theory. In general, quantum confinement effects on the energy level structure are not expected for the localized electronic states of the lanthanide ions doped in insulating nanocrystals. The electrostatic crystal field which splits the  $^{2S+1}L_J$  multiplet of a lanthanide ion up to several hundreds  $\text{cm}^{-1}$  may be divided into short-range components and long-range electric dipolar interactions [37].

#### **2.4.2 Confinement on excited-state dynamics**

The nanostructure dependence of the excited state dynamics can be derived from the interaction of the electronic excitation with the surrounding environment and its phonon modes. A variety of nanophenomena, particularly, the lifetime of excited states of lanthanide ions in nanostructures may exhibit strong size-dependence. Energy transfer rate and luminescence efficiency in lanthanide activated phosphors are also sensitive to particle size and surrounding environment [37].

##### **2.4.2.1 Radiative and nonradiative relaxation**

According to Judd–Ofelt theory, one can evaluate the radiative lifetime of any excited state of interest via Einstein spontaneous emission coefficients. The rate of relaxation,  $A$ , from an initial state  $|\Psi J\rangle$  to final state  $|\Psi' J'\rangle$  through radiative processes is given by:

$$A(\Psi J, \Psi' J') = \frac{64\pi^2(\Delta E)^3}{3h(2J+1)}(\chi\bar{F}^2 + n^3\bar{M}^2) \quad (2.31)$$

where  $F^2$  and  $M^2$  are the matrix elements of the electric dipole and magnetic dipole moments, respectively,  $\Delta E$  ( $\text{cm}^{-1}$ ) represents the energy gap between states  $|\Psi J\rangle$  and  $|\Psi' J'\rangle$ ,  $\chi = n(n^2 + 2)^2/9$  is the Lorentz correction for local field with  $n$  being the refractive index of the host material. The observed lifetime of a particular excited state,  $\tau_T$ , is determined by the sum of the inverse of the radiative and nonradiative lifetimes. Thus

$$(\tau_T)^{-1} = A(\Psi J) + W_T(\Psi J) \quad (2.32)$$

where  $A(\Psi J)$  is the total radiative relaxation rate from state  $|\Psi J\rangle$ , that is, the sum of the rates of radiative decay to all states with energy less than that of  $|\Psi J\rangle$ . If  $\tau_R$  is the total radiative lifetime of  $|\Psi J\rangle$ , then  $\tau_R = [A(\Psi J)]^{-1}$ . Similarly,  $\tau_{NR} = [W_T(\Psi J)]^{-1}$  is a total nonradiative lifetime summed over all nonradiative relaxation processes. The magnitude of the energy gap between a luminescent state and the next lower-energy state plays a major role in determining the nonradiative lifetime of that state.

As a result of ion-phonon interaction, the population of the excited state decreases via nonradiative transition from the excited state to a lower electronic state. The energy difference between the two electronic states is converted into phonon energy. This process of population relaxation is characterized by a relaxation time,  $\tau_T$ , which depends on the energy gap between the two electronic states, the frequencies of vibration modes, and temperature. At room temperature, the excited state lifetime is dominated by the nonradiative relaxation except in a few cases such as the  $^5D_0$  level of  $\text{Eu}^{3+}$  and  $^6P_{7/2}$  level of  $\text{Gd}^{3+}$  for which the energy gap is much larger than the highest phonon frequency of the lattice vibrations.

With the assumption that the phonons involved are of equal energy, a commonly used expression for the temperature-dependent multiphonon relaxation rate is,

$$W(T) = W(0) \left[ \frac{\exp(\hbar\omega_m/kT)}{\exp(\hbar\omega_m/kT) - 1} \right]^{\Delta E/\hbar\omega_m} \quad (2.33)$$

where  $\hbar\omega_m$  is the maximum phonon energy of the lattice vibrations that couples to the electronic transition of the metal ion,  $\Delta E$  is the energy gap between the populated

state and the next low-lying state, and  $W(0)$  is the spontaneous transition rate at  $T = 0$  when the phonon modes are all initially in their ground state. At low temperatures where  $\hbar\omega_m \gg kT$ , the nonradiative relaxation rate is dominated by  $W(0)$ , which can be expressed as a simple exponential function depending on the energy gap,  $\Delta E$ :

$$W(0) = C \exp(-\alpha \Delta E / \hbar\omega_m) \quad (2.34)$$

where  $C$  and  $\alpha$  are empirical parameters which are characteristic of the particular crystal. Known as the energy-gap law, this exponential dependence has been used to describe the energy-gap dependence of multiphonon transitions rates for the 4f states [37].

#### 2.4.2.2 Line broadening and shifts

One of the direct consequences of ion–phonon interaction is a broadening of the line widths of electronic transitions. A spectral line is called “sharp” if its width  $\Delta E$ , full width at half maximum intensity, is much smaller than  $\hbar\omega_D$ , where  $\omega_D$  is the Debye frequency of the solid. The temperature dependence of the widths and positions of sharp (no phonon) spectral lines has been studied by many workers on 3d, 4f and 5d ions in crystals and mostly explained in terms of a simple ion-phonon interaction as a perturbation and of a Debye phonon distribution. The ion-phonon interaction causes the thermal broadenings and shifts of the energy levels of the impurity ion [22, 38].

The broadening of an energy level is mainly due to the crystal strain inhomogeneity, direct one-phonon processes, multiphonon processes, and Raman phonon scattering processes. The width of the  $i$ th level is given by

$$\Delta E_i(\text{cm}^{-1}) = \Delta E_i^{\text{strain}} + \Delta E_i^M + \Delta E_i^D + \Delta E_i^R \quad (2.35)$$

where

$$\Delta E_i^D(\text{cm}^{-1}) = \sum_{j < i} \bar{\beta}_{ij} \left( \frac{1}{e^{\Delta E_{ij}/kT} - 1} + 1 \right) + \sum_{j > i} \bar{\beta}_{ij} \frac{1}{e^{\Delta E_{ji}/kT} - 1} \quad (2.36a)$$

$$\Delta E_i^R(\text{cm}^{-1}) = \bar{\alpha}_i \left( \frac{T}{T_D} \right)^7 \int_0^{T_D/T} \frac{x^6 e^x}{(e^x - 1)^2} dx \quad (2.36b)$$

$\Delta E_i^{strain}$  is the contribution to the width due to the random microscopic strains of the crystal, which give rise to an inhomogeneous broadening and hence produce a Gaussian line shape, and is assumed to be temperature independent.  $\Delta E_i^M$  is due to the multiphonon emission processes, which can take place between two levels whose energy difference is greater than the greatest energy of the available phonons, and has been shown to be essentially temperature independent. Multiphonon absorption processes are negligible in the temperature range of interest.  $\Delta E_i^D$  is due to direct one-phonon processes between  $i$ th energy level and other nearby levels. The first and second terms in Eq. (2.36a) correspond to one-phonon emission processes and one-phonon absorption, respectively.  $\Delta E_i^R$  is due to Raman phonon scattering processes which consist of the absorption of one phonon and the emission of another phonon without changing the electronic state of the ion.  $\bar{\alpha}_i$  and  $\bar{\beta}_{ij}$  are the coupling coefficients for the ion-phonon interaction.  $T_D$  is the effective Debye temperature of the phonon distribution. The broadenings due to the direct one-phonon, multiphonon, and Raman phonon scattering processes are homogeneous and give Lorentzian line shapes [22, 38].

It is useful to rewrite Eq. (2.36a) as follows:

$$\Delta E_i^D(cm^{-1}) = \sum_{j<i} \bar{\beta}_{ij} + \Delta E_i^{DT} \quad (2.37)$$

where

$$\Delta E_i^{DT} \equiv \sum_{j<i} \bar{\beta}_{ij} \frac{1}{e^{\Delta E_{ij}/kT} - 1} + \sum_{j>i} \bar{\beta}_{ij} \frac{1}{e^{\Delta E_{ji}/kT} - 1} \quad (2.37a)$$

We can see from Eq. (2.37) that the broadening, due to direct one-phonon processes, consist of a temperature dependent part  $\Delta E_i^{DT}$ , and a temperature independent part  $\sum_{j<i} \bar{\beta}_{ij}$  which is due to spontaneous one-phonon emission. For rare earth ions, the energy separation among the Stark levels is of the order  $10\text{-}10^2 \text{ cm}^{-1}$ , and  $\sum_{j<i} \bar{\beta}_{ij}$  could produce an observable broadening.

Now we can write Eq. (2.35) as

$$\Delta E_i(cm^{-1}) = \Delta E_i^{strain} + \Delta E_i^M + \sum_{j<i} \bar{\beta}_{ij} + \Delta E_i^{DT} + \Delta E_i^R \quad (2.38)$$

When  $T = 0$  K,

$$\Delta E_i(cm^{-1}) = \Delta E_i^{strain} + \Delta E_i^M + \sum_{j < i} \bar{\beta}_{ij} \equiv \Delta E_{i0} \quad (2.38a)$$

The  $\Delta E_i$  at  $T = 0$  is due to the random crystal strains, the spontaneous one-phonon and multiphonon emission processes, and is the residual width of the  $i$ th level.

Since the crystal strain width  $\Delta E_i^{strain}$  gives inhomogeneous broadening with a Gaussian shape and the other terms in Eq. (2.36) give rise to homogeneous broadening with a Lorentzian shape, the simple summation in Eq. (2.36) is a rough approximation. A shape composed of a homogeneous part and an inhomogeneous part can be represented by a Voigt profile. The width may be resolved into homogeneous and inhomogeneous contributions by using the Posener tables [39].

The shift of the  $i^{th}$  energy level is due to the stationary effects of the ion-phonon interaction. Using the perturbation theory, the shift is given by

$$\delta E_i(cm^{-1}) = \delta E_i^R + \delta E_i^D \quad (2.39)$$

where

$$\delta E_i^R = \alpha_i \left( \frac{T}{T_D} \right)^4 \int_0^{T_D/T} \frac{x^3}{e^x - 1} dx \quad (2.39a)$$

$$\delta E_i^D = \sum_{j \neq i} T_{ij} \beta_{ij} \left( \frac{T}{T_{ij}} \right)^2 P \int_0^{T_D/T} \frac{x^3}{e^x - 1} \frac{dx}{(T_{ij}/T^2) - x^2} \quad (2.39b)$$

The  $\alpha_i$  and  $\beta_{ij}$  are the coupling coefficients,  $T_{ij} = (E_i - E_j)/k$  is in the range of  $\pm \hbar \omega_D$ , and  $P$  denotes the principal value of the integral.

### 2.4.2.3 Modification of radiative lifetimes

The decay patterns of the luminescent  $Nd^{3+}$  ions embedded in the nanoparticles are expected to deviate from an exponential decay of the same ions in the crystal for two reasons:

- 1) The role played by the surfaces will be increasingly important as the radius of the particle is reduced, producing a deviation from exponentiality. Molecular groups

such as O-H residing on the surface may enhance the decay process due to their stiff vibrations that rob the ion of its excitation energy. We reasonably expect that a deviation from exponentiality at the beginning of the decay pattern.

2) The ensemble of particles in the sample differs also from the bulk material for the presence of the interstices between the particles. In what follows we shall describe how we can handle the problem presented by this difference [22, 38].

The rate of spontaneous electric dipole radiative relaxation of an atomic system is given by [40]

$$A(\Psi J, \Psi' J') = \frac{64\pi^2(\Delta E)^3}{3h(2J+1)} \eta F^2 \quad (2.40)$$

where  $F$  = matrix element of the electric dipole operator,  $\Delta E$  = energy gap between the states  $|\Psi J\rangle$  and  $|\Psi' J'\rangle$ , and  $\eta = \frac{n(n^2+2)^2}{9}$ ; is the Lorentz correction for the local field with  $n$  = index of refraction of the host material.

Applying those considerations to the ions embedded in the nanoparticles, we can say that the rate of their spontaneous emission (inverse of the radiative lifetime) depends on an effective index of refraction  $n_{eff}$  which consist of a combination of the index of refraction of the nanoparticle  $n_{NP}$  and of the index of refraction of the surrounding medium  $n_{med}$  :

$$n_{eff}(\chi) = \chi n_{NP} + (1 - \chi) n_{med} \quad (2.41)$$

where  $\chi$  is the filling factor indicating the fraction of space that is occupied by the nanoparticles. The validity of the usage of  $n_{eff}$  in calculating the probability of decay rests on the fact that the size of the particles is much smaller than the wavelength of light [22, 38].

#### 2.4.2.4 Modification of phonon density of states and confinement on electron–phonon interaction

Although no quantum confinement should occur in the electronic energy level structure of lanthanides in nanoparticles because of the localized 4f electronic states, the optical spectrum and luminescence dynamics of an impurity ion in dielectric nanoparticles can be significantly modified through electron–phonon interaction.

Confinement effects on electron–phonon interaction are primarily due to the effect that the phonon density of states (PDOS) in a nanocrystal is discrete and therefore the low-energy acoustic phonon modes are cut off. As a consequence of the PDOS modification, luminescence dynamics of optical centers in nanoparticles, particularly, the nonradiative relaxation of ions from the electronically excited states, are expected to behave differently from that in bulk materials.

The most essential property of acoustic vibrations in a nanoparticle is the existence of minimum size-quantized frequencies corresponding to acoustic resonances of the particle. In dielectric nanocrystals, the Debye model is not valid for evaluation of the PDOS if the radius of the nanocrystal is less than 10 nm [37].

### 3. MATERIALS AND METHODS

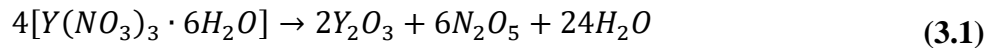
#### 3.1 Synthesis of the Nd<sup>3+</sup> Doped Y<sub>2</sub>O<sub>3</sub> Nano-Powders

Nd<sup>3+</sup> doped Y<sub>2</sub>O<sub>3</sub> samples were synthesized by using the Thermal Decomposition Technique.

##### 3.1.1 Thermal decomposition method

Thermal decomposition, also known as thermolysis, is a chemical decomposition caused by heat. The decomposition temperature of a substance is the temperature at which the substance chemically decomposes. The reaction is usually endothermic as heat is required to break chemical bonds in the compound undergoing decomposition. If decomposition is sufficiently exothermic, a positive feedback loop is created producing thermal runaway and possibly an explosion.

The method we used is based on the thermal decomposition of alginate gels. In this process yttrium nitrate hexahydrate  $Y(NO_3)_3 \cdot 6H_2O$ , neodymium nitrate hexahydrate  $Nd(NO_3)_3 \cdot 6H_2O$  and low viscosity (250 cps of 2% solution) alginic acid sodium salts with analytical grade were used as a starting reagents. Alginate is a biopolymer which is extracted from brown sea algae. It is a heteropolysaccharide which is composed of D-mannuronic and L-guluronic acids. Gelation of alginate is possible by the interaction of the carboxylate group with divalent ions [41]. Alginate is used in food industry and in medicine. The reaction that occurs in thermal decomposition process is given in Eq (3.1) and the procedure followed to obtain nano-powders is given below [42];



- 0.2M yttrium-neodymium nitrate solution is prepared by dissolving appropriate amounts of yttrium nitrate hexahydrate and neodymium nitrate hexahydrate salts in ultra pure water (conductivity <0.1  $\mu S\ cm^{-1}$ ).

- A 1% w/w alginate solution is prepared by dissolving appropriate amount of sodium alginate in ultra pure water.
- Yttrium alginate beads were obtained via dropwise additon of the alginate solution into yttrium-neodymium nitrate solution with a stainless steel needle.
- The obtained gel beads were maintained in the gelling medium under gentle magnetic stirring.
- After that, the beads were separated from the gelling medium by employing a stainless steel grid.
- The beads were placed into a porcelain crucible heated up to the desired synthesis temperature with a heating rate of 10C/min for 24 hours.
- Formed nanophosphors were annealed to temperatures 600 °C, 800 °C, 1000 °C and 1400 °C to investigate the effect of annealing temperature on particle sizes and to study the effect of particles' sizes on the emission properties of nanophosphors.

### **3.2 Structural Characterization of Nd<sup>3+</sup> Doped Y<sub>2</sub>O<sub>3</sub> Nano-powders**

Three different methods were employed to determine the morphology and the particle sizes of the synthesized samples. These are;

#### **3.2.1 X-ray diffraction (XRD)**

XRD is one of the most important structural characterization technique in materials science used to determine atomic and molecular structure of a crystal by using Bragg condition. As the name suggests, it is a diffraction pattern obtained by the collecting diffracted X-rays from the planes of the crystallites into many specific directions which satisfies the Bragg condition [43].

$$n\lambda = 2d \sin\theta \quad (3.2)$$

Since the each crystalline solid has its unique X-ray pattern like fingerprint, by measuring the angles and intensities of these diffracted beams, one can determine the mean positions of the atoms in the crystal, as well as their chemical bonds, their disorder and various other information [44]. XRD can also be used for estimating the mean crystallite sizes by using Scherrer Equation [45];

$$L = \frac{K\lambda}{\beta \cos\theta} \quad (3.3)$$

where  $L$  is the crystallite length,  $K$  is a constant that varies with the method of taking the breadth ( $0.89 < K < 1$ ),  $\lambda$  is the wavelength of the incident X-ray beam,  $\beta$  is the width of the peak at half maximum intensity of a specific phase ( $hkl$ ) in radians and  $\theta$  is center angle of the peak.

X-ray diffraction investigations were carried out with a Bruker AXS D8 Model (Cu- $K\alpha$  radiation) diffractometer at 40 kV and 30 mA setting in the  $2\theta$  range from  $20^\circ$  to  $70^\circ$ .

### 3.2.2 Scanning electron microscope (SEM)

The scanning electron microscope (SEM) is one of the most widely used instrument in materials research and is common in various forms in fabrication plants. SEM is central to microstructural analysis and therefore important to any investigation relating to the processing, properties, and behavior of materials that involves their microstructure. The SEM provides information relating to topographical features, morphology, phase distribution, compositional differences, crystal structure, crystal orientation, and the presence and location of electrical defects. SEM is also capable of determining elemental composition of micro-volumes with the addition of an x-ray or electron spectrometer and phase identification through analysis of electron diffraction patterns. The strength of the SEM lies in its inherent versatility due to the multiple signals generated, simple image formation process, wide magnification range, and excellent depth of field.

Due to these unique features, SEM images frequently appear not only in the scientific literature but also in the daily newspapers and popular magazines. SEM is relatively easy to operate and affordable and allows for multiple operation modes, corresponding to the collection of different signals [46].

SEM uses a focused beam of high-energy electrons to generate a variety of signals at the surface of solid specimens. The signals that derive from electron-sample interactions reveal information about the sample including external morphology (texture), chemical composition, and orientation of materials making up the sample. In most applications, data are collected over a selected area of the surface of the

sample, and a 2-dimensional image is generated that displays spatial variations in these properties. SEM is also capable of performing analyses of selected point locations on the sample; this approach is especially useful in qualitatively or semi-quantitatively determining chemical compositions using Energy Dispersive X-Ray Spectroscopy (EDS) [47]. SEM images and EDS analysis of the samples were made by using JEOL 840JXA SEM (equipped with EDS system for microanalysis) model equipment located in Marmara Research Center of TÜBİTAK, Gebze.

### **3.2.3 Transmission electron microscope (TEM)**

Transmission electron microscopy (TEM) is a microscopy technique whereby a beam of electrons is transmitted through an ultra thin specimen, interacting with the specimen as it passes through. An image is formed from the interaction of the electrons transmitted through the specimen; the image is magnified and focused onto an imaging device, such as a fluorescent screen, on a layer of photographic film, or to be detected by a sensor such as a CCD camera.

TEMs are capable of imaging at a significantly higher resolution than SEM, owing to the small de Broglie wavelength of electrons. This enables the instrument's user to examine fine details even as small as a single column of atoms, which is tens of thousands times smaller than the smallest resolvable object in microscope. TEM forms a major analysis method in a range of scientific fields, in both physical and biological sciences. TEMs find application in cancer research, virology, materials science as well as pollution, nanotechnology, and semiconductor research.

At smaller magnifications TEM image contrast is due to absorption of electrons in the material, due to the thickness and composition of the material. At higher magnifications complex wave interactions modulate the intensity of the image, requiring expert analysis of observed images. Alternate modes of use allow for the TEM to observe modulations in chemical identity, crystal orientation, electronic structure and sample induced electron phase shift as well as the regular absorption based imaging.

The first TEM was built by Max Knoll and Ernst Ruska in 1931, with this group developing the first TEM with resolving power greater than that of light in 1933 and the first commercial TEM in 1939 [48]. A block diagram of a TEM is shown in Figure 3.1.

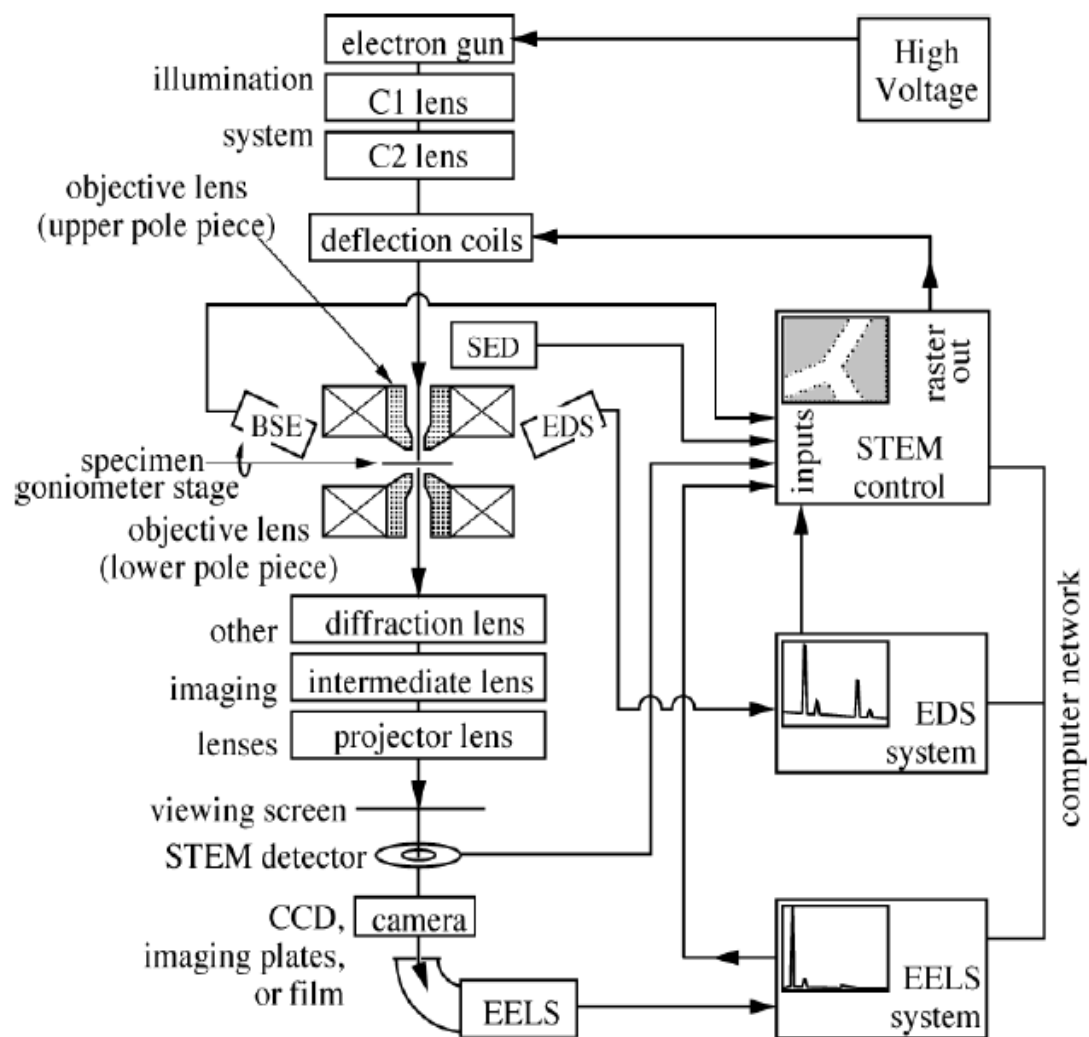


**Figure 3.1 :** Block diagram of typical TEM with STEM capability [46].

JEOL 2010F Model TEM located in Boston College was used to get images of the samples.

### 3.3 Optical Characterization

Three different types of measurements were performed on the samples;

- i) luminescence spectra,
- ii) responses of the samples to pulsed excitation,
- iii) thermal dependent spectral line-widths and line-shifts.

The components of the used instruments for these measurements are described below.

### **3.3.1 Components of the optical Set-up**

#### **3.3.1.1 Optic components**

##### **Monochromator**

We used a McPherson model 2051 one-meter scanning monochromator. The instrument is fitted with a 600 G/mm grating, blazed at 1.25  $\mu\text{m}$ . It has a resolution and wavelength resettability of 0.1  $\text{\AA}$  with repeatability of  $\pm 0.05 \text{ \AA}$ . The dispersion is 8.33  $\text{\AA}/\text{mm}$  with a 1200 G/mm grating. The scan controller used is model 789A-3, allowing to set the scanning speed, manually with thumbwheel, from 0.1 to 999.9  $\text{\AA}$  per minute. The entrance and exit slits are adjustable from 5  $\mu\text{m}$  to 2 mm.

##### **Titanium – Sapphire laser**

We used a Titan-P Model pulsed, tunable Ti-Sapphire laser, made by Schwarz Electro-Optics, for pulsed excitation. It can be tuned from 680 nm to 940 nm, and produces pulses of 10 ns duration with energy up to about 100 mJ. The system is typically operated at 10 Hz. It is equipped with a second harmonic generator crystal, resulting in laser pulses between 350 nm and 430 nm. The resonator utilizes two Ti-Sapphire crystals, a multiple prism tuning system, and a graded reflectivity mirror as the output coupler in an unstable resonator configuration. The Ti-Sapphire crystals are pumped with frequency-doubled pulses from a Q-switched Nd:YAG oscillator/amplifier system, thus also making accessible laser pulses at both 1064 nm and 532 nm.

##### **Diode laser**

We used a Laser Drive Inc. LDI 820 diode laser for the continuous wave (CW) excitation of the samples. This CW thermoelectrically cooled laser is capable of providing 3 W of output power. The laser was operated at 803.5 nm wavelength.

##### **Photomultiplier tube (PMT)**

The photomultiplier tubes used were the Hamamatsu types R1387 and 7102. The useful spectral response is from 300 to 850 nm (S-20) curve for the R1387, and 400 to 1200 nm (S-1) for the 7102. Each PMT is powered by a bench-top variable power supply. The voltage is adjusted, as required, to prevent saturation of the output. The output current of the PMT is proportional to the voltage applied to the bleeder ladder

network. Cooling for the PMT is provided by a thermoelectric cooler that cools the tube to about 50 C below ambient.

### **3.3.1.2 Sample environment**

#### **Cryogenic cooler**

The cryogenic refrigerator operates on the Gifford-McMahon (GM) principle using a closed helium gas cycle. The advantage of GM is that the compressor unit can be separated from the Cold Head which is the part of the Sample Chamber, thus allowing the flexibility of mounting the Cold Head in any position. The compressor and the Cold Head are connected with a pressure flexible tubing. The system is filled with helium to a pressure of 16 bar, capable of cooling the sample to 20K.

#### **Vacuum system**

The vacuum system lowers the pressure of the sample chamber to about  $2 \times 10^{-5}$ Torr. A mechanical roughing pump was used to achieve this vacuum.

#### **Sample chamber**

The sample chamber was manufactured by the Janis Research Co. The sample can be easily mounted on a pedestal and adjusted for orientation with the Monochromator input and the light source beam. It has five optical windows for versatility of beam positioning and steering. The sample can be cooled to about 20 K in a vacuum of  $10^{-5}$  Torr. Because of the vibration and noise generated by the cryogenic pump, the sample chamber is mounted on a steady optical table.

### **3.3.1.3 Signal conditioning**

#### **Pre-Amplifier**

The output current of the PMT anode is read as voltage via load resistor with respect to the ground potential. The effective bandwidth (BW) of the output pulse is inversely proportional to the product of the resistor and all parasitic capacitance in the PMT output circuit, including cabling. Thus to increase the BW an amplifier is put close to the PMT output and the load resistor is made as small as possible. The pre-amplifier is home-made using an ultra-low distortion high speed integrated circuit, the Analog Devices AD 8008. The chip has a BW specification of 230 MHz for a voltage gain of 2. With the pre-amplifier in place the PMT output is 50 to 1000

ohms, depending on the output signal strength. The pre-amplifier gain can be 2 or 20. The pre-amplifier is powered by AA cells.

### **Chopper**

The chopper is placed at the entrance of the monochromator continuous wave (CW) optical signal. In essence the mechanical chopper, operated at nominally 150 Hz, reduces the carrier frequency of the optical signal, thus removing all the DC biases introduced by the instrumentation and amplifiers.

### **Lock-in amplifier**

The purpose of this instrument is to amplify the low level AC signal of the PMT output, when the signal is chopped, and demodulate it to recover the base-band optical signal. In this set-up we use an EG&G Model 5206 lock-in amplifier. It has a 1  $\mu$ V to 5 V rms input sensitivity, with a carrier frequency of 0.2 Hz to 200 kHz. The signal to reference phase shift can be controlled in 0.025 degree steps from 0 to 360 degree.

### **3.3.2 Luminescence spectral measurements set-up**

The continuous emission spectra of the samples were obtained by pumping the samples with the output of a Laser Drive Inc. Model LDI-820 laser diode, that resulted in the excitation of the levels  $^2\text{H}_{9/2} - ^4\text{S}_{5/2}$ . The luminescence signal was directed toward the entrance slit of the 1 m McPherson Model 2051 monochromator and chopped at a frequency of 150 Hz before entering the slit. The monochromator provided a resolution 0.8  $\text{\AA}$  with the slits set at 50  $\mu\text{m}$  and a wavelength reproducibility of 0.1  $\text{\AA}$ .

The optical signal was detected by a Hamamatsu 7102 photomultiplier tube with a S1 response sent to an EG&G Model 5210 lock-in amplifier and recorded in a computer.

The same arrangement was used for the line-width and line-shift measurements with the entrance and output slits of the monochromator set at 80 – 150  $\mu\text{m}$ , which correspond to 1 – 2  $\text{\AA}$  spectral width and a 5  $\text{\AA}/\text{min}$  scanning rate. A schematic diagram of the system is given in Figure 3.2.

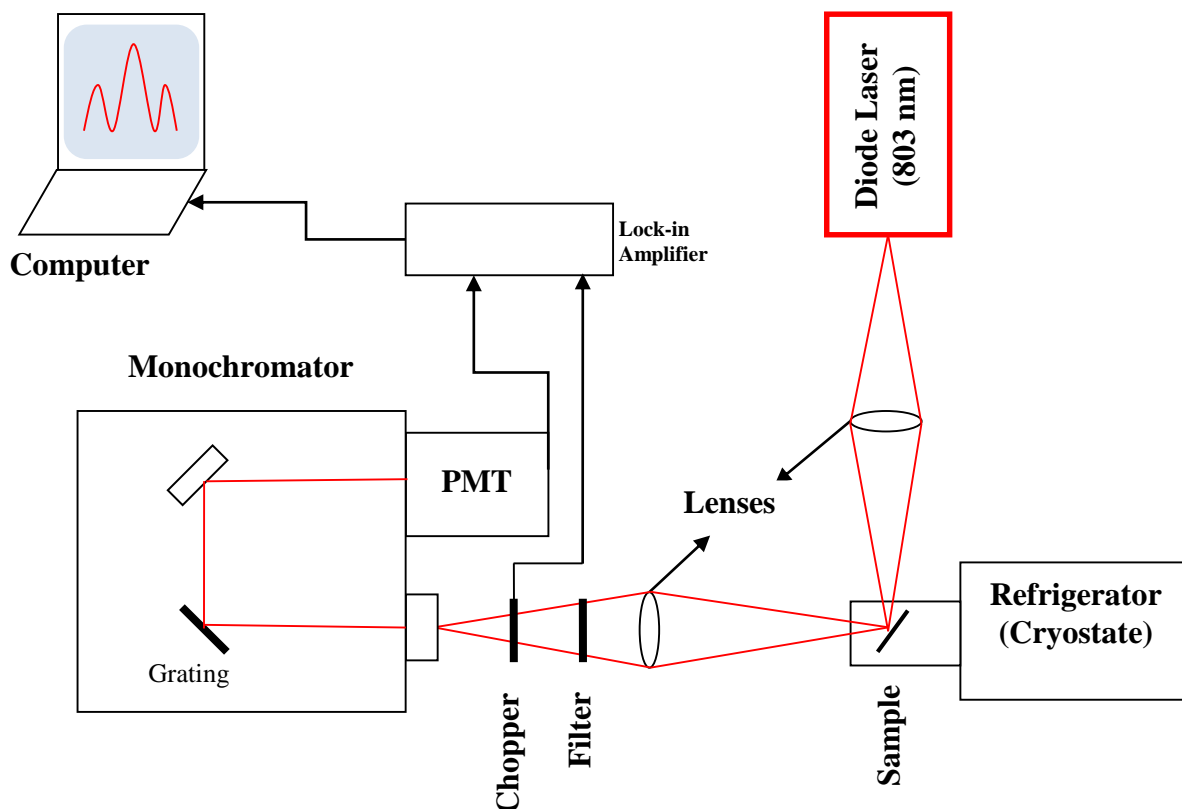


**Figure 3.2 :** Luminescence setup for the continuous light source.

### 3.3.3 Response to pulsed excitation measurements set-up

The experimental data on the responses of the samples to the pulsed excitation were obtained by using the system given in Figure 3.3. Unlike the luminescence system given in Figure 3.2, Titan P Model Ti-Sapphire laser and Tektronix Model TDS3052B oscilloscope were employed as an excitation source and for recording the response of the samples to the pulsed excitation, respectively.

For the experiments in the temperature range 30-300 K, the samples were mounted on the cold finger of a closed cycle Helium refrigerator. This system uses a Janis Research Model RD dewar connected with a Leybold Model RW2 compressor. The temperature was controlled by using the Lake Shore Cryotronics 805 Model controller. For the experiments at higher temperatures the samples were placed on a hot plate which provided up to 700 K temperatures and the surface temperatures of the samples were precisely measured by using a J-type thermocouple.

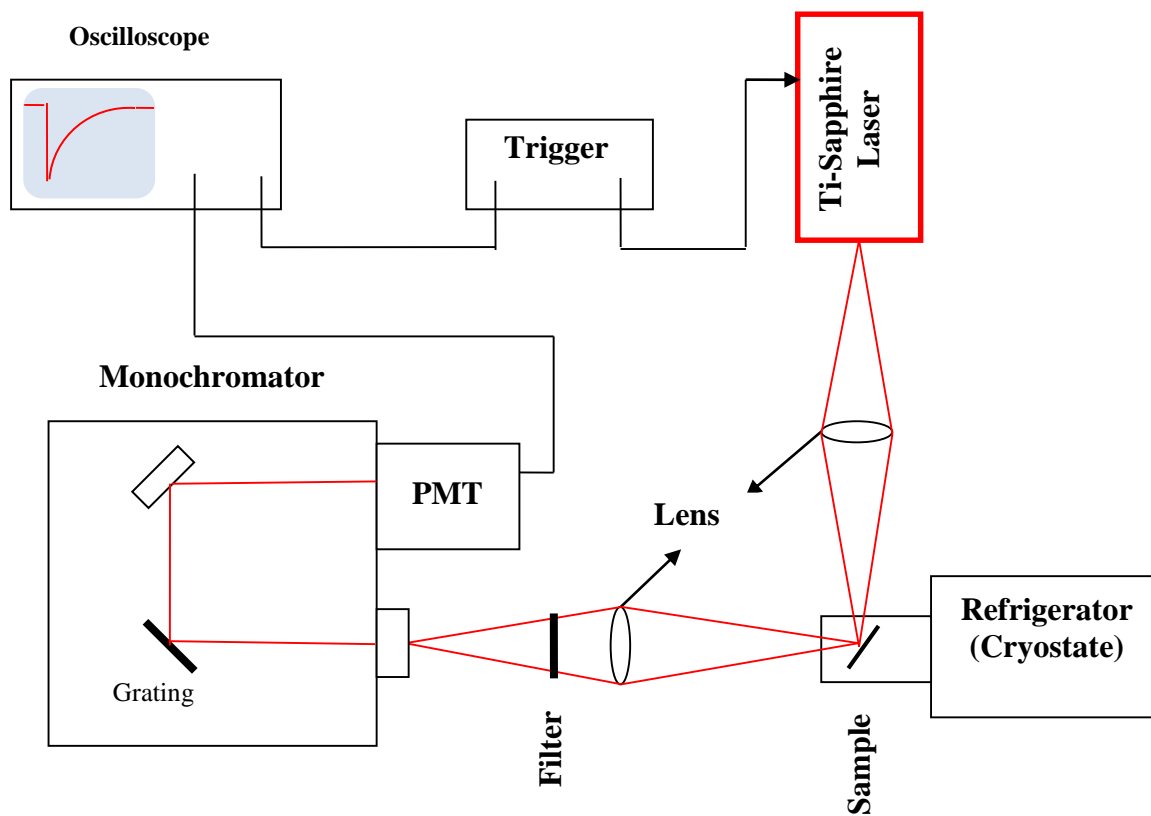


**Figure 3.3 :** Block scheme of the response to pulsed excitation measurements set-up.

## 4. FABRICATION AND SPECTRAL INVESTIGATION OF 1% Nd<sup>3+</sup> DOPED Y<sub>2</sub>O<sub>3</sub> NANO-PARTICLES

### 4.1 Introduction

New avenues to research have been opened by the fabrication of nano-powders doped with optically active ions. Experimental results indicate that the energy levels are not much affected by the spatial confinement, whereas the dynamical properties are dependent on the size of the nano-particles. Another important result indicates that nano-powders doped with optically active ions may luminesce even when the dopant concentration exceeds the maximum concentration at which solids of the same nature can emit luminescence radiation [49, 50].

The problem of the role played by the particles' surfaces versus their inner parts needs investigation, especially in regard to the setting of the phonon spectrum in the presence of the spatial confinement.

Thermal decomposition is a powerful and cheap wet chemical technique that can be used to synthesize Y<sub>2</sub>O<sub>3</sub> nanopowders. This process is based on the chemical decomposition of the materials caused by heat [42]. In this study, we used thermal decomposition to synthesize Y<sub>2</sub>O<sub>3</sub> nano-powders. The composition of the prepared formulations, synthesis and annealing temperatures and mean crystallite sizes are given in Table 4.1.

**Table 4. 1 :** Formulations of yttrium-neodymium alginate solution prepared, synthesis and annealing temperatures and mean particle sizes estimated from Scherrer Equation.

Alginate (% w/w)	Yttrium Nitrate (Molar)	Neodymium Nitrate (Molar)	Synthesis Temperature ( °C)	Annealing Temperature ( °C)	Mean Size (nm)
1	%99 of 0,2M	%1 of 0,2M	350	--	13,8
			400	--	16.0
			450	--	20.4
			500	--	27.1
			500	600	32.3
			500	800	40.0
			500	1000	49.7
			500	1400	248.2

## 4.2 Experimental

### 4.2.1 Preparation of the Nd<sup>3+</sup> doped Y<sub>2</sub>O<sub>3</sub> powders

Nanosized Y<sub>2</sub>O<sub>3</sub> samples doped with 1.0 %mol Nd<sup>3+</sup> ions concentration were prepared by thermal decomposition of yttrium-neodymium alginate. Yttrium nitrate hexahydrate Y(NO<sub>3</sub>)<sub>3</sub>·6H<sub>2</sub>O, neodymium nitrate hydrate Nd(NO<sub>3</sub>)<sub>3</sub>·H<sub>2</sub>O and low-viscosity (250 cps of 2% solution) alginic acid sodium salt of an analytic grade were purchased from the Sigma Aldrich Company.

The yttrium-neodymium alginate beads were prepared by thermal decomposition method according to the prescription given in the literature [42]. 0.2M 100ml yttrium-neodymium nitrate solution were prepared by dissolving the appropriate amount of the yttrium nitrate and neodymium nitrate salts in ultra pure water. Also 50ml alginate solution with 1%w/w concentration were prepared by dissolving an appropriate amount of the sodium alginate salt in the ultra pure water under magnetic stirring.

Alginate is a biopolymer which is extracted from three species of brown algae. It is a linear heteropolysaccharide composed of D-mannuronic acid and L-guluronic acid. Gelation of alginate is possible by the interaction of the carboxylate group with divalent ions and the formation of beads can be achieved by dropwise addition of sodium alginate into divalent solution by using a syringe with a needle or pipette [41, 42]. The formation of the yttrium-neodymium alginate beads was achieved by the dropwise addition of the sodium alginate solution into yttrium-neodymium salts solution by using a syringe.

The prepared beads were kept in their gelling medium for 30 minutes under gentle stirring; then they were removed from their gelling medium, placed in a porcelain crucible and heated to different temperatures ranging from 350 to 500°C for 24h with a heating rate of 10 °C/min in an electric furnace in air medium. Some of the products obtained were annealed at 600, 800, 1000 and 1400°C, to investigate the particle size dependence on the annealing temperature.

### 4.2.2 Structural characterization

X-ray diffraction investigations were carried out with a Bruker AXS D8Model (Cu-K $\alpha$  radiation) diffractometer at 40 kV and 30 mA setting in the 2 $\theta$  range from 20° to

70° with a scanning steps of 0.02°. A JEOL 6335F model scanning electron microscope was used to get SEM images of the samples. Elemental analysis was made by using an energy dispersive spectroscopy (EDS) attached to SEM. TEM images of the samples were obtained by using a JEOL 2010F model transmission electron microscope operated at 200 kV with a field emission gun. TEM specimens were prepared by depositing a few drops of a sample dispersed in ethanol by using an ultrasonic bath, on a carbon coated copper grid.

#### **4.2.3 Spectroscopic measurements**

The continuous emission spectra of the samples were obtained by pumping the samples with the output of a Laser Drive Inc. Model LDI-820 laser diode, that resulted in the excitation of the levels  $^2H_{9/2} - ^4S_{5/2}$ . The luminescence signal was directed toward the entrance slit of a 1 m McPherson Model 2051 monochromator and chopped at a frequency of 250 Hz before entering the slit. The monochromator provided a resolution 0.8 Å with the slits set at 50 µm and a wavelength reproducibility of 0.1 Å.

The optical signal was detected by a Hamamatsu 7102 photomultiplier tube with an S1 response, sent to a EG&G Model 5210 lock-in amplifier and recorded in a computer.

The same arrangement was used for the line-width and line-shift measurements with the entrance and output slits of the monochromator set at 80 – 150 µm, which correspond to 1 -2 Å spectral width and a 5 Å/min scanning rate.

The experimental data on the responses of the samples to pulsed excitation were obtained by using a Schwarz Electro-Optics Inc. Model Titan-P Model Titanium-Sapphire laser and a Tektronix Model TDS3052B oscilloscope.

For the experiments in the temperature range 34-300 K, the samples were mounted on the cold finger of a closed cycle Helium refrigerator. This system uses a Janis Research Model RD dewar connected with a Leybold Model RW2 compressor. The temperature was controlled by using the Lake Shore Cryotronics 805 Model controller. For the experiments at higher temperatures the samples were placed on a hot plate which provided up to 700 K temperatures and the surface temperatures of the samples were precisely measured by using a J-type thermocouple.

## 4.3 Experimental Results

### 4.3.1 Structural characterization

The XRD patterns of the 1 % Nd<sup>3+</sup> doped Y<sub>2</sub>O<sub>3</sub> samples are given in Figure 4.1. The crystal structure and phase of all samples were analyzed by using these patterns. The cubic phase of the yttria without any other phases was identified by comparing the peak positions and the intensities with those in the Joint Committee on Powder Diffraction Standards (JCPDS) data files. It was clearly seen that the peak positions correspond well to the standard card with number 41-1105.

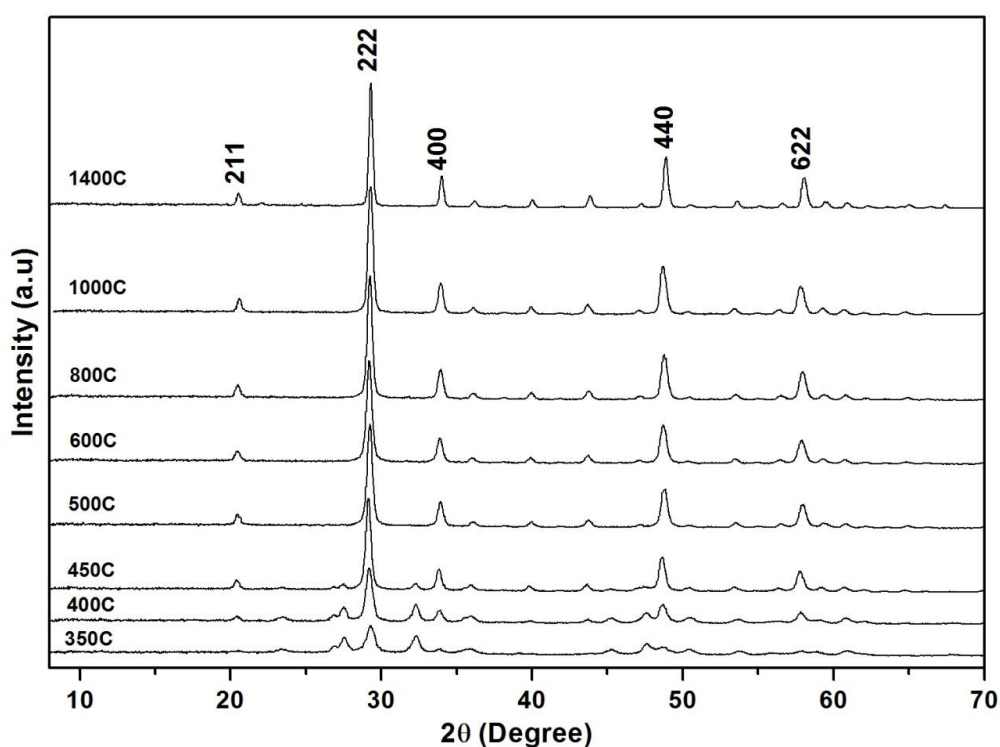


**Figure 4. 1:** XRD patterns of the 1 % Nd<sup>3+</sup> doped Y<sub>2</sub>O<sub>3</sub> nanopowders.

Figure 4.2 shows the SEM images of the Y<sub>2</sub>O<sub>3</sub> samples which were as-synthesized at 500°C and annealed at 1000°C. The nanopowders with spherical shapes are relatively uniform and have an average diameter of ~30 nm and ~50 nm in as-prepared (500°C) and annealed (1000°C) samples, respectively. It is clearly seen from the SEM images that the particle sizes of the samples strongly depend on the synthesis and annealing temperature and show an increasing tendency with the increasing annealing temperature. Also SEM images confirmed the particle sizes estimated from XRD measurements by using Scherrer Equation. The inset of Figure 4.2 shows the EDS (Energy Dispersive X-Ray Spectroscopy) spectra of the samples.

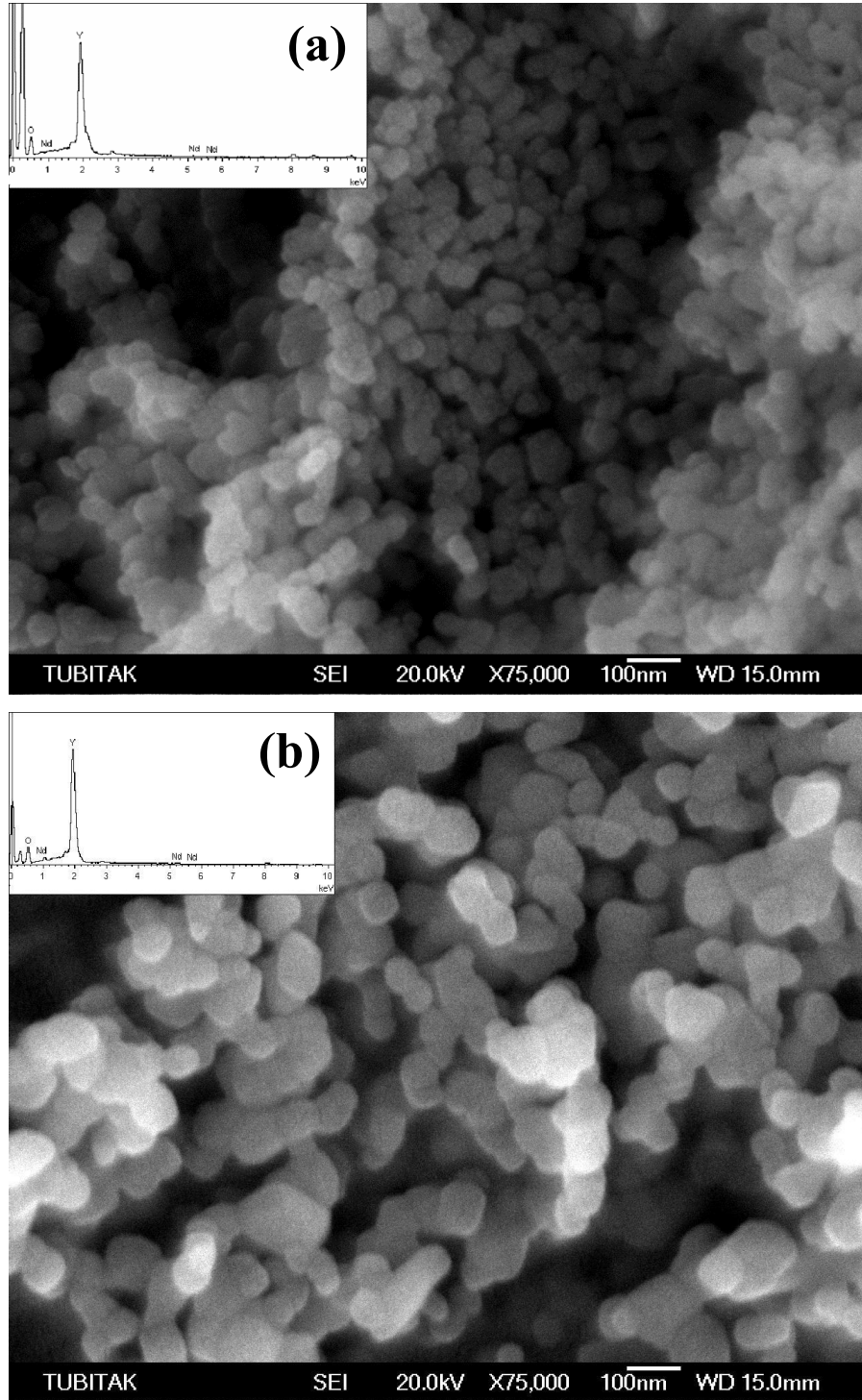


**Figure 4. 2:** (a) SEM image of as-prepared (500 °C) 1 % Nd<sup>3+</sup> doped Y<sub>2</sub>O<sub>3</sub> nanopowders (inset: corresponding EDS spectrum) (b) SEM image of 1 % Nd<sup>3+</sup> doped Y<sub>2</sub>O<sub>3</sub> nanopowders annealed at 1000 °C (inset: corresponding EDS spectrum).

We also conducted a series of TEM measurements to confirm the particle sizes and the morphologies of the synthesized samples. Representative TEM images are given in Figure 4.3. It is clearly seen from the micrographs that the particle sizes are in

good agreement with the results obtained from both of XRD and SEM measurements.

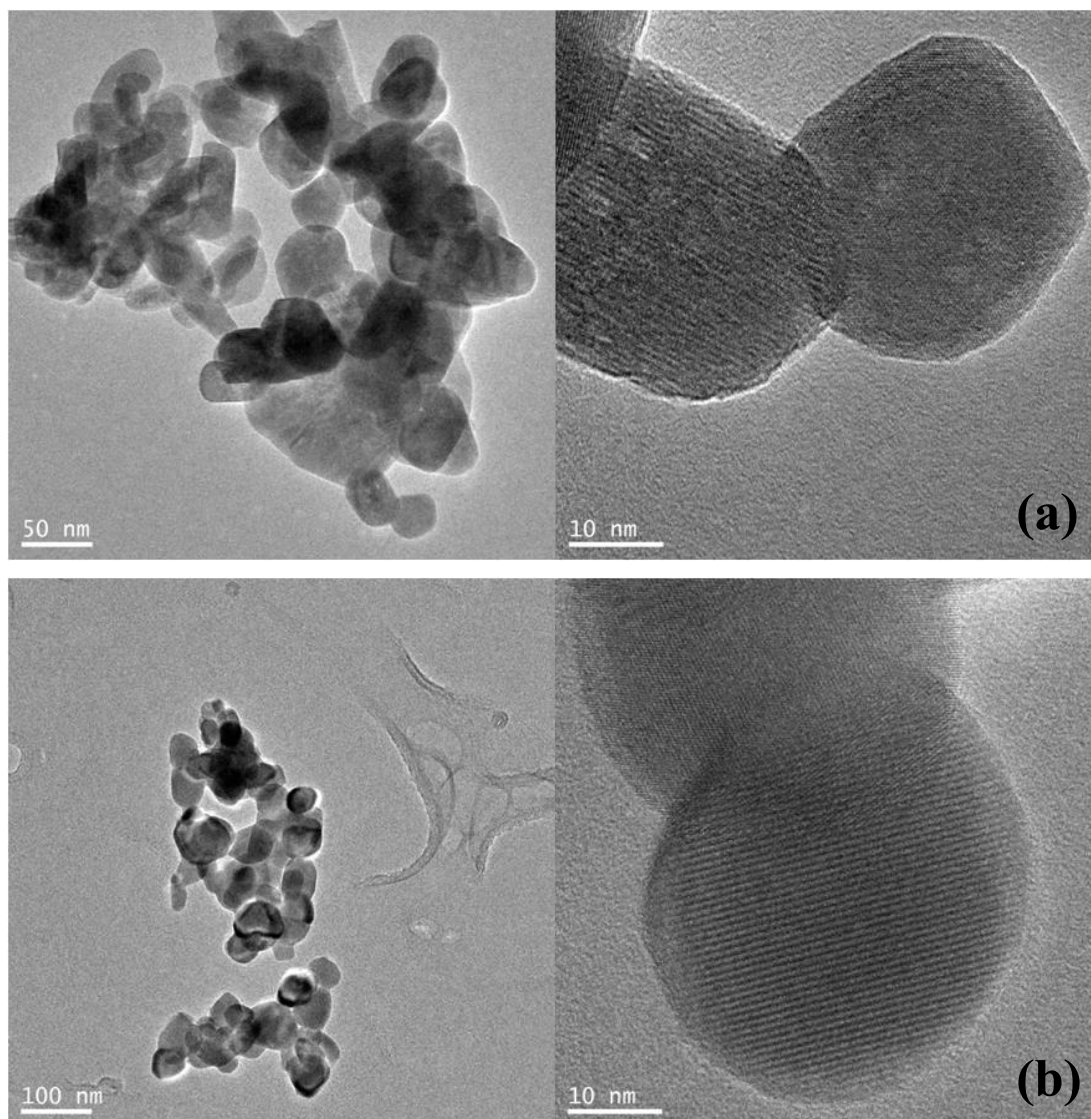


**Figure 4. 3:** Representative TEM micrographs of 1 % Nd<sup>3+</sup> doped Y<sub>2</sub>O<sub>3</sub> sample (a) synthesized at 350°C and (b) annealed at 1000°C.

#### 4.3.2 Spectroscopic characterization

The measurements of continuous luminescence spectra were conducted from 35 to 300 K and in the 850 – 1150 nm wavelength range. The luminescence spectra of all the samples at 35 K and 300 K and the corresponding energy level scheme are given in Figure 4.4a-b and Figure 4.5, respectively.

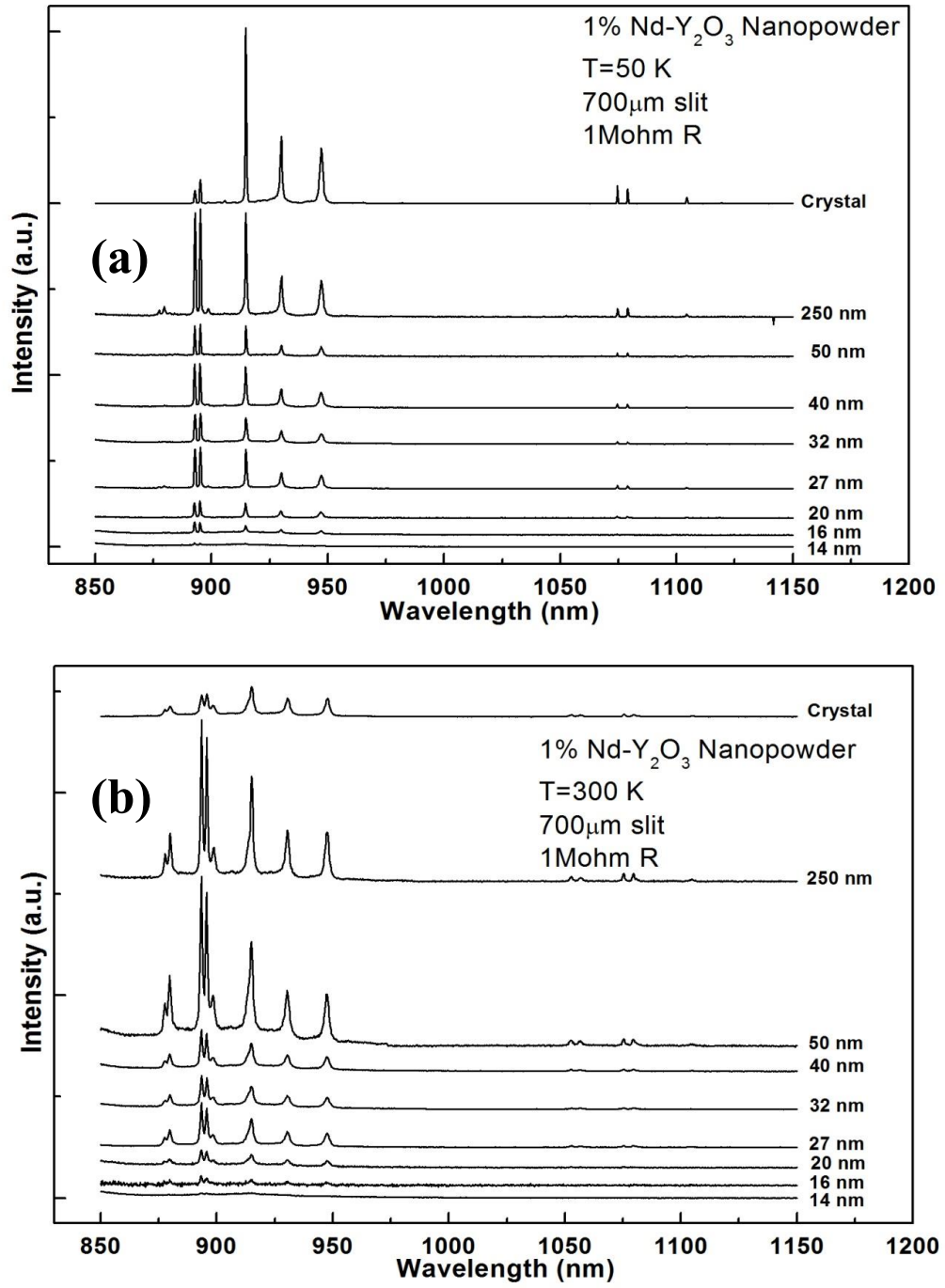


**Figure 4. 4:** Continuous emission spectra of samples at (a) 35 K and (b) 300 K.

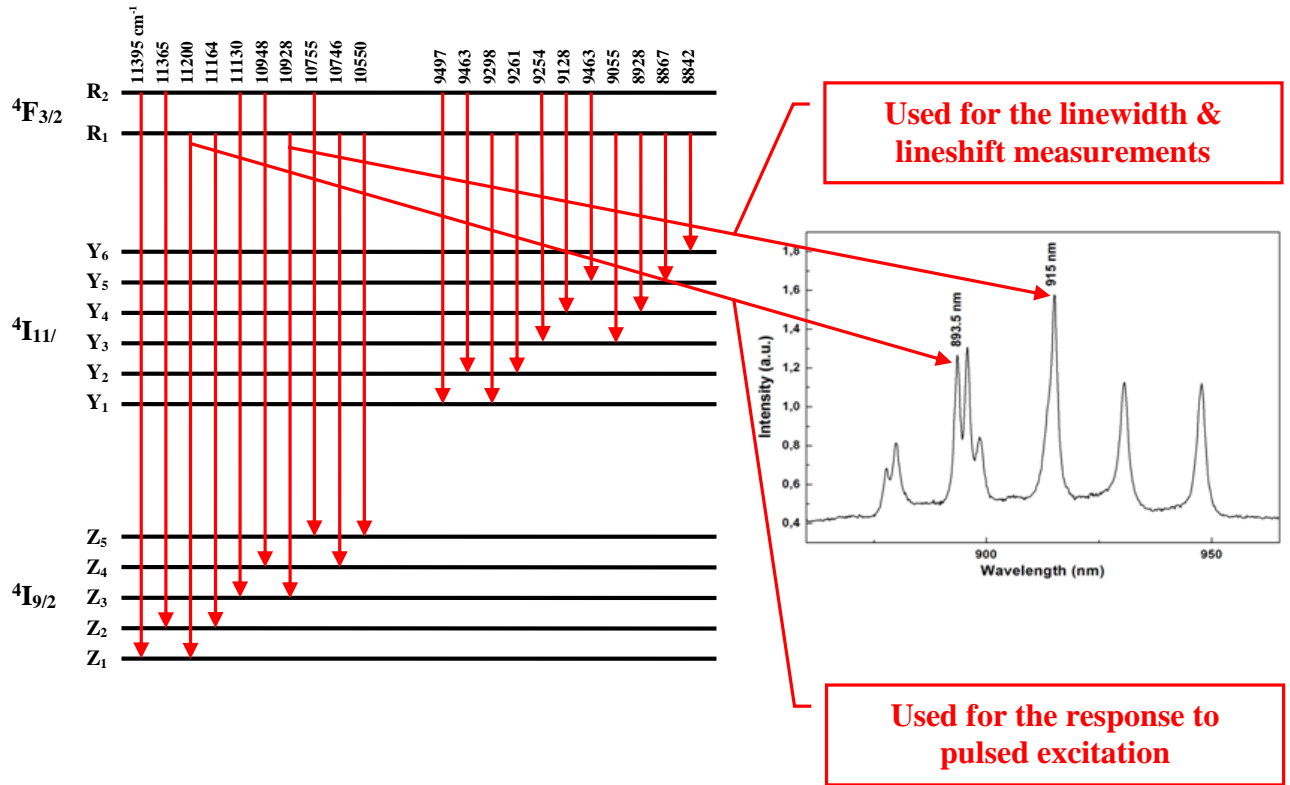


**Figure 4. 5:** Energy level scheme of Nd<sup>3+</sup> in Y<sub>2</sub>O<sub>3</sub>.

The emission spectra of the samples consist of two groups of emission peaks due to the  $^4F_{3/2} \rightarrow ^4I_{9/2}$  and  $^4F_{3/2} \rightarrow ^4I_{11/2}$  transitions. We note that the general aspect of the spectra is the same for all the samples. The intensity of the emission lines increase for all samples with the decreasing temperature; it is also found to increase with the increasing particle sizes. The spectra with greatest intensity are those of the crystal. Examining the spectra in detail we see that the smaller is the size of the particles, the wider are the spectral lines and the greater is the shift of each line toward longer wavelengths with respect to the corresponding line in the crystal. Figure 4.6 presents the shift of a well isolated line at 914.5 nm with respect to the corresponding line in the crystal. This is the line we have chosen in order to study the effects of temperature on the width and position of the spectral lines of the samples. The results of these measurements are reported in Figure 4.7 and 4.8.

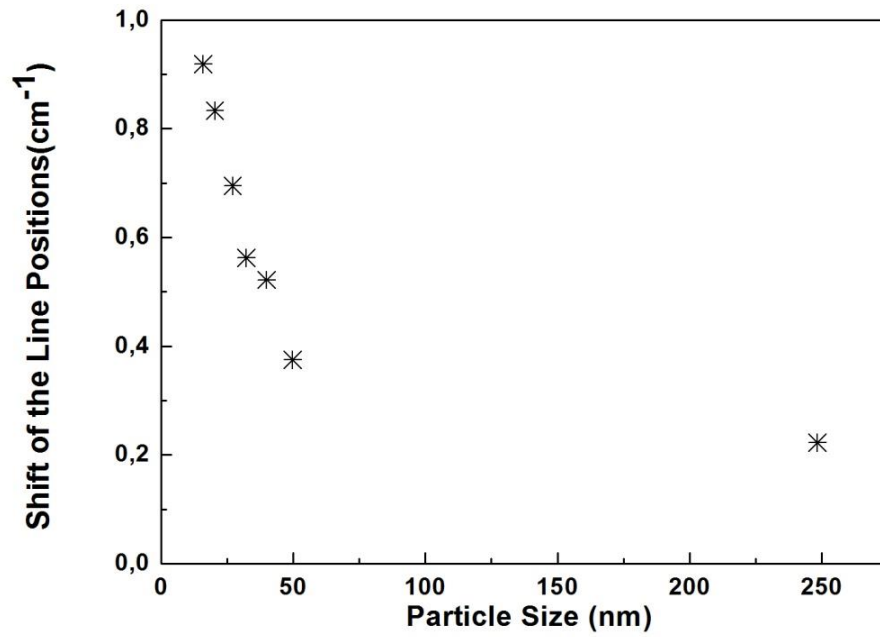


**Figure 4. 6:** Red-shift of a line position of different samples with respect to the crystal line.

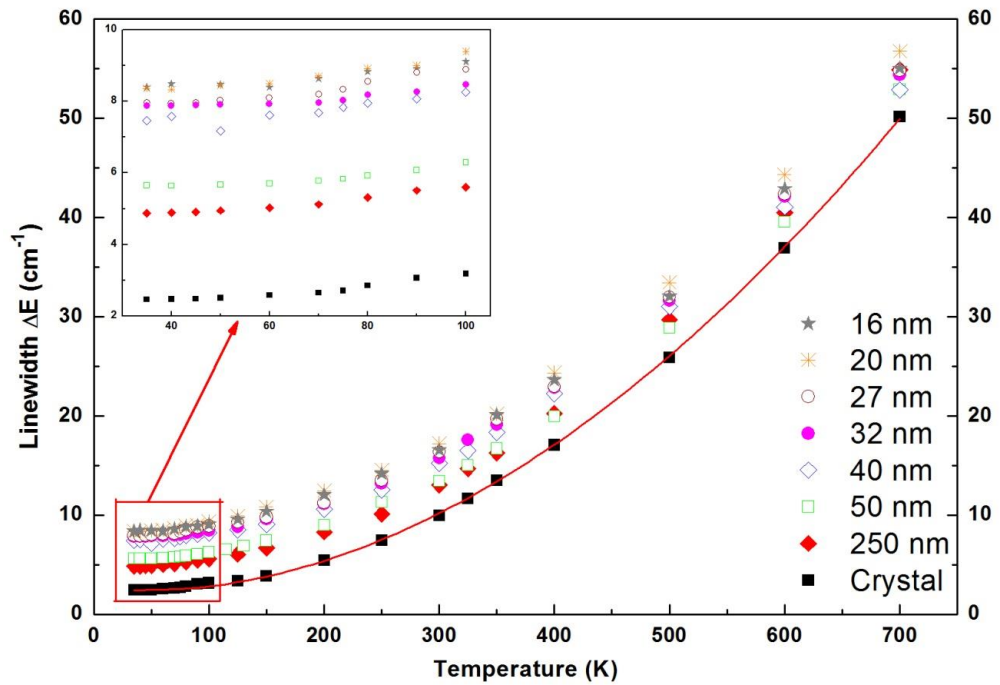


**Figure 4. 7:** Variation of linewidth as a function of temperature in 1 % Nd<sup>3+</sup> doped Y<sub>2</sub>O<sub>3</sub>. The dots are experimental results and the solid curve is the theoretical fittings with respect to the crystal line.

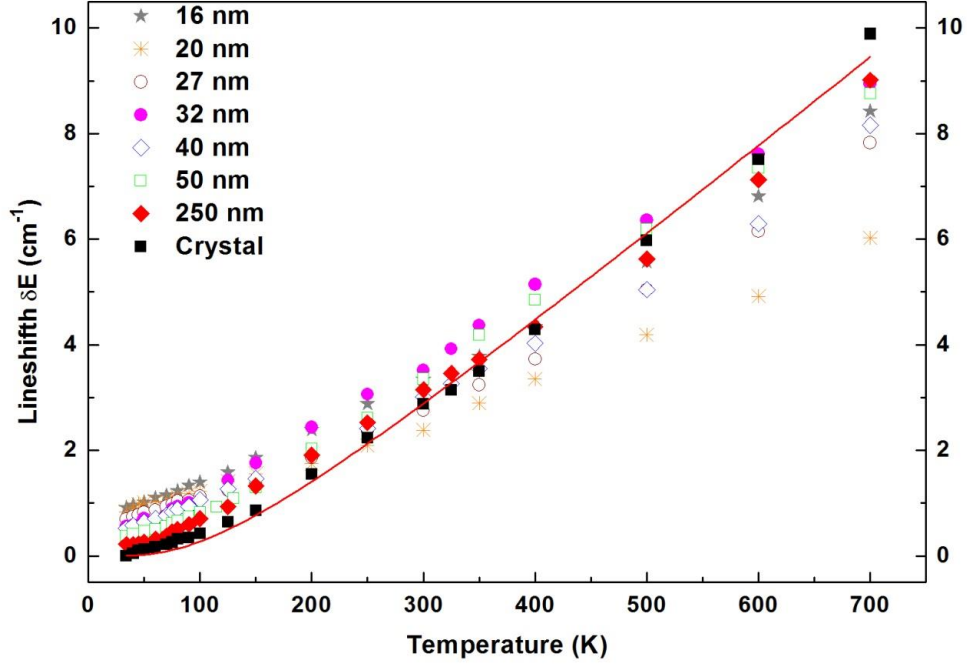


**Figure 4. 8:** Line-shift as a function of temperature 1% Nd<sup>3+</sup> doped Y<sub>2</sub>O<sub>3</sub>. The solid red line is the theoretical fitting to the crystals' experimental data.

The measurements of the response of the samples to pulsed excitation were carried out in the 35 – 700 K temperature range. The results are given Figure 4.9a–d. Since the luminescence output of the Nd-doped samples consists of spectral lines related to transitions that initiate in the doublet  $^4F_{3/2}$ , the response of these systems to pulsed excitation is the same, regardless of the spectral line at which it is measured. We have chosen to measure this response at  $\lambda = 892.5$  nm (see Figure 4.5). The lifetime of the  $^4F_{3/2}$  doublet is host-dependent: it is 480  $\mu$ s in YLF [51], 230  $\mu$ s in YAG [52, 53], 33  $\mu$ s in YVO<sub>4</sub> [51, 52], and 260  $\mu$ s in Y<sub>2</sub>O<sub>3</sub> [53] etc., but it is generally independent of temperature due to the large gap between the  $^4F_{3/2}$  doublet and the lower  $^4I_{15/2}$  multiplet [54]. We have found that the lifetime of the  $^4F_{3/2}$  doublet in the Y<sub>2</sub>O<sub>3</sub> crystal the value  $\sim 250$   $\mu$ s, almost independent of temperature.

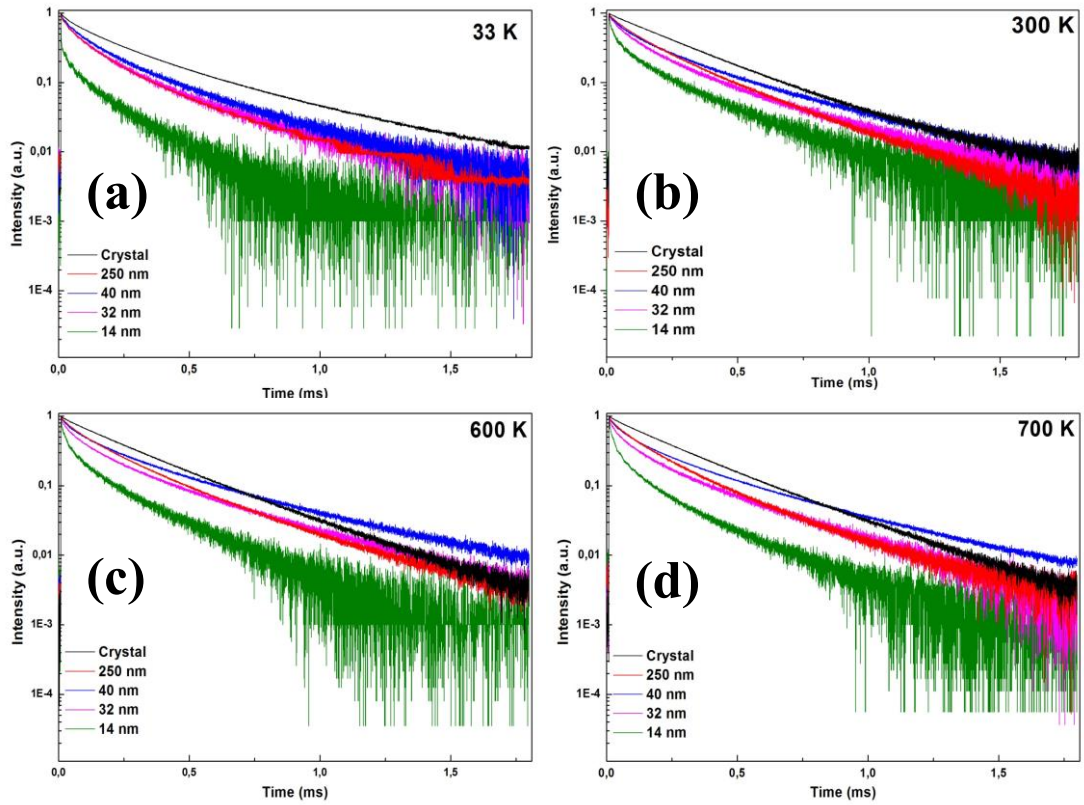


**Figure 4. 9:** Response to pulsed excitation results of all powders at (a) 33 K (b) 300K (c) 600 K (d) 700 K.

The response pattern of the crystal is close to an exponential, more so at high temperatures. The response of the powder samples deviates from exponentiality at early times and then becomes exponential with a decay constant greater than that of the crystal, so that at a time after the initial response the two patterns (the pattern of the crystal and that of the sample) cross out.

The smaller is the particle and the lower is the temperature the greater is the deviation of the initial pattern from exponentiality and the longer is the time at which the two patterns cross. Figure 4.10 presents the lifetimes of all the samples as function of temperature. When a decay pattern was exponential, the lifetime was calculated from an exponential fit. When a pattern was not exponential, we took as measure of the lifetime the area under the decaying signal, having set the intensity of the initial signal equal to one.

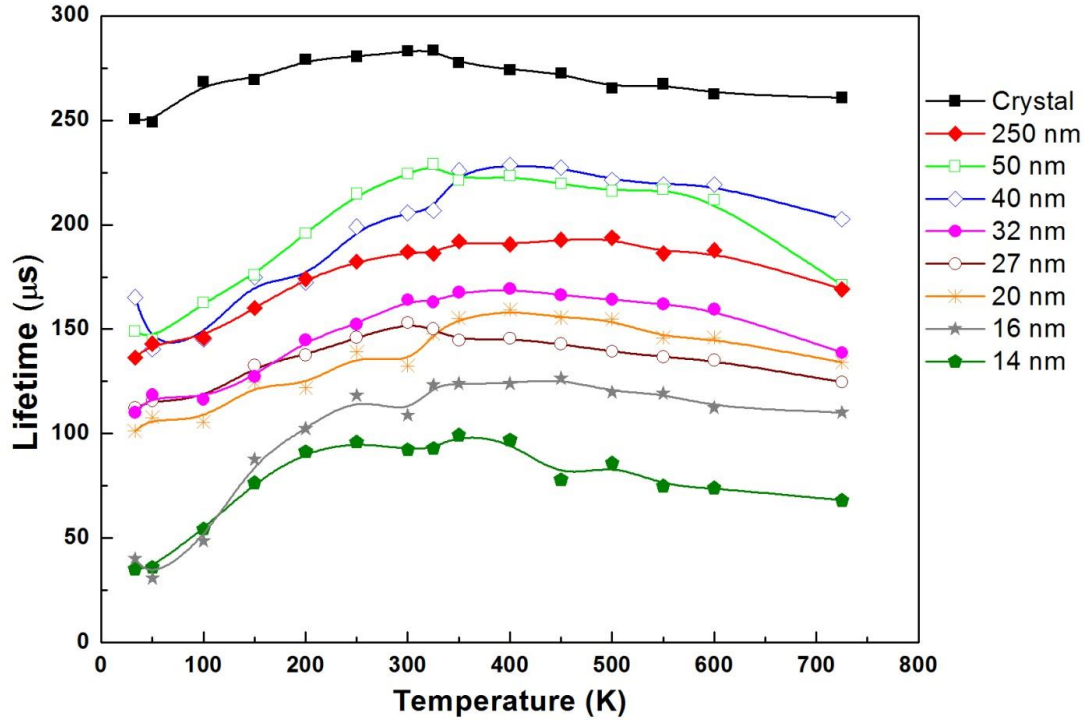


**Figure 4. 10:** Variation of lifetimes with the temperature.

#### 4.4 Discussion of Results

##### 4.4.1 Structural properties

The cubic phase of the yttria was determined by using XRD patterns. It was observed that the lattice parameter increases with the addition of dopant ions and found up to 10.6051 Å which is the proof of the incorporation of the Nd<sup>3+</sup> ions into Y<sup>3+</sup> sites due to the larger ionic radius of the Nd<sup>3+</sup> (112.3 pm) than Y<sup>3+</sup> (104 pm) [15, 55]. It was observed that the widths of the diffraction lines broadened with the decreasing temperature because of the decreasing crystallite sizes. The most narrow line was observed for the sample annealed at 1400°C. The crystallite sizes of the powders were estimated by using the Scherrer Equation [45] reported below:

$$L = \frac{K\lambda}{\beta \cos \theta} \quad (4.1)$$

where L is the crystallite length, K is a constant that varies with the method of taking the breadth (0.89<K<1),  $\lambda$  is the wavelength of the incident X-ray beam,  $\beta$  is the width of the peak at half maximum intensity of a specific phase (hkl) in radians and  $\theta$  is center angle of the peak. The (222) peaks were used to estimate the particles' size.

As seen from the Figure 4.1 and our calculations given in the Table 4.1, the particle size of the samples increases with increasing annealing temperature.

The SEM and TEM images confirmed the particle sizes calculated by using the Scherrer Equation. A nebulous structure which we attributed to the existence of organic compound (alginate) was seen in some SEM images of the samples. This structure disappears with increasing annealing temperature. On the other hand the EDS results confirm the presence of Nd<sup>3+</sup> content. All of the structural characterization measurements showed that the particle sizes can be effectively controlled by the synthesis and annealing temperature, and increase with increasing treatment temperature.

#### 4.4.2 Spectroscopic response

The general aspect of the spectral output of the powder samples strongly resembles the spectra of the crystal confirming the fact that the confinement provided by the restrictions of the particles' sizes does not affect by much the energy levels of the Nd<sup>3+</sup> ion.

The shifts reported in Figure 4.6 indicate that their magnitude becomes greater the smaller is the dimension of the particle. It seems then legitimate to attribute this behavior to the increasingly important role played by the surfaces in smaller particles. The Nd ions at the surface are in a different environment with respect to the ions in the interior of the material. In a crystal the ions in the surface are a negligible minority with respect to the ions in the bulk of the material, but in a particle it is not so. In very small particles going from the surface toward the center of the particle, there is gradation in the Nd-O bond lengths, approaching the conditions of Nd in a single bulk crystal. It is possible that, even in the interior of the particle, the conditions of the environment in the bulk will never be reached. This may account for the fact that the shift of the lines increases with decreasing of the particles' sizes.

The results concerning the thermal line broadening were handled as follows.

The experimental data were compared with the following equation [38]

$$\Delta E(cm^{-1}) = \Delta E_0 + \Delta E^R \quad (4.2)$$

where

$$\Delta E^R = \bar{\alpha} \left( \frac{T}{T_D} \right)^7 \int_0^{T_D/T} \frac{x^6 e^x}{(e^x - 1)^2} dx \quad (4.2a)$$

In Eq. (4.2),  $\Delta E_0$  is the temperature independent-residual width from the two levels due to random crystal strains and spontaneous phonon emission processes and  $\Delta E^R$  is the temperature-dependent contribution to the width due to the Raman scattering of phonons:  $\bar{\alpha}$ ,  $T_D$  and  $\Delta E_0$  are treated as adjustable parameters to get best fit (a least square fit) to the experimental line-width data shown in Figure 4.7.

The values of the parameters that were used to produce the fitting of the experimental data with the theoretical formula are listed in Table 4.2. It is of interest to note that the residual line-width at low temperature increases with decreasing particle size.

**Table 4. 2 :** Best fit parameters ( $\alpha$ ,  $\bar{\alpha}$ ,  $T_D$ , and  $\Delta E_0$ ) obtained from line-shift and line-width measurements.

Particle Size	Line shifts			Line widths	
	$T_D$ [K]	$\alpha$ [cm <sup>-1</sup> ]	$\Delta E_0$ [cm <sup>-1</sup> ]	$T_D$ [K]	$\bar{\alpha}$ [cm <sup>-1</sup> ]
Crystal	429	22	2,46	440	95
248.2 nm	285	12	4,88	397	80
49.7 nm	263	11	5,65	360	62
40 nm	258	9,1	7,46	305,7	44
32.3 nm	207	8,3	7,88	305,5	46
27.1 nm	352	12	7,96	210	21
20.4 nm	236	5,7	8,36	109	5.9
16 nm	272	9.5	8,40	194	18

The effect of temperature on the position of the chosen sharp line is presented in Figure 4.8. We determined that the line position is red-shifted with increasing temperature. The experimental data were compared with the following Eq. (4.3) that expresses the shift as due to the process of emission and absorption of virtual phonons [38]:

$$\delta E(cm^{-1}) = \delta E^R = \alpha \left( \frac{T}{T_D} \right)^4 \int_0^{T_D/T} \frac{x^3}{e^x - 1} dx \quad (4.3)$$

where  $\alpha$  and  $T_D$  are treated as adjustable parameters to get a best fit. The line position at  $T = 0$  K was estimated by extrapolating the experimental data to zero temperature. The corresponding fitting values of  $\alpha$  and  $T_D$  for each line are listed in Table 4.2.

The fitting values of the coupling coefficients  $\bar{\alpha}$  and  $\alpha$  obtained for the line-widths and line-shifts are typical for rare-earth ion doped laser crystals. They are usually less than  $100 \text{ cm}^{-1}$ . In case of transition metal ion the coupling coefficients  $\bar{\alpha}$  and  $\alpha$  are usually about  $500 \text{ cm}^{-1}$  [56, 57].

The decay patterns of the luminescent  $\text{Nd}^{3+}$  ions embedded in the nanoparticles are expected to deviate from an exponential decay of the same ions in the crystal for two reasons:

- 1) The role played by the surfaces will be increasingly important as the radius of the particle is reduced, producing a deviation from exponentiality. Molecular groups such as O-H residing on the surface may enhance the decay process due to their stiff vibrations that rob the ion of its excitation energy. We reasonably expect that a deviation from exponentiality at the beginning of the decay pattern.
- 2) The ensemble of particles in the sample differs also from the bulk material for the presence of the interstices between the particles. In what follows we shall describe how we can handle the problem presented by this difference.

The rate of spontaneous relaxation of an atomic system is given by [40]

$$A(\Psi J, \Psi' J') = \frac{64\pi^2(\Delta E)^3}{3\hbar(2J+1)} \eta F^2 \quad (4.4)$$

where  $F$ ; matrix element of the electric dipole operator,  $\Delta E$  = energy gap between the states  $|\Psi J\rangle$  and  $|\Psi' J'\rangle$ , and  $\eta = \frac{n(n^2+2)^2}{9}$ ; Lorentz correction for the local field with  $n$ = index of refraction of the host material.

Applying those considerations to the ions embedded in the nanoparticles, we can say that the rate of their spontaneous emission (inverse of the radiative lifetime) depends on an effective index of refraction  $n_{eff}$  which consist of a combination of the index of refraction of the nanoparticle  $n_{NP}$  and of the index of refraction of the surrounding medium  $n_{med}$  :

$$n_{eff}(x) = \chi n_{NP} + (1 - \chi) n_{med} \quad (4.5)$$

where  $\chi$  is the filling factor indicating the fraction of space that is occupied by the nanoparticles. The validity of the usage of  $n_{eff}$  in calculating the probability of decay rests on the fact that the size of the particles is much smaller than the wavelength of light [37].

Since the ratio  $\chi$  is independent of the size of the nanoparticles the tails of the response patterns of the particles with different sizes should be parallel after they cross the pattern corresponding to the crystal response to pulsed excitation.

The responses of the samples to pulsed excitation present the following interesting aspects:

- 1) At each temperature the decay patterns depend on the size of the particles with increasingly greater deviation from exponentiality for smaller particles (see Figure 4.9a-d)
- 2) The patterns that deviate from exponentiality eventually cross the exponential pattern of the crystal. The greater is the deviation the more distant in time is the crossing. A possible explanation of these experimental finding is the existence of large amount of O–H groups at the surface of the each particle, which considering the stiff O–H vibration, could provide a quenching of the luminescence and the shortening of the lifetime.
- 3) All the decay patterns of the particles of different sizes become paralel after they cross the decay pattern of the ions in the crystal. This behavior indicates that the effective index of refraction is lower for the nanoparticles than for the single crystal, hence decreasing the radiative decay rate, and the filling factor  $\chi$  is independent of the particles size.

## 4.5 Conclusions

This study was focused on the synthesis and characterization of  $Y_2O_3$  nanophosphors doped with 1 % Neodymium ( $Nd^{3+}$ ) ions. Nanoparticles were synthesized by using the thermal decomposition technique and annealed at different temperatures to control particle sizes. The synthesized particles were structurally characterized by using X-ray diffraction (XRD), scanning electron microscope (SEM) and transmission electron microscope (TEM). The cubic phase of the  $Y_2O_3$  was determined and the size of the particles was found to range from ~ 15 to 300 nm.

A series of spectroscopic measurements on a number of these nano-particle samples were performed. For comparison we also characterized spectroscopically an  $\text{Y}_2\text{O}_3$  crystal sample.

For each sample the emission spectrum was accurately measured in a wide range of temperatures ranging from 30 to 300K. The spectra consisted of the  $\text{Nd}^{3+}$  ion's narrow spectral lines corresponding to transitions from the  $^4\text{F}_{3/2}$  doublet level to the  $^4\text{I}_{11/2}$  and  $^4\text{I}_{9/2}$  many-folds.

We also measured the width and the position of a well isolated line in the temperature range 30–700K. The results indicate that the residual width at low temperatures is larger for powders with smaller particle sizes.

Finally measurements were performed on the decay patterns of  $\text{Nd}^{3+}$  ions following a pulsed excitation. These measurements were conducted in the temperature range of 30 – 700 K. Such patterns vary considerably with the size of the nano-particle, so that they may be considered signatures of these sizes. When comparing the decay patterns of the powders with the exponential decays of the  $\text{Y}_2\text{O}_3:\text{Nd}^{3+}$  crystal we found larger deviations from exponentiality for the powders of smaller particles sizes, and smaller deviations from exponentiality at high temperatures.



## **5. SYNTHESIS AND SPECTRAL CHARACTERIZATION OF YTTRIUM OXIDE NANO-POWDERS DOPED WITH Nd<sup>3+</sup> IONS WITH A LARGE RANGE OF CONCENTRATIONS**

The introduction of Nd<sup>3+</sup> dopants in yttrium oxide nano-powders at concentrations as high as 10% has motivated the study of their emission as function of concentration. The luminescence from these systems as function of temperature, particle size, and concentration of Nd<sup>3+</sup> has been studied and the trends been able to be established is given below.

### **5.1 Introduction**

The production of luminescent materials in the form of nano-powders has given rise to a new and important chapter in the investigations of such materials. Spectroscopy has the necessary tools to conduct these investigations and a large number of possibilities and situations exist due to the fact that a new parameter enters the scenario, the size of the nano-particles. In addition, the reduction of these materials to nano-powder form allows them to luminescence even when they are doped with the ions responsible for their spectroscopic properties at concentrations so high that they would not present any light emission when used in the same systems in bulk crystalline form [49, 50, 58, 59].

The expansion of experimental situations, and in particular that of the range of possible dopant concentrations, has motivated the investigation whose results we now report.

As it has been generally found the attention of the researchers experimenting on doped nano-powder systems has to be directed to parameters which are sensitive to the particular situations of such systems. These parameters do not include ‘static’ features, e.g. energy levels, but ‘dynamical’ features, e.g. decay patterns and rise patterns of the luminescence emission. Of importance is also the possible broadening effect that the concentration may have on the spectral lines [22].

## 5.2 Experimental Part

### 5.2.1 Preparation of the samples

In this thesis, Nano-sized  $Y_2O_3$  samples doped with  $x = 0.2, 0.5, 1.0, 2.0, 5.0, 10.0$  mol %  $Nd^{3+}$  ions ( $Y_{2-x}Nd_xO_3$ ) were prepared by thermal decomposition of yttrium-neodymium alginate gels. Yttrium nitrate hexahydrate  $Y(NO_3)_3 \cdot 6H_2O$ , neodymium nitrate hydrate  $Nd(NO_3)_3 \cdot H_2O$  and low-viscosity (250 cps of 2% solution) alginic acid sodium salt used for the preparation of yttrium-neodymium alginate beads were of analytical grade and were purchased from Sigma-Aldrich Company. The details about the synthesis procedure are given in our earlier works [22, 23, 60]. Briefly, this method is based on the thermal decomposition of the yttrium-neodymium alginate gels. The obtained nano-powders were then annealed at 600, 800 and 1000 °C, for 24 hours with the heating rate of 10 °C/min to control the particle sizes.

### 5.2.2 Structural characterization

Analysis of the crystal structure of the Nd-doped samples was performed by X Ray Diffraction (XRD) method. XRD investigations were carried out with a Bruker AXS D8 Model (Cu-K $\alpha$  radiation –  $\lambda = 1.5418$  Å) diffractometer at 40 kV and 30 mA setting in the  $2\theta$  range from 20° to 70° with scanning steps of 0.02°. The average crystallite size  $L$  of the powders was estimated by using the Scherrer Equation [45];

$$L = \frac{K\lambda}{\beta \cos\theta} \quad (5.1)$$

where  $K$  is a constant varying with the method of taking the breadth ( $0.89 < K < 1$ , with  $K=0.89$  for spherical particles),  $\lambda$  is the wavelength of the incident X-ray beam,  $\beta$  is the width at half maximum of the XRD peak of a specific lattice plane ( $hkl$ ) in radians and  $\theta$  is the center angle of the considered Bragg reflection (XRD peak by the plane ( $hkl$ )).

As a further confirmation of the average particle size, electron microscope images of the samples were visualized by a JEOL 6335F model scanning electron microscope (SEM).

### 5.2.3 Spectroscopic measurements

Luminescence measurements were performed by pumping the samples with the output of a Laser Drive Inc. Model LDI-820 laser diode ( $\lambda = 808$  nm) that resulted in the excitation of the levels  $^2H_{9/2} - ^4S_{5/2}$ . The luminescence signal was directed toward the entrance slit of a 1 m McPherson Model 2051 monochromator and chopped at a frequency of 250 Hz before entering the slit. The monochromator provided a resolution 0.8 Å with the slits set at 50  $\mu\text{m}$  and a wavelength reproducibility of 0.1 Å. The entrance and output slits of the monochromator were set to 80  $\mu\text{m}$  for continuous emission spectrum measurements and to 600  $\mu\text{m}$  for response to pulsed excitation measurements.

The optical signal was detected by a Hamamatsu 7102 photomultiplier tube with an S1 response, sent to a EG&G Model 5210 lock-in amplifier and recorded in a computer.

The experimental data on the responses of the samples to pulsed excitation were obtained by using a Schwarz Electro-Optics Inc. Model Titan-P Model Titanium-Sapphire laser and a Tektronix Model TDS3052B oscilloscope.

For the experiments in the temperature range 30-300 K, the samples were mounted on the cold finger of a closed cycle Helium refrigerator. This system uses a Janis Research Model RD dewar connected with a Leybold Model RW2 compressor. The temperature was controlled by using the Lake Shore Cryotronics 805 Model controller.

## 5.3 Experimental Results

The X-ray diffraction patterns of the as-synthesized and thermally treated samples at 1000 °C are shown in Figure 5.1 as a function of the  $\text{Nd}^{3+}$  content. The diffraction peaks observed in the XRD-pattern can be indexed to cubic phase  $\text{Y}_2\text{O}_3$  (JCPDF: 25/1200); no other phase was detected. The observed diffraction peaks correspond to the Bragg diffraction from the (211), (222), (400), (411), (332), (431), (440), (532), (622) and (613) planes. Only the (hkl) values of the most prominent peaks are indicated in the XRD pattern with the strongest peak observed at  $2\theta \approx 29.5^\circ$  corresponding to the plane (222) for all the samples. The room temperature lattice parameter of the unit cell of the yttria cubic phase estimated by the XRD patterns

was 10.6051 Å which is in good agreement with the JCPDS database of pdf number 83–0927 [61]. The crystallite size of the samples, calculated by the Debye-Scherrer formula applied to the diffraction feature (222), resulted to be in the range 20 – 60 nm. The representative SEM images of the thermally treated at 1000 °C samples are shown in Figure 5.2 and confirm such an estimation.

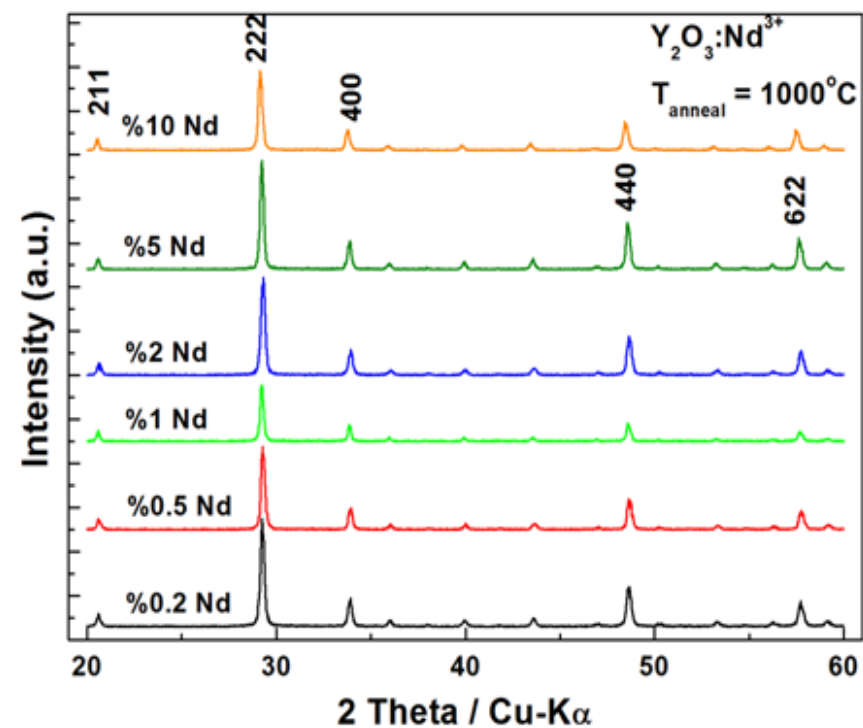
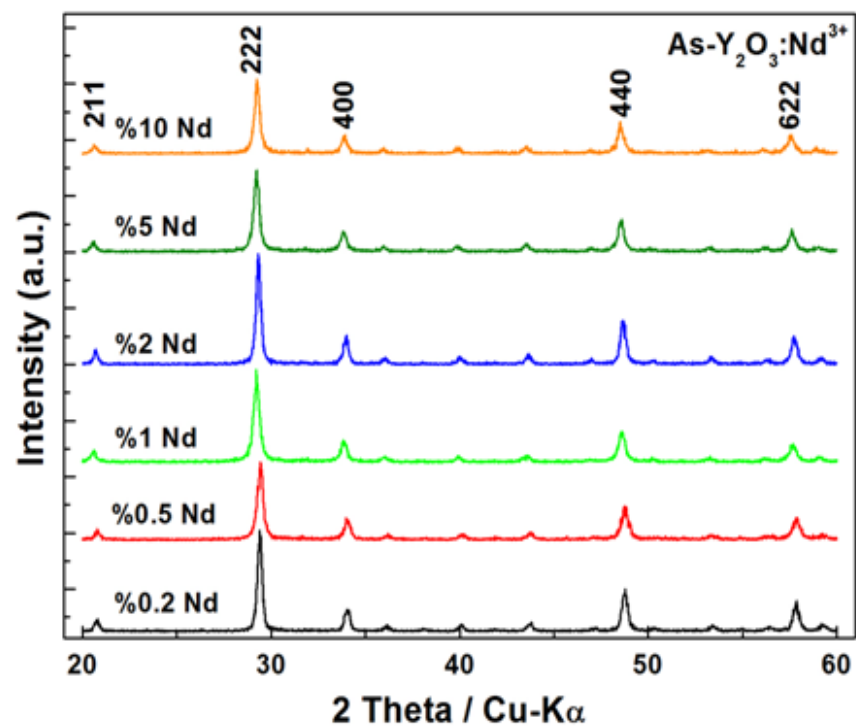


**Figure 5. 1** XRD patterns of the samples (a) as-synthesized, (b) annealed at  $1000^\circ\text{C}$ .

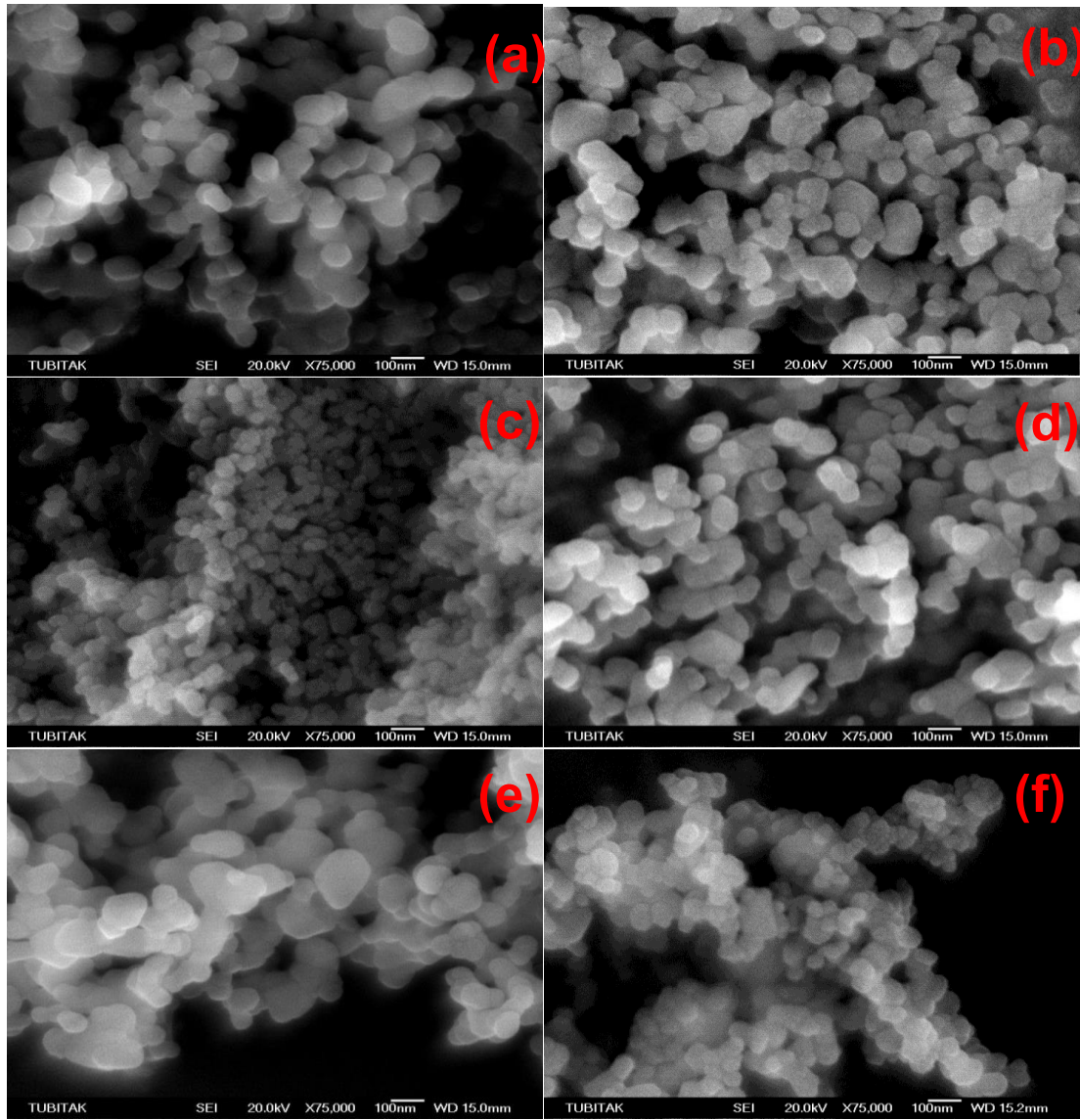


**Figure 5. 2:** SEM images of the (a) 0.2 %, (b) 0.5 %, (c) 1 %, (d) 2 %, (e) 5 %, (f) 10 %  $\text{Nd}^{3+}$  doped  $\text{Y}_2\text{O}_3$  annealed at 1000 °C.

The continuous emission spectra of the samples were collected in the 30 – 300 K temperature range and in the 850 – 1150 nm wavelength range and the continuous emission spectra of the samples with 20 nm particle size at 30K and 300 K are given in Figure 5.3. Two groups of emission lines associated with the  $^4\text{F}_{3/2} \rightarrow ^4\text{I}_{9/2}$  and the  $^4\text{F}_{3/2} \rightarrow ^4\text{I}_{13/2}$  radiative transitions of  $\text{Nd}^{3+}$  have been observed for all samples. We were able to see emission of  $\text{Nd}^{3+}$  even at 10 %  $\text{Nd}^{3+}$  doped  $\text{Y}_2\text{O}_3$ . The intensity of the sharp emission peaks was found to increase with  $\text{Nd}^{3+}$  concentration going from 0.2 to 0.5 % and then decrease at higher concentrations. As it can be also clearly seen from Figure 5.3 sharp emission peaks become wider with increasing  $\text{Nd}^{3+}$  concentration.

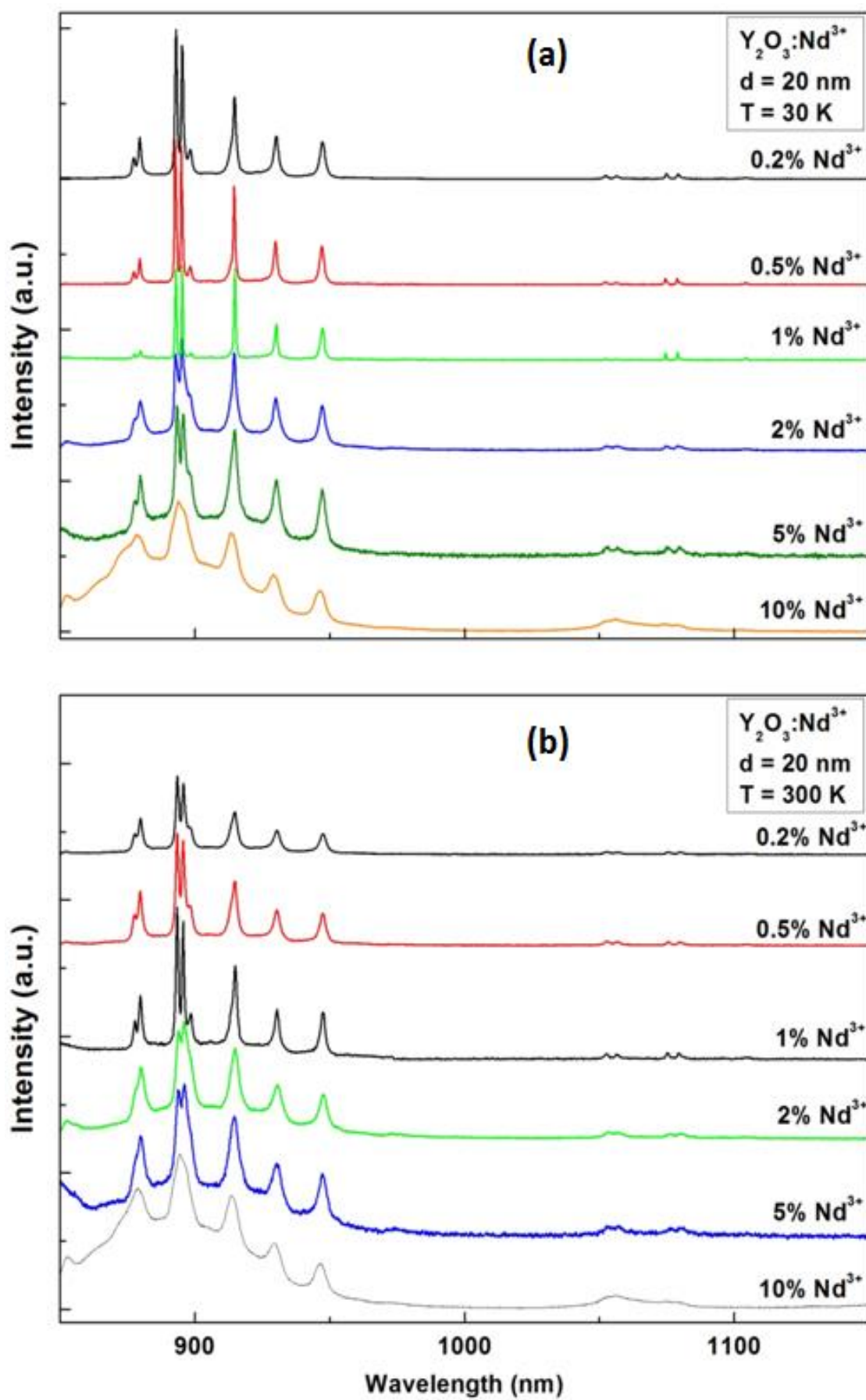


**Figure 5. 3:** Continuous emission spectra at (a) 30 K and (b) 300 K.

The representative continuous emission spectra given in Figure 5.4 show the shifting and broadening of the  $\text{Nd}^{3+}$  spectral lines of 0.2 %  $\text{Nd}^{3+}$  doped  $\text{Y}_2\text{O}_3$  as a function of temperature.

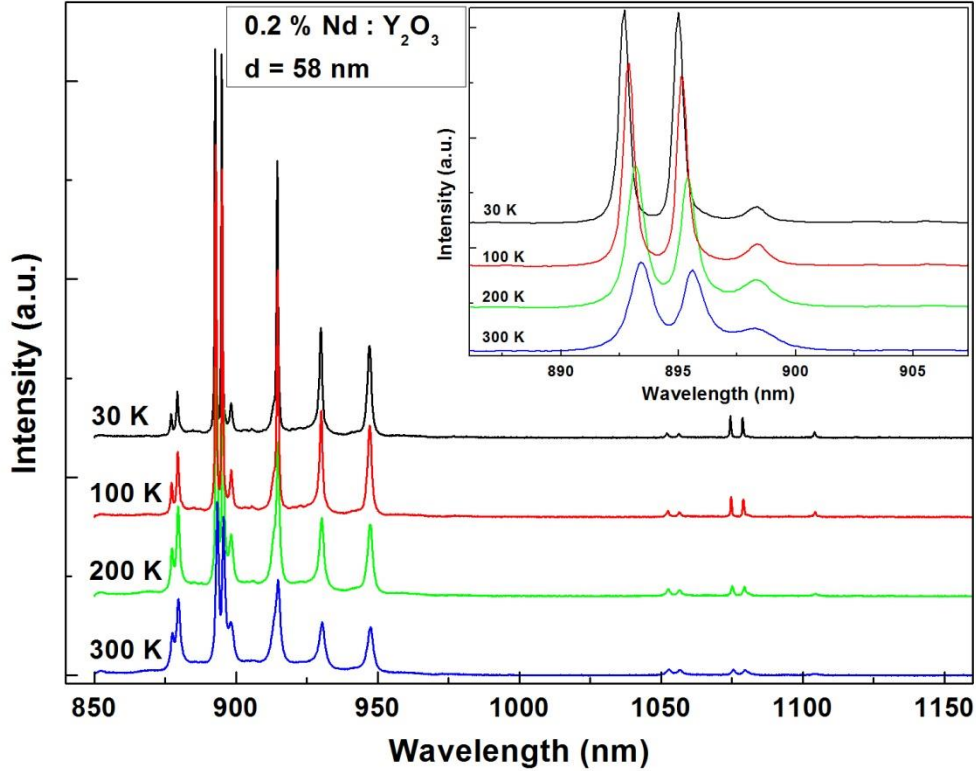


**Figure 5. 4:** Representative broadening and shifting of the sharp emission peaks of 0.2 %  $\text{Nd}^{3+}$  doped  $\text{Y}_2\text{O}_3$ .

We also investigated the effect of particle size on the luminescence spectral lines. We found that for concentrations other than 10 % the intensity of the emission increases with particle size. On the contrary when the concentration is 10 % the reverse trend takes place (see Figure 5.5). It was also observed at this concentration that the peaks become wider and the Stark level splitting was not visible.

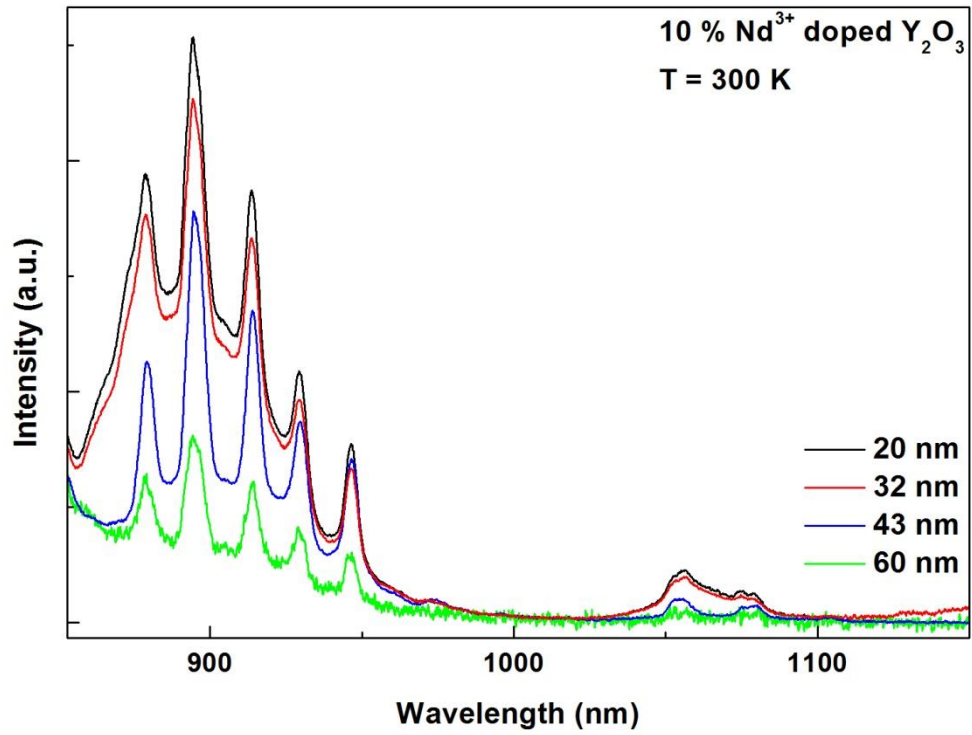


**Figure 5. 5:** Particle size dependence of the emission spectra of 10 %  $\text{Nd}^{3+}$  doped  $\text{Y}_2\text{O}_3$ .

The decay patterns of the samples were measured in the 30 – 300 K temperature range. In what follows we shall designate as “decay time” the area under a decaying curve with the initial value of the intensity set at 1. The obtained results are summarized below;

- i. All decay patterns are not exponential.
- ii. The longest decay time was observed for the 0.5 %  $\text{Nd}^{3+}$  samples. The decay times were found to increase with  $\text{Nd}^{3+}$  concentration going from 0.2 to 0.5 % and then decrease at higher concentrations (see Figures 5.6 and 5.7).

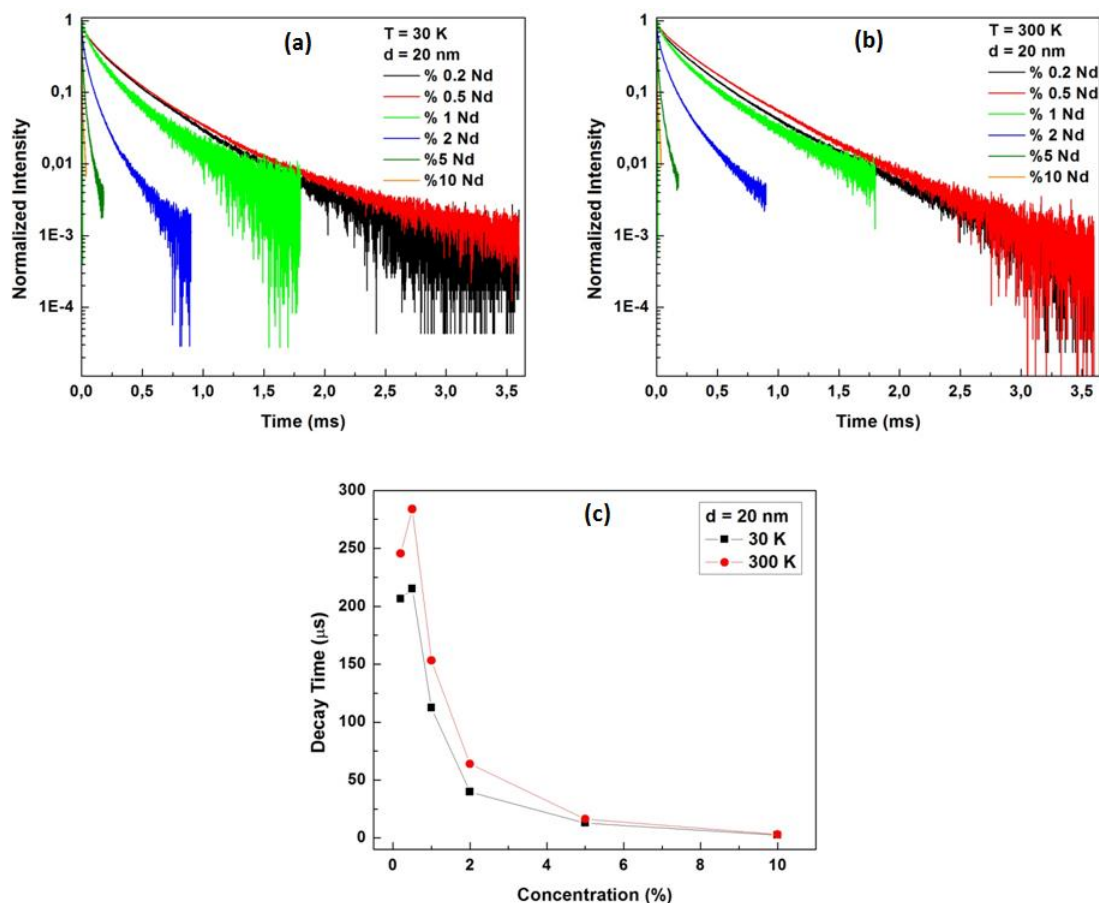


**Figure 5. 6:** Decay patterns of the samples with 20 nm particle size at (a) 30 K, (b) 300 K and (c) the variation of the decay times as function of concentration.

- iii. The decay patterns were found to deviate more from exponentiality with increasing  $\text{Nd}^{3+}$  concentration (see Figures 5.6 and 5.7).

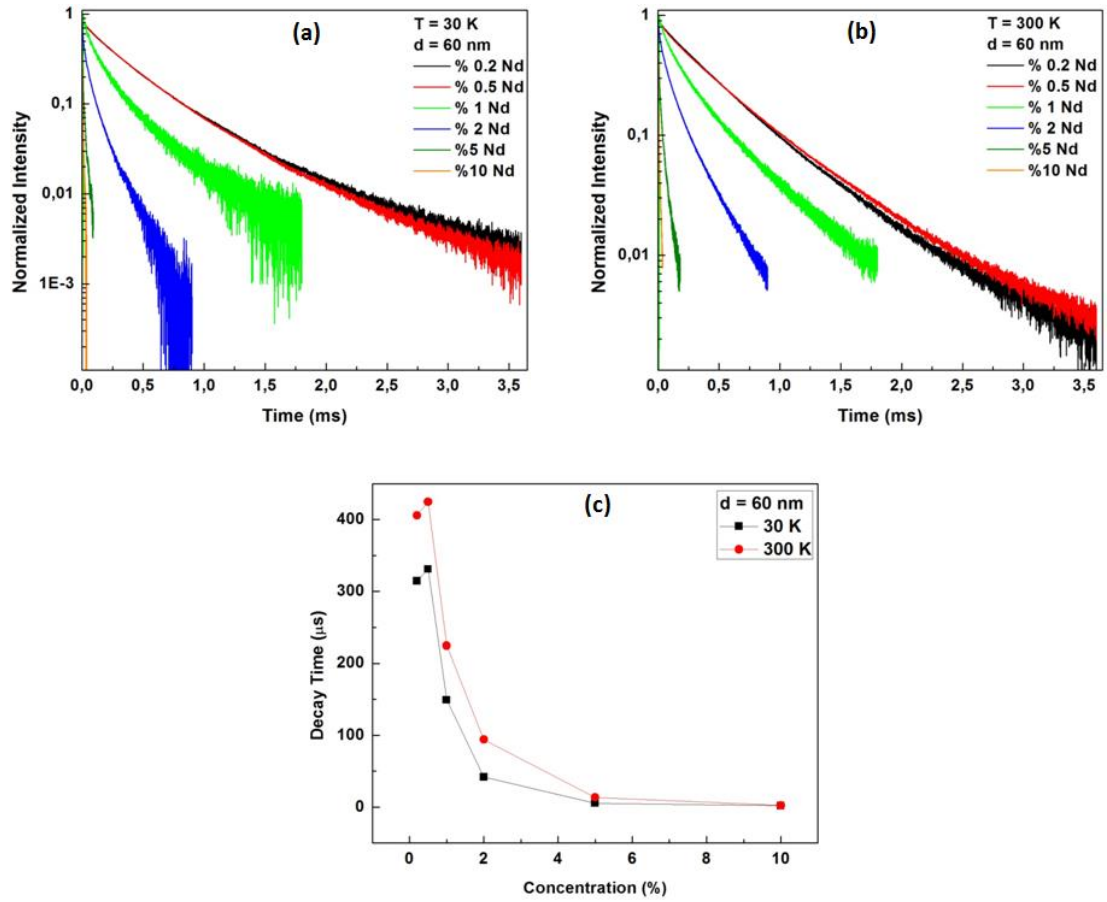


**Figure 5. 7;** Decay patterns of the samples with 60 nm particle size at (a) 30 K, (b) 300 K and (c) the variation of the decay times as function of concentration.

- iv. The decay patterns of all samples become slightly longer with increasing temperature (see Figure 5.8).
- v. The decay patterns deviates more from exponentiality at low temperatures (see Figure 5.8).

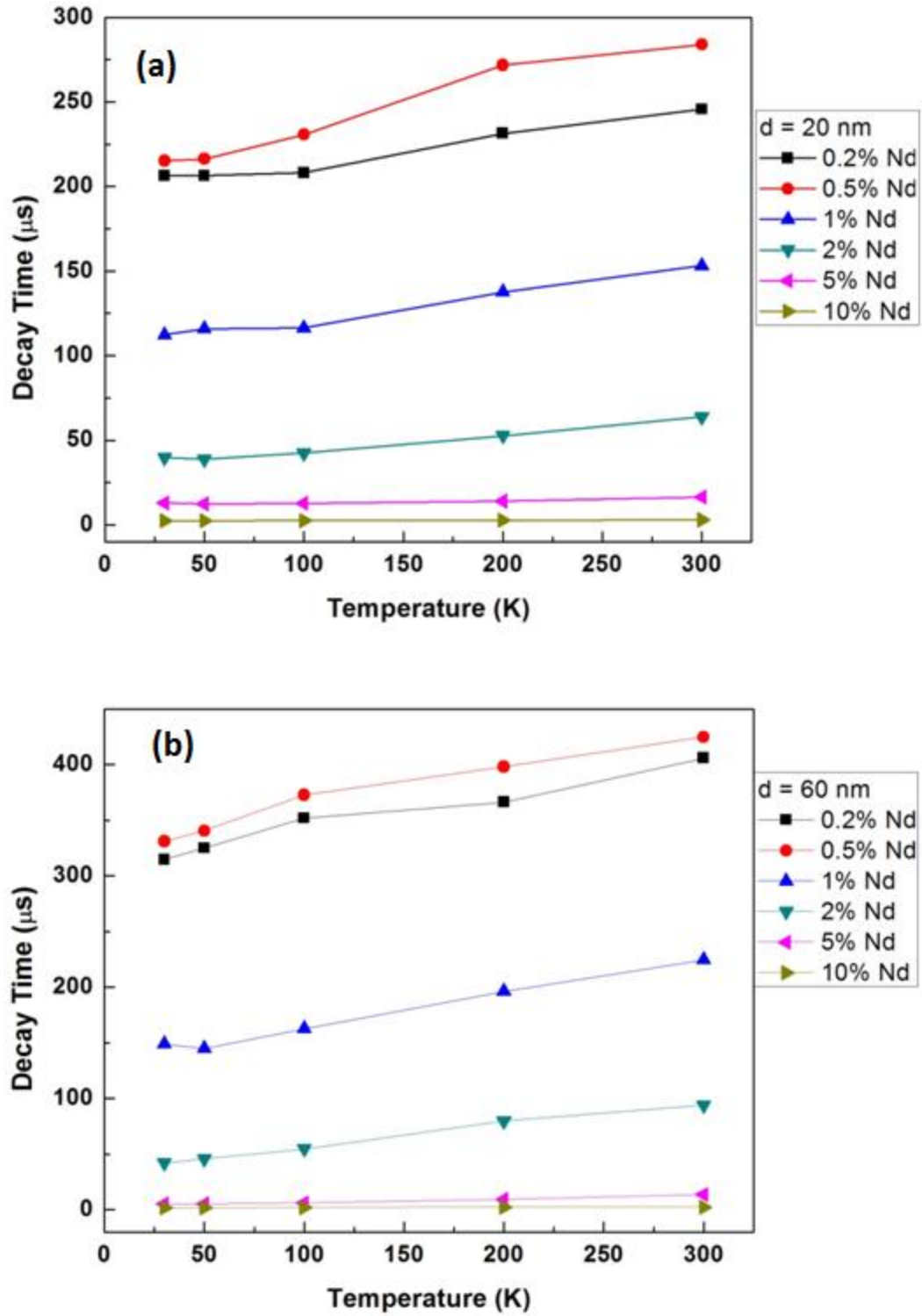


**Figure 5. 8:** Variation of the decay times of the samples with (a) 20 nm and (b) 60 nm particle sizes as a function of temperature.

- vi. The decay patterns deviate more from exponentiality with decreasing particle sizes (see Figure 5.9).

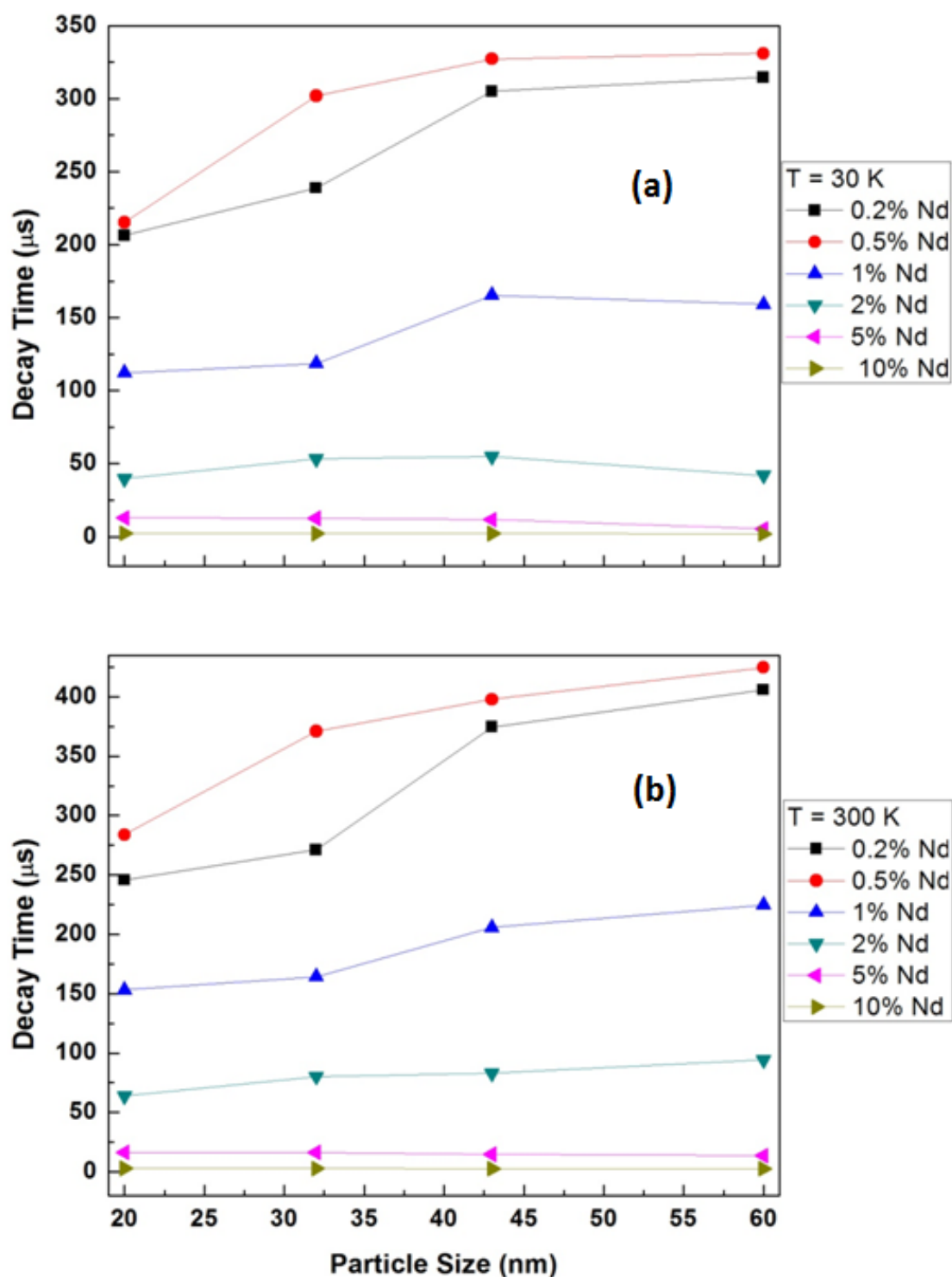


**Figure 5. 9:** Variation of the decay times as a function of particle size at **(a)** 30 K and **(b)** 300 K.

The decay times were found to increase with increasing particle sizes up to 2 % Nd<sup>3+</sup> doped Y<sub>2</sub>O<sub>3</sub>. No remarkable decay time difference was observed for different particle sizes of 5 % and 10 % Nd<sup>3+</sup> doped samples (see Figure 5.9).

## 5.4 Discussion of the Results

The general behavior of the emission output of luminescent systems as function of concentration of dopant is as follows:

- a) The dopant concentrations generally used in crystals is of very few percents. Within these limits an increase of the emission is generally noted with the increase of concentration. Beyond these limits the luminescence is quenched. At concentration of 10% generally no emission can be seen.
- b) When the system has only one emitting level (such in the case for  $\text{Nd}^{3+}$ ) the decay time of the luminescence presents the same trend regarding the dopant concentration as the intensity.

The most important finding regarding the emission in our samples is the presence of emission at high concentrations (10%) of the  $\text{Nd}^{3+}$  dopant. When doped with these concentrations no emission is presented by a crystal.

This finding is in accordance with the mechanism that quenches the emission in a luminescent system. At high concentrations it is easier to the excitation to move resonantly from ion to ion and eventually find a “killer” site. The limited size of the particles impedes the easy transfer of excitation energy and the eventual encounter with killer sites.

For both intensity and decay time we detect the same trend with increasing concentration: an initial increase in value followed by a decrease.

As for the decay time an interesting result is the increase of it with temperature that takes place at any concentration. A possible explanation of this effect is the following. The emission from  $\text{Nd}^{3+}$  ions actually comes out of the doublet  $^4\text{F}_{3/2}$ . The two levels are so close to that they are thermalized even at very low temperature. The lifetime of two thermalized levels is a combination of the lifetimes of the two levels, each weighed according to the population residing in each level. If the intrinsic lifetime of the upper level of the doublet is longer than the intrinsic lifetime of the lower level, then an increase of the lifetime with temperature may occur. This seems to be the case in the nano-powdered samples of  $\text{Y}_2\text{O}_3:\text{Nd}^{3+}$ . This occurrence, not seen in the crystal, is most probably due to the sensitivity of the dynamical parameter “decay time” to the particular environment provided by nano-powders.

Finally let's spend a few words on the lack of exponentiality of the decay patterns. The Nd ions at the surface are in a different environment with respect to the ions in the interior of the material. In a crystal the ions in the surface are a negligible minority with respect to the ions in the bulk of the material, but in a particle it is not so. In very small particles going from the surface toward the center of the particle there is a gradation in the Nd-O bond lengths, approaching the conditions of Nd<sup>3+</sup> in a single bulk crystal. It is possible that, even in the interior of the particle, the conditions of the environment in the bulk will never be reached. The observed decay patterns are a superposition of the decay curves of ions in different positions in each particle.

## **5.5 Conclusions**

The results obtained point to the additional information provided by the reduction of luminescent systems to nano-powder form, extending from high dopant concentrations at which luminescence is observed to the behavior of decay patterns deviating from exponentiality. They indicate the possibility of harvesting interesting new information by spectroscopically investigating laser type systems reduced to nano-particle form.



## **6. UNCONVENTIONAL PRODUCTION OF BRIGHT AND EFFICIENT WHITE LIGHT EMISSION BY ND - DOPED AND NOMINALLY UN-DOPED Y<sub>2</sub>O<sub>3</sub> NANO-POWDERS**

### **6.1 Introduction**

Nano-phosphors (nanoscale-sized solid, inorganic crystallites showing luminescence upon excitation) based on rare earth (RE) doped Y<sub>2</sub>O<sub>3</sub> are important optical materials, with Y<sub>2</sub>O<sub>3</sub> being the best host matrix for RE-dopants due to its chemical and thermal stability, similar ionic radius with respect to RE ions and cut off phonon energy of 380 cm<sup>-1</sup>. Among optical materials, lanthanide ions have attracted the interest of researchers for their ability to up-convert infrared light to the visible one. Particularly, neodymium (Nd) ion, besides being very efficient for solid-state laser applications, is a very good candidate for accomplishing such up-conversion process [62, 63].

Nano-phosphor based lighting is widely used but is suffering a drawback due to the fact that the luminescence spectra do not cover the whole visible light range (380-780 nm), namely a white light (WL) spectrum close to that of the sunshine. Therefore such artificial lighting sources are not optimal for indoor lighting or displaying [64] and the production of WL by engineered luminescence spectra remains an active research field.

Nano-powders doped multiply with lanthanide ions have been found to emit WL. When a near-infrared (NIR) diode laser was used to excite (with high power above a certain threshold) nano-crystalline insulating powders containing lanthanide ions, a very bright white or yellowish light was observed, corresponding to a strong broad emission band covering almost the whole visible region [65-70].

A number of researchers have found anti-Stokes wide band emission by exciting nano-crystals of compounds in which Nd was one of the dopants [71] or a full stoichiometric part of the system [69, 72, 73].

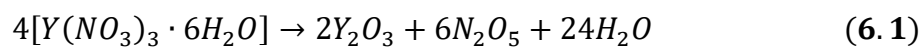
Strek et al. have reported the bright up-converted WL emission from  $\text{LiYbP}_4\text{O}_{12}$  [68],  $\text{NdAlO}_3$  [69] and  $\text{LiNdP}_4\text{O}_{12}$  [72, 73] nano-crystals under low pressure and infrared (IR) excitation. The production of WL spectrum have also been reported by J. Wang et al. by using just lanthanide oxides ( $\text{Yb}_2\text{O}_3$ ,  $\text{Sm}_2\text{O}_3$ ,  $\text{CeO}_2$ ) [66] and  $\text{Yb}_3\text{Al}_5\text{O}_{12}$ ,  $(\text{Yb},\text{Y})_2\text{O}_3$  crystals [67]. Sato et al. [74], Nolas et al. [75] and Zhou et al. [76] showed that the RE dopants reduce the thermal conductivity of the YAG, Skutterudites and Lanthanum Zirconate ceramics. Also Roura et al. [77, 78] observed broadband emission from SiC nano-particles and mechanically milled Si.

Notably, while the WL production reported in the literature was obtained by materials doubly doped with different RE ions or including RE ions as stoichiometric components, we have observed WL by singly Nd doped and nominally un-doped insulating oxide materials too. In this respect, this paper reports our detailed experimental studies on the broadband “white light” (such nomenclature is supported by the evaluated Commission Internationale de l’Eclairage (CIE) coordinates) emitted following the IR laser-light excitation of Nd-doped  $\text{Y}_2\text{O}_3$  ( $\text{Y}_2\text{O}_3:\text{Nd}$ ) nano-crystals with different Nd concentrations ranging from zero to 20%. Surprisingly, we observed WL even in the nominal absence of Nd dopant in the samples. Moreover no WL was found to be emitted by  $\text{Nd}^{3+}$ -doped  $\text{Y}_2\text{O}_3$  bulk crystals.

## 6.2 Experimental

### 6.2.1 Preparation of the $\text{Y}_2\text{O}_3:\text{Nd}^{3+}$ nano-powders

Samples of nano-sized  $\text{Y}_2\text{O}_3$  particles doped with trivalent Nd concentration of 2, 5, 10 and 20 % were prepared by thermal decomposition of yttrium-neodymium alginate. Details on the preparation method were described elsewhere [22, 23, 60]. Briefly, this method is based on the thermal decomposition of alginate gels. In this process yttrium nitrate hexahydrate  $\text{Y}(\text{NO}_3)_3 \cdot 6\text{H}_2\text{O}$  (99.8%), neodymium nitrate hexahydrate  $\text{Nd}(\text{NO}_3)_3 \cdot 6\text{H}_2\text{O}$  (99.9%) and low viscosity (250 cps of 2% solution) alginic acid sodium salts with analytical grade are used as starting reagents. The reaction that occurs in thermal decomposition process is given in the equation below



The nano-particles were synthesized at 500°C and then annealed at 600, 800, 1000 and 1400 °C. The effect of such annealing treatment was to increase the particle size from 20 to 248 nm.

Here-after the Nd-doped Y<sub>2</sub>O<sub>3</sub> samples will be referred to as Y<sub>2</sub>O<sub>3</sub>:Nd(%) where % stands for the corresponding Nd doping percentage.

Commercially available Y<sub>2</sub>O<sub>3</sub> nano-samples with particle sizes of 20 to 40 nm and with the purity of 99.999% purchased from US Research Nanomaterials, Inc. were also used to obtain WL emission.

### 6.2.2 Structural characterization of the Y<sub>2</sub>O<sub>3</sub>:Nd<sup>3+</sup> samples

Analysis of the crystal structure of the Nd-doped samples was performed by X Ray Diffraction (XRD) patterns. XRD investigations were carried out with a Bruker AXS D8 Model (Cu-K $\alpha$  radiation) diffractometer at 40 kV and 30 mA setting in the  $2\theta$  range from 20° to 70° with scanning steps of 0.02°. The average crystallite size  $L$  of the powders was estimated by using the Scherrer Equation [45];

$$L = \frac{K\lambda}{\beta \cos\theta} \quad (6.2)$$

where  $K$  is a constant varying with the method of taking the breadth ( $0.89 < K < 1$ , with  $K=0.89$  for spherical particles),  $\lambda$  is the wavelength of the incident X-ray beam,  $\beta$  is the width at half maximum of the XRD peak of a specific lattice plane ( $hkl$ ) in radians and  $\theta$  is the center angle of the considered Bragg reflection (XRD peak by the plane ( $hkl$ )).

As a further confirmation of the average particle size, SEM images of the samples were obtained by a JEOL 6335F model scanning electron microscope.

### 6.2.3 Emission characterization

The continuous emission WL spectra were produced by pumping the samples with the output of a Laser Drive Inc. Model LDI-820 laser diode operating at 803.5 nm with the maximum output power of 3 W or of a similar diode operating at 975 nm with the maximum output of 10 W. The signal was directed toward the entrance slit of a 1 m McPherson Model 2051 monochromator and chopped at a frequency of 250 Hz before entering the slit. The monochromator provided a resolution 0.8 Å with the slits set at 50  $\mu$ m and a wavelength reproducibility of 0.1 Å. The optical signal was

detected by Hamamatsu R1387 photomultiplier tube with an S20 response, sent to a EG&G Model 5210 lock-in amplifier and recorded in a computer.

Two spectral regions were investigated:

1. A region from 850 to 1500 nm where the emission from the  $^4F_{3/2}$  level of Nd occurs, and
2. An optical region from 400 to 900 nm where the WL emission occurs.

To perform experiments in the temperature range 30-300 K, the samples were mounted on the cold finger of a closed cycle Helium refrigerator. This system uses a Janis Research Model RD dewar connected with a Leybold Model RW2 compressor. The temperature of the cold finger was controlled by using a Lake Shore Cryotronics 331 Model temperature controller.

The rise pattern and the decay pattern of the WL were measured by using a shutter that allowed the light to reach its full intensity and then cut sharply the pumping power, operating with a repetition cycle of 10 sec.

The use of the diode operating at 975 nm allowed us to investigate the effect of excitation wavelength on the WL output of the samples.

An Avantes AvaLight-Hal-Cal calibration light source was used to correct our spectra for the sensitivity of our system.

We had also at our disposal an Allied Scientific Pro ASP-MK350 model illuminance meter that allowed us to measure the CIE (International Commission on Illumination) coordinates, the CCT(Correlated Color Temperature), the CRI(Color Rendering Index), illuminance, and to view the spectrum of the WL. We also measured the above parameters of a 60 W commercial incandescent bulb for comparison.

### 6.3 Experimental Results

The X-ray diffraction patterns of the as-synthesized  $Y_2O_3:Nd$  samples are shown in Figure 6.1 as function of the Nd content. The diffraction peaks observed in the XRD-pattern can be indexed to cubic phase  $Y_2O_3$  (JCPDF: 25/1200); no other phase was detected. The observed diffraction peaks correspond to the Bragg diffraction from the (211), (222), (400), (411), (332), (431), (440), (532), (622) and (613) planes.

Only the (hkl) values of the most prominent peaks are indicated in the XRD pattern with the strongest peak observed at  $2\theta = \sim 29.5^\circ$  corresponding to the plane (222) for all the samples. The room temperature lattice parameter of the unit cell of the yttria cubic phase estimated by the XRD patterns was 10.6051 Å which was in good agreement with the JCPDS database of pdf number 83-0927. Notably, as the Nd concentration increases from 2 % to 10 %, the prominent diffraction peaks become sharper and more intense thus suggesting a refinement of the sample crystallinity and/or increased nano-powder sizes. One would expect that an increase of the Nd<sup>3+</sup> ion concentration would lead to peaks with slightly broader width and reduced intensity, but the observed results agree with report according to which a Nd<sup>3+</sup> dopant may act as an heterogeneous nucleation and crystallization site [79] and improve the sample crystallinity. On the other hand, doping-induced microstrain and local distortion of the host lattice structure due to the difference in the ionic radii between the Y host cation (0.9 Å) and Nd dopant (0.980 Å) are expected effects because of the relevant doping level of our samples. The crystallite size of the as synthesized phosphors, calculated by the Debye-Scherrer formula applied to the diffraction feature (222), resulted to be in the range 25 – 30 nm. The SEM image of the sample with Nd concentration of 2% shown in Figure 6.2 confirms such estimation.

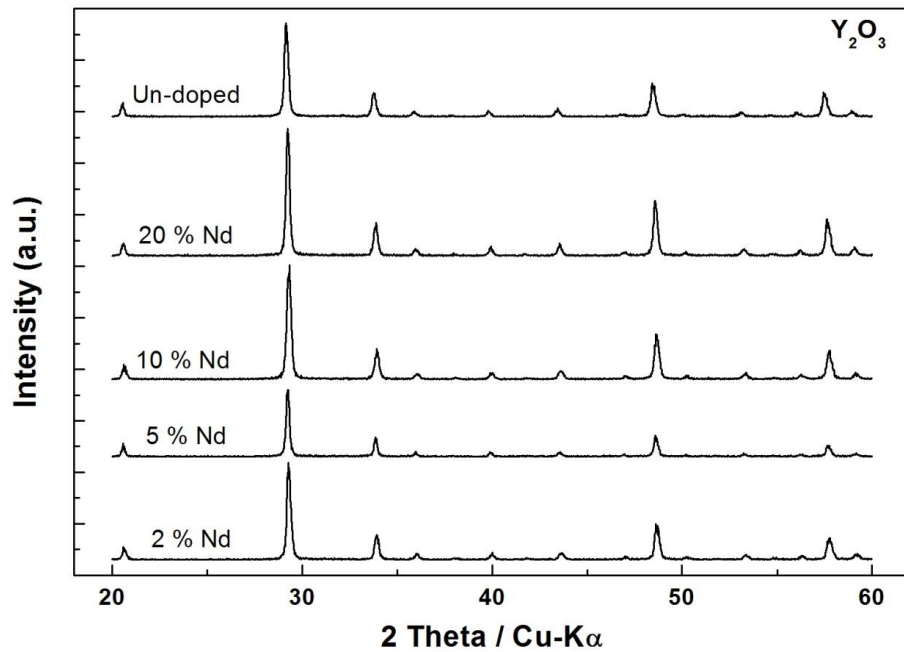


**Figure 6. 1:** XRD patterns of the samples.

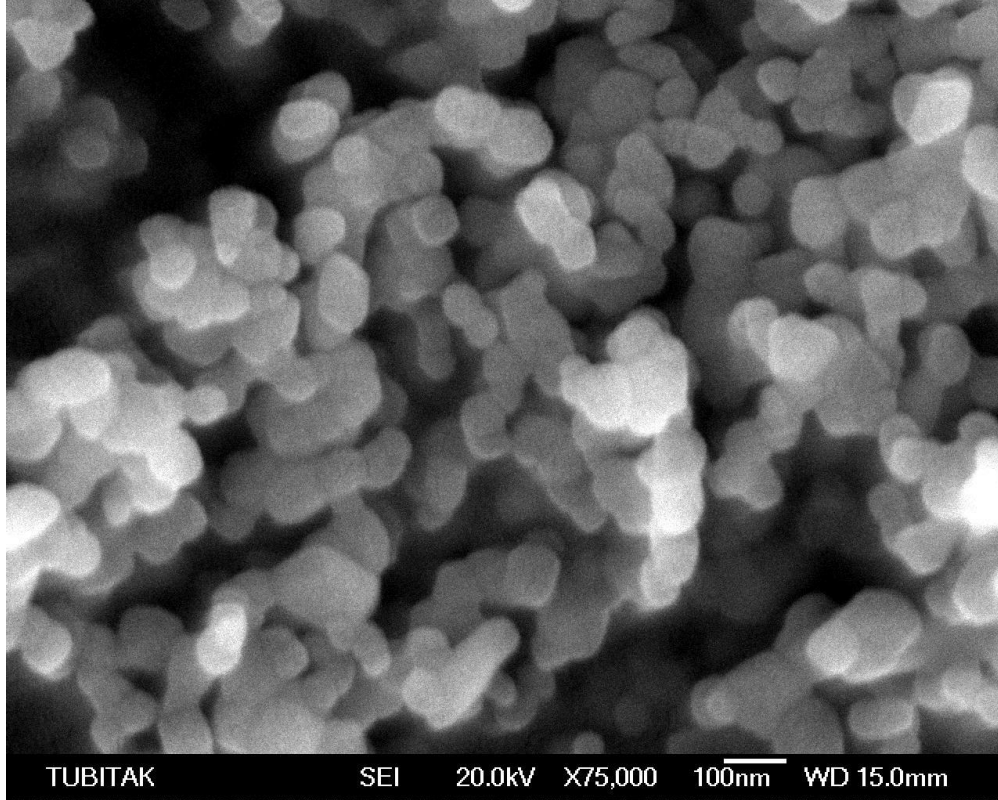


**Figure 6. 2:** Representative SEM image of the  $\text{Y}_2\text{O}_3\text{:Nd}(2\%)$ .

### 6.3.1 Results of 803.5 nm excitation

Turning to the emission properties of the  $\text{Y}_2\text{O}_3\text{:Nd}$  samples excited by the 803.5 nm wavelength, the IR spectrum consists of three groups of spectral lines due to the  $^4\text{F}_{3/2} \rightarrow ^4\text{I}_{9/2}$ ,  $^4\text{I}_{11/2}$  and  $^4\text{I}_{13/2}$  transitions. The general aspect of the spectra was found to be similar for Nd content ranging up to 10 %. Notably for Nd concentration of 10% it is not possible to see any Nd-related IR emission in bulk crystals; this is an indication that the concentration at which the luminescence quenches is higher in the nano-powders than the one in the crystal [80].

Since the IR emission of the  $\text{Y}_2\text{O}_3\text{:Nd}^{3+}$  systems was already investigated in our previous papers [22, 23], it will not be considered further. Instead, in the present paper our attention will be focused on the WL band accompanying the IR emission of our samples as a function of the Nd dopant content.

In this regard, Figures 6.3 (a) and (b) show the WL spectrum collected in the 400-900 nm wavelength range of the samples  $\text{Y}_2\text{O}_3\text{:Nd}(20\%)$  and  $\text{Y}_2\text{O}_3\text{:Nd}(0\%)$ , corresponding to the highest (20%) and lowest (0%) Nd content, respectively, under excitation at 803.5 nm with pumping power of 2 W and various environment

temperatures. Some of our preliminary results on WL emitted by infrared excited un-doped metal oxide nano-powders have been reported elsewhere [81, 82]. The WL spectra under examination were emitted by samples with nano-particle size of 26 nm. The spectrum of the doped sample consists of a wide band with three dips associated with the absorption of the Nd ion (the 803.5 nm wavelength matches with the strong absorption of the Nd ions in this region). The three dips due to the absorption of Nd can clearly be seen in the measured spectrum (Figure 6.3 (a)), the corrected spectrum (Figure 6.3 (a)) and the spectrum measured by using the illuminance meter (Figure 6.4 (a)). There is also a good agreement between Figures 6.3 (d) and 6.4 (b), corresponding to the spectrum corrected and measured by using the illuminance meter, respectively, of the un-doped sample.

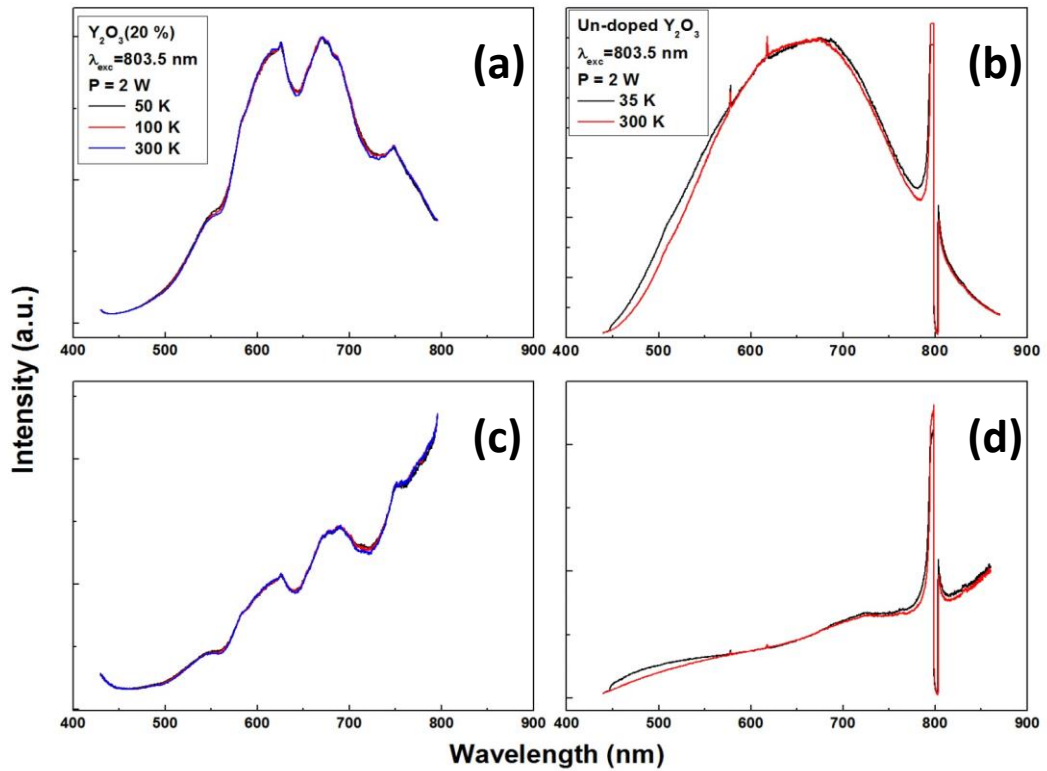


**Figure 6. 3:** Environment temperature dependence and the general aspect of the white light spectrum under 803.5 nm excitation (a) uncorrected spectrum of 20% Nd doped sample (b) uncorrected spectrum of un-doped sample (c) corrected spectrum of 20% Nd doped sample for system response (d) corrected spectrum of un-doped sample for system response.

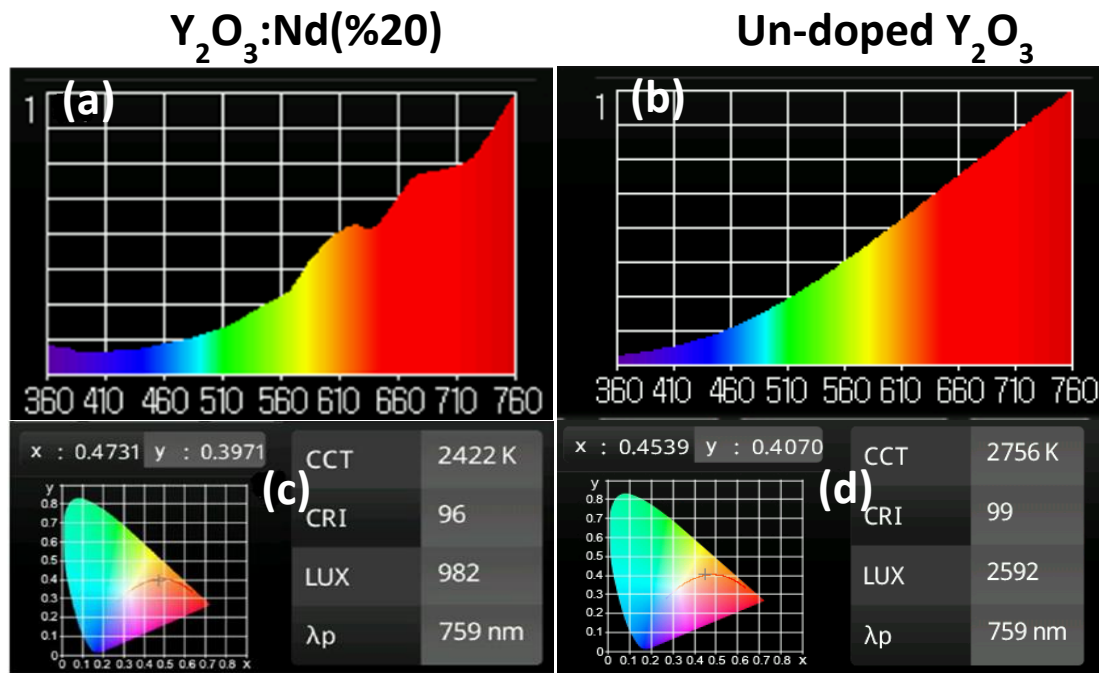


**Figure 6. 4:** (a) Measured spectrum of 20% Nd doped sample by using illuminance meter (b) measured spectrum of un-doped sample by using illuminance meter (c) the CIE coordinates and the measured CCT, CRI values for 20% Nd doped sample (d) the CIE coordinates and the measured CCT, CRI values for un-doped sample.

The parameters CCT, CRI, illuminance and Commission Internationale de l'Eclairage (CIE) coordinates of the WL emitted by both doped and un-doped samples under examination are shown in the corresponding figures (Figures 6.4 (a) and (b)) and summarized in Table 6.1.

**Table 6. 1 :** Summary of results when using 803.5 nm excitation.

Sample	CIE	CCT	CRI	Efficiency
$Y_2O_3:Nd(20\%)$	$x = 0.47$ $y = 0.39$	2422 K	96	327 lum/W
Un-doped $Y_2O_3$	$x = 0.45$ $y = 0.40$	2756 K	99	864 lum/W
Incandescent Lamp (60 W)	$x = 0.46$ $y = 0.41$	2666 K	99	636 lum /W

It was observed that both CCT and CRI:

- i) decrease turning from the un-doped to the doped sample ;
- ii) depend on the pumping power: while the CCT value goes up, CRI was found to go down with decreasing pumping power:
- iii) depend on the environmental pressure around the sample: while the CCT value goes up, CRI was found to go down with increasing environmental pressure.

In regard to point i), the reduction of CCT and CRI upon increasing Nd content could be ascribed to the strong absorption of the Nd ions clearly observable from Figure 6.3.

One important CIE Standard Illuminant is the color point A, located in the CIE color space by the coordinates (0.448, 0.408) and called warm white point with CCT of 2856 K. This point marks the chromaticity of tungsten incandescent lamps, namely the artificial light sources most comfortable for human eye. Accounting for the lighting standards, we also compared the performance of our samples with the one of a 60 Watt incandescent lamp (Figure 6.5 and Table 6.1). Notably, the CIE coordinates, CCT and CRI values of our obtained WL emission are very close to those of a commercial incandescent bulb source: CRI approaching the theoretical limit (100) and CCT closer to the warm white point were measured for the un-doped sample. Moreover, as a power excitation of 3 W was used for the 803.5 nm pumping diode, the efficiency of the WL emitted by our samples seems to be better than the one of the incandescent lamp source (Table 6.1).

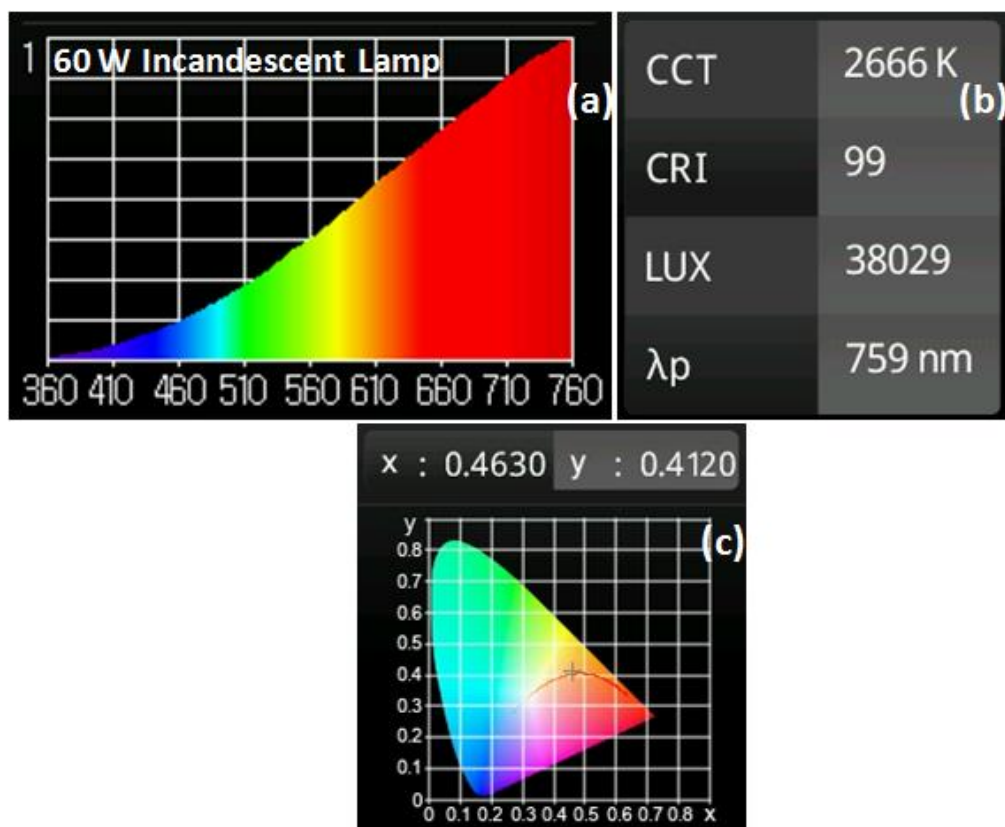


**Figure 6. 5:** (a) Measured spectrum, (b) CCT, CRI and illuminance values, and (c) CIE coordinates of a commercial 60W incandescent bulb obtained by using illuminance meter.

WL emission from commercially available 99.999% pure  $\text{Y}_2\text{O}_3$  nano-powder was also obtained under both of 803.5 nm and 975 nm laser diode excitation. The general aspects of the WL emission from commercial  $\text{Y}_2\text{O}_3$  were found to be the same as the ones observed for our synthesized samples.

The investigation of the WL dependence on the nature and pressure of the background gas revealed that while it was easy to obtain WL under low pressure, it was possible to obtain WL at atmospheric pressure by increasing the pumping power. In this respect, as Figure 6.6 shows for the un-doped sample with nano-particle size of 26 nm, the WL intensity falls down rapidly upon increasing the background pressure. Figure 6.6 is representative, since the same behavior is shown by Nd-doped samples. The threshold value of the pumping power to obtain WL under 0.02 mbar pressure was found to decrease with increasing dopant concentration: 0.7 Watts and 0.12 Watts for nominally un-doped and heavily doped materials, respectively. We were also able to detect WL at atmospheric pressure and in such a case the threshold power value was 0.73 Watts and 1.1 Watts for the 20 % Nd doped and the nominally

un-doped sample, respectively. Such findings indicate that the presence of the Nd ions makes easier to induce WL.

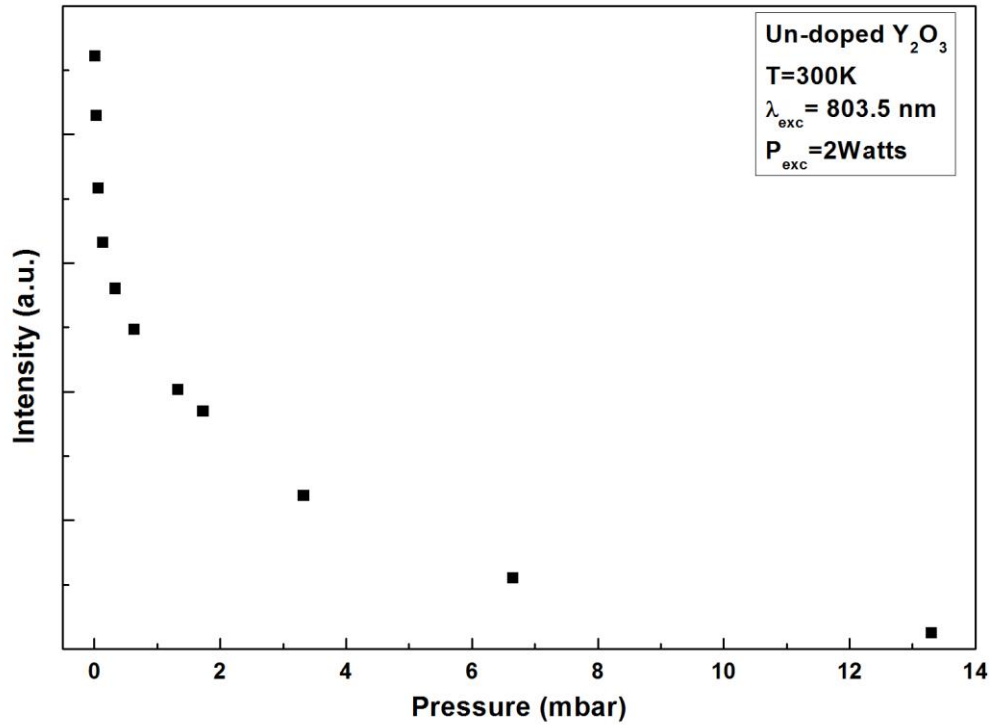


**Figure 6. 6:** Pressure dependence of the white light intensity in nominally un-doped  $Y_2O_3$ .

Tests dealing with the nature of the background gas were also performed. After filling the evacuated sample chamber with nitrogen ( $N_2$ ), quenching of the WL was observed. Similar results were observed by using helium (He), another inert gas. All of the performed checks indicate that the WL is sensitive to the pressure of the gas present in the sample chamber, as long as this gas is inert.

The changes in the WL intensity with pumping power in an un-doped sample with 26 nm powder size (shown in Figure 6.7) demonstrate that WL intensity 'I' varies with the pumping power 'P' according to the law  $I=P^n$ , n being an exponent depending on either the exciting wavelength or the laser diode pumping power (LD Power). As the fit results in Figure 6.7 indicate, the exponent  $n$  is found as 3.08 and 4.63 by linear fitting for two different linear region of the experimental data.

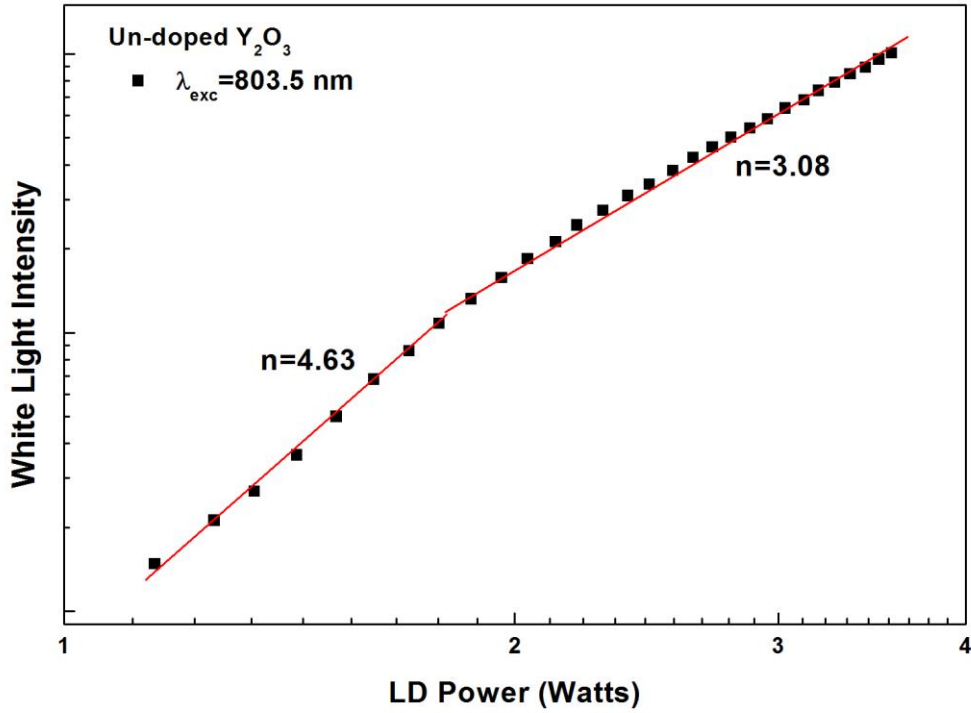


**Figure 6. 7:** White light intensity variation with pumping power in nominally un-doped  $\text{Y}_2\text{O}_3$ .

In order to further characterize the WL we measured its rise pattern and decay pattern, counting on such parameters being more sensitive to the conditions of measurements and to the composition of the samples. We summarize as follows our experimental findings for what concerns the WL emitted by the un-doped sample:

- i) The decay patterns of the un-doped  $\text{Y}_2\text{O}_3$  were found to be sensitive to the temperature of the sample holder, as shown in Figure 6.8.

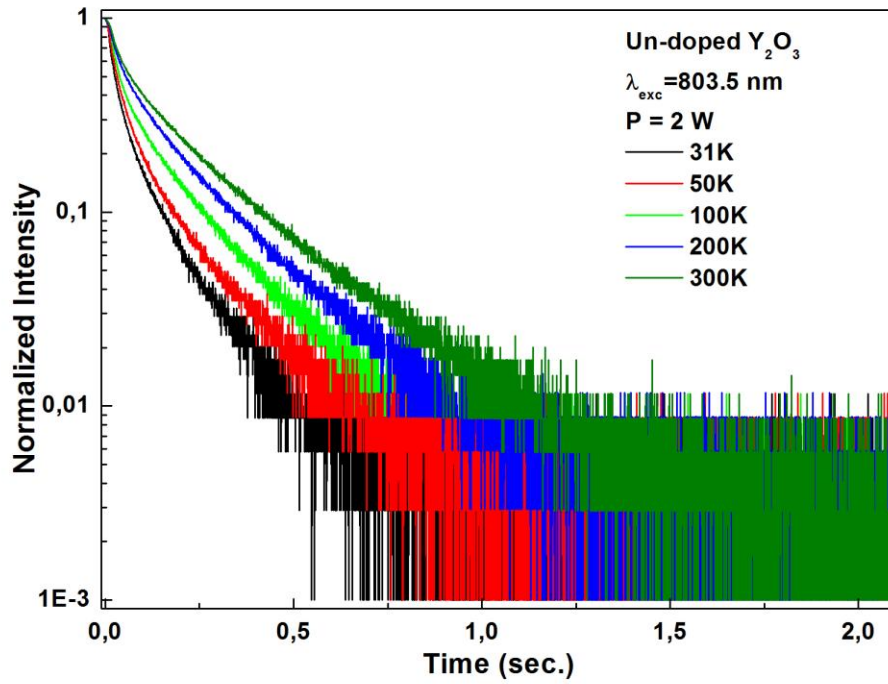


**Figure 6. 8:** Dependence of decay patterns on environment temperature in nominally un-doped  $\text{Y}_2\text{O}_3$ .

- ii) The decay patterns were found to be very sensitive to the environment pressure showing faster falling down with increasing pressure (Figure 6.9).

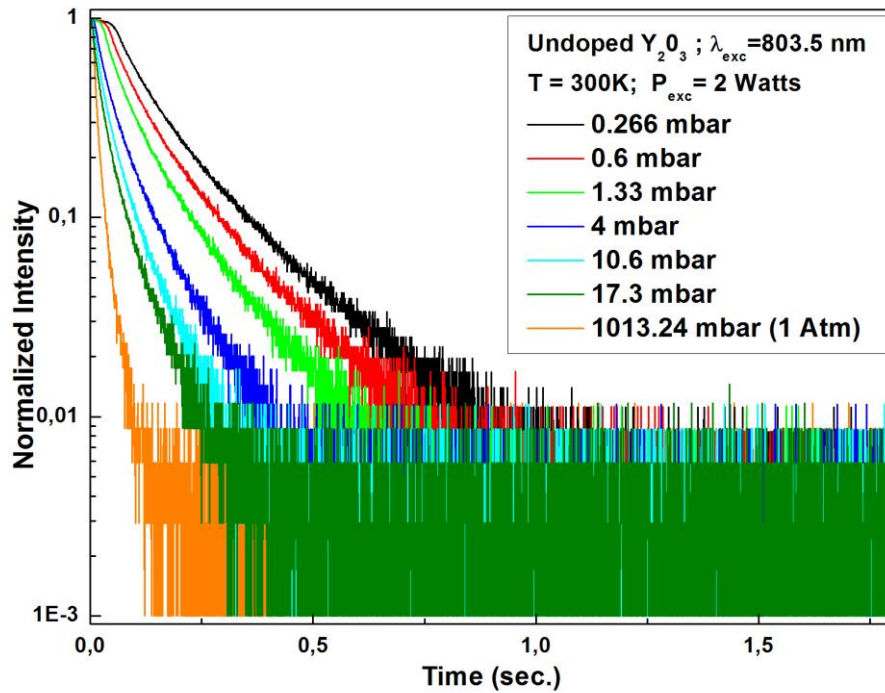


**Figure 6. 9:** Variation of decay patterns with environment pressure in nominally un-doped  $\text{Y}_2\text{O}_3$ .

iii) The decay patterns and rise patterns vs. the pumping powers shown in Figs 6.10 and 6.11, respectively indicate that, while no significant pumping power-dependence of the WL decay patterns occurs, the rising patterns are very sensitive to the pumping power, becoming shorter with increasing pumping power.

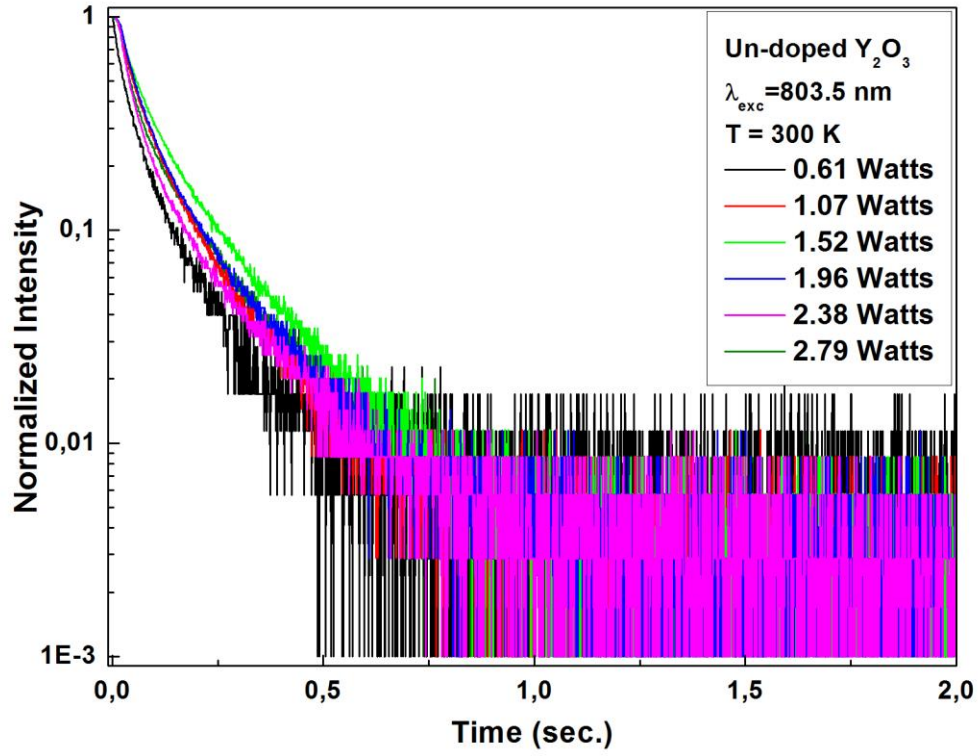


**Figure 6. 10:** Dependence of decay patterns on pumping power in nominally un-doped  $\text{Y}_2\text{O}_3$ .

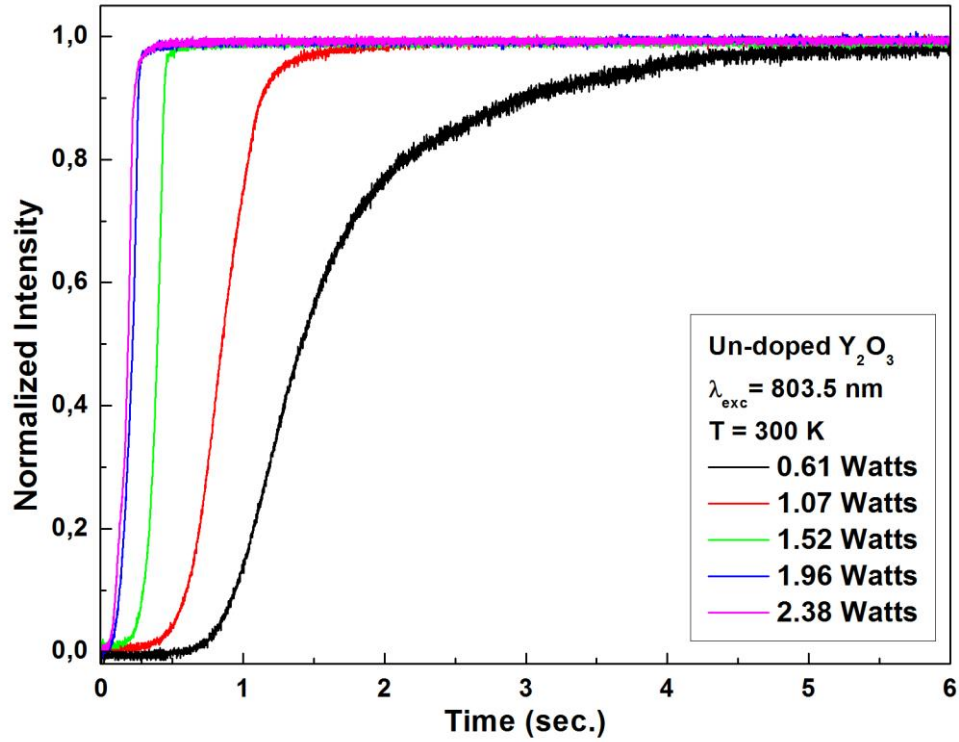


**Figure 6. 11:** Rise pattern dependence on pumping power in nominally un-doped  $Y_2O_3$ .

Considering now the results on the  $Y_2O_3:Nd(20\%)$  sample, Figure 6.12 reports that the WL spectrum changes in intensity and in detail by changing the diode pumping power: the dips due to absorption by the Nd ions progressively disappear with increasing pumping power and the emission intensity is enhanced by increasing the pumping power. Such experimental findings suggest mechanisms of filling/saturation of the dopant energy levels.

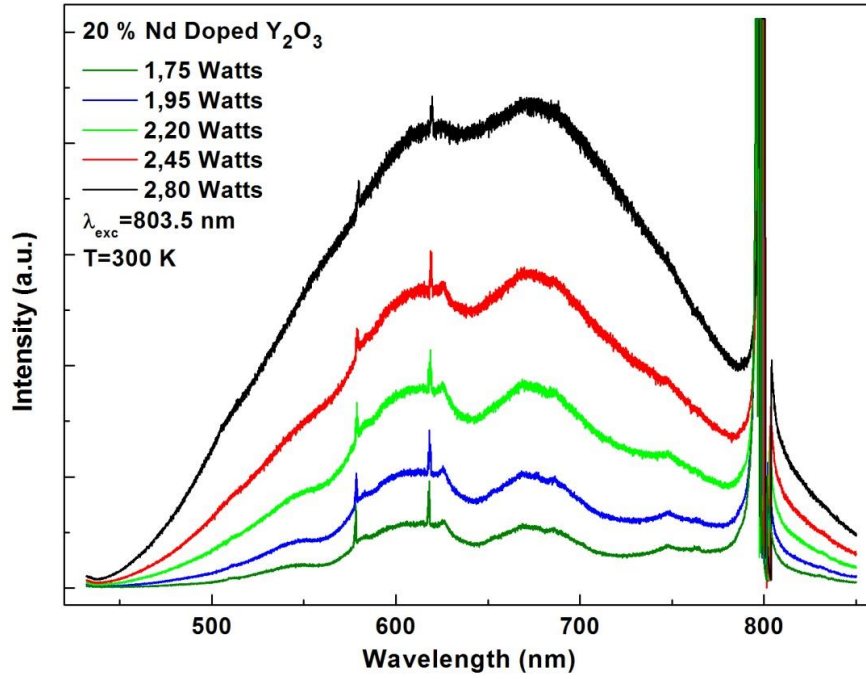


**Figure 6. 12:** Pumping power dependence of the white light spectrum in 20 % Nd doped  $\text{Y}_2\text{O}_3$  with size of 26 nm.

In addition to the result in Figure 6.12, our measurements showed the following:

- i) The decay patterns did not vary sensibly with Nd concentration (Figure 6.13), thus suggesting that the WL decay is mainly an host-dependent effect.

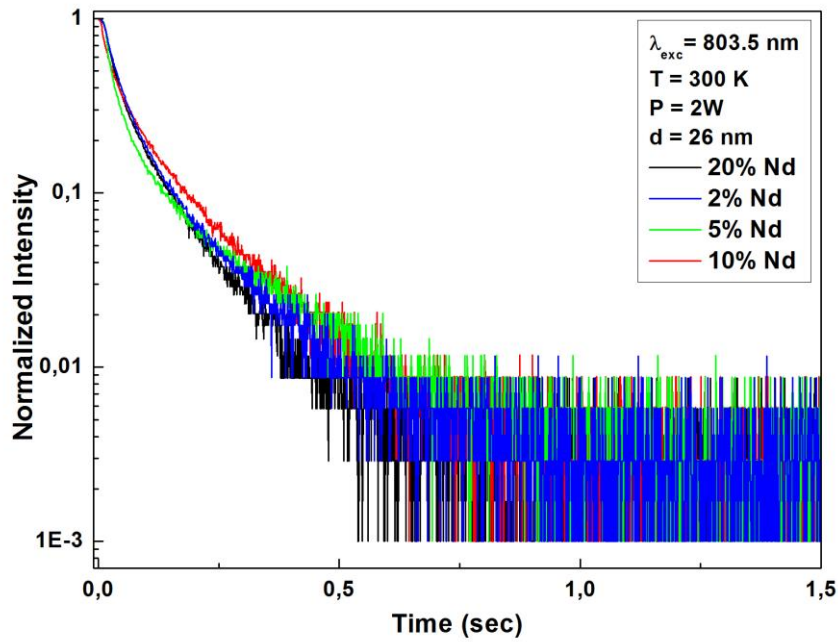


**Figure 6. 13:** White light decay patterns variation with the Nd concentration.

- ii) The onset of the WL strongly depends on Nd concentration with a delay before the rise of the WL to its maximum value longer with decreasing Nd content (Figure 6.14).

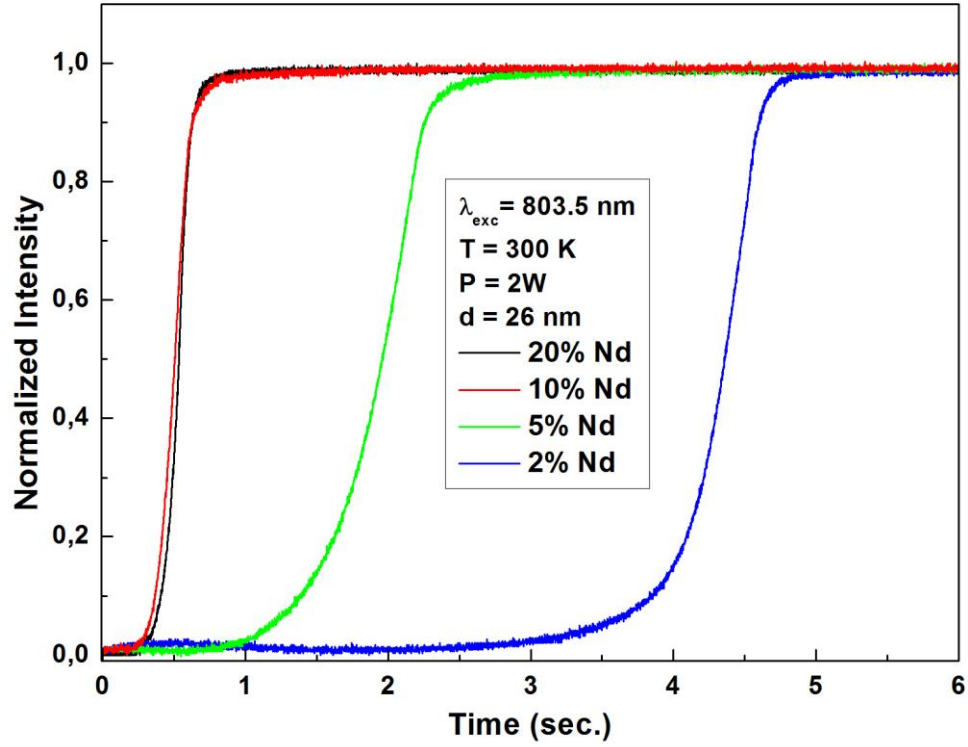


**Figure 6. 14:** Rise pattern dependence on Nd concentration.

- iii) The decay patterns associated with the  $\text{Y}_2\text{O}_3\text{:Nd}(10\%)$  sample plotted vs. particle size show that while no difference is observable in the 20 to 50 nm size range, the pattern corresponding to 250 nm decays more slowly (Figure 6.15).

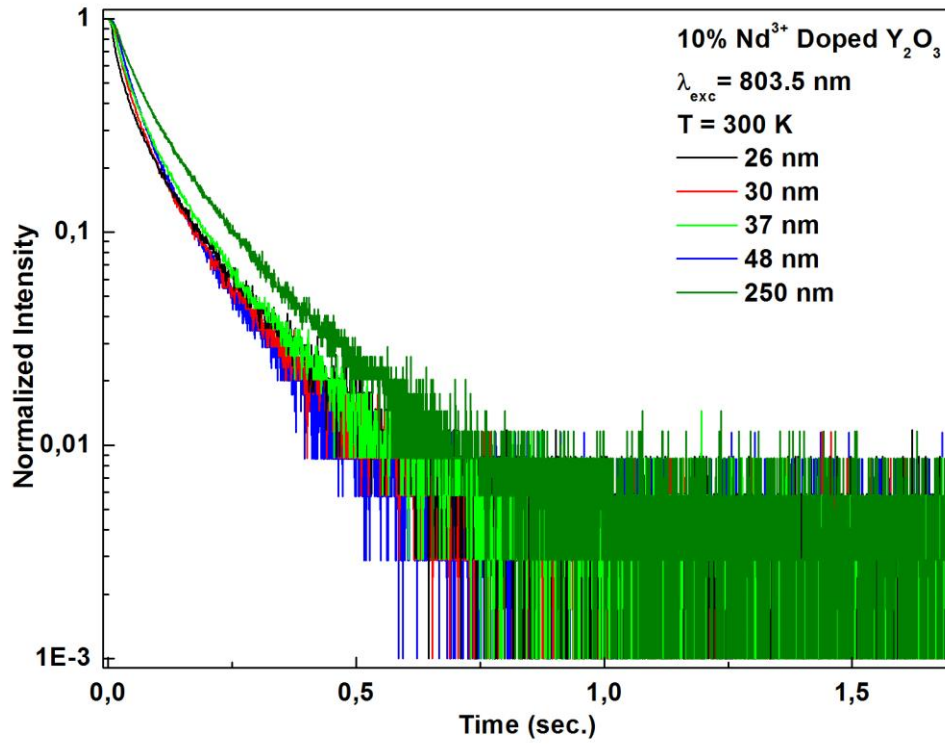


**Figure 6. 15:** Dependence of decay patterns on powder size in 10 % Nd Y<sub>2</sub>O<sub>3</sub>.

The rise pattern behavior of the Y<sub>2</sub>O<sub>3</sub>:Nd(10%) sample depends on the particle size, namely it decreases and becomes steeper with decreasing particles size (Figure 6.16).

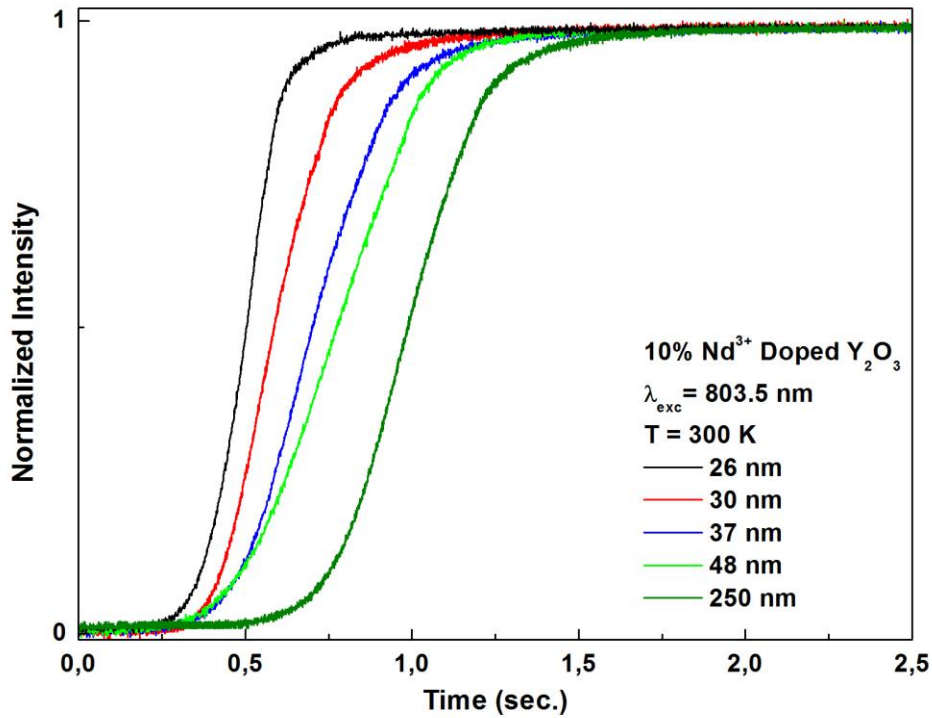


**Figure 6. 16:** Rise pattern dependence on powder size 10 % Nd Y<sub>2</sub>O<sub>3</sub>.

### 6.3.2 Results of 975 nm excitation

Turning to the laser diode operating at 975 nm, once again WL was observed when exciting the samples with such a source. The acquired spectrum was corrected for the sensitivity of the apparatus and also measured by using the illuminance meter for both doped and un-doped samples. We also measured the spectrum of the un-doped sample after the excitation at various times with time interval between successive measurements of 10 minutes.

The following was inferred by our experiments:

- i) the general aspect of the broadband WL spectrum was similar to the one obtained by using the 803.5 nm exciting source (Figure 6.17) with a red-shift of the peak position up to 50 nm;

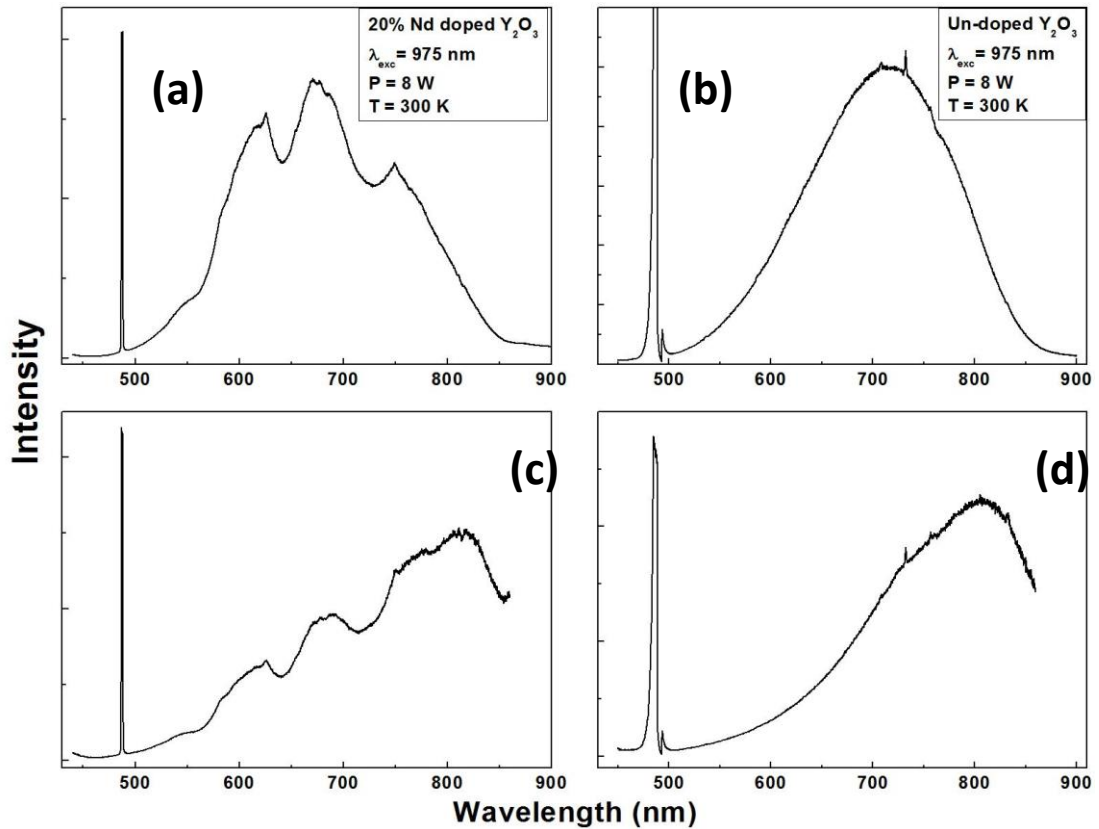


**Figure 6. 17:** General aspect of the white light spectrum under 975 nm excitation (a) uncorrected spectrum of 20% Nd doped sample (b) uncorrected spectrum of un-doped sample (c) corrected spectrum of 20% Nd doped sample for system response (d) corrected spectrum of un-doped sample for system response.

- ii) the threshold pumping power value was 6 Watts at 0.02 mbar;
- iii) a pressure value as low as 0.02 mbar was sufficient to obtain WL and no WL was detectable under atmospheric conditions;

- iv) the corrected spectra and those measured by the illuminance meter (Figure 6.18) look similar and are in good agreement both for doped and un-doped samples;

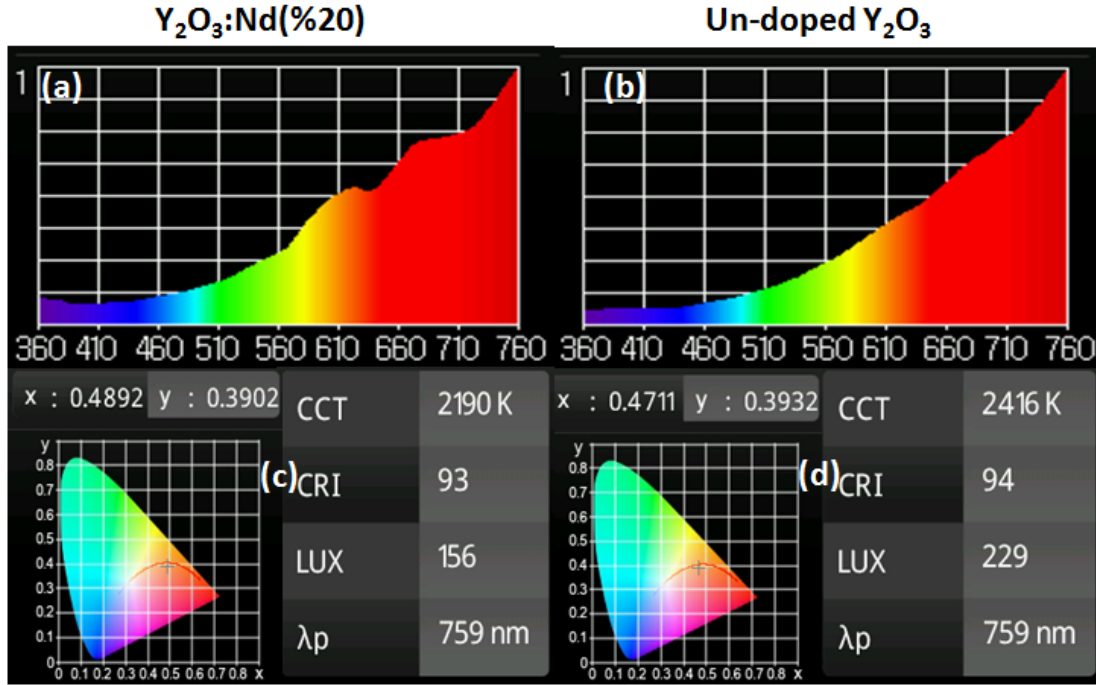


**Figure 6. 18:** (a) Measured spectrum of 20% Nd doped sample by using illuminance meter (b) measured spectrum of un-doped sample by using illuminance meter (c) the CIE coordinates and the measured CCT, CRI values for 20% Nd doped sample (d) the CIE coordinates and the measured CCT, CRI values for un-doped sample.

- v) while measuring the emission of the un-doped samples in 10 minutes steps, a blue-shift of the emission peak was observed (Figure 6.19) and, moreover, the intensity was found to increase 8 times with time and the spectrum became stable after 5 successive measurements. The amount of the shift was 15 nm which corresponds to temperature change of 77 K according to Wien Displacement Law;

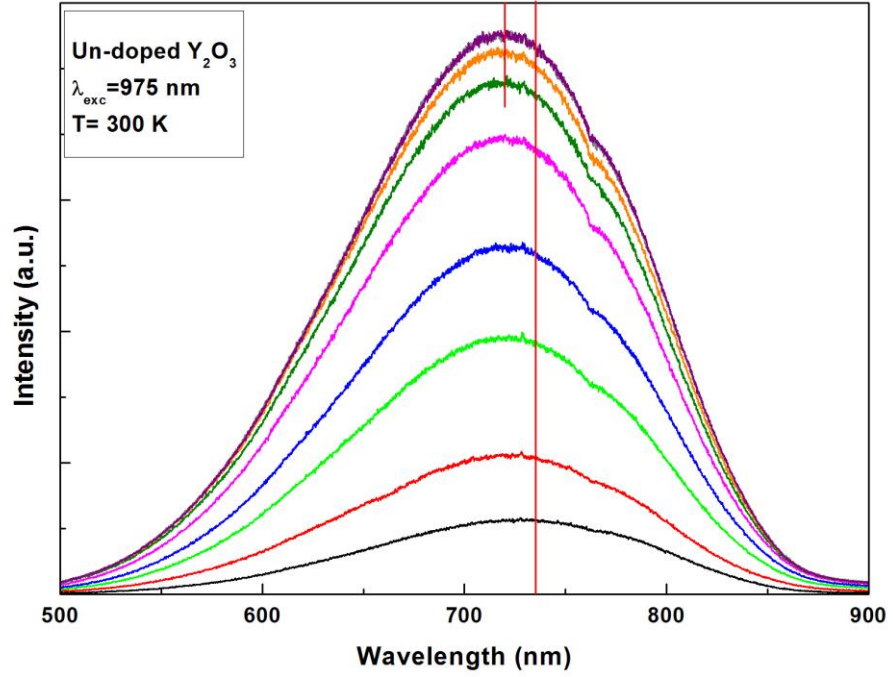


**Figure 6. 19:** The change of the WL spectrum under 975 nm excitation with time.

- vi) in regard to the observed pumping power-dependence of the WL spectrum, with increasing pumping power an intensity change and a blue-shift of 19 nm of the WL spectrum were detected (Figure 6.20);

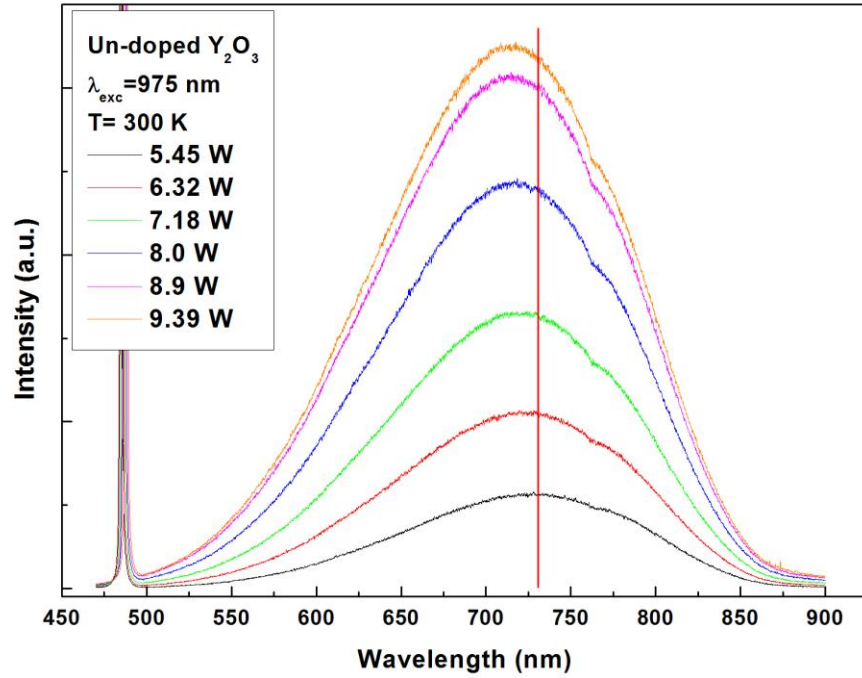


**Figure 6. 20:** The change of the WL spectrum with changing pumping power of 975 nm laser diode.

- vii) the intensity variation with pumping power under 975 nm excitation, shown in Figure 6.21, indicated a strong dependence of the WL emission on this power;

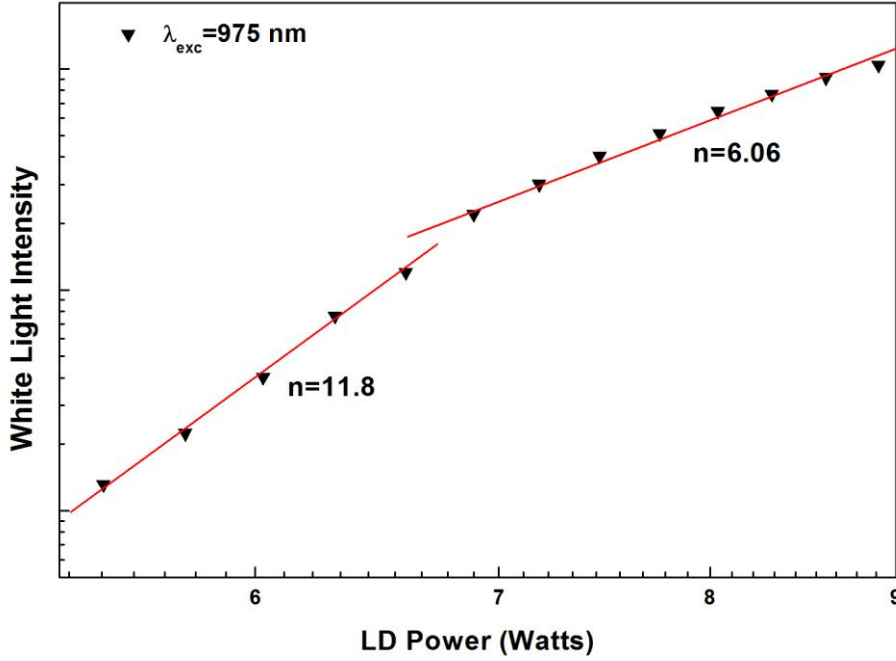


**Figure 6. 21:** Power dependence of the WL intensity under 975 nm excitation.

- viii) all the decay patterns were found to be non exponential, as observed in all previously examined cases;

Turning to the sample characterization according to the lighting standards parameters, CIE coordinates, CCT, CRI and illuminance of the WL emitted from doped and un-doped samples under 975 nm excitation were measured. The results are given in Figs. 18a and 18b and summarized in Table 6.2.

**Table 6. 2 :** Summary of results when using 975 nm excitation.

Sample	CIE	CCT	CRI	Efficiency
Y <sub>2</sub> O <sub>3</sub> :Nd(20%)	x = 0.49 y = 0.39	2190 K	93	19.5 lum/W
Un-doped Y <sub>2</sub> O <sub>3</sub>	x = 0.47 y = 0.39	2416 K	94	28.6 lum/W

Notably, as already observed under 803.5 nm excitation source, both of CCT and CRI values were found to decrease with the presence of the dopant. However, the same samples exhibited a better WL performance under the 803.5 nm than under the 975 nm excitation. Moreover, a dependence on either the pumping power or environment pressure was observed for both CCT and CRI in the case under examination (975 nm excitation). In detail, while CCT goes up, the CRI value was found to go down with decreasing (increasing) pumping power (environment pressure).

As a further result, WL emission from commercially available 99.999% pure  $\text{Y}_2\text{O}_3$  nano-powders was also obtained under both of 803.5 nm and 975 nm laser diode excitation. The general aspects of the WL emission from commercial  $\text{Y}_2\text{O}_3$  were found to be the same as the ones observed for our synthesized samples.

#### **6.4 Discussion of the Results**

The amount of experimental results of our experiments demands careful consideration of their general aspects. The following basic observations can be made:

1. Since no WL emission was observed by bulk samples of Nd-doped  $\text{Y}_2\text{O}_3$  exposed to the same exciting infrared light as the nano-particle samples, definitely the observed production of WL can be considered as typical of the nanoscale regime.
2. The spectral distribution of the WL is to a large extent independent on the Nd concentration and even the presence of the Nd dopant. While Nd occurrence favors the WL generation but is not necessary to induce such process, the presence of Nd makes it easier to obtain WL emission under low pumping power and higher environment pressure conditions.
3. The temperature of the sample's holder does not influence the spectral shape and seemingly the intensity of the WL emission.
4. The pressure in the sample environment has a great influence on the intensity of the WL. It acts in the opposite sense with respect to the intensity of the exciting infrared light: low pressure favors the emission of WL, and a strong excitation does likewise. The latter occurrence is expected: more exciting light results in greater absorption and consequently in a stronger emission. The former effect, the influence of pressure, needs a more elaborate

explanation. As nano-crystalline  $\text{Y}_2\text{O}_3$  is very hygroscopic, adsorption of water on the nano-particle surface is very likely [83, 84] and this could contribute to the absorption of the pumping wavelengths. But adsorbed water molecules easily evaporate with decreasing environment pressure, even at room temperature, and due to the excitation-induced warming up effect. Hence, surface adsorption of  $\text{H}_2\text{O}$  could contribute to the absorption of the infrared radiation at high atmospheric pressure, because  $\text{H}_2\text{O}$  has a relatively broad absorption band peaking at 760 nm and at 800 nm its absorption coefficient is  $0.02 \text{ cm}^{-1}$  [83]. The pressure dependence of the WL intensity indicates the occurrence of de-excitation mechanisms. As the nature of the gas-nano-particle interaction is not chemical when inert gases are considered, at given pressure conditions, the fact that the WL intensity is lower in the presence of light inert gases indicates the effective role of the collision density. Therefore, the pressure dependence of the WL intensity can be accounted for adsorption of polar species on the nano-particle surface as well as scattering effects gas-nano-particle causing de-excitation and/or heating dissipation. In this regard an alternative or concurrent pressure-dependent de-excitation mechanism can be invoked based on the thermal conductivity of the nano-powders. This parameter is enhanced by the ambient pressure and reduced when this pressure is lowered. At low pressures the crystallites are more isolated from each other and from the cold finger and can reach higher temperatures favoring the emission of WL.

5. The characterization of the spectral properties and of the processes taking place in the nano-systems must include the investigation of such dynamical characteristics as the patterns related to the rise of the WL intensity following the sudden excitation by the infrared radiation and the decay pattern that follow the sudden interruption of such a radiation. In this regard we may say that, as expected, the dynamical parameters are remarkably sensitive to the variation of such experimental conditions as temperature of the samples (see Figure 6.8), pressure of the samples' environment (see Figure 6.9) or dimension of the powder crystallites (see Figure 6.16). One expected outcome of the measurements of the decay patterns of the WL is their independence of how much energy was stored in the system (see Figure 6.10).

6. The most noticeable aspect of the decay patterns is their deviation from exponentiality. Such behavior could be inferred by the role played by the powders' surfaces, role that becomes more important as the radius of the particle is reduced. Going from the surface to the center of a particle one would encounter a variety of conditions, with each condition determining a different decay patterns. The observed pattern is the superposition of the various different patterns. Accordingly the deviation from an experimental pattern is in general more pronounced in smaller particles.
7. The spectral distribution of the detected WL resembles very closely the one of an incandescent lamp, which is still unmatched with respect to its color quality, meaning inherent resembling the sun light which is the most comfortable for human perception. We have demonstrated the possibility to obtain WL with very high efficiency and CRI approaching the theoretical limit with an alternative approach. Our experimental results make our WL emission very interesting at both fundamental and applicative levels and open the way to an alternative route with respect to incandescent lamps.

The following considerations deal with occurrences that manifest themselves in different ways depending on the wavelength of the exciting infrared light.

1. The WL spectrum produced by the 975 nm excitation is not significantly different from that produced from the 803.5 nm excitation. The dependence of the WL intensity on the fourth power of the exciting 803.5 nm diode power suggests the multi-photon aspect of the absorption process. In fact, an interpretation of the exponent  $n$  occurring in the law  $I=AP^n$  is just in terms of number of photons in multi-photon absorption events. The same can be inferred in the case of the other exciting wavelength (975 nm). However, being a 975 nm photon less energetic than an 803.5 nm photon, more photons are required to induce multi-photon absorption in the un-doped system. This is indeed the case: the WL intensity was found to be proportional to a higher exponent  $n$  of the power of the exciting 975 nm source (Figure 6.21).
2. Of particular interest is Fig 6.12 which shows the WL spectrum of 20% Nd-doped  $Y_2O_3$  nano-powder sample, with dips corresponding to Nd absorption. The dips become shallower as the excitation power increases, showing that as

this power increases the absorption process seems to receive dominant contribution from the host material rather than from Nd-based processes.

3. The decay patterns following the 975 nm excitation are not significantly different than those following the 803.5 nm excitation, as one would expect. The different experimental conditions may produce different amount of excitation, but this should have no effect on the unfolding of the spontaneous decay.
4. The wavelength of excitation has a greater influence on the rise patterns than on the decay patterns. A most notable effect is produced by the 975 nm excitation on the rise patterns, by which the WL intensity reaches its maximum value. Figure 6.19 is illustrative in this regard. In it we can see that it took about one hour for the WL intensity to reach its maximum intensity. Figure 6.20 represents a similar behavior obtained by exciting the sample with increasing power of the 975 nm light, confirming that the pattern represented in Figure 6.19 reflect a gradual absorption of the exciting infrared light. Such an occurrence is indeed, to our best knowledge, never seen before.

The important thing to notice is that the wavelength of the exciting infrared light has an effect on the time it takes the system to fully absorb this light. For practical applications wavelengths like 975 nm would have to be avoided and attention should be given to a proper choice of the infrared wavelengths that would ensure a prompt absorption response.

## 6.5 Conclusions

We have presented some experimental results concerning the emission of WL by Nd-doped and, very importantly, nominally un-doped  $\text{Y}_2\text{O}_3$  nano-particles under different conditions of excitation. Our study was directed toward the investigation of the basic parameters controlling the onset and build-up of the observed WL and its decay following the sudden cut-off of the exciting light. We found that the presence of Nd as an optically active dopant in the nano-particles favored the production of the WL, but was not essential for this production.

Another important parameter was the pressure in the sample environment: low pressure favored the emission of the WL. However, we found that under appropriate conditions WL emission could be obtained even at atmospheric pressure. This last

result points to the potential applications of systems like the one we examined to the field of lighting.



## **7. BROADBAND VISIBLE WHITE LIGHT EMISSION FROM NOMINALLY UN-DOPED AND Cr<sup>3+</sup> DOPED GARNET NANOPOWDERS**

Synthetic garnet nano-powders of Y<sub>3</sub>Al<sub>5</sub>O<sub>12</sub> (YAG) and Gd<sub>3</sub>Ga<sub>5</sub>O<sub>12</sub> (GGG) were produced and the occurrence of a broadband bright visible emission by nominally un-doped YAG and GGG as well as Cr<sup>3+</sup> doped GGG depending on the environment pressure as well as exciting on the pumping power was demonstrated. The results indicate that high intensity infrared laser irradiation in samples not only leads to heating (melting effects) but also produce a visible broadband emission. Low pressure of the powders' environment favors the white light emission by lowering the threshold pumping power. A hypothesis on the nature of the emission is presented.

### **7.1 Introduction**

White light (WL) optical emission from inorganic materials is an important research subject of research emerged in the last decade that finds numerous applications, especially in the fields of lighting and signaling. The majority of the papers that have appeared in the literature have dealt with WL obtained by using a blue or an ultraviolet (UV) light emitting diode exciting one or more suitable and efficient phosphors (only a yellow phosphor, both yellow and red phosphors or both green and red phosphors), with the combination of the emitted radiations originating the WL [85]. According to this strategy i) yellow phosphors enable to get WL with high efficiency but with low color rendering index (CRI), ii) yellow and proper red phosphors let achieve WL with appropriate CRI and moderate luminescence efficiency and iii) emission by green and red phosphors provides WL with high CRI but with low efficiency [86].

Other approaches exploit up-conversion mechanism with a suitable near-infrared (NIR) source excitation with high power above a certain threshold and nano-crystalline powders of a transparent host material doped with lanthanide ions [87]. In several cases, very bright white or yellowish light was observed, corresponding to an

intense and broadband emission-band covering almost the whole visible region [65-70]. The broadband emission was assigned to blackbody thermal emission in some cases, to charge transfer luminescence in other cases, or to a combination of these two processes. For what concerns materials, previously reported WL production stemmed from transparent host materials at least co-doped with rare earth (RE) ions or including RE ions as stoichiometric components.

In particular, the garnets  $\text{Y}_3\text{Al}_5\text{O}_{12}$  (YAG) and  $\text{Gd}_3\text{Ga}_5\text{O}_{12}$  (GGG) are well known in nanocrystalline form [88] and are among the most widely used laser host materials [89] because of their hardness, general stability against chemical and mechanical changes, optical isotropy, good thermal conductivity and low-thermal expansion, high-optical transparency, low-acoustic loss, high threshold for optical damage and high receptiveness to rare earth ions. While YAG has slightly better thermal and optical properties than GGG, GGG is more easily available and in better crystalline quality than YAG.

To the best of our knowledge, no study is available examining the possibility to generate broad-band WL emission by nominally un-doped or transition-metal-doped insulating oxide materials. Hence, this paper demonstrates the occurrence of broadband bright visible emission, depending on environment pressure and pumping power, by either nominally un-doped YAG and GGG or  $\text{Cr}^{3+}$  doped GGG nanocrystalline samples excited by monochromatic CW infrared light (803.5 nm).

## **7.2 Experimental**

### **7.2.1 Synthesis procedures**

To produce powders with grain size in the range of nanometers, the Pechini method [90] and the co-precipitation approach [92] were exploited. The former method besides being simple and inexpensive, has the advantage of providing reproducible and monodispersed samples. It is a common method for the synthesis of metal oxide materials with the aid of an organic polymer and a chelating agent to form a polyester network which can be eliminated by thermal treatment.

Four nanocrystalline garnet samples were investigated in our study:

- i) two samples of nominally undoped YAG, briefly named (YAG)<sub>Pech</sub> and (YAG)<sub>co</sub> hereafter, prepared by the Pechini method [93] and by coprecipitation [91], respectively;
- ii) one nominally undoped GGG sample, named (GGG)<sub>Pech</sub> hereafter, prepared by the Pechini method [94];
- iii) one Cr-doped GGG sample, named GGG:Cr hereafter, with 1 mol% Cr<sup>3+</sup> (substituting Ga<sup>3+</sup>)

The reagents used in the synthesis are given in Table 7.1. The heat treatment was carried out for 16 hours at 800 °C for the samples prepared by the Pechini method, and 3 hours at 900 °C for the YAG sample made by coprecipitation. The metallic precursors were obtained from Sigma-Aldrich, apart from Al(NO<sub>3</sub>)<sub>3</sub>·9H<sub>2</sub>O (Alfa Aesar).

**Table 7. 1:** Garnet samples under investigation.

Sample	Synthesis	Doping	Metal source and purity	Metal source and purity	Dopant source and purity
(YAG) <sub>Pech</sub>	Pechini	Nominally undoped	Y(NO <sub>3</sub> ) <sub>3</sub> ·6H <sub>2</sub> O (99.8%)	Al(NO <sub>3</sub> ) <sub>3</sub> ·9H <sub>2</sub> O (99.999%)	
(YAG) <sub>co</sub>	Coprecipitation	Nominally undoped	Y(NO <sub>3</sub> ) <sub>3</sub> ·6H <sub>2</sub> O (99.8%)	NH <sub>4</sub> Al(SO <sub>4</sub> ) <sub>2</sub> ·12H <sub>2</sub> O (>99%)	
GGG-U	Pechini	Nominally undoped	Gd <sub>2</sub> O <sub>3</sub> (99.99+%)	Ga(NO <sub>3</sub> ) <sub>3</sub> ·8.31H <sub>2</sub> O (99.999%)	
GGG:Cr	Pechini	1 mol% Cr <sup>3+</sup> (substituting Ga <sup>3+</sup> )	Gd <sub>2</sub> O <sub>3</sub> (99.99+%)	Ga(NO <sub>3</sub> ) <sub>3</sub> ·8.31H <sub>2</sub> O (99.999%)	Cr(NO <sub>3</sub> ) <sub>3</sub> ·9H <sub>2</sub> O (99.99+%)

## 7.2.2 Structural characterization

The powder samples were ground in a mortar and then deposited in a low-background sample stage for the X-ray powder diffraction (XRPD) pattern collection. XRPD patterns were measured with a Thermo ARL X'TRA powder diffractometer, operating in Bragg–Brentano geometry (to increase intensity and angular resolution), equipped with a Cu-anode X-ray source (K $\alpha$ ,  $\lambda$ =1.5418 Å) and using a Peltier Si(Li) cooled solid state detector. The patterns were collected with a scan rate of 0.003°/s, time of exposure 9.0 s/step and 2 $\theta$  range of 24–90°. The phase identification was performed with the PDF-4+2008 database provided by the International Centre for Diffraction Data (ICDD).

The crystallite sizes of the single phase samples were evaluated using the Williamson-Hall method.

### **7.2.3 Spectroscopic measurements**

The continuous emission spectra of the samples were obtained by pumping the samples with the output of a Laser Drive Inc. Model LDI-820 diode laser operated at 803.5 nm. The signal was directed toward the entrance slit of a 1 m McPherson Model 2051 monochromator and chopped at a frequency of 250 Hz before entering the slit. The monochromator provided a resolution 0.8 Å with the slits set at 50 µm and a wavelength reproducibility of 0.1 Å.

The optical signal was detected by a Hamamatsu R1387 photomultiplier tube with an S20 response, sent to a EG&G Model 5210 lock-in amplifier and recorded in a computer.

The temporal evolution (decay and rise patterns) of the visible broadband emission intensity of all the samples was measured by employing a shutter to switch on or interrupt the diode laser beam and a Tektronix Model TDS3052B oscilloscope.

The samples were mounted on the cold finger of a closed cycle Helium refrigerator. This system uses a Janis Research Model RD dewar connected with a Leybold Model RW2 compressor. The temperature of the cold finger was controlled by using a Lake Shore Cryotronics 805 Model controller and could be changed from 30 to 300 K.

An Avantes AvaLight-Hal-Cal calibration light source was used to correct our spectra for the sensitivity of our system.

An Allied Scientific Pro ASP-MK350 Model Illuminance Meter was used to measure the CIE (International Commission on Illumination) coordinates, the CCT (Correlated Color Temperature), the CRI(Color Rendering Index), the luminous flux, and to view the spectrum of the WL.

## **7.3 Results and Discussion**

### **7.3.1 Structural Characterization of the Samples**

The X-ray patterns corresponding to the four samples are shown in Fig. 7.1. The results of the structural investigation are summarized in Table 2:

- i) the (YAG)<sub>co</sub>, (GGG)<sub>Pech</sub> and GGG:Cr samples were found to be nanocrystalline, single phase with a cubic garnet structure and with particle sizes in the range 50-80 nm (Table 7.2);

**Table 7. 2:** Structural characterization of the garnet samples under investigation.

Sample	Phase purity	Particle size
(YAG) <sub>Pech</sub>	Not single phase: 7% distorted YAG	n.a.
(YAG) <sub>co</sub>	Single phase	55 nm
GGG-U	Single phase	53 nm
GGG:Cr	Single phase	78 nm

- ii) the (YAG)<sub>Pech</sub> sample was found to contain about 7 mass % of a slightly distorted garnet phase with a stoichiometry close to  $Y_{3.03}Al_{4.97}O_{12}$  [95] and, even if the average size of such mixed phase sample was not determined, peak broadening indicates its nano-crystalline nature.  $Y_{3.03}Al_{4.97}O_{12}$  arises from  $Y_3Al_5O_{12}$  by substitution of a small portion of  $Al^{3+}$  ions, occupying the trigonally distorted octahedral site (with  $S_6$  symmetry), with  $Y^{3+}$  ones. Due to the mismatch of the ionic radii of  $Al^{3+}$  and  $Y^{3+}$  (the latter is larger than the former), the cell edge of  $Y_{3.03}Al_{4.97}O_{12}$  is bigger than the one of  $Y_3Al_5O_{12}$ . As a consequence, the diffraction peaks of  $Y_{3.03}Al_{4.97}O_{12}$  are shifted towards lower 2 theta values, with respect to the ones of  $Y_3Al_5O_{12}$ . (Fig 7.1(a)).

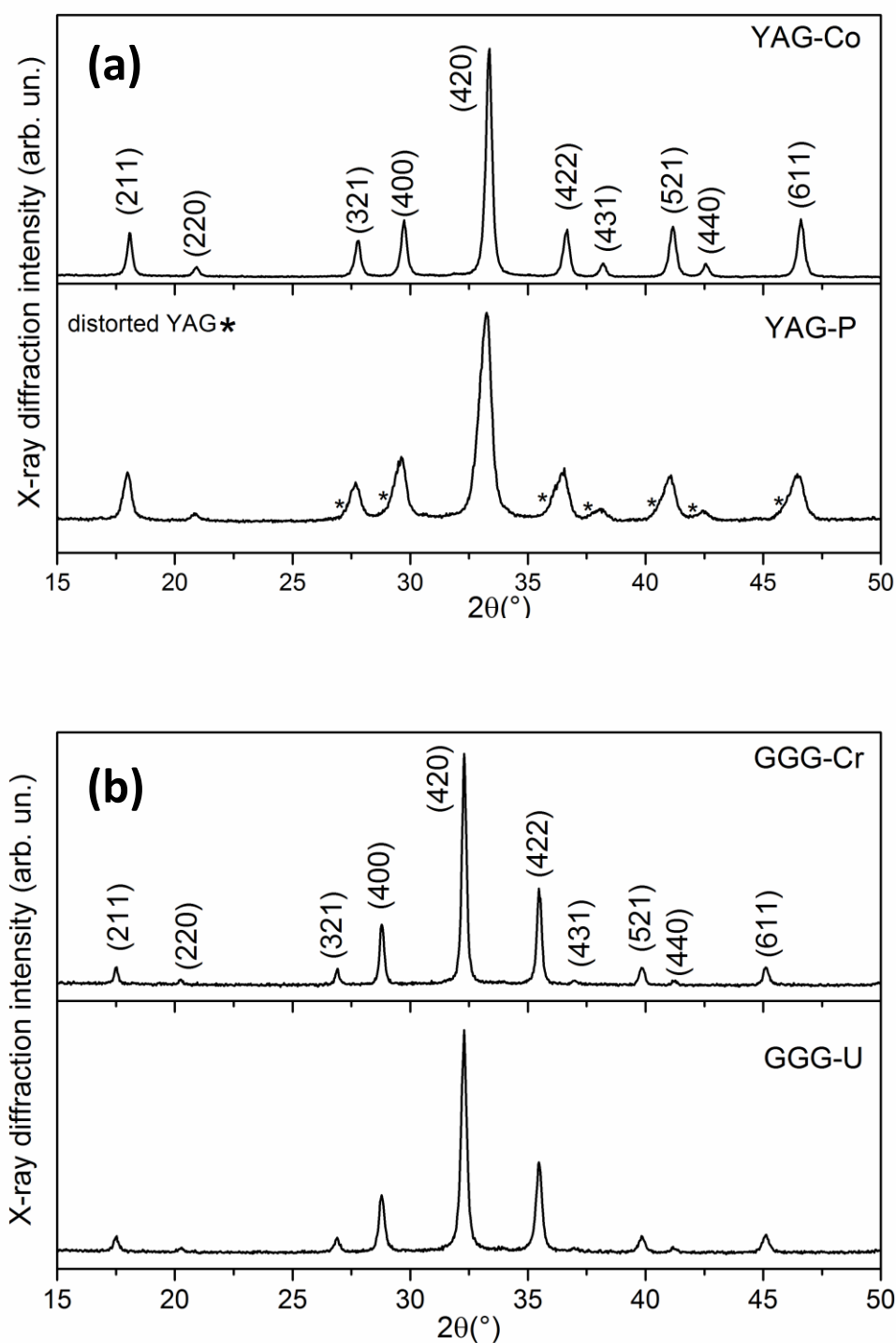


**Figure 7. 1:** XRD patterns of (a) YAG and (b) GGG samples.

It has been reported in the literature that nanocrystalline garnet materials show weak aggregation of the particles and the relatively small particle size is accompanied by significant porosity and surface area [96].

### 7.3.2 Spectroscopic Investigation of the Samples

The onset of a broad emission band extending from 400 to 900 nm was observed peaking in the anti-Stokes side of the exciting laser line (Fig. 7.2) with the samples under a pressure of 0.032 mbar, the cold finger at 300 K and the laser exciting power raised above a certain threshold (0.2 W for GGG:Cr and 1.05 W for (YAG)<sub>co</sub>).

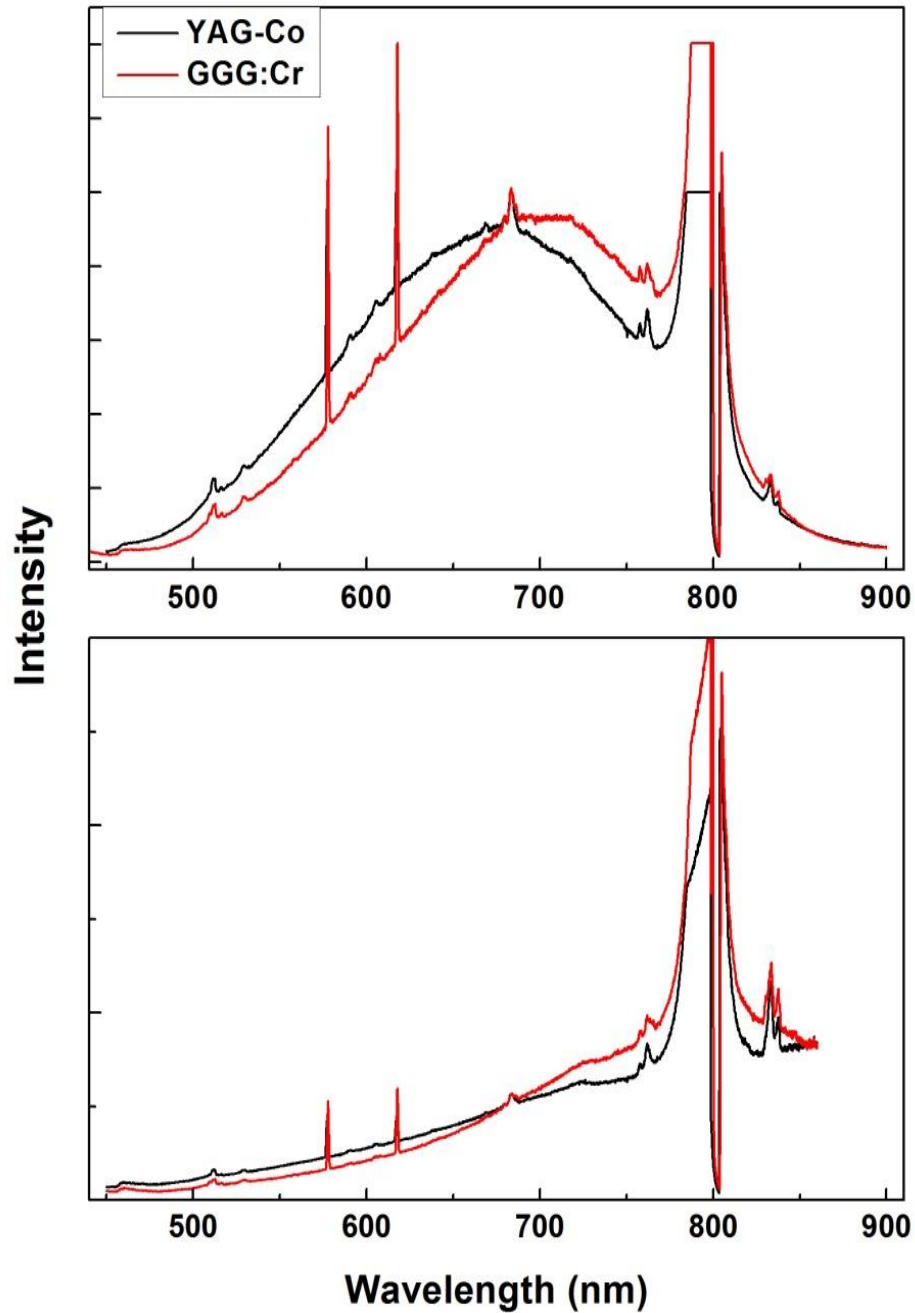


**Figure 7. 2:** (a) Spectral profiles of the broad band emission for (YAG)<sub>co</sub> and GGG:Cr (b) corrected spectra of YAG-Co and GGG-Cr for system response.

In the experimental conditions described above, a broad band emission could be visually observed with the maximum exciting power of 3.25 W for the other two samples, (YAG)<sub>Pech</sub> and (GGG)<sub>Pech</sub>, but its persistence was very short and no meaningful measurements could be carried out. For these reasons, in what follows, only the emission properties of the samples GGG:Cr and (YAG)<sub>co</sub> will be dealt with. Accordingly Fig. 7.2a reports the WL found emitted these two samples. The peak intensities are located at 680 and 700 nm for (YAG)<sub>co</sub> and GGG, respectively.

The spikes that appear in Fig. 7.2a, superimposed to the WL band are due to the spurious modes of the laser.

The WL was incoherent and with no preferential spatial direction. Fig. 7.2b reports the spectra in Fig. 7.2a corrected for the system response and Fig. 7.3 presents the spectra of the WL emitted by the two samples measured by using an illuminance meter. We may note the similarity of the spectra in Figs. 7.2a and 7.3.

The chromaticity coordinates were found to be  $x=0.42$  and  $y=0.36$  for (YAG)<sub>co</sub> and  $x=0.45$  and  $y=0.37$  for GGG:Cr. These values lie in the greenish yellow region and correspond to correlated color temperature (CCT) values of approximately 2859 and 2530 K with the CRI of 91 and 92, respectively (see Fig. 7.3).

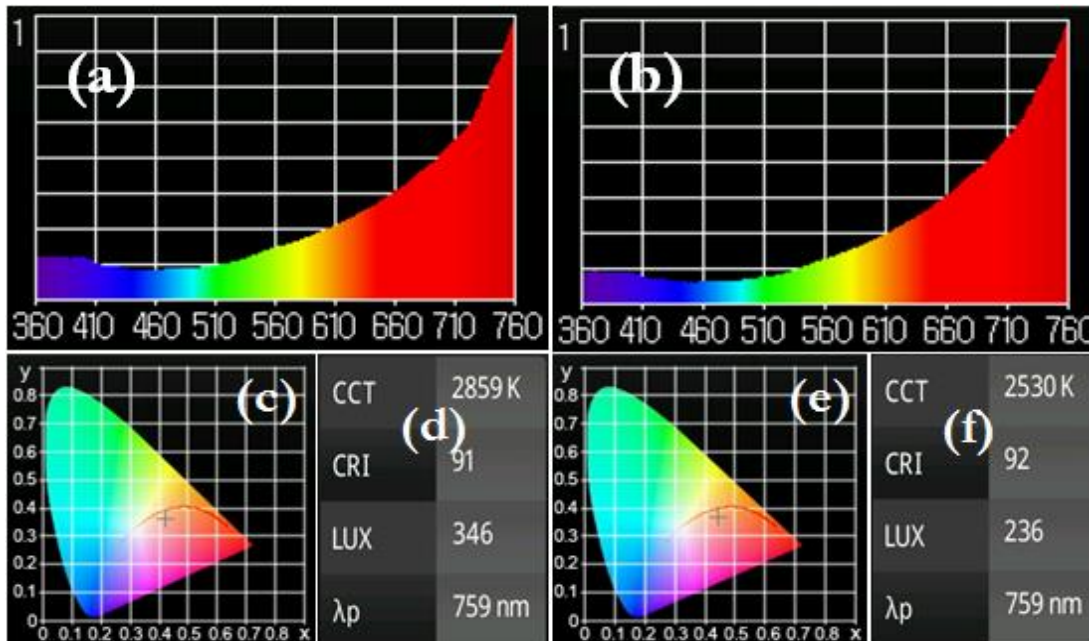


**Figure 7. 3:** (a) Measured spectrum for (YAG)<sub>co</sub> by using illuminance meter (b) measured spectrum for GGG:Cr by using illuminance meter (c) CIE coordinates for (YAG)<sub>co</sub> (d) CIE coordinates for GGG:Cr (e) CCT, CRI and illuminance values for (YAG)<sub>co</sub> (f) CCT, CRI and illuminance values for GGG:Cr.

We also measured the WL emitted by two samples when varying the temperature of the cold finger and noted that neither the profile nor the emission intensity appear to change significantly. This result, per se, indicates that the emitting part of the sample is at such high temperature that a change of temperature of the cold finger has no relevant effect on the WL emission (see Figure 7.4).

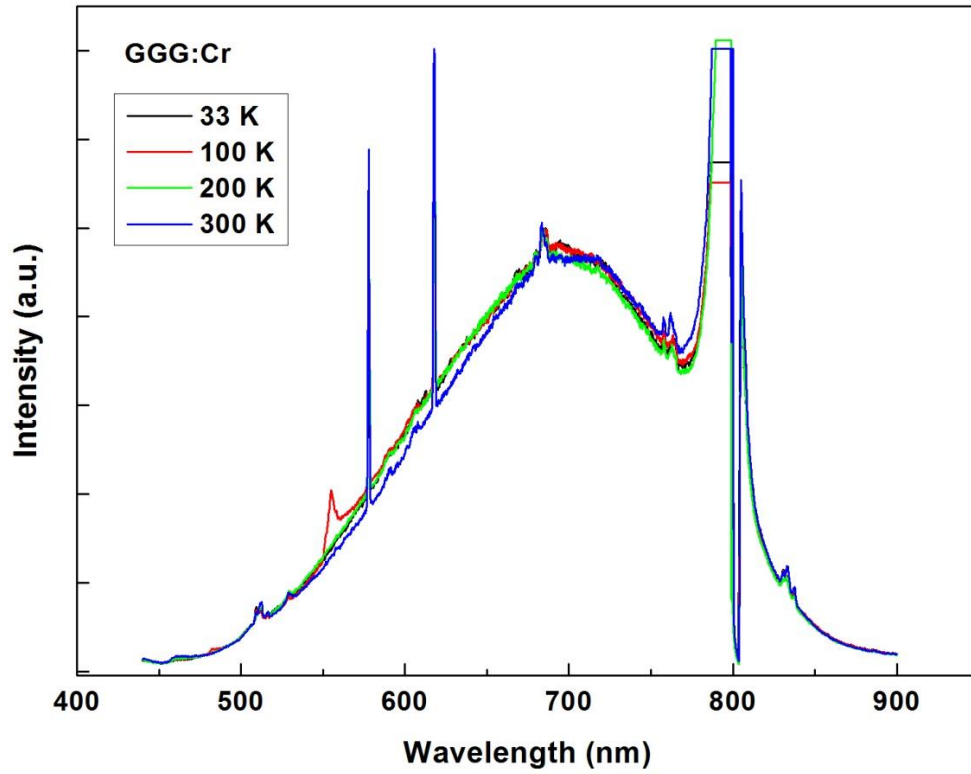


**Figure 7. 4:** Temperature evolution of the broad band emission of GGG:Cr in the range 33-300 K.

The emission intensity exhibits dependence on either the excitation power or the pressure of the sample surroundings. The peak emission intensity increases with the excitation power in a highly non-linear way, and the increase is more rapid for (YAG)<sub>co</sub> than for GGG:Cr (Figure 7.5). In fact, the power dependence of the intensity can be approximated by  $I = AP^n$ , where  $I$  is the peak intensity,  $A$  is a constant,  $P$  is the diode laser power and the exponent  $n$  is 4.8 for (YAG)<sub>co</sub> and 3.7 for GGG:Cr, respectively.

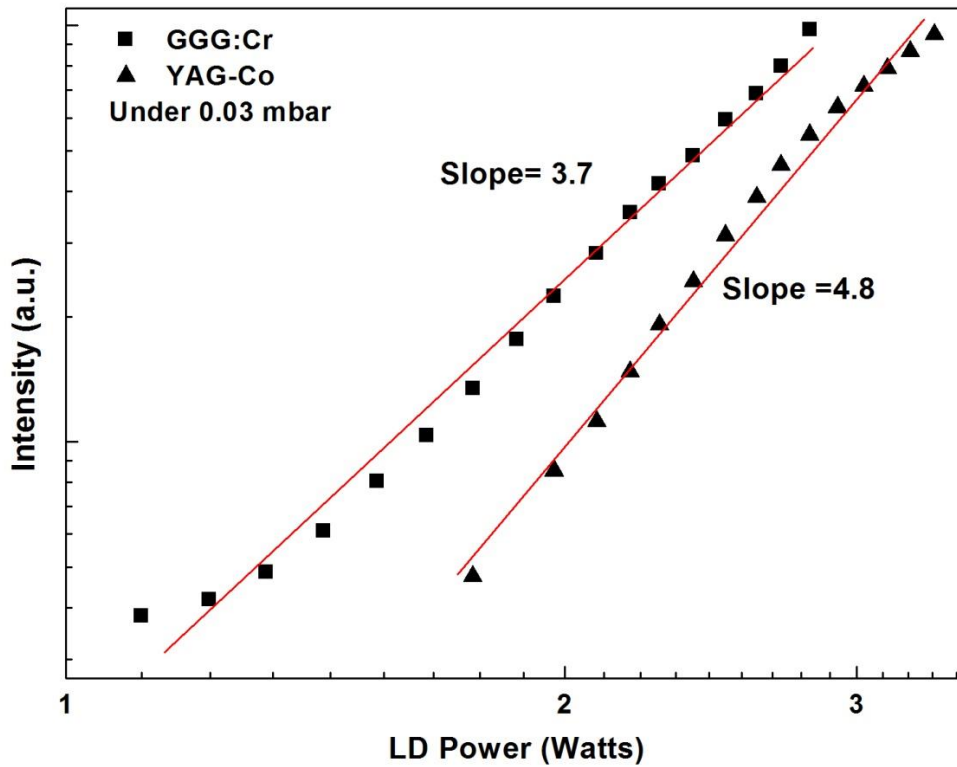


**Figure 7. 5:** Evolution of the broad band peak intensity as a function of the diode laser power for (YAG)<sub>co</sub> and GGG:Cr. The atmospheric pressure was 0.03 mbar.

These findings have relevance on the mechanism by which the 803.5 nm radiation is absorbed and deposited in the sample. Accounting for the intrinsic energy band gaps of the considered host materials (6.6 eV for YAG and 5.4 eV for GGG), no direct interband linear absorption could occur by the host material at the considered exciting photon energy (1.28 eV). However, the high intensity radiation provided by the laser diode may be expected to produce a multiphoton absorption.

Non resonant (i.e. without the presence of intermediate gap states) multiphoton absorption would require 5.07 and 4.21 incident photons for YAG and GGG, respectively. Based on the estimation of the exponent  $n$  occurring in the law  $I=AP^n$  (Fig. 7.5), a resonant multi-photon absorption is likely to occur for YAG [97-100].

As for the absorption mechanism in GGG:Cr, we need to consider the possible role played by the  $\text{Cr}^{3+}$  ion. The WL emission of the GGG:Cr sample has a weak tail in spectral region near the exciting wavelength that happens to fall in an absorption band of  $\text{Cr}^{3+}$  [101].

Investigations of GGG doped with  $\text{Cr}^{3+}$  ions report that such material strongly absorbs radiation with wavelength lower than 700 nm: two broad and intense absorption bands at 610 and 430 nm are typical for  $\text{Cr}^{3+}$  octahedrally-coordinated by O atoms [91]. Broadband emission by  $\text{Cr}^{3+}$  ion is known as due to the coupling between the electronic levels of the 3d-like electrons and the lattice vibrations and  $\text{Cr}^{3+}$  fluorescence properties are sensitive to the crystal field strength [102, 103]. The  $^4\text{A}_2$  ground level and the excited levels  $^2\text{E}$  and  $^4\text{T}$  are involved in the emission dynamics. At low temperature the  $\text{Cr}^{3+}$  ion luminescence is dominated by the  $^2\text{E} \rightarrow ^4\text{A}_2$  transitions (with peaks at 730, 726, and 706 nm) [104, 105] and at room temperature a wide band occurs peaking at 719 nm.

Since our samples GGG:Cr and  $(\text{YAG})_{\text{co}}$  yield broadband visible emission with analogous features (Fig. 7.2) and no temperature-dependence is exhibited by the broadband emission of the sample GGG:Cr (Fig. 7.3), then the occurrence of the visible broadband emission cannot be ascribed to the Cr presence. That is, the similarities of the emission properties of  $(\text{YAG})_{\text{co}}$  and GGG:Cr suggest that the nature of the general emission mechanism may be the same in both materials.

The experimental findings indicate that the only nominally un-doped sample that shows stable broadband emission is  $(\text{YAG})_{\text{co}}$ , fabricated by using relatively low purity starting source reagents of both Y and Al [ $\text{Y}(\text{NO}_3)_3 \cdot 6\text{H}_2\text{O}$  (99.8%) and  $\text{NH}_4\text{Al}(\text{SO}_4)_2 \cdot 12\text{H}_2\text{O}$  (>99%)]. On the other hand, no stable broad band emission was observed at atmospheric pressure by the samples  $(\text{GGG})_{\text{Pech}}$ , fabricated by very high purity reagents [ $\text{Gd}_2\text{O}_3$  (99.99+%) and  $\text{Ga}(\text{NO}_3)_3 \cdot x\text{H}_2\text{O}$  ( $x=8.31$ ; 99.999%)], and  $(\text{YAG})_{\text{Pech}}$ , produced by using a high purity reagent [ $\text{Al}(\text{NO}_3)_3 \cdot 9\text{H}_2\text{O}$  (99.999%)] and a low purity reagent [ $\text{Y}(\text{NO}_3)_3 \cdot 6\text{H}_2\text{O}$  (99.8%)]. Even if the very different behavior of our samples deserves further investigation, the following remarks can be made based on our experimental study.

The GGG-based samples (GGG:Cr and  $(\text{GGG})_{\text{Pech}}$ ), were synthesized by the better approach but consist of nano-crystallites with different sizes (78 nm for GGG:Cr and 53 nm for  $(\text{GGG})_{\text{Pech}}$ ). This issue can be related to the Cr-dopant. In fact, while synthesis thermal- treatments induce thermally activated nucleation due to improved superficial mobility, Cr-doping can be active in promoting heterogeneous nucleation by enhanced density of nucleation sites. In fact, the smaller ionic radius of  $\text{Cr}^{3+}$  ions as compared to  $\text{Gd}^{3+}$  cations introduces lattice-potential well favoring dopant

effectiveness as nucleation centre. Since larger nano-crystals exhibit improved crystalline quality, this refined structural order yield less defects which means reduction of the channels of non-radiative loss and, therefore, could result in measurable and stable broadband emission.

Turning to the YAG-based samples ((YAG)<sub>co</sub> and (YAG)<sub>pech</sub>), they were synthesized by different approaches and exhibited very different structural features: (YAG)<sub>co</sub> was single-phase with 55 nm-large nano-crystals and (YAG)<sub>pech</sub> was not-single phase with distorted lattice. While Y-based precursors with equal purity were used to synthesize both samples, the used Al precursors had very different purity (99.999 % for (YAG)<sub>pech</sub> and 99 % for (YAG)<sub>co</sub>). Even if the nature of these impurities is presently unknown, we point out that  $\text{Cr}^{3+}$ ,  $\text{Cu}^{2+}$ ,  $\text{Fe}^{3+}$  and other transition metal ions are common metallic impurities in nominally pure compounds containing  $\text{Al}^{3+}$  [106, 107]. Therefore, the overall minor purity of reagents may be responsible of the distorted phase of the sample (YAG)<sub>pech</sub>. Once again, the different density of structural defects could account for the lack of stable visible broadband emission by (YAG)<sub>pech</sub> as compared to (YAG)<sub>co</sub>.

Another contribution to the reduction/suppression of the visible broadband emission might be the water ( $\text{H}_2\text{O}$ ) residing on the nano-particle surface, due to either synthesis residuals or adsorption in atmospheric pressure [83]. Since  $\text{H}_2\text{O}$  has a relatively broad absorption band peaking at 760 nm and at 800 nm its absorption coefficient is  $0.02 \text{ cm}^{-1}$  [84], it could contribute to the absorption of the 803.5 radiation. Under equal conditions of background pressure, the different surface-to-volume ratio of the GGG-based samples involves greater density of adsorbed water on the surface of the sample (GGG)<sub>pech</sub> as compared to GGG:Cr, thus contributing to suppress broadband emission by (GGG)<sub>pech</sub>. Such conclusion is supported by the experimental finding that (GGG)<sub>pech</sub> yields only unstable visible broadband emission at very high pumping power (nearly 3.25 W) under atmospheric pressure conditions. For what concerns (YAG)<sub>pech</sub> and (YAG)<sub>co</sub> different water adsorption can only stem from the surface-characteristics as induced by the synthesis procedure.

As for the dependence of the WL emission on the pressure present in the sample chamber Fig. 7.6 reports such pressure dependence for the GGG:Cr sample at the pumping power of 2 W; the WL intensity decreases sharply with increasing pressure. For the sample (YAG)<sub>co</sub>, no experiment as a function of pressure was carried out, as

the broadband emission is measurable only for the lowest available atmospheric pressures (below 0.1 mbar).

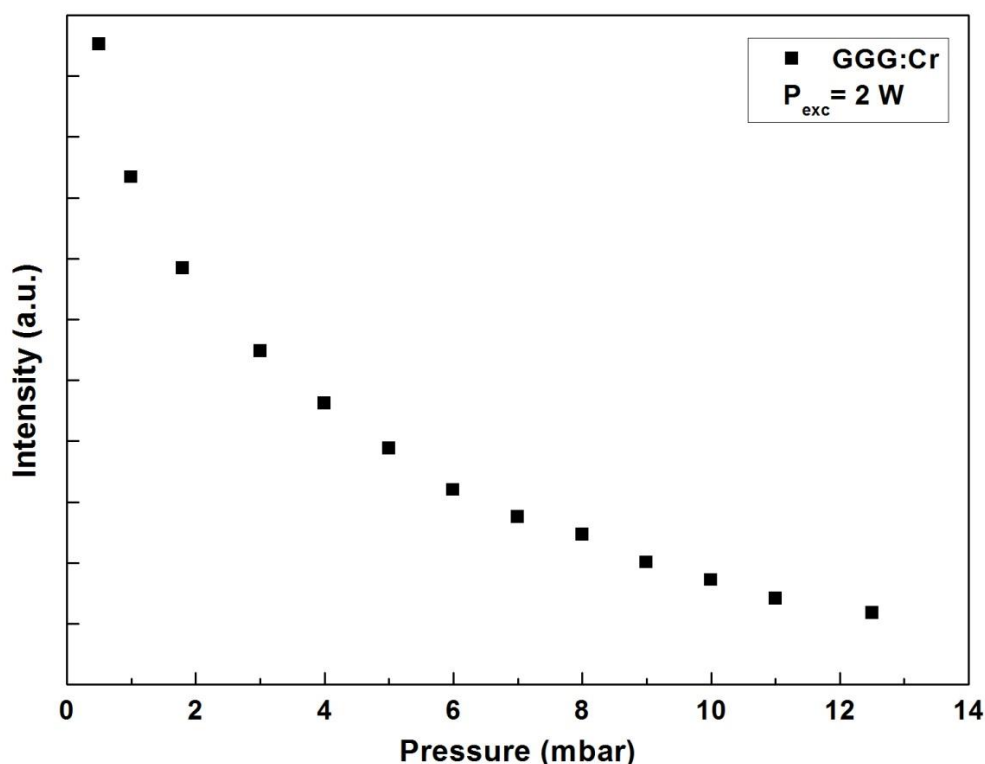


**Figure 7. 6:** Evolution of the broad band peak intensity as a function of the atmospheric pressure for GGG:Cr. The excitation power was 2 W.

The pressure dependence of the broadband emission can be due to the adsorption of polar species on the sample surface and the scattering events involving the nano-powder surface and molecules of the background atmosphere that cause electron de-excitation and/or heating dissipation. The heating effects on the samples after their exposure to the laser beam are demonstrated by their partial melting that can be ascribed to the low thermal conductivity of nano-materials and reduced melting temperature as compared to the bulk counterpart. In this regard an alternative or concurrent pressure-dependent de-excitation mechanism can be invoked based on the thermal conductivity of the nano-powders. This parameter is enhanced by the ambient pressure and reduced when this pressure is lowered. At low pressures the crystallites are more isolated from each other and from the cold finger and can reach higher temperatures favoring the emission of WL.

The decay and rise patterns of the visible broadband emission of the sample GGG:Cr, acquired at room temperature and under atmospheric pressure conditions, are shown in Figures 7.6 and 7.7, respectively. Following the instantaneous interruption of the diode laser irradiation by a shutter, the emission intensity decays in a non-exponential way, with an e-folding time on the order of 0.1 s (Figure 7.6). However, the decay rate appears to be strongly affected by the atmospheric pressure, as the first e-folding time for GGG:Cr approximately changes from 50 to 150 ms for pressures varying from 21 to 0.032 mbar.

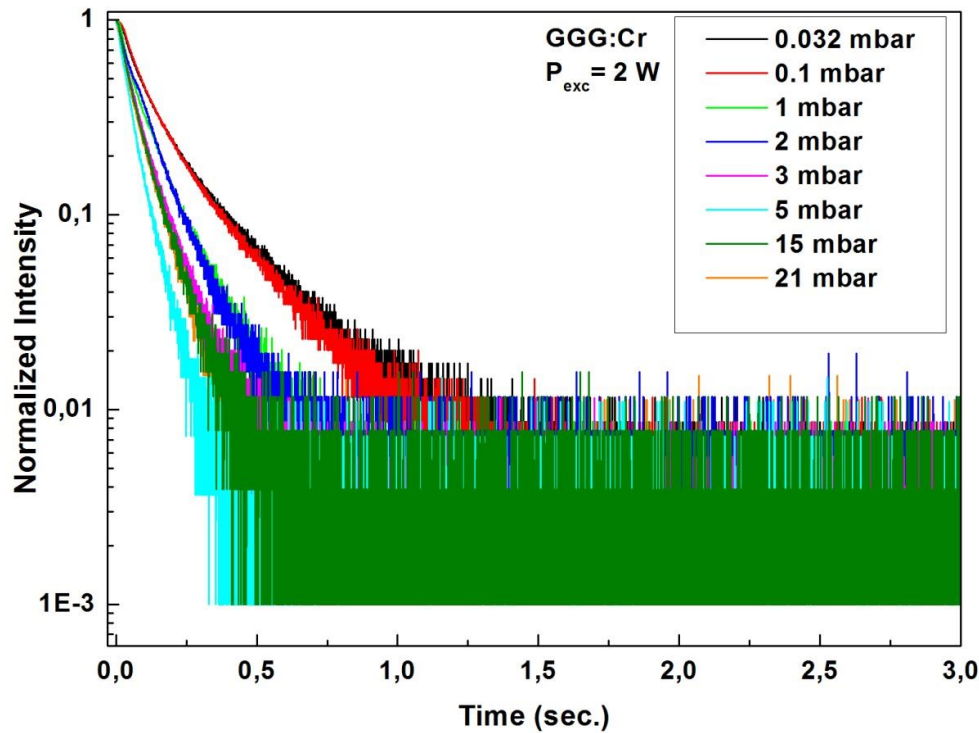


**Figure 7. 7:** Decay of the broadband emission intensity at 675 nm as a function of the atmospheric pressure for GGG:Cr at room temperature. The excitation power was 2 W.

After the instantaneous opening of the shutter blocking the 803.5 nm CW excitation, the broadband intensity increases slowly as a function of the excitation pumping power (Fig. 7.8). In all the cases the rise of the emission intensity is not fast, but takes up to a few seconds to reach a common steady-state value. The rise becomes faster when the power is increased. Similar results were obtained for the (YAG)<sub>co</sub> samples.

The active role of the de-excitation mechanisms aided by the background pressure is consistent with decay rate strongly affected by the atmospheric pressure and fastly

decreasing for increasing pressure (Fig. 7.6). Notably, while at the lowest background pressures the decay pattern is non-exponential, for increasing pressure nearly linear trend is approached. Since the decay accounts for both radiative and non-radiative processes and the contribution stemming from the background pressure is just an extrinsic non-radiative loss channel, such a finding suggests that just above the threshold pressure the decay time of the broadband emission is dominated by the material intrinsic mechanisms. High pumping power favors the onset of step-like build up of the broadband emission (Fig. 7.7). Such an evidence suggests that this emission is related to state-filling and threshold-filling mechanisms. As increasing pumping power means an increasing population of the excited level; the emission intensity is expected to build up proportionally to the filling of the excited states. In this picture, at low pumping power, the insufficient level filling should account for the tailing-effect observed in the rise-time curves (Fig. 7.7) corresponding to the lowest pumping-powers (1.7 and 2.2 W). The step-like increase of the WL onset for pumping power up 2.73 W can be indicative of a threshold filling-process.

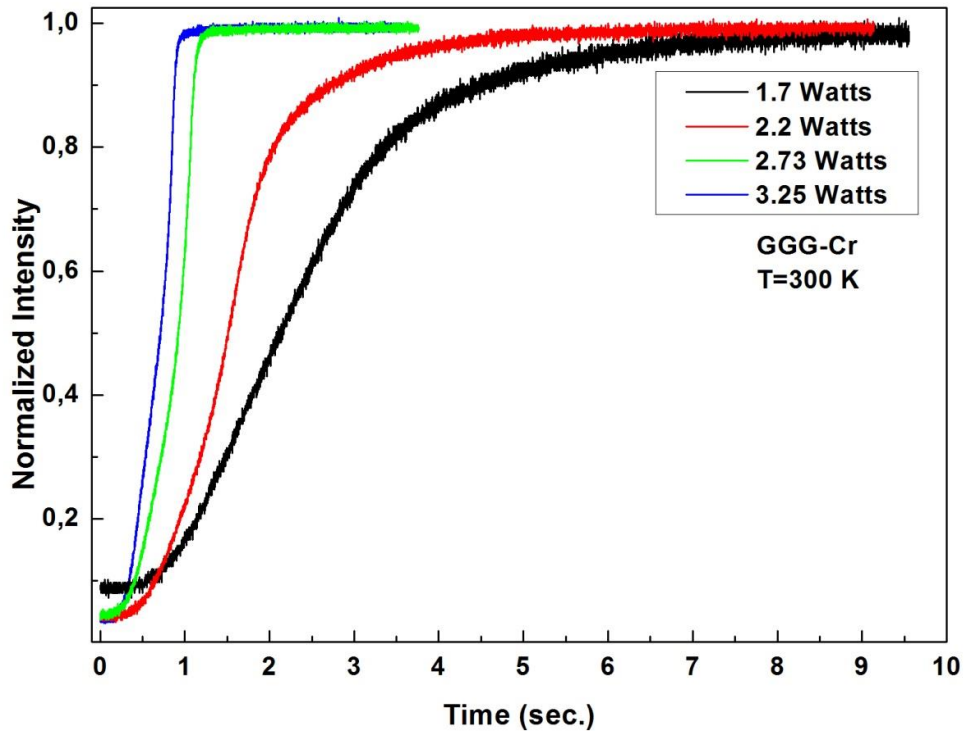


**Figure 7. 8:** Temporal rise of the broadband intensity at 675 nm as a function of the excitation power at ambient pressure (0.03 mbar).

## 7.4 Conclusions

Visible broadband emission is reported in the literature by materials at least doubly doped with different rare earth ions or including them as stoichiometric components. The present study demonstrates that this emission can be obtained by nominally undoped oxide materials and, for the first time, by transition-metal-doped insulating oxide materials. This study has presented the occurrence of broadband bright visible emission by either nominally un-doped YAG and GGG or  $\text{Cr}^{3+}$  doped GGG nanocrystalline samples excited by monochromatic CW infrared light (803.5 nm). It has also demonstrated the influence of the experimental conditions (synthesis approach, purity of the precursor powder, environment pressure and pumping power) in favoring or suppressing the broadband emission. Based on the analysis of the data and on our preliminary results [81, 82], it can be inferred that the observed broadband emission is due to a host dependent general mechanism.

## **8. LASER DIODE INDUCED WHITE LIGHT EMISSION OF $\gamma$ -Al<sub>2</sub>O<sub>3</sub> NANO-POWDERS**

A broadband white light emission was observed ranging from 450 to 900 nm from nominally un-doped  $\gamma$ -Al<sub>2</sub>O<sub>3</sub> nano-powders under 803.5 nm and 975 nm laser diode excitations. The white light emission has a strong dependence on both the environment pressure and the pumping laser power. We spectroscopically characterized this white light emission in a systematic way by collecting spectra, measuring decay- and rise patterns and changing parameters such as pumping power, pumping wavelength, environment temperature and pressure.

### **8.1 Introduction**

The production of white light (WL) has challenged physicists and engineers and has been widely studied due to its numerous applications in lighting, displays and so on. Much attention has gone to binary and ternary lanthanides doped materials [108-111], mixing the emissions of LEDs that emit three primary colors (red, green, blue) [112] and using some phosphor based LEDs [113, 114] to obtain WL. Some recent studies have also shown that certain ultra-small semiconductor nano-crystals can emit WL [115-117]. WL emission from metal oxide nano-powders has only been achieved by the addition of lanthanides doubly or triply and, to the best of our knowledge, there is no information about WL emission from un-doped metal oxides in the literature.

### **8.2 Experimental**

$\gamma$ -Al<sub>2</sub>O<sub>3</sub> nano-powders with the crystalline size of < 50 nm and the surface area of >40 m<sup>2</sup>/g were purchased from Sigma-Aldrich.

The continuous emission spectra of the samples were obtained by pumping the samples with the output of a Laser Drive Inc. Model LDI-820 diode laser operating at 975 nm or 803.5 nm. The signal was directed toward the entrance slit of a 1 m

McPherson Model 2051 monochromator and chopped at a frequency of 250 Hz before entering the slit. The monochromator provided a resolution of 0.8 Å with the slits set at 50 µm and a wavelength reproducibility of 0.1 Å.

The optical signal was detected by a Hamamatsu R1387 photomultiplier tube with an S20 response, sent to a EG&G Model 5210 lock-in amplifier and recorded in a computer.

The experimental data on the responses of the samples to sudden changes in excitation were obtained by employing a shutter to interrupt the diode laser beam and a Tektronix Model TDS3052B oscilloscope.

In order to obtain data on the temperature dependence of this WL in the range of 34 K to 300 K, the samples were mounted on the cold finger of a closed cycle Helium refrigerator. The powdered sample was put in the indentation of a copper sample holder attached to the cold finger of the dewar (see Figure 8.1). A copper sample holder with a small hole in the middle into which the sample was filled was used to attach to the cold finger of the dewar. This system uses a Janis Research Model RD dewar connected to a Leybold Model RW2 compressor. The temperature of the sample holder was controlled using a Lake Shore Cryotronics 805 Model controller.

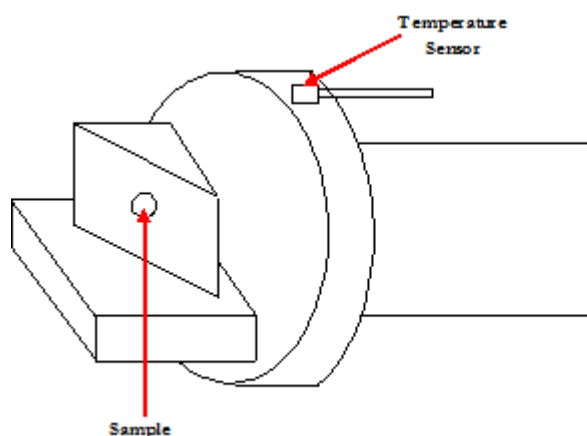


**Figure 8. 1:** Scheme of the sample environment.

For comparison with the original sample, an agate mortar and pestle was used to grind down the grains into a finer powder as the  $\gamma\text{-Al}_2\text{O}_3$  came in a granular form similar to table salt. A little pressure was applied so that the grains simply broke apart. All measurements were performed before and after grinding.

An Avantes AvaLight-Hal-Cal calibration light source was used to correct the spectrum for the sensitivity of the system.

An Allied Scientific Pro ASP-MK350 Model Illuminance Meter was also used to allow measurements of the International Commission on Illumination (CIE) coordinates, the Correlated Color Temperature (CCT), the Color Rendering Index (CRI) and the illuminance values of the WL to be obtained.

### 8.3 Experimental Results

The WL spectrum consists of a wide band that varies between 450 – 900 nm as shown in Figures 8.2(a) and (b). Figure 8.2(a) gives the spectrum directly obtained from the monochromator. This spectrum needed to be corrected for the response of the system using a calibration light source, and this corrected spectrum is given Figure 8.2 (b). The broad spectra appear to be structureless, minus the fact that there is a spike in the spectrum due to the exciting laser diode. Since the monochromator in the system operates in the second order a spike at half of the excitation wavelength appeared in the spectrum. The WL spectrum of the  $\gamma$ -Al<sub>2</sub>O<sub>3</sub> after grinding is also given in Figures 8.2(a) and (b). A shift in the peak positions and a slight change in shape can be seen in both Figure 8.2(a) and (b). The value of the blue shift after grinding is 6.7 nm. This difference between the peak positions before and after grinding corresponds to a temperature difference of 40 K according to Wien's Displacement Law.

The WL spectrum was also measured using the illuminance meter. These results are given in Figure 8.2 (c). The corrected spectrum and the spectrum measured using illuminance meter look similar.

WL output from the sample under 803.5 nm excitation was obtained, but its persistence was very short and no meaningful measurements could be carried out with the apparatus. However, the WL spectrum was obtained using the illuminance meter, shown in Figure 8.2 (d).

The CIE coordinates were found to be  $x=0.392$  and  $y=0.334$  under 975 nm excitation and  $x=0.365$  and  $y=0.324$  under 803.5 nm excitation. These values lie in the yellowish region and correspond to CCT values of approximately 3285 K and 4012

K, each with a CRI of 86, respectively. The total incident luminous flux values were found to be 53 and 392, respectively. The results are summarized in Figure 8.3.

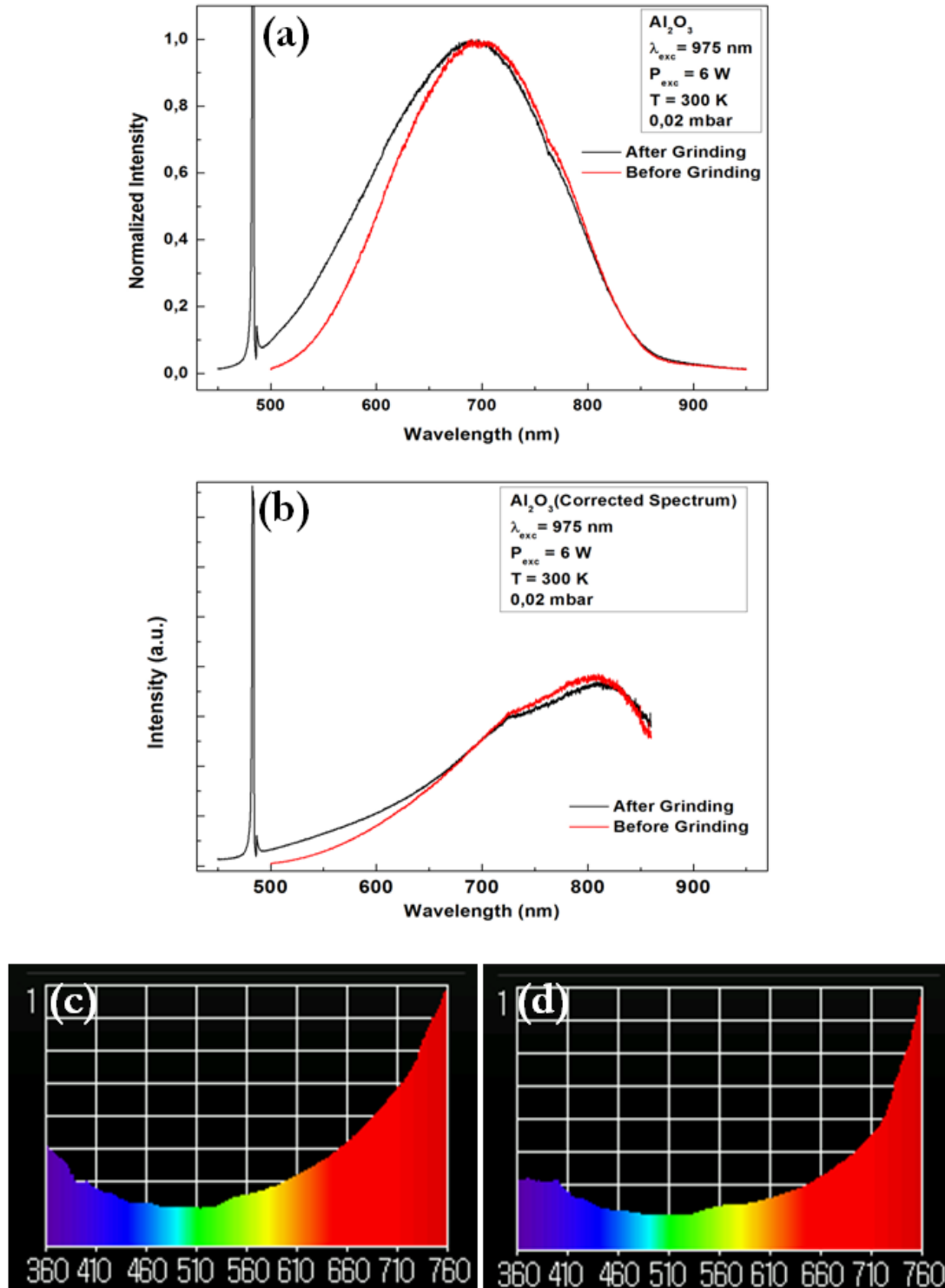


**Figure 8. 2:** (a) Spectral profile of the WL emission from  $\gamma$ - $\text{Al}_2\text{O}_3$  nano-powders before and after grinding, (b) corrected spectra for the system response, (c) measured spectrum under 975 nm excitation by using illuminance meter, (d) measured spectrum under 803 nm excitation by using illuminance meter.

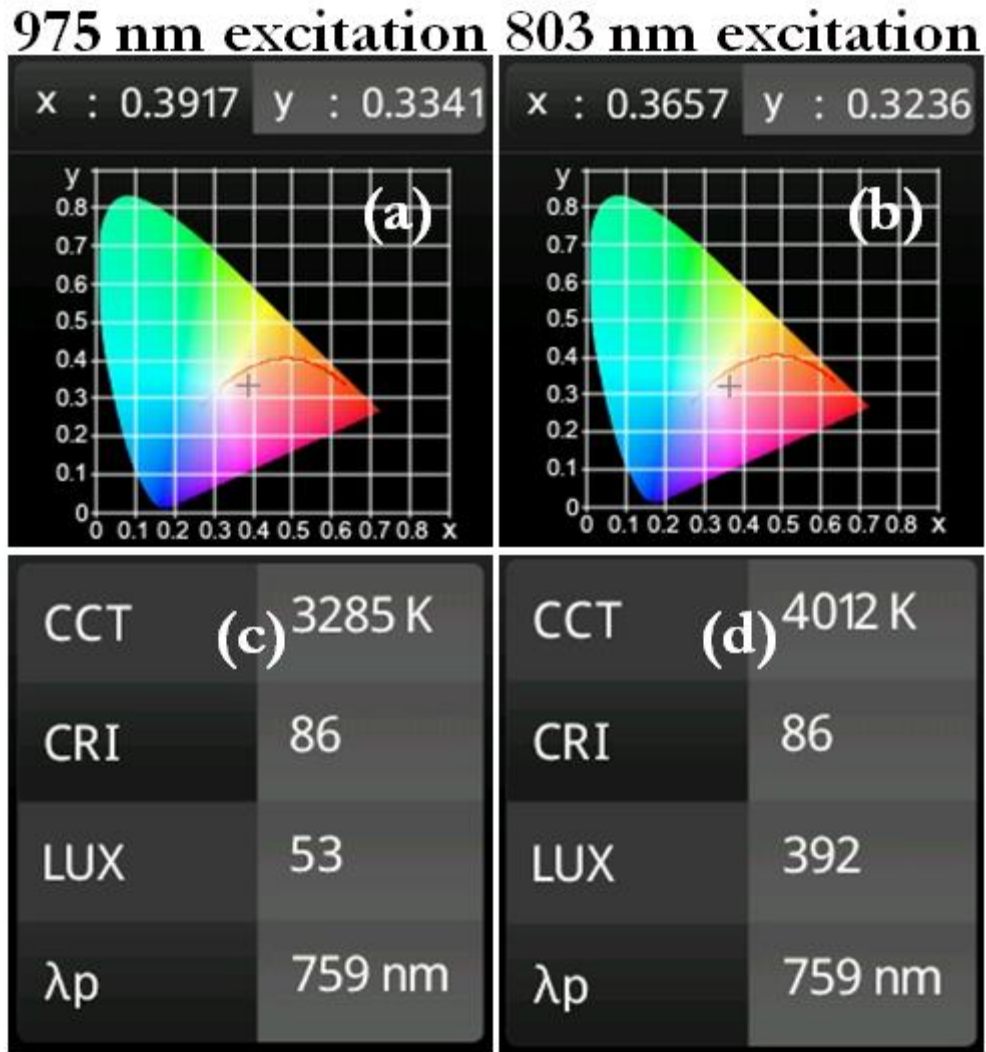


**Figure 8. 3:** (a) CIE coordinates of WL under 975 nm excitation, (b) CIE coordinates of WL under 803 nm excitation, (c) CCT, CRI and illuminance values of WL under 975 nm excitation, (d) CCT, CRI and illuminance values of WL under 803 nm excitation.

A strong dependence on the pumping laser power was also observed. The threshold pumping power value to obtain WL emission was 3.5 Watts. When the power was increased threefold, the WL intensity increased by 75 times its original value. These results are given in Figure 8.4. The power dependence of the intensity can be approximated by the relation  $I = AP^n$ , where  $I$  is the peak intensity of the spectrum,  $A$  is a constant,  $P$  is the diode laser power and the exponent  $n$  is found to be 4.75.

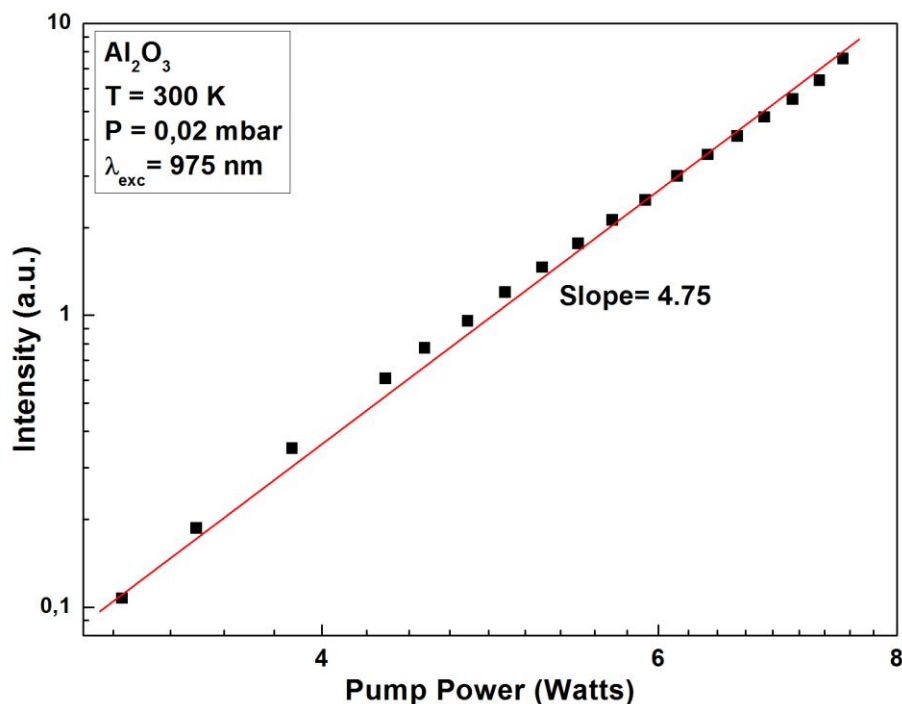


**Figure 8. 4:** Pumping laser power dependence of the WL emission intensity.

A strong dependence on the laser pumping power can also be seen from Figure 8.5, which shows the pumping power dependence of the WL spectrum. A blue shift in peak positions as pumping power increases can also be seen in Figure 8.5 with a value of 21.6 nm. This difference between the peak positions at low and high power values corresponds to a temperature difference of 129 K according to Wien's Displacement Law.

The WL spectrum from  $\gamma\text{-Al}_2\text{O}_3$  was collected as a function of temperature of the sample holder, ranging from 34 K to 300 K. No dependence of the WL spectrum on this temperature was observed.

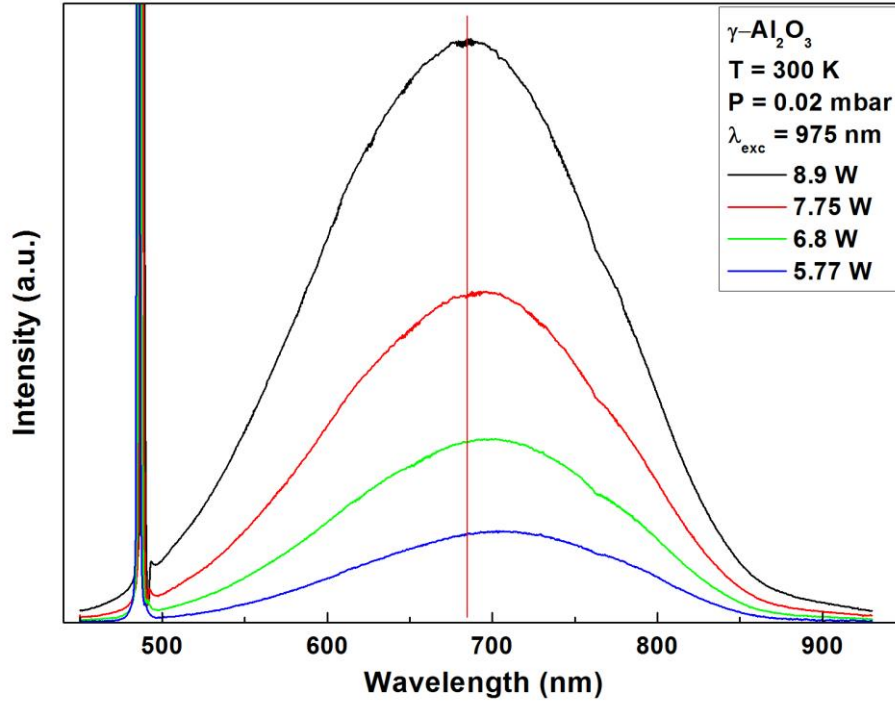


**Figure 8. 5:** Pumping laser power dependence of the WL spectrum.

A strong dependence on the atmospheric pressure surrounding the sample was observed. WL emission was not possible to obtain at room pressure. This pressure dependence of WL emission is given in Figure 8.6. As seen from the Figure, when the pressure is reduced 400 times, the WL intensity increases 25 times.

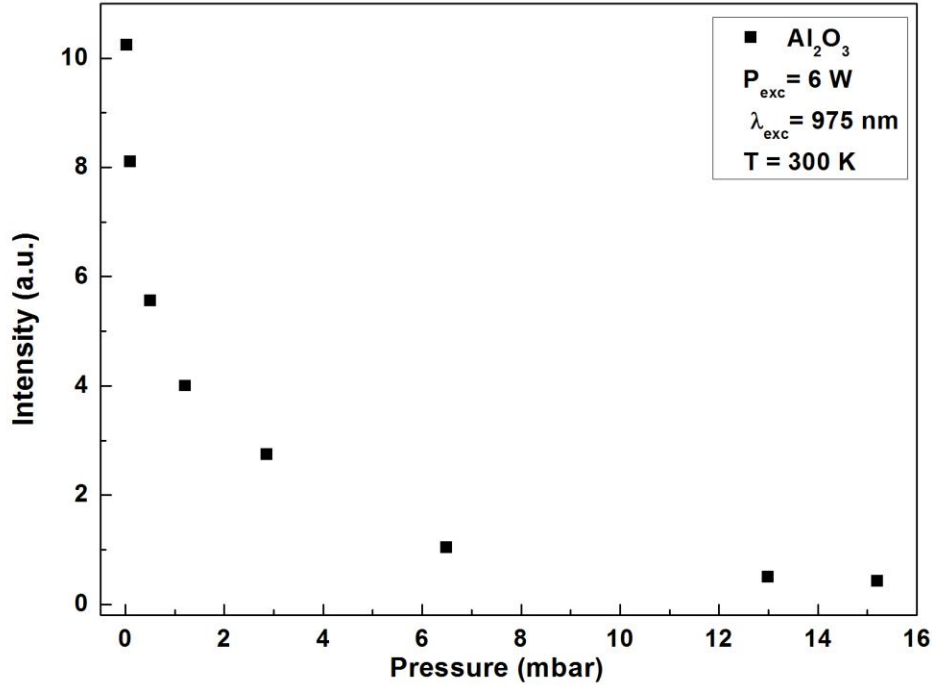


**Figure 8. 6:** Pressure dependence of the WL emission intensity.

In order to provide further characterization the decay patterns and rise patterns of this emission were also measured by changing the parameters that this emission is sensitive to. The results are summarized below:

1. It was observed that the decay patterns did not change as a function of pumping power (see Figure 8.7), and the rise patterns seemed to increase in length with decreasing pumping power as seen from Figure 8.8.

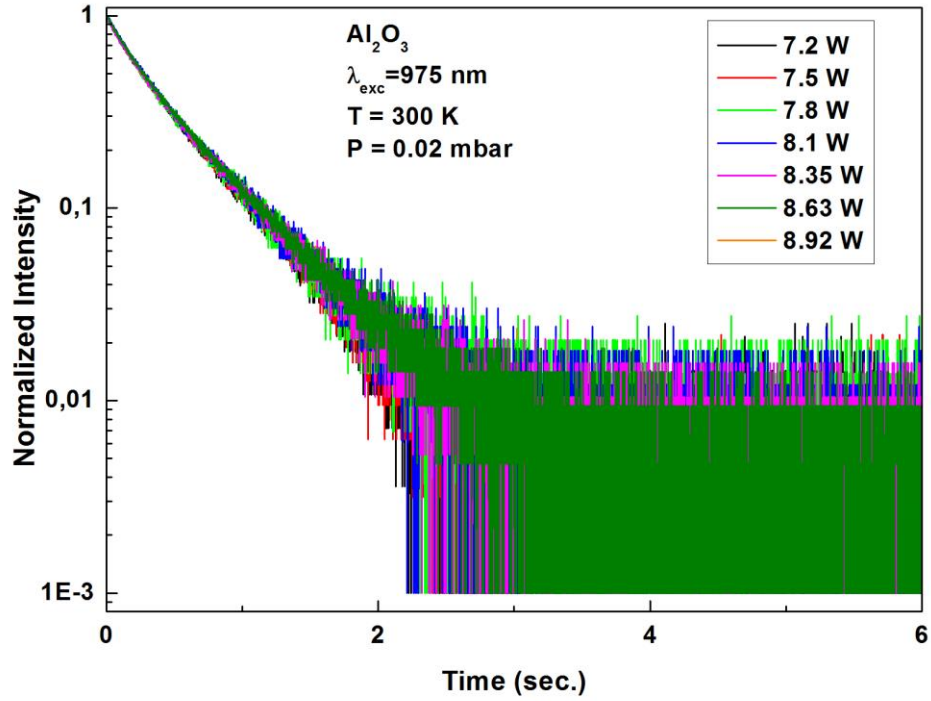


**Figure 8. 7:** Pumping laser power dependence of the decay pattern of the WL emission.

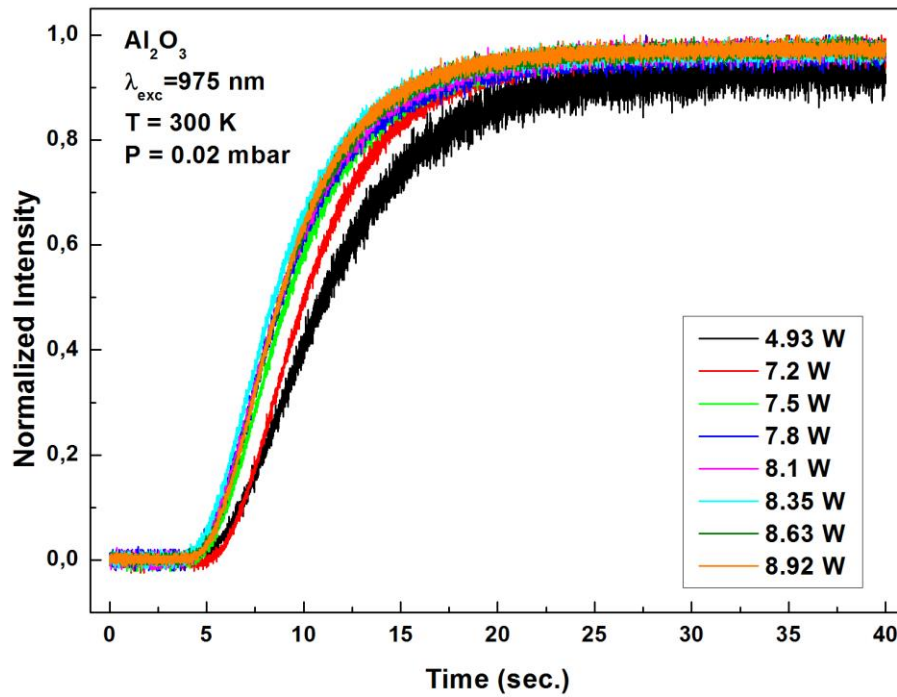


**Figure 8. 8:** Pumping laser power dependence of the rise pattern of the WL emission.

- The decay patterns of the WL at different wavelengths were found to differ as seen in Figure 8.9 but there was no change in the rise patterns as seen in Figure 8.10.

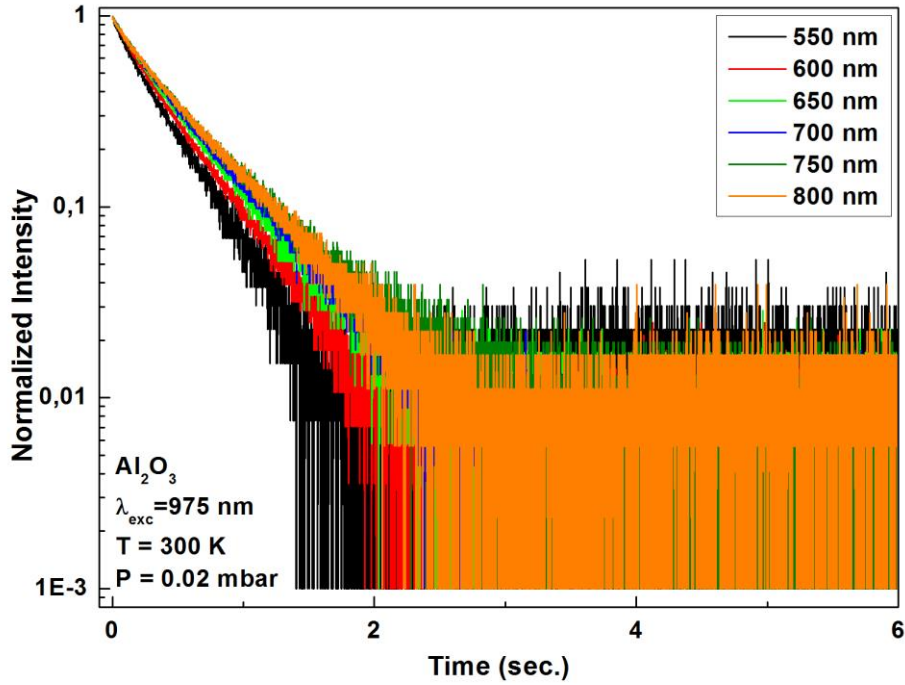


**Figure 8. 9:** Decay times measured at different wavelength positions in the WL spectrum.

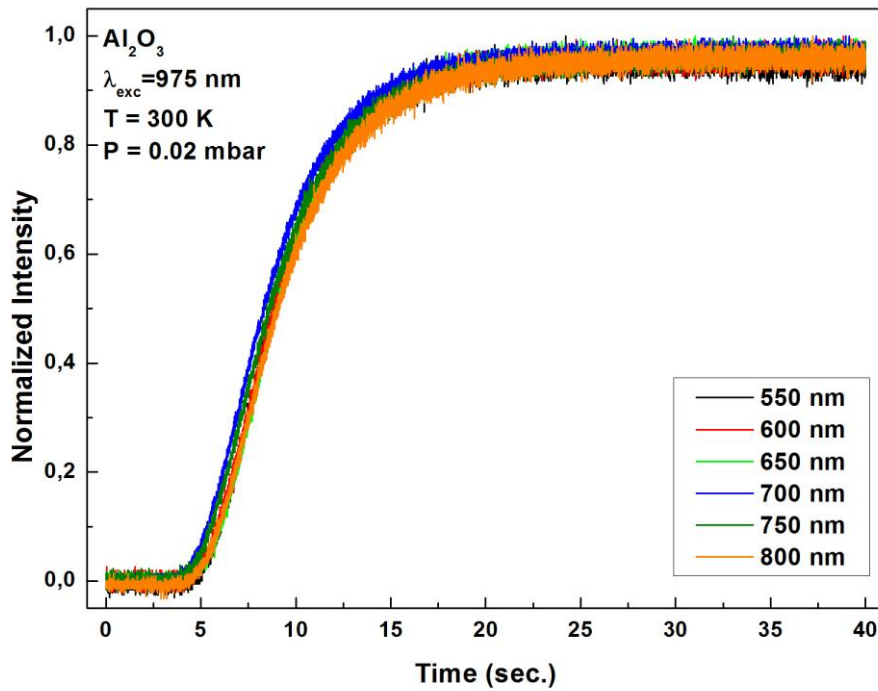


**Figure 8. 10:** Risetimes measured at different wavelength positions in the WL spectrum.

3. The sample holder's temperature dependence of the decay and rise patterns was also measured. There was no relevant change in both the decay and rise patterns with this temperature as seen from Figures 8.11 and 12.

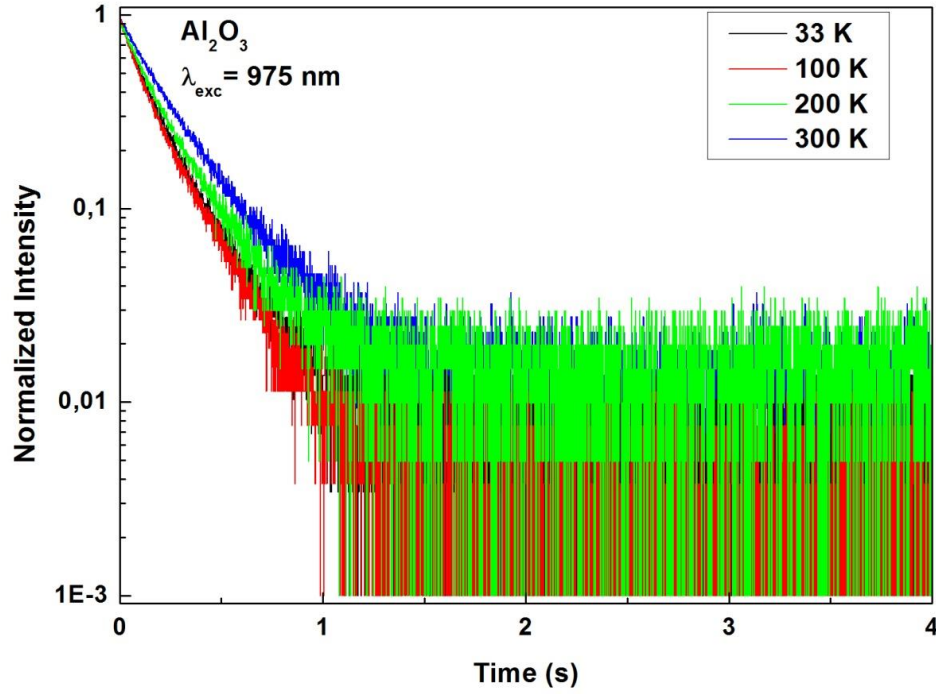


**Figure 8. 11:** Environment temperature dependence of the decay pattern of the WL.

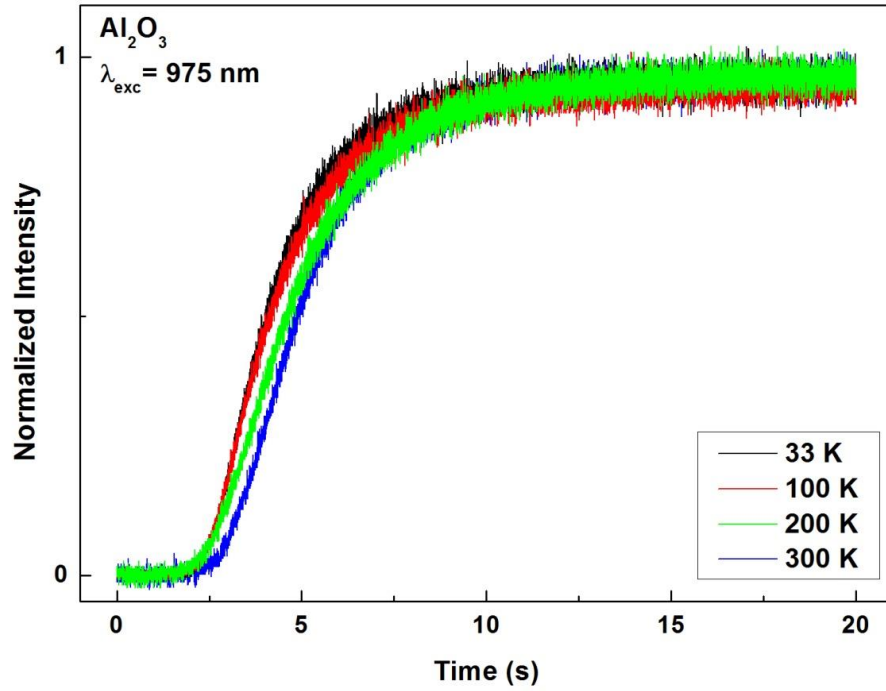


**Figure 8. 12:** Environment temperature dependence of the rise pattern of the WL.

4. A correlation was observed between grinding the grains and the corresponding decay and rise times of the WL. It was found that grinding caused the decay and rise patterns to be shorter than they were before grinding the grains down. The lengths of the decay patterns before and after grinding were found to be 490 ms and 332 ms, respectively.
5. All measurements were repeated to see if grinding the sample had any effect on these results. There were no differences except for the peak position shift in the spectrum and the decreasing length of the decay and rise patterns as discussed above.

## 8.4 Discussion of the Results

The production of WL has already been achieved and reported in the literature. In some recent works, Strek et al [69, 71, 72] showed the possibility of obtaining WL emission from lanthanide ions doped nano-materials. J. Wang et al [66] reported WL emission from lanthanide oxides. However, to the best of our knowledge, there is no information in the literature about WL emission of un-doped metal oxides.

The production of WL emission by laser diode excitation of the un-doped  $\gamma$ -Al<sub>2</sub>O<sub>3</sub> nano-powders was obtained under low surrounding pressure. When discussing the mechanism for the production of the WL, absorption and emission processes need to be considered separately. As the  $\gamma$ -Al<sub>2</sub>O<sub>3</sub> is transparent in a wide range of wavelengths [118], the first problem with obtaining WL under 975 nm excitation is addressing the absorption mechanism of the excitation wavelengths, namely the deposition of the energy. There could be some type of impurities which are responsible for the deposition of the energy, but we do not have any idea about the impurities that exist in the sample at this point. Some researchers have reported a relatively broad absorption band of H<sub>2</sub>O molecules peaking at 760 nm and 800 nm [84]. This could, in principle, be the mechanism responsible for the deposition of energy in this case. However, since low pressure was required for obtaining WL emission and it is well known that water can easily evaporate even at room temperature at low pressure values, this explanation seems unlikely. As mentioned above,  $\gamma$ -Al<sub>2</sub>O<sub>3</sub> has a wide bandgap of 7 eV; it is clear that the absorption process is multiphotonic due to the sub-band energy of the exciting photon. This is confirmed by the fact that WL production requires an attentive focusing of the diode laser beam

on the powder. The process of absorption could be resonant with the band gap or nonresonant; in the latter case it would bring electrons in the conduction band.

A result that confirms the multiphoton aspect of absorption is the dependence of the intensity of the WL on the power (4.75) of the excitation wavelength (Figure 8.4): the required 177 nm (7 eV) energy necessary for the excitation of alumina [118] requires five photons of wavelength 975 nm (1.27 eV).

The 21.6 nm blue shift of the peak position with increasing pumping power (see Figure 8.5), which corresponds to a temperature change of 129 K, is due to the change of the surface temperature of the sample.

As seen from Figure 8.6, the emission of WL increased with decreasing pressure. This behavior cannot be explained on the basis of optical emission due to the wide transparency region of  $\gamma$ -Al<sub>2</sub>O<sub>3</sub>, as well as the unknown impurities. However, a thermally originating mechanism could be related with this observation. Radiative thermal emission from lanthanide ions doped materials [71] and from silicon [77] nano-particles has been observed in the literature but it has never been observed for un-doped metal oxides. A similar intensity-pressure dependence has been reported previously in the literature for SiC nano-particles and mechanically milled Si which was then attributed to thermally originating emission and related to the low thermal conductivities of the nano-materials [77, 78, 119].

It is important to note that laser induced partial melting of the samples was observed during the experiments. This observation indicates that the sample had reached temperatures close to or above its melting point (this value was provided from Sigma Aldrich to be 2040 °C). Researchers have reported experimental and theoretical studies on the relationship between laser induced heating and melting of some metal nano-particles and the optical properties of the materials [120].

There is no dependence of the decay patterns of the emission on the applied pumping power, but the rise patterns seem to be slightly dependent on this applied pumping power. They become longer with decreasing pumping power, seemingly because, as the pumping power decreases, the sample surface takes longer to heat up. This behavior can also be considered as a feature of thermal radiation.

Another important observation is the variation of the decay patterns measured at different wavelengths. Decay patterns become longer as the wavelength values on

the spectrum increases. A possible explanation of this is that the temperature of the sample decreases during the measurement of the decay pattern, thus shifting the spectrum toward longer wavelengths and causing the disappearance of the short wavelength emission.

The measurements of the lengths of the decay patterns before and after grinding were found to be 490 ms and 332 ms, respectively. Also we observed a 6.7 nm of blue shift of the peak positions after grinding. This may be due to a possible change of the surface shape or of the grain sizes as a result of this grinding. It has been shown in the literature that even grinding done using an agate mortar and pestle may cause relevant structural changes of the materials [121-123].

The most important result that points to a thermally originated WL is the similarities of the obtained WL spectrum with that of an incandescent lamp.

## **8.5 Conclusions**

The production of the WL under laser diode excitation has been achieved using commercially obtained  $\gamma$ -Al<sub>2</sub>O<sub>3</sub> nano-powders with a particle size of <50 nm. Strong surrounding pressure and pumping power dependence of the WL emission have been observed. The decay and rise patterns of the emission have also been measured with lengths of several hundred milliseconds and several tens of second, respectively. In accordance with the results and observations, the WL emission from the  $\gamma$ -Al<sub>2</sub>O<sub>3</sub> has been attributed to thermal radiation.

## **9. PECULIAR EFFECTS ACCOMPANYING THE PRODUCTION OF WHITE LIGHT BY IR EXCITED NANOPARTICLES**

### **9.1 Introduction**

We have recently achieved, in collaboration with other researchers, the production of a broad band (ranging from 400 to 900 nm) white light (WL) following the monochromatic infrared light (803.5 and 975 nm) excitation of both nominally undoped and rare earth and transition metal ions-doped oxide nano-powders. Experimental results indicate that such emission feature is a nano-scale phenomenon [81, 82], cannot be ascribed to an overlap of sharp emission bands in the un-doped case and, even if assisted by the dopant presence, is a host matrix-related process.

The spectral distribution of the detected WL resembles very closely that of an incandescent lamp, which in turn is still unmatched with respect to its color quality, mimicking the sunlight, the most comfortable light to human eyes. We have demonstrated the possibility to obtain WL with very high efficiency and CRI approaching the theoretical limit with an alternative approach. Our experimental results make our WL emission very interesting at both the fundamental and the applicative level and may open the way to an alternative route with respect to incandescent lamps.

The band produced by the different compounds occupies similar regions of the spectrum. The characterization of the various samples had to rely on parameters more sensitive to particular situations, such as patterns of decay and of rise in intensity.

We shall recount briefly the conditions of the experiments and summarize the results and then we shall focus our attention on the peculiar aspects of some of our results.

## 9.2 Experimental

The samples used in this work with the information about synthesis procedure and the average particle sizes are summarized in Table 9.1. The details about synthesis procedure and structural characterization were described elsewhere[22, 23, 60, 90, 91].

The continuous emission WL spectra were produced by pumping the samples with the output of a Laser Drive Inc. Model LDI-820 laser diode operating at 803.5 nm with the maximum output power of 3 W or of a similar diode operating at 975 nm with the maximum output of 10 W. The signal was directed toward the entrance slit of a 1 m McPherson Model 2051 monochromator and chopped at a frequency of 250 Hz before entering the slit. The monochromator provided a resolution 0.8 Å with the slits set at 50 µm and a wavelength reproducibility of 0.1 Å. The optical signal was detected by Hamamatsu R1387 photomultiplier tube with an S20 response, sent to a EG&G Model 5210 lock-in amplifier and recorded in a computer.

The rise pattern and the decay pattern of the WL were measured by using a shutter that allowed the light to reach its full intensity and then cut sharply the pumping power. We used a 850 nm cut-on long pass filter to avoid second harmonic contribution of the short wavelength values.

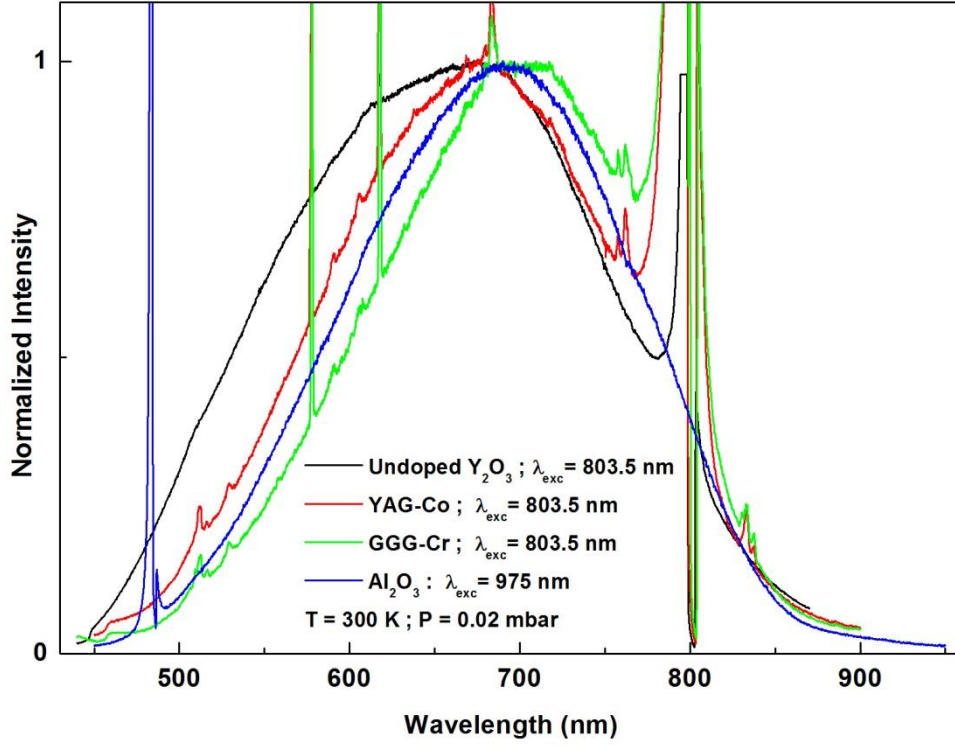
## 9.3 Experimental Results

Table 9.1 reports the average particle sizes estimated by using XRD patterns and confirmed by SEM measurements.

**Table 9. 1:** The samples studied, synthesizing procedure, average particle sizes.

Sample	Synthesizing Procedure	Mean Particle Size (nm)
Y <sub>2</sub> O <sub>3</sub>	Thermal Decomposition [22, 23, 60]	25
Al <sub>2</sub> O <sub>3</sub>	Purchased from Sigma Aldrich	< 50
YAG	Chemical Coprecipitation [91]	55
GGG-Cr	Pechini Method [90]	78

Figure 9.1 shows the obtained WL spectra collected in the 400-900 nm wavelength range for the  $\text{Y}_2\text{O}_3$ ,  $\text{Al}_2\text{O}_3$ , YAG and GGG samples, respectively. The spectra are similar in their general aspects.



**Figure 9. 1:** WL spectrum of all samples. The spikes in the spectrum are due to spurious modes in the laser diode emission.

We shall summarize the experimental results that we obtained by characterizing a representative system, the  $\text{Y}_2\text{O}_3$  un-doped system which emits WL when excited by either 803.5 or 975 nm infrared laser light.

The WL emitted under these two conditions occupies similar regions of the spectrum. We shall briefly mention the results of the characterization.

1. Since no WL emission was observed by bulk samples of Nd-doped  $\text{Y}_2\text{O}_3$  exposed to the same exciting infrared laser light as the nano-powder samples, definitely the observed production of WL can be considered as typical of the nano-scale regime.
2. The spectral distribution of the WL is to a large extent independent on the Nd concentration and even the presence of the Nd dopant. While WL occurrence favors the WL generation but is not necessary to induce such process, the

presence of Nd makes easier to obtain WL emission under low pumping power and higher environment pressure conditions.

3. The temperature of the sample's holder does not influence the spectral shape and seemingly the intensity of the WL emission.
4. The pressure in the sample environment has a great influence on the intensity of the WL. It acts in the opposite sense with respect to the intensity of the exciting infrared light: low pressure favors the emission of WL, and a strong excitation does likewise.
5. The most noticeable aspect of the decay patterns is their deviation from exponentiality. Such behavior could be inferred by the role played by the powders' surfaces, role that becomes more important as the radius of the particle is reduced. Going from the surface to the center of a particle one would encounter a variety of conditions, with each condition determining a different decay patterns. The observed pattern is the superposition of the various different patterns. Accordingly, the deviation from an experimental pattern is in general more pronounced in smaller particles.
6. The spectral distribution of the detected WL resembles very closely the one of an incandescent lamp, which is still unmatched with respect to its color quality, since it resembles the sunlight, which is the most comfortable for human perception.

The following considerations deal with occurrences that manifest themselves depending on the wavelength of the exciting infrared light.

5. The WL spectrum produced by the 975 nm excitation is not significantly different from that produced by 803.5 nm excitation. The dependence of the WL intensity on the fourth power of the exciting 803.5 nm diode power suggests the multi-photon aspect of the absorption process. In fact, an interpretation of the exponent  $n$  occurring in the law  $I=AP^n$  is just in terms of number of photons in multi-photon absorption events. The same can be inferred in the case of the other exciting wavelength (975 nm). However, being a 975 nm photon less energetic than a 803.5 nm photon, more photons are required to induce multi-photon absorption in the un-doped system. This is indeed the case: the WL intensity found to be proportional to a higher exponent  $n$  of the power of the exciting 975 nm source.

The decay patterns following the 975 nm excitation are not significantly different than those following the 803.5 nm excitation, as one would expect. The different experimental conditions may produce different amount of excitation, but this should have no effect on the enfolding of the spontaneous decay.

#### 9.4 Peculiar Occurrences

The wavelength of the excitation has a greater influence on the rise patterns than on the decay patterns of the  $\text{Y}_2\text{O}_3$ . This is evident when comparing the two figures (Figure 9.2 and 9.3) that report the rise patterns following the excitation by 803.5 and 975 nm laser lights, respectively.

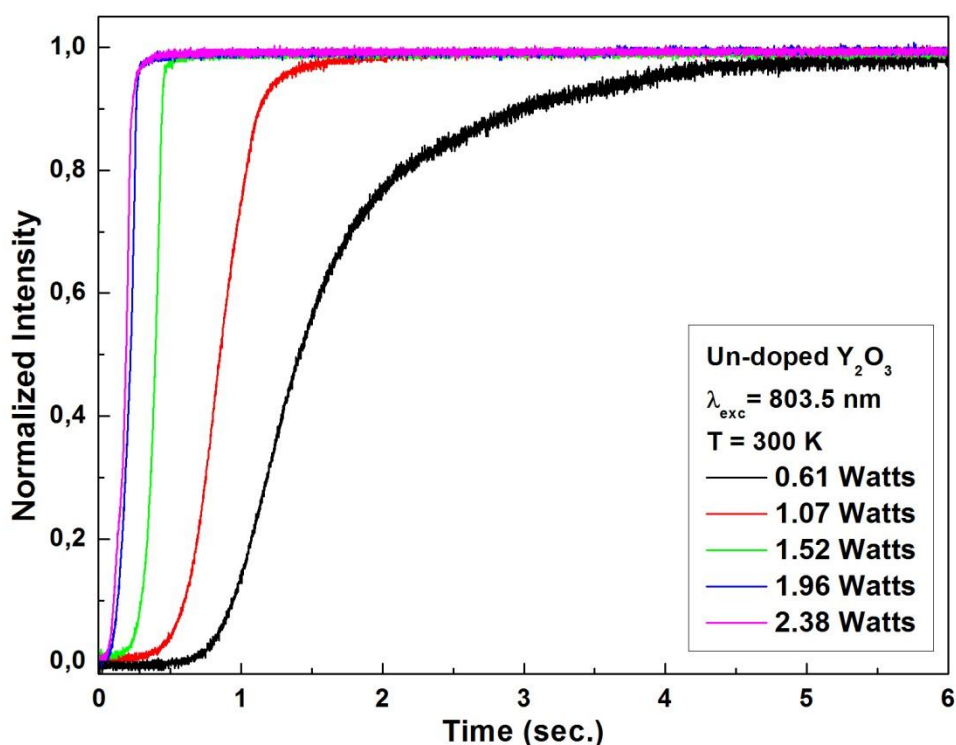


**Figure 9. 2:** Rise pattern dependence on pumping power in un-doped  $\text{Y}_2\text{O}_3$  (803.5 nm excitation).

An interesting feature that emerges when comparing the two figures is that the very first part of the Figure 9.3 pattern represented in the insert resembles the rise pattern of Figure 9.2.

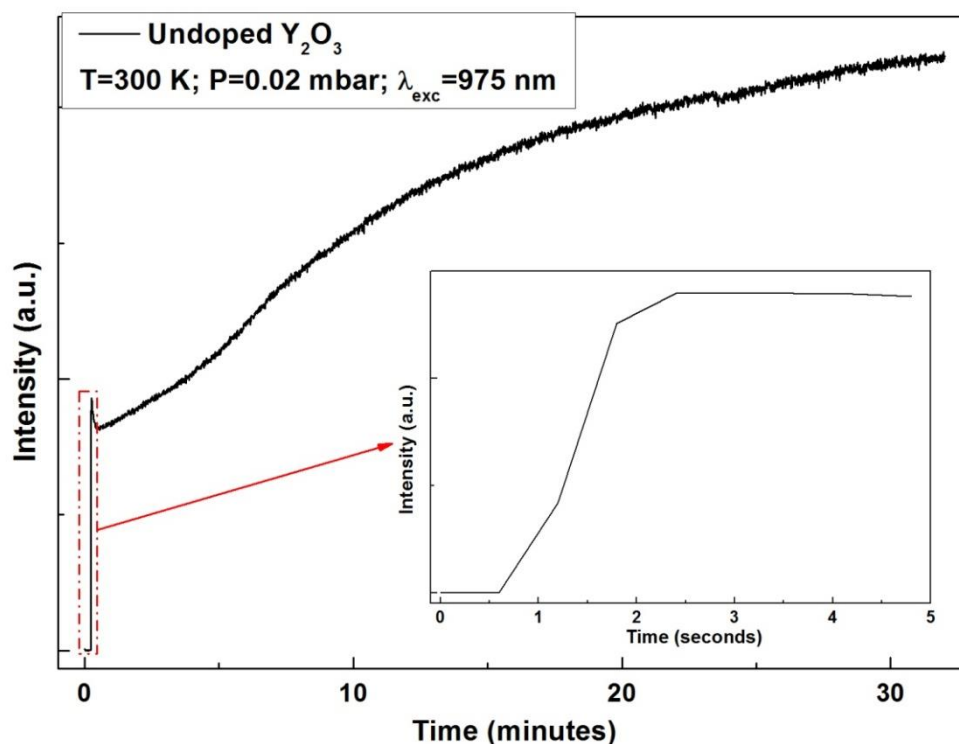


**Figure 9. 3:** Rise pattern of un-doped  $\text{Y}_2\text{O}_3$  under 975 nm excitation. The inset is the expanded sharp rise of the pattern.

The spectra that appear in Figure 9.4 are an additional illustration of the process presented in Figure 9.3. They represent the WL emission of the un-doped  $\text{Y}_2\text{O}_3$  nanopowders taken at different times after exposing the sample to the 975 nm laser radiation. The measurement of each spectrum took ten minutes; it took about an hour for the spectrum to reach its ultimate intensity.

Another peculiar effect regards the decay patterns of the WL. We have examined in detail the decay patterns of the samples listed in Table 9.1 by looking at them at different wavelengths. A typical result of our investigation is presented in Figure 9.5 where we show the decay pattern of  $\text{Y}_2\text{O}_3$  at different wavelengths.

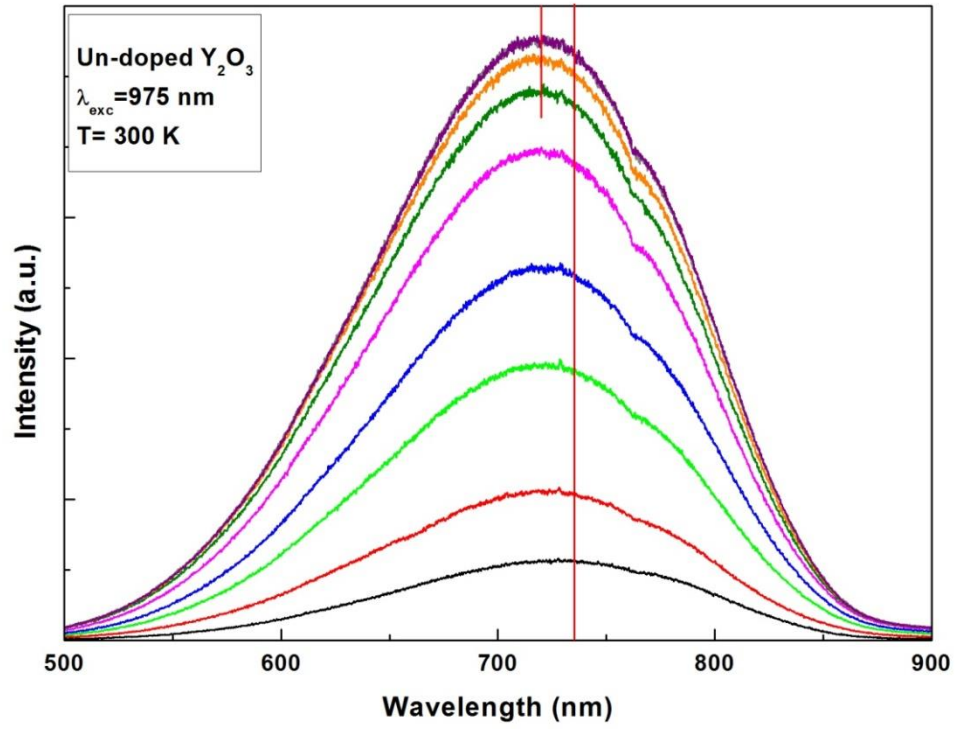


**Figure 9. 4:** The blue shift of the WL spectrum of  $\text{Y}_2\text{O}_3$  with time under 975 nm excitation.

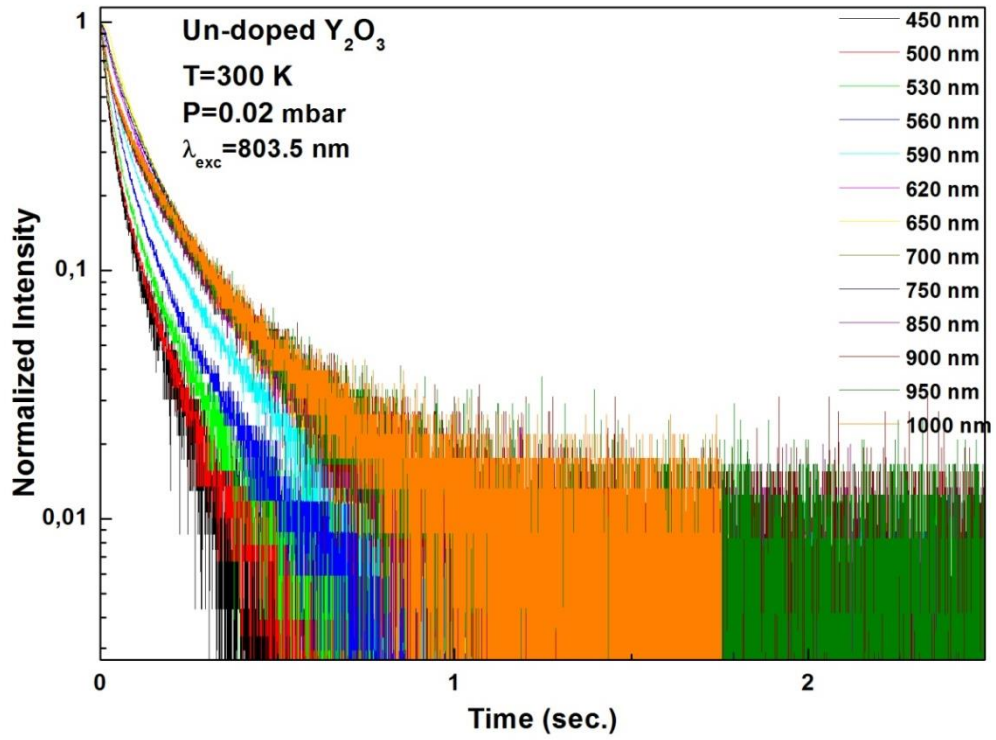


**Figure 9. 5:** Representative decay patterns of nominally un-doped  $\text{Y}_2\text{O}_3$  measured at different part of the WL spectrum.

We have taken as a measure of the rapidity of a “lifetime” determined by determining  $1/e$  times of the decays. The results are presented in Figure 9.6, where we can see that the lifetime increases starting at  $\sim 400$  nm and, having reached a maximum, regain practically its initial value at  $\sim 800$  nm.

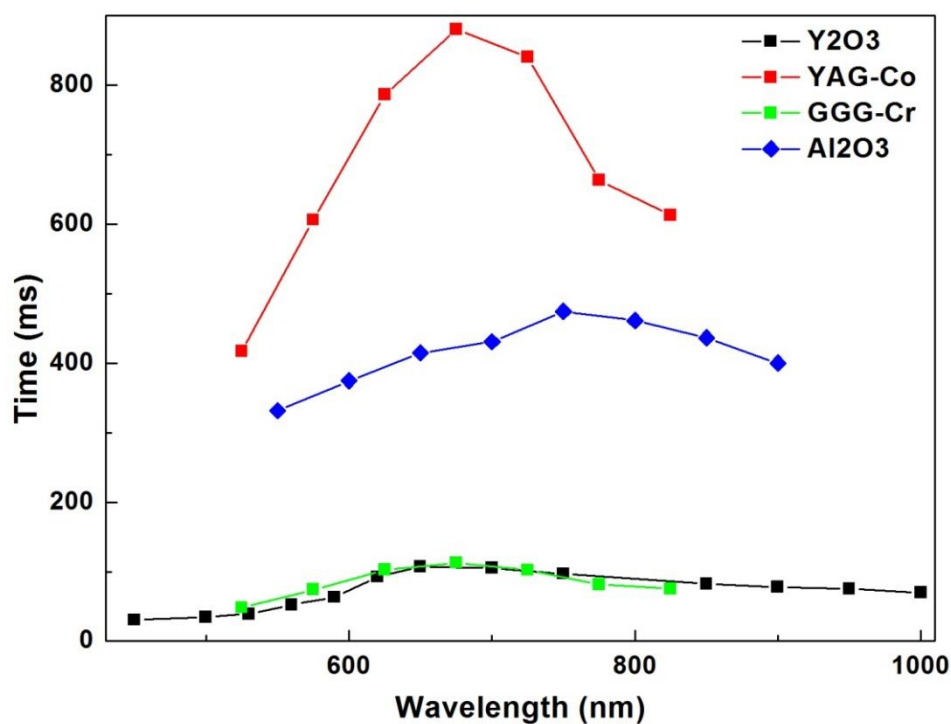


**Figure 9. 6:**  $1/e$  time distribution of all samples as a function of measured wavelength.

## 10. CONCLUSIONS

This dissertation covers the results of an experimental study which provides detailed information about synthesis, structural and optical characterization of  $\text{Y}_2\text{O}_3$  nano-powders activated with  $\text{Nd}^{3+}$  ions. Since the photonics technology evolves everyday and requires new and suitable materials, this dissertation builds a better understanding of these materials by conducting these measurements and revealing the results which serve as the basis for the ultimate goal of this dissertation. Hence, a set of experiments have been conducted in a systematic way to fully characterize the samples.

All the nano-powders studied were synthesized using the thermal decomposition technique and the crystalline sizes of samples successfully controlled by thermal annealing.

The obtained nano-powders were then structurally characterized by XRD, SEM and TEM measurements to determine crystalline sizes, morphology and phases of the material occurred. The results of the structural characterization showed that the crystalline sizes of the materials varied from 15 to 250 nm according to the Scherrer Formula and the results were confirmed by the SEM and TEM measurements. The cubic phase of the  $\text{Y}_2\text{O}_3$  was determined without any other phases with the lattice parameter of 10.6051.

The luminescence spectra and the response to pulsed excitation measurements were carried out at temperatures ranging from 30 to 300 K to characterize samples optically. Those of the  $\text{Y}_2\text{O}_3$  single bulk crystal were also measured for comparison. The general aspect of the luminescence spectra of the samples was found to be similar but some differences were observed with changing the size of the powder,  $\text{Nd}^{3+}$  concentrations and the environment temperatures. The intensity of the sharp emission bands were found to decrease with decreasing powder sizes and increasing  $\text{Nd}^{3+}$  concentration and increasing environment temperatures. The width of the sharp emission bands were also observed to widen with decreasing powder sizes and increasing  $\text{Nd}^{3+}$  concentration and environment temperature. The thermal broadening

and the shift of the sharp emission bands were also studied. The emission bands were found to broaden and the line positions to red shift with increasing environment temperature. The most intense and narrowest emission peaks were observed for the single crystal of  $\text{Y}_2\text{O}_3$ .

The response to pulsed excitation measurements showed that all the decay patterns of the samples were non-exponential except for the single crystal. The longest decay time was observed for the crystal and it was shown that the decay times of the nano-powders decreased with decreasing crystalline sizes and increasing  $\text{Nd}^{3+}$  concentration. The decay time measurements indicate that the decay curves of the nano-powders deviate more from exponentiality with decreasing crystalline sizes and increasing  $\text{Nd}^{3+}$  concentration. It was also observed that decay times of the nano-powders show a slight temperature dependence and they become longer with increasing temperature which is abnormal when compared to other materials, of which the lifetimes either remain constant or decrease with increasing temperature.

Most of the observed properties of the materials studied were explained in a reasonable manner. The differences in the luminescence spectra and the decay curves were attributed to nano-sizes of the materials and the effect of the concentration quenching of the optically active ions. Even if materials are in nano-size, they showed an enough strong emission due to transitions between energy levels of the optically active ions. The thermal dependence of both luminescence spectra and the decay curves of the materials are due to the role played by the phonons. The increasing tendency of the lifetimes with increasing environment temperature which was observed for all samples was attributed to the effect on the emission lifetime of the thermally population of the most energetic  $^4\text{F}_{3/2}$  Stark level.

The most important finding of this thesis which led us to make a patent application was production of bright and wideband white light (WL) from the nano-powders induced by a laser diode emission. The WL emission from the studied nano-powders was first observed in  $\text{Nd}^{3+}$  doped samples at relatively high pumping power levels of the excitation laser diode. Since WL emission was also obtained from %99.999 pure commercial  $\text{Y}_2\text{O}_3$ , such emission feature cannot be ascribed to an overlap of sharp emission bands of the dopant REIs in the un-doped case and, even if assisted by the  $\text{Nd}^{3+}$  presence, is a host matrix-related process, a nano-scale phenomenon. The WL emission was also observed from un-doped and  $\text{Cr}^{3+}$  activated YAG and GGG nano-

powders and un-doped  $\text{Al}_2\text{O}_3$  nano-powders. The pending patent application is given in Appendix A.

The prospects for future works are given below in light of the information and results that we gathered during the period of preparation of this dissertation.

- a) Since the particles with the crystalline sizes less than 10 nm are considered as quantum dots and the powders studied are not less than 10 nm in diameter, any other ways or synthesis procedures might be use to obtain particles with sizes less than 10 nm.
- b) Since the low phonon energies are cut off in nano-materials, the role of the phonons on the luminescence properties of the samples can be studied in details for the present samples using Raman Spectroscopy and/or Neutron Scattering Techniques.
- c) Since the handling of studied materials is difficult, synthesizing of the nano-structured transparent ceramics of the  $\text{Nd}^{3+}$  doped  $\text{Y}_2\text{O}_3$  can be considered to investigate their potential usage as a host material of solid state lasers and for possible contributions to photonics technology.
- d) The production of the WL from nano-powders is still in its infancy and still there are some unknowns about WL that should be answered. Going further with this WL emission, we should fully explain the process that takes place for the production of the WL. To do so the role played by the phonons, crystalline sizes and the dopant REIs for the production of the WL should be investigated. Different type of materials with different crystalline sizes should also be considered.
- e) Since the handling of these materials in nano-powder form and their adaptation to technology in this form is difficult, the production of the WL from these materials in thin film and nano-structured transparent ceramics form can be tried since this makes them more suitable for adaptation to technology.
- f) The nano-powders can be introduced into some type of glass matrix such as silica which is transparent in a wide spectral region and has a stabilizing effect on nano-particle aggregation. Since  $\text{Y}_2\text{O}_3$  is very hygroscopic and this has a serious drawback on the free standing yttria nano-powders by adsorbing

moisture and carbon dioxide from the surrounding atmosphere, introducing them into silica matrix can masoned a wall between the surrounding atmosphere and the REIs which are generally reside on the surface of the material due to the large surface areas of nano-materials. As mentioned in the chapters 6 to 9, the production of the WL is directly related to the low thermal conductivity of the nano-materials and as a result several thermal contact points between each nano-particle which causes the heating of the powders by excitation laser source. Hence, if we introduced them into silica glass matrix homogeneously, this may make them well isolated from each other and this may cause no energy (heat) losses from each particle. Introducing them into silica matrix make them more adaptable to technology.

I can predict that the study of the doped oxides in nano-powders form will continue to be interest to researchers in the field of spectroscopy and that the present work on the production of WL will spur research about its related processes and applications to the field of lighting.

## REFERENCES

- [1] **P. K. Sharma, M. H. Silavi, R.Noss, H.Schmidt**, (1999), Tailoring the particle size from  $\mu\text{m}$ — $\text{nm}$  scale by using a surface modifier and their size effect on the fluorescence properties of europium doped yttria, *J. Lumin.*, 82, 187-193.
- [2] **H. Huang, G. Q. Xu, W. S. Chin, L. M. Gan, C. H. Chew**, (2002), Synthesis and characterization of  $\text{Eu:Y}_2\text{O}_3$  nanoparticles *Nanotechnol.*, 13, 318-323.
- [3] **G. Tessari, M. Bettinelli, A. Speghini, D. Ajo, G. Pozza, L. E. Depero, B. Allieri, L. Sangaletti**, (1999), Synthesis and optical properties of nanosized powders: lanthanide-doped  $\text{Y}_2\text{O}_3$ , *Appl. Surf. Sci.*, 144-145, 686-689.
- [4] **M. Nazarov, J. H. Kang, D. Y. Jeon, S. Bukesov, T. Akmaeva**, (2005), Synthesis and luminescent performances of some europium activated yttrium oxide based systems, *Opt. Mater.*, 27, 1587-1592.
- [5] **T. Kim Anh, L. Q. Minh, N. Vu, T. T. Huong, N. T. Huong, C. Barthou, W. Strek**, (2003), Nanomaterials containing rare-earth ions Tb, Eu, Er and Yb: preparation, optical properties and application potential, *J. Lumin.*, 102-103, 391-394.
- [6] **X. Hu, Q. Yang, C. Dou, J. Xu, H. Zhou**, (2008), Fabrication and spectral properties of  $\text{Nd}^{3+}$ -doped yttrium lanthanum oxide transparent ceramics, *Opt. Mater.*, 30, 1583-1586.
- [7] **B. M. Walsh, J. M. McMahon, W. C. Edwards, N. P. Barnes, R. W. Equall, R. L. Hutcheson**, (2002), Spectroscopic characterization of  $\text{Nd:Y}_2\text{O}_3$ : application toward a differential absorption lidar system for remote sensing of ozone, *J. Opt. Soc. Am. B*, 19, 2893-2903.
- [8] **S. Varma**, (2004) Synthesis and Characterization of Nanostructured Ceramic Luminescent Materials Master Thesis, University of Nevada, Reno,.
- [9] **X. Y. Chen, H. Z. Zhuang, G. K. Liu, S. Li, S. Niedbala**, (2003), Confinement on energy transfer between luminescent centers in nanocrystals, *J. Appl. Phys.*, 94, 5559-5565.
- [10] **L.G. Jacobson, B.L. Bennet, R.E. Muenchausen, J.F. Smith, D. W. Cooke**, (2007), Luminescent properties of nanophosphors, *Radiat. Meas.*, 42, 675-678.
- [11] **Z. Huang, X. Sun, Z. Xiu, S. Chen, Chi-Toy Tsai**, (2004), Precipitation synthesis and sintering of yttria nanopowders, *Mater. Lett.*, 58, 2137-2142.

- [12] **T. Ye, Z. Guiven, Z. Weipin, X. Shangda**, (1997), Combustion synthesis and photoluminescence of nanocrystalline  $\text{Y}_2\text{O}_3\text{:Eu}$  phosphors, *Mater. Res. Bullet.*, 32, 501-506.
- [13] **R. Subramanian, P. Shankar, S. S. Ramakrishnan, P. C. Angela, H. Venkataraman**, (2001), Synthesis of nanocrystalline yttria by sol–gel method, *Mater. Lett.*, 48, 342-346.
- [14] **A. Konrad, T. Fries, A. Gahn, F. Kummer**, (1999), Chemical vapor synthesis and luminescence properties of nanocrystalline cubic  $\text{Y}_2\text{O}_3\text{:Eu}$ , *J. Appl. Phys.*, 86, 3129-3133.
- [15] **R. Srinivasan, N. R. Yogamalar, J. Elanchezhian, R. J. Joseyphus, A. C. Bose**, (2010), Structural and optical properties of europium doped yttrium oxide nanoparticles for phosphor applications, *J. Alloys Compd.*, 496, 472-477.
- [16] **T. K. Anh, P. Benalloul, C. Barthou, L. T. Giang, N. Vu, L. Minh**, (2007). Luminescence, Energy Transfer, and Upconversion Mechanisms of  $\text{Y}_2\text{O}_3$  Nanomaterials Doped with  $\text{Eu}^{3+}$ ,  $\text{Tb}^{3+}$ ,  $\text{Tm}^{3+}$ ,  $\text{Er}^{3+}$ , and  $\text{Yb}^{3+}$  Ions, *J. Nanomater.*, 2007, 48247.
- [17] **J. A. Capobianco, F. Vetrone, T. D'Alesio, G. Tessari, A. Speghini, M. Bettinelli**, (2000). Optical spectroscopy of nanocrystalline cubic  $\text{Y}_2\text{O}_3\text{:Er}^{3+}$  obtained by combustion synthesis, *Phys. Chem. Chem. Phys.*, 2, 3203-3207.
- [18] **J. G. Sole, L. E. Bausa, D. Jaque**, (2005) An Introduction to the Optical Spectroscopy of Inorganic Solids, John Wiley&Sons, England.
- [19] **B. Henderson, G. F. Imbusch**, (1989) Optical Spectroscopy of Inorganic Solids, Oxford University Press, New York.
- [20] **G. H. Dieke**, (1968) Spectra and Energy Levels of Rare Earth Ions in Crystals, Interscience, New York.
- [21] **G. Bilir, G. Özen**, (2011). Optical absorption and emission properties of  $\text{Nd}^{3+}$  in  $\text{TeO}_2\text{--WO}_3$  and  $\text{TeO}_2\text{--WO}_3\text{--CdO}$  glasses, *Physica B: Condensed Matter.*, 406(21), 4007-4013.
- [22] **G. Bilir, G. Ozen, J. Collins, B. Di Bartolo**, (2014). Fabrication and spectral investigation of  $\text{Y}_2\text{O}_3\text{:Nd}^{3+}$  nanoparticles, *Appl. Phys. A*, 115(1), 263-273.
- [23] **G. Bilir, G. Ozen, J. Collins, B. Di Bartolo**, (2013). Synthesis and Spectroscopy of Nanoscale  $\text{Y}_2\text{O}_3\text{:Nd}^{3+}$  Phosphors, *ECS Trans.*, 50(41), 1-7.
- [24] <<http://chemistry.about.com/od/elementgroups/a/rareearths.htm>> date retrieved 02.22.2013.
- [25] **R. W. G. Wyckoff**, (1935) The Structure of Crystals” (2nd Ed.), Reinhold Publishing Corporation, Newyork.
- [26] <<http://jpkc.whut.edu.cn/web18/main/wangluo/webelements/webelements/compounds/text/y/o3y2-1314369.html>>date retrieved 02.22.2013.

- [27] **C. R. Ronda, T. Jüstel**, (2008) *Luminescence: From Theory to Applications*, Ed. C. R. Ronda WILEY-VCH Verlag GmbH & Co. KGaA, Weinheim.
- [28] **Y. Masumoto** (2007) *Fundamentals of Phosphors*, Eds. W. M. Yen, S. Shionoya, H. Yamamoto, p.61, CRC Press Taylor&Francis Group, USA.
- [29] **B. Karaoğlu**, (2008) *Kuantum Mekanikine Giriş*, Seçkin Yayıncılık, İstanbul.
- [30] **B. Karaoğlu**, (2009) *İstatistik Mekanikine Giriş*, Seçkin Yayıncılık, Adana.
- [31] **Y. Wang, N. Herron**, (1991). Nanometer-sized semiconductor clusters: materials synthesis, quantum size effects, and photophysical properties, *J. Phys. Chem.*, 95, 525-532.
- [32] **W. R. Algar, U. J. Krull**, (2009). *Biosensing Using Nanomaterials*, Ed. Arben Merkoçi, Wiley, New Jersey,.
- [33] <<http://en.wikipedia.org/wiki/Nanoparticle>> date retrieved 01.30.2013.
- [34] **B. R. Judd**, (1962). Optical Absorption Intensities of Rare-Earth Ions, *Phys. Rev.*, 127, 750-761.
- [35] **W. T. Carnall, P. R. Fields, K. Rajnak**, (1968). Electronic Energy Levels in the Trivalent Lanthanide Aquo Ions. I.  $\text{Pr}^{3+}$ ,  $\text{Nd}^{3+}$ ,  $\text{Pm}^{3+}$ ,  $\text{Sm}^{3+}$ ,  $\text{Dy}^{3+}$ ,  $\text{Ho}^{3+}$ ,  $\text{Er}^{3+}$ , and  $\text{Tm}^{3+}$ , *J. Chem. Phys.*, 49, 3797-3806.
- [36] **W. T. Carnall, P. R. Fields, B. G. Wybourne**, (1965). Spectral Intensities of the Trivalent Lanthanides and Actinides in Solution. I.  $\text{Pr}^{3+}$ ,  $\text{Nd}^{3+}$ ,  $\text{Er}^{3+}$ ,  $\text{Tm}^{3+}$ , and  $\text{Yb}^{3+}$ , *J. Chem. Phys.*, 42, 4424-4442.
- [37] **G. Liu and X. Chen**, (2007) *Handbook on the Physics and Chemistry of Rare Earths*, (Vol. 37, Chapter 233) Eds. K.A. Gschneidner, Jr., J.-C.G. Bünzli and V.K. Pecharsky, Elsevier, North Holland.
- [38] **B. Di Bartolo**, (2010). *Optical Interactions in Solids* (2nd Ed., p. 385), World Scientific, Singapore.
- [39] **D. W. Posener**, (1959). The shape of spectral lines: tables of the Voigt profile  $a/\pi \int e^{-y^2} dy/a^2 + (x-y)^2$ , *Aust. J. Phys.* 12, 184-196.
- [40] **M. F. Reid**, (2000). *Crystal Field Handbook*, D. J. Newman and B. Ng (Eds), (p. 190) Cambridge University Press, Cambridge.
- [41] **W. R. Gomboltz, S. F. Wee**, (1998). Protein release from alginate matrices, *Adv. Drug Deliv. Rev.*, 31, 267-285.
- [42] **S. Baskoutas, P. Giabouranis, S. N. Yannopoulos, V. Dracopoulos, L. Toth, A. Chrissanthopoulos, N. Bouropoulos**, (2007). Preparation of ZnO nanoparticles by thermal decomposition of zinc alginate, *Thin Sol. Film.*, 515, 8461-8464.
- [43] **A. Clearfield, N. Bhuvaneshin**, (2005). *Encyclopedia of Inorganic Chemistry* (2nd Ed.), Ed. R. Bruce King, Wiley,.
- [44] <<http://materials.binghamton.edu/labs/xray/xray.html>> date retrieved 02.22.2013.

- [45] **P. Scherrer**, (1918). Bestimmung der Größe und der inneren Struktur von Kolloidteilchen mittels Röntgenstrahlen, *Göttinger Nachrichten Gesell.*, 2, 98-100.
- [46] **B. Fultz**, (2003). "Characterization of Materials" Ed. E. N. Kaufmann, (p. 1050) John Wiley & Sons, New Jersey.
- [47] <[http://serc.carleton.edu/research\\_education/geochemsheets/techniques/SEM.html](http://serc.carleton.edu/research_education/geochemsheets/techniques/SEM.html)>date retrieved 02.22.2013.
- [48] <[http://en.wikipedia.org/wiki/Transmission\\_electron\\_microscopy](http://en.wikipedia.org/wiki/Transmission_electron_microscopy)>date retrieved 02.22.2013.
- [49] **R.E. Muenchausen, L.G. Jacobsohn, B.L. Bennett, E.A. McKigney, J.F. Smith, J.A. Valdez, D.W. Cooke**, (2007). Effects of Tb doping on the photoluminescence of Y<sub>2</sub>O<sub>3</sub>:Tb nanophosphors, *J. Lumin.*, 126, 838-842.
- [50] **X. Qin, Y. Ju, S. Bernhard, N. Yao**, (2005). Flame Synthesis of Y<sub>2</sub>O<sub>3</sub>:Eu Nanophosphors Using Ethanol as Precursor Solvents, *J. Mater. Res.*, 20, 2960-2968.
- [51] **W. Koechner**, (2006). Solid State Laser Engineering (6th Ed.), Springer, Berlin.
- [52] **R. Moncorgé**, (2005). "Spectroscopic Properties of Rare Earths in Optical Materials", Eds. G. Liu, B. Jacquier, Springer Berlin Heidelberg, Newyork.
- [53] **C. Fouassier**, (2005) "Encyclopedia of Inorganic Chemistry.", (2nd Ed) Eds. R. Bruce King, Wiley.
- [54] **S. Singh, W. A. Bonner, W. H. Grodkiewicz, M. Grasso, L. G. Van Uitert**, (1976). Nd-doped yttrium aluminum garnet with improved fluorescent lifetime of the <sup>4</sup>F<sub>3/2</sub> state, *Appl. Phys. Lett.*, 29, 343-345.
- [55] **Y. Q. Jia**, (1991), Crystal radii and effective ionic radii of the rare earth ions, *J. Solid State Chem.*, 95, 184-187.
- [56] **J. T. Karpick, B. Di Bartolo**, (1972). Thermal dependence of the positions and widths of the fluorescence lines of Cr<sup>3+</sup> and Er<sup>3+</sup> in YAG, *Il Nuovo Cimento*, 7(1), 62-70.
- [57] **X. Chen, B. Di Bartolo, N. Barnes, B. Walsh**, (2004). Thermal tuning and broadening of the spectral lines of trivalent neodymium in laser crystals, *Phys. Stat. Sol. B* 241(8), 1957-1976.
- [58] **M. A. Flores-Gonzalez, G. Ledoux, S. Roux, K. Lebbou, P. Perriat, O. Tillement**, (2005). Preparing nanometer scaled Tb-doped Y<sub>2</sub>O<sub>3</sub> luminescent powders by the polyol method, *J. Solid State Chem.* 178(4), 989-997.
- [59] **Z. Wei, L. Sun, C. Liao, C. Yan**, (2002). Fluorescence intensity and color purity improvement in nanosized YBO<sub>3</sub>:Eu, *Appl. Phys. Lett.*, 80(8) 1447-1449.
- [60] **H. Kaygusuz, G. Bilir, F. Tezcan, F. B. Erim, G. Özen**, (2014). Biopolymer-assisted synthesis of yttrium oxide nanoparticles, *Particuology*, 14, 19-23.

- [61] JCPDS X-Ray Powder Diffraction File No. 83–0927.
- [62] **R. Balda, M. Sanz, A. Mendioroz, J. Fernandez, L. S. Griscom, J. L. Adam,** (2001). Infrared-to-visible upconversion in Nd<sup>3+</sup>-doped chalcogenide glasses, *Phys. Rev. B.*, *64*, 144101.
- [63] **D. L. Russell, K. Holliday,** (2001). Upconversion and energy transfer dynamics in Nd<sup>3+</sup>:KLiYF<sub>5</sub>, *Opt. Commun.*, *191*, 277-294.
- [64] **S. Pimputkar, J. S. Speck, S. P. DenBaars, S. Nakamura,** (2009). Prospects for LED lighting, *Nat. Photonics*, *3*, 180-182.
- [65] **S. Redmond, S. C. Rand, X. L. Ruan, M. Kaviani,** (2004). Multiple scattering and nonlinear thermal emission of Yb<sup>3+</sup>, Er<sup>3+</sup>:Y<sub>2</sub>O<sub>3</sub> nanopowders, *J. Appl. Phys.*, *95*(8), 4069-4077.
- [66] **J. Wang, P. A. Tanner,** (2009). Upconversion for White Light Generation by a Single Compound, *J. Am. Chem. Soc.* *132*(3), 947-949.
- [67] **J. Wang, J. H. Hao, P. A. Tanner,** (2010). Luminous and tunable white-light upconversion for YAG (Yb<sub>3</sub>Al<sub>5</sub>O<sub>12</sub>) and (Yb,Y)<sub>2</sub>O<sub>3</sub> nanopowders, *Opt. Lett.*, *35*(23), 3922-3924.
- [68] **W. Stręk, L. Marciniak, A. Bednarkiewicz, A. Łukowiak, R. Wiglusz, D. Hreniak,** (2011). White emission of lithium ytterbium tetrakisphosphate nanocrystals, *Opt. Express*, *19*(15), 14083-14092.
- [69] **W. Stręk, L. Marciniak, D. Hreniak, A. Łukowiak,** (2012). Anti-Stokes bright yellowish emission of NdAlO<sub>3</sub> nanocrystals, *J. Appl. Phys.* *111*(2), 024305.
- [70] **R. K. Verma, S. B. Rai,** (2013). Continuum emission in Nd<sup>3+</sup>/Yb<sup>3+</sup> co-doped Ca<sub>12</sub>Al<sub>14</sub>O<sub>33</sub> phosphor: Charge transfer state luminescence versus induced optical heating, *Chem. Phys. Lett.*, *559*, 71-75.
- [71] **L. Marciniak, W. Stręk, A. Bednarkiewicz, A. Łukowiak, D. Hreniak,** (2011). Bright upconversion emission of Nd<sup>3+</sup> in LiLa<sub>1-x</sub>Nd<sub>x</sub>P<sub>4</sub>O<sub>12</sub> nanocrystalline powders, *Opt. Mater.*, *33*(10), 1492-1494.
- [72] **W. Stręk, L. Marciniak, A. Bednarkiewicz, A. Łukowiak, D. Hreniak, R. Wiglusz,** (2011). The effect of pumping power on fluorescence behavior of LiNdP<sub>4</sub>O<sub>12</sub> nanocrystals, *Opt. Mater.*, *33*(7), 1097-1101.
- [73] **T. S. Atabaev, Y. Hwang, H. Kim,** (2012). Color-tunable properties of Eu<sup>3+</sup>- and Dy<sup>3+</sup>-codoped Y<sub>2</sub>O<sub>3</sub> phosphor particles, *Nanoscale Res. Lett.*, *7*, 556.
- [74] **Y. Sato, J. Akiyama, T. Taira,** (2009). Effects of rare-earth doping on thermal conductivity in Y<sub>3</sub>Al<sub>5</sub>O<sub>12</sub> crystals, *Opt. Mater.*, *31*(5), 720-724.
- [75] **G. S. Nolas, G. A. Slack, D. T. Morrelli, T. M. Tritt, A. C. Ehrlich,** (1996). The effect of rare-earth filling on the lattice thermal conductivity of skutterudites, *J. Appl. Phys.*, *79*(8), 4002-4008.
- [76] **H. Zhou, D. Yi,** (2008). Effect of rare earth doping on thermo-physical properties of lanthanum zirconate ceramic for thermal barrier coatings, *J. Rare Earth*, *26*(6), 770-774.

- [77] **P. Roura, J. Costa**, (2002). Radiative thermal emission from silicon nanoparticles: a reversed story from quantum to classical theory, *Eur. J. Phys.*, 23(2), 191-203.
- [78] **P. Roura, J. Costa, M. L. Miguel, B. Garrido, J. Fort, J. R. Morante, E. Bertran**, (1999). Black-body emission from nanostructured materials, *J. Lumin.*, 80(1-4), 519-522.
- [79] **W. Liu, H. Wang, S. Zhan, W. Li**, (2011). Splitting and broadening of the emission bands of  $\text{Y}_2\text{O}_3\text{:Eu}^{3+}, \text{Nd}^{3+}$  and its dependence on  $\text{Nd}^{3+}$  concentration and annealing temperature, *J. Mater. Sci.*, 46(23), 7620-7625.
- [80] **X. Hou, S. Zhou, T. Jia, H. Lin, H. Teng**, (2011). Effect of Nd concentration on structural and optical properties of Nd: $\text{Y}_2\text{O}_3$  transparent ceramic, *J. Lumin.*, 131(9), 1953-1958.
- [81] **G. Bilir, B. Di Bartolo**, (2014). Production of bright, wideband white light from  $\text{Y}_2\text{O}_3$  nano-powders induced by laser diode emission, *Opt. Mater.*, 36(8), 1357-1360.
- [82] **G. Bilir, J. Liguori**, (2014). Laser diode induced white light emission of  $\gamma\text{-Al}_2\text{O}_3$  nano-powders, *J. Lumin.*, 153, 350-355.
- [83] **F. Vetrone, J. C. Boyer, J. A. Capobianco, A. Speghini, M. Bettinelli**, (2003). Luminescence Spectroscopy and Near-Infrared to Visible Upconversion of Nanocrystalline  $\text{Gd}_3\text{Ga}_5\text{O}_{12}\text{:Er}^{3+}$ , *J. Phys. Chem. B*, 107(39), 10747-10752.
- [84] **J. A. Curcio, C. C. Petty**, (1951). The Near Infrared Absorption Spectrum of Liquid Water, *J. Opt. Soc. Amer.*, 41(5), 302-304.
- [85] **S. T. Tan, X. W. Sun, H. V. Demir, S. P. Denbaars**, (2012). Advances in the LED Materials and Architectures for Energy-Saving Solid-State Lighting Toward “Lighting Revolution”, *IEEE Photon. J.*, 4(2), 613-619.
- [86] **L. Chen, C. C. Lin, C. W. Yeh, R. S. Liu**, (2010). Light Converting Inorganic Phosphors for White Light-Emitting Diodes, *Materials*, 3(3), 2172-2195.
- [87] **V. Mahalingam, F. Mangiarini, F. Vetrone, V. Venkatramu, M. Bettinelli, A. Speghini, J. A. Capobianco**, (2008). Bright White Upconversion Emission from  $\text{Tm}^{3+}/\text{Yb}^{3+}/\text{Er}^{3+}$ -Doped  $\text{Lu}_3\text{Ga}_5\text{O}_{12}$  Nanocrystals, *J. Phys. Chem. C*, 112(46), 17745-17749.
- [88] **A. Speghini, F. Piccinelli, M. Bettinelli**, (2011). Synthesis, characterization and luminescence spectroscopy of oxide nanopowders activated with trivalent lanthanide ions: The garnet family, *Opt. Mater.* 33(3), 247-257.
- [89] **J. E. Geusic, H. M. Marcos, L. G. Van Uitert**, (2010). Laser oscillations in Nd-doped yttrium aluminum, yttrium gallium and gadolinium garnets, *Appl. Phys. Lett.*, 4(10), 182-184.
- [90] **M. P. Pechini**, (1967). Method of preparing lead and alkaline earth titanates and niobates and coating method using the same to form a capacitor, US Patent, US 3330697 A

- [91] G. Özen, J. Collins, M. Bettinelli, B. Di Bartolo, (2013). Luminescence of  $\text{Y}_3\text{Al}_5\text{O}_{12}$  nano-particles doped with praseodymium ions, *Opt. Mater.*, 35(7) 1360-1365.
- [92] G. Zhao, T. Li, X. He, J. Xu, (2002). Preparation of gadolinium gallium garnet polycrystalline material by coprecipitation method, *Mater. Lett.*, 56(6), 1098-1102.
- [93] P. Mazur, D. Hreniak, J. Niittykoski, W. Stręk, J. Hölsä, (2005). Formation of nanostructured  $\text{Tb}^{3+}$ -doped yttrium aluminium garnets by the glycol route, *Mater. Sci.–Poland*, 23(1), 261-268.
- [94] M. Daldosso, D. Falcomer, A. Speghini, P. Ghigna, M. Bettinelli, (2008). Synthesis, EXAFS investigation and optical spectroscopy of nanocrystalline  $\text{Gd}_3\text{Ga}_5\text{O}_{12}$  doped with  $\text{Ln}^{3+}$  ions ( $\text{Ln} = \text{Eu}, \text{Pr}$ ), *Opt. Mater.* 30(7), 1162-1167.
- [95] M. Allibert, C. Chatillon, (1974). Étude du diagramme de phase dans le système  $\text{Gd}_2\text{O}_3\text{-Ga}_2\text{O}_3$ , *J. Cryst. Growth*, 23(4), 289-294.
- [96] D. Hreniak, W. Stręk, P. Gluchowski, M. Bettinelli, A. Speghini, (2008). The influence of the specific surface of grains on the luminescence properties of  $\text{Nd}^{3+}$ -doped  $\text{Y}_3\text{Al}_5\text{O}_{12}$  nanopowders, *Appl. Phys. B*, 91(1), 89-93.
- [97] Y. N. Xu, W. Y. Ching, B. K. Briceen, (2000). Electronic structure and bonding in garnet crystals  $\text{Gd}_3\text{Sc}_2\text{Ga}_3\text{O}_{12}$ ,  $\text{Gd}_3\text{Sc}_2\text{Al}_3\text{O}_{12}$ , and  $\text{Gd}_3\text{Ga}_3\text{O}_{12}$  compared to  $\text{Y}_3\text{Al}_3\text{O}_{12}$ , *Phys. Rev. B*, 61(3), 1817-1824.
- [98] J. P. Perdew, (1985). Density functional theory and the band gap problem, *Int. J. Quantum Chem.*, 28, 497-523.
- [99] A. O. Matkovsky, D. Yu Sugak, Yu P. Kostikov, (1990). *Inorganic Materials*, 26(4).
- [100] W. Lotz, (1970). Electron Binding Energies in Free Atoms, *J. Opt. Soc. Am.*, 60(2), 206-210.
- [101] H. Örüçü, G. Özen, B. Di Bartolo, J. Collins, (2012). Site-Selective Spectroscopy of Garnet Crystals Doped with Chromium Ions, *J. Phys. Chem. A*, 116(15), 8815-8826.
- [102] G. Boulon, (2012). Fifty years of advances in solid-state laser materials, *Opt. Mater.*, 34(3), 499-512.
- [103] B. Struve, G. Huber, (1985). The effect of the crystal field strength on the optical spectra of  $\text{Cr}^{3+}$  in gallium garnet laser crystals, *Appl. Phys. B*, 36(4), 195-201.
- [104] A. Monteil, W. Nie, C. Madej, G. Boulon, (1990). Multisites  $\text{Cr}^{3+}$  in GGG and GSGG garnets, *Opt. Quant. Electron.*, 22, S247-S257.
- [105] L. Kostyk, A. Luchechko, Ya. Zakharko, O. Tsvetkova, B. Kukliński, (2009). Cr-related centers in  $\text{Gd}_3\text{Ga}_5\text{O}_{12}$  polycrystals, *J. Lumin.*, 129(3), 312-316.
- [106] S. Mahlik, B. Kukliński, M. Grinberg, L. Kostyk, O. Tsvetkova, (2010). Luminescence and luminescence kinetics of  $\text{Gd}_3\text{Ga}_5\text{O}_{12}$  polycrystals doped with  $\text{Cr}^{3+}$  and  $\text{Pr}^{3+}$ , *Acta Phys. Pol. A*, 117(1), 117-121.

- [107] **N. L. Olenovich, G. A. Gromadskaya, I. S. Anbinder**, (1975). Spectral determination of impurities in some pure aluminum compounds, *J. Appl. Spectrosc.*, *23*(3), 1161-1163.
- [108] **H. Yang, G. Lakshminarayana, Y. Teng, S. Zhou, J. Qui**, (2009). Tunable luminescence from  $\text{Sm}^{3+}$ ,  $\text{Ce}^{3+}$  codoped  $\text{Al}_2\text{O}_3\text{--La}_2\text{O}_3\text{--SiO}_2$  glasses for white light emission, *J. Mater. Res.*, *24*, 1730-1734.
- [109] **R. M. Martinez, E. Alvarez, A. Speghini, C. Falcony, U. Caldino**, (2010). White light generation in  $\text{Al}_2\text{O}_3\text{:Ce}^{3+}\text{:Tb}^{3+}\text{:Mn}^{2+}$  films deposited by ultrasonic spray pyrolysis, *Thin Sol. Film.*, *518*, 5724-5730.
- [110] **N. K. Giri, K. Mishra, S. B. Rai**, (2011). Upconversion Based Tunable White-Light Generation in  $\text{Ln:Y}_2\text{O}_3$  Nanocrystalline Phosphor ( $\text{Ln} = \text{Tm/Er/Yb}$ ), *J. Fluoresc.*, *21*, 1951-1958.
- [111] **H. Hu, Y. Bai**, (2012). Upconversion white luminescence of  $\text{TeO}_2\text{:Tm}^{3+}\text{/Er}^{3+}\text{/Yb}^{3+}$  nanoparticles, *J. Alloys Compd.*, *527*, 25-29.
- [112] **S. Muthu, F. J. P. Schurmans, M. D. Pashley**, (2002). Red, green, and blue LEDs for white light illumination, *IEEE Journal of Selected Topics in Quantum Electronics*, *8*, 333-338.
- [113] **R. Mueller-Mach, G. Mueller, M. R. Krames, H. A. Hoppa, F. Stadler, W. Schnick, T. Juestel, P. Schmidt**, (2005). Highly efficient all-nitride phosphor-converted white light emitting diode, *Phys. Stat. Sol. (A)*, *202*, 1727-1732.
- [114] **W. M. Yen, S. Shionoya, H. Yamamoto**, (2006) Phosphors Handbook, (pp.534-540) CRC Press Taylor&Francis Group, Boca Raton.
- [115] **S. Sapra, S. Mayilo, T. A. Klar, A. L. Rogach, J. Feldman**, (2007). Bright White-Light Emission from Semiconductor Nanocrystals: by Chance and by Design, *Adv. Mater.*, *19*, 569-572.
- [116] **A. D. Dukes, P. C. Samson, J. D. Keene, L. M. Davis, J. P. Wikswo, S. J. Rosenthal**, (2011). Single-Nanocrystal Spectroscopy of White-Light-Emitting CdSe Nanocrystals, *J. Phys. Chem. A*, *115*, 4076-4081.
- [117] **Y. T. Chen, C. L. Cheng, Y. F. Chen**, (2008). Giant white and blue light emission from  $\text{Al}_2\text{O}_3$  and ZnO nanocomposites, *Nanotechnol.*, *19*, 445707.
- [118] **R. Ahuja, J. M. Osorio-Guillen, J. S. de Almedia, B. Holm, W. Y. Ching, B. Johansson**, (2004). Electronic and optical properties of  $\gamma\text{-Al}_2\text{O}_3$  from ab initio theory, *J. Phys.: Condens. Matter.*, *16*, 2891-2900.
- [119] **P. Roura, J. Costa, G. Sardin, J. R. Morante, E. Bertran**, (1994). Photoluminescence in silicon powder grown by plasma-enhanced chemical-vapor deposition: Evidence of a multistep-multiphoton excitation process, *Phys. Rev. B*, *50*, 18124.
- [120] **S. Bruzzone, M. Malvaldi**, (2009). Local Field Effects on Laser-Induced Heating of Metal Nanoparticles, *J. Phys. Chem. C*, *113*, 15805-15810.
- [121] **T. Ban, K. Okada, T. Hayashi, N. Otsuka**, (1992). Mechanochemical effects for some  $\text{Al}_2\text{O}_3$  powders of dry grinding, *J. Mater. Sci.*, *27*, 465-471.

- [122] **W. A. Yarbrough, R. Roy**, (1986). Extraordinary effects of mortar-and-pestle grinding on microstructure of sintered alumina gel, *Nature*, 322, 347-349.
- [123] **P. J. Sanchez-Soto, A. Wiewiora, M. A. Aviles, A. Justo, L. A. Perez-Maqueda, J. L. Perez-Rodriguez, P. Bylina**, (1997). Talc from Puebla de Lillo, Spain. II. Effect of dry grinding on particle size and shape, *Appl. Clay Sci.*, 12, 297-312.



## APPENDIX

### The Pending Patent Application (USPTO Application # 14298602)

#### METHOD AND DEVICE FOR PRODUCING WHITE LIGHT FROM $Y_2O_3$ NANO-POWDERS

##### Cross Reference to related Co-Pending Applications

- 5 This application claims the benefit of U.S. provisional application Serial No. 61/831,925 filed on June 6, 2013 and entitled Production of Bright, Wideband White Light from  $Y_2O_3$  Nano-powders Induced by Laser Diode Emission, the contents of which are expressly incorporated herein by reference.

##### 10 Field of the Invention

The present invention relates to a method and a device for producing white light from  $Y_2O_3$  nano-powders.

##### Background of the Invention

- 15 The production of white light has challenged physicists and engineers for a long time and continues to do so. Lanthanide ions have attracted the interest of researchers for their ability to up-convert infrared light to the visible. Attention has gone to binary and ternary lanthanides doped materials such as glasses, bulk crystals and nano-powders. Some studies have shown that certain ultra-small semiconductor nano-crystals can emit white  
20 light when doped with certain ions. White light has also been obtained by mixing the emissions of light emitting diodes (LEDs) that emit three primary colors (red, green, blue) and by using some phosphor based LEDs.

- It would be desirable to provide an inexpensive method and device for producing white  
25 light from commercially available oxides without doping, with improved efficiency and light characteristics similar to incandescent lights

##### Summary of the Invention

- The present invention describes a method and a device for producing white light from  
30  $Y_2O_3$  nano-powders.

In general, one aspect of the invention provides a method for producing white light including the following. First, providing a light conversion module comprising undoped metal oxide powder comprising particles having a size of less than 50 nm. Next, providing a light source configured to generate excitation light having a wavelength in the near infrared (NIR) region. Next, directing the excitation light towards the undoped metal oxide powder, exciting the undoped metal oxide powder with the excitation light, and thereby causing the undoped metal oxide powder to emit white light having a continuous spectral distribution in the range of 440 nm to 900 nm.

Implementations of this aspect of the invention include the following. The undoped metal oxide powder comprises  $Y_2O_3$ . The light source is a laser diode and is configured to generate excitation light having a wavelength of 803.5 nm. The light conversion module further includes a sealed container configured to encase the undoped metal oxide powder and the sealed container comprises a pressure of less than 8 mbars. The emitted white light has International Commission on Illumination (CIE) color coordinates of  $x=0.45$  and  $y=0.40$ . The emitted white light has a correlated color temperature (CCT) value in the range of 2700K to 3300K and color rendering index (CRI) in the range of 90 to 100. The emitted white light has a correlated color temperature (CCT) value of 2756K and color rendering index (CRI) of 99. The emitted white light intensity depends exponentially upon the light source power. The  $Y_2O_3$  is synthesized via thermal decomposition of Yttrium-Alginate. The undoped metal oxide powder has a purity of 99.999%. The light source is configured to provide an output power of at least 3 Watts. The method further includes focusing the excitation light onto the undoped metal oxide powder. The light conversion module further includes a substrate comprising a depression and the undoped metal oxide powder is tightly packed and compressed into the depression. The substrate is maintained at a temperature in the range of 30 K-300 K.

In general, in another aspect, the invention provides a device for producing white light including a light conversion module and a light source. The light conversion module includes undoped metal oxide powder comprising particles having a size of less than 50 nm. The light source is configured to generate excitation light having a wavelength in the

near infrared (NIR) region. The excitation light is directed towards the undoped metal oxide powder, the undoped metal oxide powder is excited with the excitation light, and the excited undoped metal oxide powder emits white light having a continuous spectral distribution in the range of 440 nm to 900 nm. The device further includes a focusing  
5 element for focusing the excitation light onto the undoped metal oxide powder. The light conversion module further includes a substrate comprising a depression and the undoped metal oxide powder is tightly packed and compressed into the depression.

Among the advantages of the invention may be one or more of the following. The  
10 invention provides an inexpensive method and device for producing white light. The emitted light is multidirectional, bright, has characteristics similar to incandescent lamps and is about 30% more efficient than incandescent lamps.

#### 15 **Brief Description of the Drawings**

Referring to the figures, wherein like numerals represent like parts throughout the several views:

FIG. 1 is a graph of X-ray diffraction (XRD) patterns of samples of an embodiment of the  
20 invention;

FIG. 2 is a Scanning Electron Microscope (SEM) image of the samples of an embodiment;

25 FIG. 3 is a graph of a white light spectrum of an embodiment;

FIG. 4 is a graph of white light intensity dependence on pressure of an embodiment;

FIG. 5 is a graph of white light intensity variation with pumping power of an  
30 embodiment;

FIG.6 depicts the CCT, CRI, and illuminance values in (a), the white light spectrum measured using an illuminance meter in (b) and the CIE coordinates of the measured light in (c) for one embodiment; and

- 5 FIG. 7 is a schematic drawing of a device for producing white light from  $Y_2O_3$  nano-powders.

#### Detailed Description of the Invention

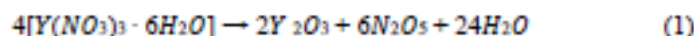
The present invention describes a method and a device for producing white light from  
10  $Y_2O_3$  nano-powders.

Referring to FIG. 7, a device 100 for producing white light from  $Y_2O_3$  nano-powders includes a light conversion module 120 and a light source 110. The light conversion module 120 includes undoped metal oxide powder 140 having particles with a size of less  
15 than 50 nm. The undoped metal oxide powder is compressed and tightly packed within a depression 132 of a substrate 130. The light source 110 generates excitation light having a wavelength in the near infrared region. In one example, the excitation light source 110 is a laser diode emitting light at 803.5 nm. The excitation light 115 is directed towards the undoped metal oxide powder 140, the undoped metal oxide powder is excited with the  
20 excitation light, and the excited undoped metal oxide powder emits white light having a continuous spectral distribution in the range of 440 nm to 900 nm. The excitation light 115 is focused onto the undoped metal oxide powder 140 via a focusing element 116, such as an optical fiber and/or a lens.

#### 25 *Experimental*

The materials used in the experiments were nano-sized  $Y_2O_3$  samples prepared by the inventors, and other commercially available  $Y_2O_3$  nano-samples. Nano-sized  $Y_2O_3$  samples were prepared by thermal decomposition of Yttrium-Alginate. This method is based on the thermal decomposition of alginate gels. In this process Yttrium Nitrate  
30 Hexahydrate  $Y(NO_3)_3 \cdot 6H_2O$  and low viscosity (250 cps of 2% solution) alginic acid sodium salts with analytical grade were used as starting reagents. The reaction that occurs

in thermal decomposition process is given in the following equation;



X-ray diffraction investigations were carried out with a Bruker AXS D8 Model (Cu-K $\alpha$  radiation) diffractometer at 40 kV and 30 mA setting in the  $2\theta$  range from 20° to 70° with scanning steps of 0.02°. A JEOL 6335F model scanning electron microscope was used to get SEM images of the samples.

Commercially available Y<sub>2</sub>O<sub>3</sub> nano-powders (<50 nm) were also purchased from Sigma Aldrich and used for the production of white light.

The continuous emission spectra of the samples were collected by pumping the samples with the output of a Laser Drive Inc. Model LDI-820 laser diode, which was operated at 803.5 nm. The luminescence signal was directed toward the entrance slit of a 1 m McPherson Model 2051 monochromator and chopped at a frequency of 250 Hz before entering the slit. The monochromator provided a resolution 0.8 Å with the slits set at 50 µm and a wavelength reproducibility of 0.1 Å. The optical signal was detected by Hamamatsu R1387 photomultiplier tube with an S-20 response, sent to an EG&G Model 5210 lock-in amplifier and recorded in a computer.

For the experiments in the temperature range 30-300 K, the samples were mounted on the cold finger ( sample holder) of a closed cycle Helium refrigerator. This system uses a Janis Research Model RD dewar connected with a Leybold Model RW2 compressor. The temperature of the sample holder was controlled by using a Lake Shore Cryotronics 331 Model temperature controller. The measurements of continuous luminescence spectra were conducted from 30 to 300 K and in the 440 – 870 nm wavelength range.

#### *Results of the Structural Characterization*

The cubic phase of the Ytria with the 10.604Å lattice parameter was determined by using XRD patterns. The particle sizes of the powders were estimated by using the Scherrer Equation reported below;

$$L = (K\lambda) / (\beta \cos\theta) \quad (2)$$

where L is the crystallite length, K is a constant that varies with the method of taking the breadth ( $0.89 < K < 1$ ),  $\lambda$  is the wavelength of the incident X-ray beam,  $\beta$  is the width of the peak at half maximum intensity of a specific phase (hkl) in radians and  $\theta$  is center angle of the peak. The (222) peak was used to estimate particle sizes. The XRD results are shown in Figure 1.

The SEM images confirmed the particle sizes estimated by using the Scherrer Equation, as shown in Figure 2.

#### *The Production of White Light and Results of the Spectroscopic Characterization*

The production of white light was achieved by illuminating the  $Y_2O_3$  nano-powder sample with the beam of the laser diode operating at 803.5 nm with an output power of 3 Watts. All measurements were performed with the sample's temperature in the region 30 K to 300 K. Since the  $Y_2O_3$  nano-powders were synthesized by using the cheap thermal decomposition technique, the cost of the production of white light by using such a method is very small.

The white light spectrum obtained in our measurements is shown in Figure 3. The spectrum is smooth and extends from 450 to 900 nm. The big spike present at ~800 nm is due to scattered laser light. The much smaller spikes at ~580 nm and ~620 nm are also due to scattered light from the laser diode that oscillates also at these wavelengths.

The inventors also checked the possible white light emission from commercially available Ytria nano-powders and were able to obtain it from these materials. The inventors didn't notice any dependence of the white light spectrum on the temperature of the sample holder.

All measurements were performed under low pressure because of the strong dependence of the white light on pressure. It was observed that the production of the white light

becomes easier under low pressure. The inventors were able to obtain white light under room temperature and atmospheric pressure conditions by using more pumping power than under vacuum. Figure 4 represents the white light intensity dependence on the pressure and, as it can be seen from this figure, while pressure reduces  $10^3$  times, the white light intensity increases 40 times.

The inventors also put some nitrogen and helium into the sample chamber and verified that the type of inert gas in the sample's environment is not responsible for the quenching of light. What quenches the white light is the pressure of the gas in the sample's chamber.

As seen from Figure 5, the inventors observed a notable change of the white light intensity with the varying pumping power. The parameter  $n$  presented in the figure represents the experimental dependence of the light intensity on the pumping power.

To measure the "color" of the white light the inventors calculated the CIE (International Commission on Illumination) coordinates and determined them as  $x=0.50$ ,  $y=0.44$  for focused and  $x=0.54$ ,  $y=0.44$  for unfocused LD beam. These CIE results are shown in Figure 6 (c). FIG. 6 also depicts the CCT, CRI, and illuminance values in (a), and the white light spectrum measured using an illuminance meter in (b).

Several embodiments of the present invention have been described. Nevertheless, it will be understood that various modifications may be made without departing from the spirit and scope of the invention. Accordingly, other embodiments are within the scope of the following claims.

What is claimed is:

1. A method for producing white light comprising:  
providing a light conversion module comprising undoped metal oxide powder comprising particles having a size of less than 50 nm;  
providing a light source configured to generate excitation light having a wavelength in the near infrared (NIR) region;  
directing the excitation light towards the undoped metal oxide powder and exciting the undoped metal oxide powder with the excitation light, and thereby causing the undoped metal oxide powder to emit white light having a continuous spectral distribution in the range of 440 nm to 900 nm.
2. The method of claim 1, wherein the undoped metal oxide powder comprises  $Y_2O_3$ .
3. The method of claim 1, wherein the light source comprises a laser diode configured to generate excitation light having a wavelength of 803.5 nm.
4. The method of claim 1, wherein the light conversion module further comprises a sealed container configured to encase the undoped metal oxide powder and the sealed container comprises a pressure of less than 8 mbars.
5. The method of claim 1, wherein said emitted white light comprises International Commission on Illumination (CIE) color coordinates of  $x=0.45$  and  $y=0.40$ .
6. The method of claim 1, wherein said emitted white light comprises a correlated color temperature (CCT) value in the range of 2700K to 3300K.
7. The method of claim 1, wherein said emitted white light comprises color rendering index (CRI) in the range of 90 to 100.
8. The method of claim 1, wherein the emitted white light intensity depends exponentially upon the light source power.

9. The method of claim 2, wherein the  $Y_2O_3$  is synthesized via thermal decomposition of Yttrium-Alginate.
- 5 10. The method of claim 1, wherein the undoped metal oxide powder comprises a purity of 99.999%.
11. The method of claim 1, wherein the light source is configured to provide an output power of at least 3 Watts.
- 10 12. The method of claim 1, further comprising focusing the excitation light onto the undoped metal oxide powder.
13. The method of claim 1, wherein the light conversion module further comprises a substrate comprising a depression and the undoped metal oxide powder is tightly packed and compressed into the depression.
- 15 14. The method of claim 13, wherein said substrate comprises a temperature in the range of 30 K-300 K.
- 20 15. A device for producing white light comprising:  
a light conversion module comprising undoped metal oxide powder comprising particles having a size of less than 50 nm;  
a light source configured to generate excitation light having a wavelength in the  
25 near infrared (NIR) region;  
wherein the excitation light is directed towards the undoped metal oxide powder, the undoped metal oxide powder is excited with the excitation light, and the excited undoped metal oxide powder emits white light having a continuous spectral distribution in the range of 440 nm to 900 nm.
- 30

16. The device of claim 15, wherein the undoped metal oxide powder comprises  $Y_2O_3$ .
17. The device of claim 15, wherein the light source comprises a laser diode  
5 configured to generate excitation light having a wavelength of 803.5 nm.
18. The device of claim 15, wherein the light conversion module further comprises a sealed container configured to encase the undoped metal oxide powder and wherein the sealed container comprises a pressure of less than 8 mbars.
- 10 19. The device of claim 15, wherein the emitted white light intensity depends exponentially upon the light source power.
20. The device of claim 15, wherein the undoped metal oxide powder comprises a  
15 purity of 99.999%.
21. The device of claim 15, further comprising a focusing element for focusing the excitation light onto the undoped metal oxide powder.
- 20 22. The device of claim 15, wherein the light conversion module further comprises a substrate comprising a depression and the undoped metal oxide powder is tightly packed and compressed into the depression.

25

30

### Abstract

A device for producing white light includes a light conversion module and a light source. The light conversion module includes undoped metal oxide powder comprising particles having a size of less than 50 nm. The light source generates excitation light having a wavelength in the near infrared region. The excitation light is directed towards the undoped metal oxide powder, the undoped metal oxide powder is excited with the excitation light, and the excited undoped metal oxide powder emits white light having a continuous spectral distribution in the range of 440 nm to 900 nm.

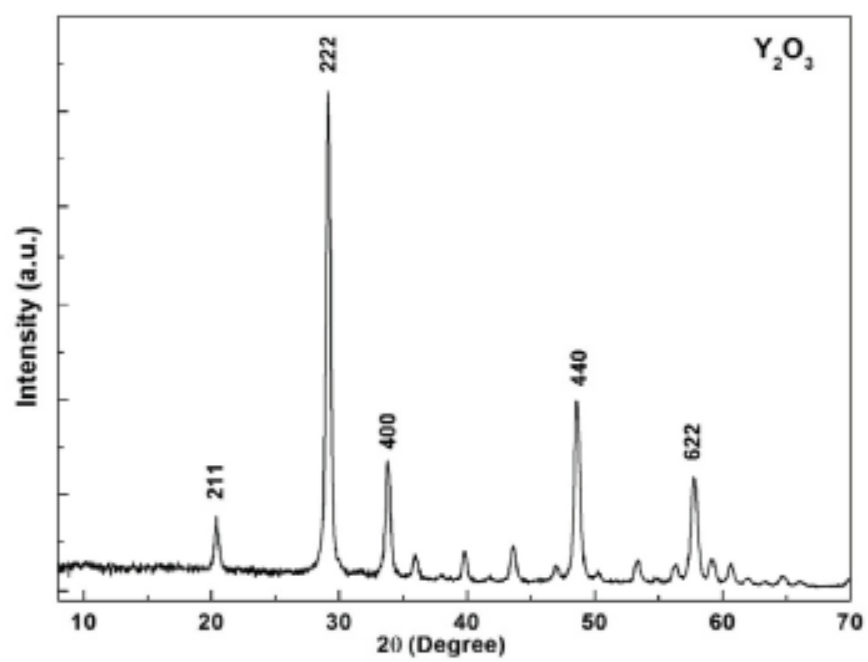
10

15

20

+

1/7

*FIG. 1*

+

+

2/7

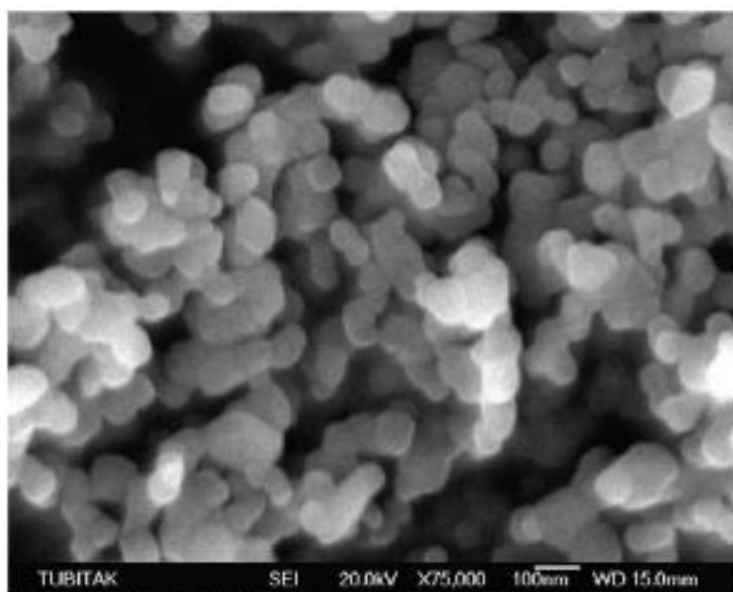


*FIG. 2*

+

+

3/7

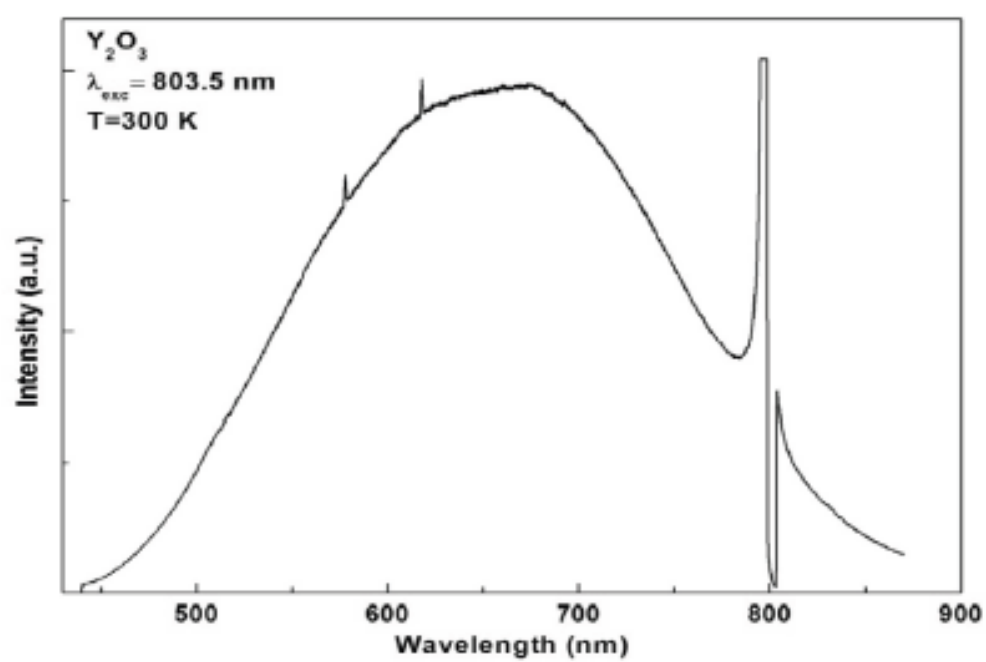


FIG. 3

+

4/7

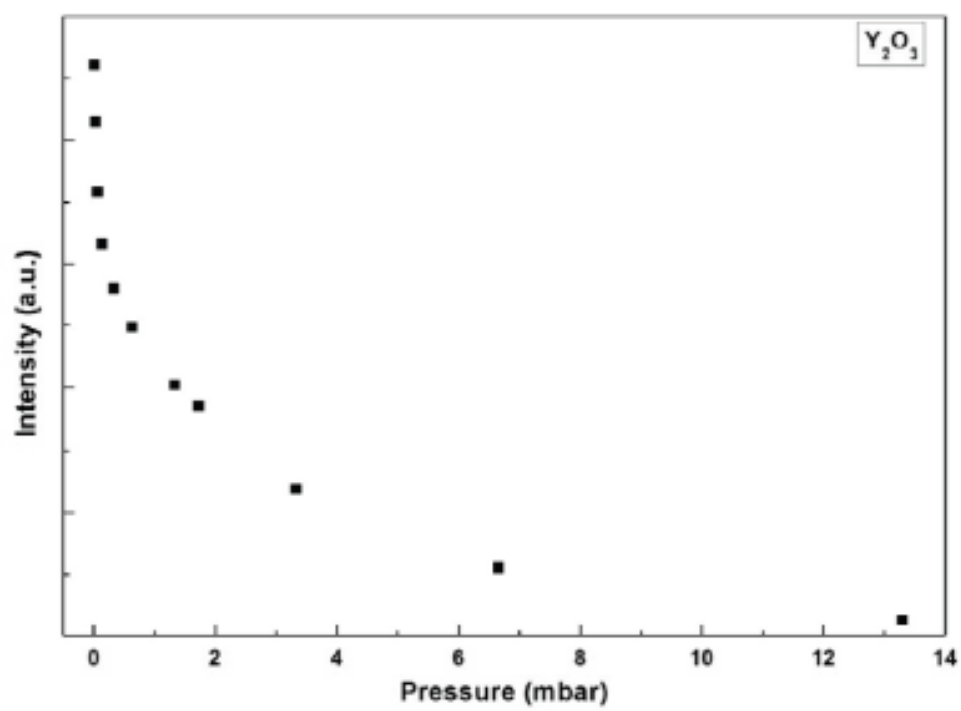


FIG. 4

5/7

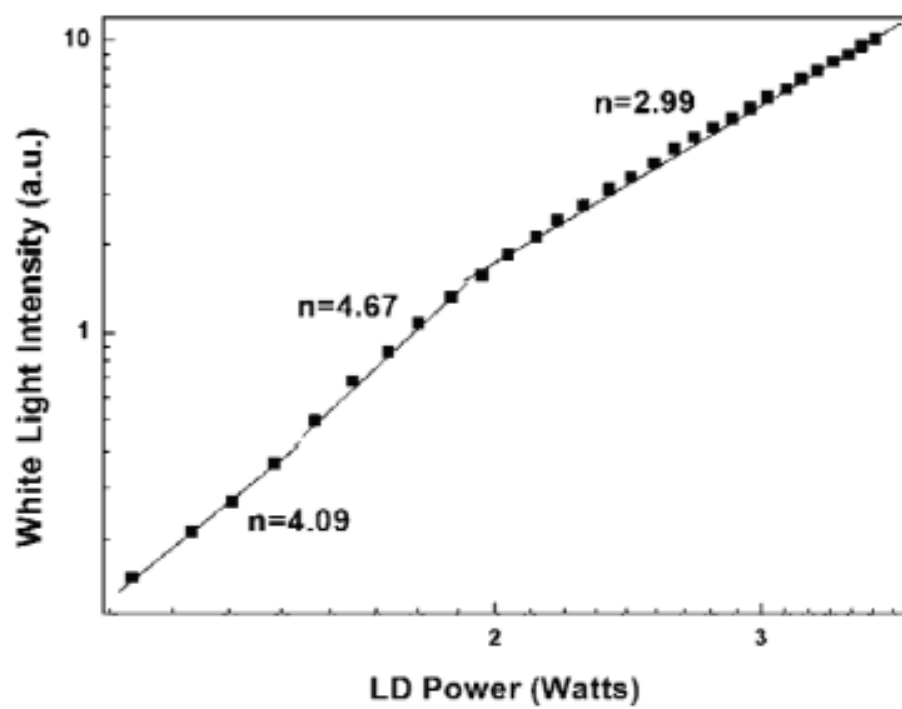


FIG. 5

+

6/7

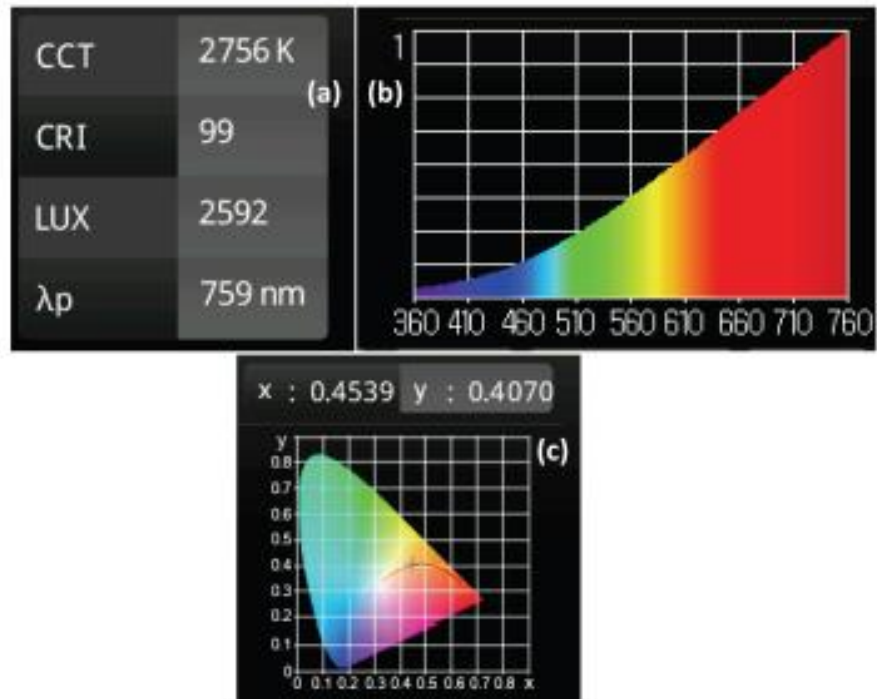


FIG. 6

+

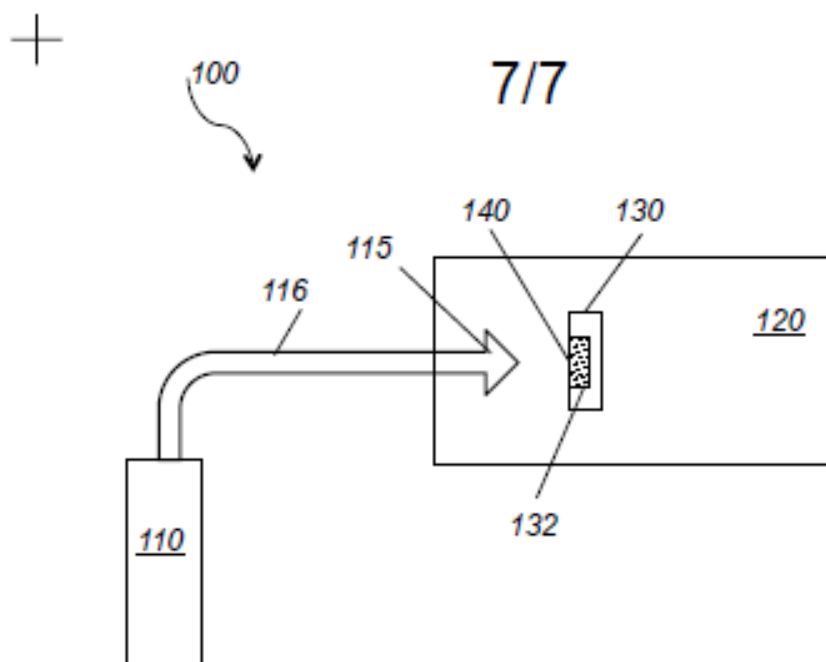


FIG. 7

## CURRICULUM VITAE



**Name Surname** :Gökhan BİLİR  
**Place and Date of Birth** :Ankara / 05.09.1980  
**Address** :Istanbul Technical University, Department of Physics Engineering, B4-208, 34469 Maslak/Istanbul  
**E-Mail** :[bilirg@itu.edu.tr](mailto:bilirg@itu.edu.tr)  
**B.Sc.** :Physics / Kafkas University  
**M.Sc.** :Physics / Kafkas University

## PUBLICATIONS/PRESENTATIONS ON THE THESIS

### PUBLICATIONS

**G. Bilir**, G. Ozen, B. Di Bartolo, “Synthesis and Spectral Characterization of Yttrium Oxide Nano- powders Doped with  $\text{Nd}^{3+}$  Ions with a Large Range of Concentrations” Opt. Mater., **42C**, (2015) 281-286.

**Gökhan Bilir**, Gönül Özen, Baldassare Di Bartolo, “Peculiar Effects Accompanying the Production of White Light by IR Excited Nano-particles”, Opt. Spectrosc., **118**(1) (2015) 114-117.

**Gökhan Bilir**, Joseph Liguori, “Laser diode induced white light emission of  $\gamma\text{-Al}_2\text{O}_3$  nano-powders ”, J. Lumin., **153** (2014) 350-355.

**G. Bilir**, G. Özen, J. Collins, M. Cesaria, B. Di Bartolo, “Unconventional Production of Bright White Light Emission by Nd-doped and Nominally Un-doped  $\text{Y}_2\text{O}_3$  nano-powders”, IEEE Photonics Journal, **6**(4) (2014) 8200518.

**G. Bilir**, G. Özen, M. Bettinelli, F. Piccinelli, M. Cesaria, B. Di Bartolo “Broadband Visible Light Emission from Nominally Un-doped and  $\text{Cr}^{3+}$  doped Garnet Nano-powders”, IEEE Photonics Journal, **6**(4) (2014) 2201211.

Hakan Kaygusuz, **Gökhan Bilir**, Filiz Tezcan, F. Bedia Erim, Gönül Özen, Particuology, **14** (2014) 19-23.

**Gökhan Bilir**, Baldassare Di Bartolo, “Production of bright, wideband white light from  $\text{Y}_2\text{O}_3$  nano-powders induced by laser diode emission”, Opt. Mater., **36** (8) (2014) 1357-1360.

**G. Bilir**, G. Ozen, J. Collins, B. Di Bartolo, “Fabrication and Spectral Investigation of  $\text{Y}_2\text{O}_3:\text{Nd}^{3+}$  nanoparticles”, Appl. Phys. A, **115**(1) (2014) 263-273.

**Gokhan Bilir**, Gonul Ozen, John Collins, Baldassare Di Bartolo, “Synthesis and Spectroscopy of Nanoscale  $\text{Y}_2\text{O}_3:\text{Nd}^{3+}$  Phosphors”, ECS Transactions, **50**(41) (2013) 1-7.

## BOOK CHAPTERS

**Gokhan Bilir**, Gonul Ozen, John Collins, Maura Cesaria, Baldassare Di Bartolo, “Fluoresence–Based Studies of Nanoparticles” in Nano-structures for Optics and Photonics, edited by B. Di Bartolo, J. Collins, L. Silvestri, pp. 257-272 (2015).

Maura Cesaria, **Gokhan Bilir**, Gonul Ozen, M. Bettinelli, John Collins, Fabio Piccinelli, Baldassare Di Bartolo, “Incandescent Lamp-like White Light Emission from Doped and Undoped Oxide Nanopowders” in Nano-structures for Optics and Photonics, edited by B. Di Bartolo, J. Collins, L. Silvestri, pp. 273-284 (2015).

## PATENTS

**Gökhan Bilir**, Baldassare Di Bartolo, “Production of Bright, Wideband White Light from  $\text{Y}_2\text{O}_3$  Nano-powders Induced by Laser Diode Emission” Appl. # 14298602, 2014

## PRESENTATIONS

**G. Bilir**, G. Ozen, J. Collins, B. Di Bartolo, “Emission of White Light from Doped and Un-doped Oxide Nano-powders”, ECS Fall Meeting 2014, Cancun, Mexico.

**G. Bilir**, G. Ozen, J. Collins, B. Di Bartolo, “Investigation of the Emission Properties and the Effect of  $\text{Nd}^{3+}$  Concentration in  $\text{Nd}^{3+}$  doped  $\text{Y}_2\text{O}_3$  nano-powders” ICL 2014, Wroclow-POLAND.

**Gokhan Bilir**, Gonul Ozen, John Collins, Baldassare Di Bartolo, “White Light Emission from  $\text{Y}_2\text{O}_3$  Nano-powders Induced by Laser Diode Excitation” MRS Fall Meeting&Exhibition, Boston, MA, December 2013 – Poster Presentation.

**G. Bilir**, G. Ozen, J. Collins, B. Di Bartolo, “Fabrication and Spectral Investigation of  $\text{Y}_2\text{O}_3:\text{Nd}^{3+}$  Nano-Particles” 224<sup>th</sup> ECS Meeting, San Francisco, California, USA, October 2013 – Oral Presentation

**Gökhan Bilir**, Marco Bettinelli, Fabio Piccinelli, John Collins, Maura Cesaria, Gonul Ozen and Baldassare Di Bartolo, “Spectroscopic Studies of Nanoparticles” International School of Atomic and Molecular Spectroscopy Nano-structures for Optics and Photonics, Erice-Italy, 4-19 July 2013 – Oral Presentation

**G. Bilir**, G. Ozen, J. Collins, B. Di Bartolo, “Synthesis and Spectroscopy of Nanoscale  $\text{Y}_2\text{O}_3:\text{Nd}^{3+}$  Phosphors” 222<sup>nd</sup> ECS Meeting, Honolulu, Hawaii, USA, October 2012

**G. Bilir**, G. Ozen, J. Collins, B. Di Bartolo, “Spectroscopy of  $\text{Y}_2\text{O}_3$  Nano-powders Doped with Neodymium” International School of Atomic and Molecular Spectroscopy Nano-structures for Optics and Photonics, Workshop, Erice-Italy, 3-9 July 2012 – Oral Presentation

**G. Bilir**, G. Ozen, “Optical and Structural Characterization of  $\text{Y}_2\text{O}_3:\text{Nd}^{3+}$  Phosphors via Thermal Decomposition Method” NanoTR – VI, Çeşme, İzmir, Turkey, 2010

**G. Bilir** and G. Ozen, "Luminescence Properties of Nanoscale  $\text{Y}_2\text{O}_3:\text{Nd}^{3+}$  Phosphors," in Solid-State and Organic Lighting, OSA Technical Digest (CD) (Optical Society of America, 2010), paper JWA10

## OTHER PUBLICATIONS, PRESENTATIONS

**Gokhan Bilir**, Laser Phys. Lett., 12 (2015) 045901.

M. Erdem, M. K. Ekmekci, H. Orucu and **G. Bilir**, “Structural and Spectroscopic Properties of  $\delta$ -Y<sub>2</sub>Si<sub>2</sub>O<sub>7</sub> Nanopowders Activated with Nd<sup>3+</sup> Ions” Int. J. Appl. Ceram. Tec., Accepted (August 2014).

**G. Bilir**, N. Mustafaoglu, G. Ozen, B. Di Bartolo, Spectrochim. Acta A, **83** (2011) 314-321.

**G. Bilir**, G. Ozen, Physica B:Condensed Matter, **406** (2011) 4007-4013.

**G. Bilir**, G. Ozen, D. Tatar, M.L. Öveçoğlu, Opt. Commun., **284** (2011) 863-868.

M. Karabulut, **G. Bilir**, G.M. Mamedov, A. Seyhan, R. Turan, J. Lumin., **128** (2008) 1551-1555.

## PRESENTATIONS

Joseph Liguori, **Gökhan Bilir**, “A new source of White Light: Oxide Nano-powders Illuminated by a Laser Diode” NES APS Spring 2014 Meeting of the New England Section of the American Physical Society, Boston College, Chestnut Hill, MA, April 2014 – Oral Presentation

Gaozan Ding, Xuesheng Chen, Baldassare Di Bartolo, **Gökhan Bilir**, “Optical Properties of Erbium or Neodymium Ions in Different Kinds of Host Materials- Ceramics versus Single Crystals” NES APS Spring 2014 Meeting of the New England Section of the American Physical Society, Boston College, Chestnut Hill, MA, April 2014 – Poster Presentation

J. Liguori, **G. Bilir**, G. Özen, B. Di Bartolo, “Non-conventional white light emission of Al<sub>2</sub>O<sub>3</sub> induced by laser diode emission”, APS Fall 2013 Meeting of the New England Section of the American Physical Society, Bridgewater-MA, October 2013 – Oral Presentation

L. Wu, X. Chen, **G. Bilir**, B. Di Bartolo, “Investigation of Optical Ceramic Materials Nd: PLZT at different Nd Concentrations and Temperatures” APS Spring 2013 Meeting of the New England Section of the American Physical Society, Bridgewater-MA, March 2013 – Poster Presentation

H. Mammadov, M. Karabulut, **G. Bilir**, R. Turan, A. Seyhan “Azot İyonu Ekilmiş GaSe<N> Kristallerinde Eksiton Fotolüminesansı” TFD 23rd International Conference, Muğla, Turkey, 2005

